Cranfield University

Andrew John Bell

Temperatures in High Efficiency Deep Grinding

School of Applied Sciences

PhD Thesis

Cranfield University

School of Applied Sciences

PhD Thesis

2009

Andrew John Bell

Temperatures in High Efficiency Deep Grinding

Supervisors: Prof. D.J. Stephenson

&

Dr. T. Jin

February 2009

This thesis is submitted in partial fulfilment of the requirements for the Degree of Doctor of Philosophy

Abstract

This research considers the temperatures generated in the workpiece during profile and cylindrical traverse grinding in the High Efficiency Deep Grinding (HEDG) regime. The HEDG regime takes large depths of cut at high wheel and workpiece speeds to create a highly efficient material removal process. This aggressive processing generates high temperatures in the contact zone between the wheel and workpiece. However, the beneficial contact angle and the rapid removal of the heated wheel – workpiece contact zone results in low temperatures in the finished surface.

Temperatures in the ground surface can be predicted with knowledge of the specific grinding energy and the grinding parameters used. Specific grinding energies recorded at high specific material removal rates demonstrated a constant value of specific grinding energy dependent on cutting and contact conditions, improving accuracy of the predictive model. This was combined with a new approach to burn threshold modelling, which demonstrated an improved division of damaged and undamaged surfaces.

Cutting and contact conditions in the grinding profile vary dependent on their position. This thesis shows how temperatures vary with location and estimates the partitioning of the heat flux to the regions of the grinding profile. This suggested a constant partitioning of energy to each of the three surfaces considered independently of specific material removal rates. Further a potential link was shown between the surface and the sidewall of the grinding profile, which allows temperatures in a secondary surface to be predicted given knowledge of that in the primary.

Finally, the work has demonstrated the feasibility of the Superabrasive Turning process. Using small values of feed per turn and high workpiece feedrates promoted high values of removal rate with low depths of thermal penetration in the as ground surface. Thus the process has become viable for high speed cylindrical traverse grinding.

Acknowledgements

Firstly I would like to thank my supervisors Professor D.J. Stephenson and Dr. T. Jin for their guidance in the research process and helping me to maintain my focus in a world of so many interesting things.

Within the School of Applied Sciences, Dr Ian Walton, Mr A. Baldwin and Mr J. Hedge for their help in preparing the machines and samples for the development of the research.

To Mum, Dad & Chris, this is the result of thirty years of unwavering belief and patience. You taught me to read, to measure twice and cut once, to fight for what I believe in. I am a reflection of your time and effort, thank you.

Table of Figures

Table of Tables

Notation

A	Material constant
A_{corner}	Area of the peripheral face and peripheral edge in surface and cylindrical traverse grinding respectively
a_e	Depth of cut
$A_{sidewall}$	Area of the side face and leading edge in surface and cylindrical traverse grinding respectively
$A_{surface}$	Area of the edge radius and leading edge radius in surface and cylindrical traverse grinding respectively
b	Width of cut (also feed per turn in cylindrical traverse grinding)
C	C-factor for grinding
c	Specific heat capacity of the workpiece material
d_e	Equivalent workpiece diameter
D_w	Diameter of the workpiece in cylindrical grinding
e_c	Specific grinding energy
e_{ch}	Limiting grinding chip energy
$^{fi}/_{co}$	Ratio of the temperature in the contact surface to the temperature in the finished surface
h	Length of chord
h_{ch}	Convection coefficient to the grinding chip
h_f	Convection coefficient to the workpiece
h_s	Convection coefficient to the grinding wheel
h_w	Convection coefficient to the workpiece
k	Thermal conductivity
L	Peclet number
l_c	Wheel – workpiece contact length
P_{net}	Net grinding power or power required in material removal
Q'_w	Specific material removal rate
q_{ch}	Heat flux to the grinding chip
q_f	Heat flux to the grinding fluid
q_s	Heat flux to the grinding wheel
q_t	Total heat flux generated during grinding
q_w	Heat flux to the workpiece
r_0	Abrasive grain radius
R_s	Wheel partition ratio

R_w	Workpiece partition ration
r_{we}	Wheel edge radius
r_{wh}	Wheel radius
r_{wk}	Workpiece radius
R_{ws}	Wheel – workpiece partition ratio
t	Chip formation process constant
T_b	Boiling temperature of the grinding fluid
T_{max}	Maximum temperature
T_{mp}	Melting point of the grinding chip material
T_s	Temperature at the finished workpiece surface
v_s	Wheel speed
v_t	Traverse velocity in cylindrical traverse grinding
v_w	Workpiece velocity (rotational velocity in cylindrical grinding)
α	Thermal diffusivity
β_w	Thermal property = $\sqrt{k \cdot \rho \cdot c}$
θ_m	Maximum dimensionless temperature rise
θ_m	Maximum temperature rise
θ_{ms}	Maximum surface temperature rise
θ_{wh}	Wheel sector angle in cylindrical grinding
θ_{wk}	Workpiece sector angle in cylindrical grinding
ρ	Density of the workpiece material

1.0 Introduction

High Efficiency Deep Grinding (HEDG) is a relatively new and novel approach to the requirement of reducing manufacturing costs and improving machining precision. As with any new technology, the step from laboratory research to industrial application requires thorough process prove-out. This thesis forms an integral part of the development of an industrially viable HEDG process as part of the Cranfield Innovative Manufacturing Research Centre (IMRC) funded SATURN project.

The SATURN project was developed to study the Superabrasive Turning process, essentially cylindrical traverse grinding with electroplated CBN wheels when undertaken with HEDG parameters. Of particular importance to the research was an improved understanding of the thermal behaviour of the HEDG process and the ability to predict accurately when and where thermal damage may occur. This required consideration not only of the cylindrical traverse grinding process, but also of its surface grinding counterpart, simple profile grinding.

The research has been supported by a number of industrial collaborators throughout the supply chain, each with their own particular interest in one of the many fields of grinding. Renold Precision Technologies and their subsidiary Holroyd are machine tool manufacturers and produce the Edgetek range of machine tools; they are the supplier of the Edgetek machine tools used for the development of the HEDG process. Saint-Gobain manufactures the Cubic Boron Nitride abrasives and also their own ranges of electroplated grinding wheels that were used exclusively throughout the grinding trials. Castrol are one of a number of cutting fluids manufacturers and supplied all cutting fluids for this research.

1.1 Background to the Research

Single set-up machining is highly desirable for controlling tolerances and reducing manufacturing costs. Traditional process chains for high tolerance cylindrical components often include a rough turning or turn-milling process, followed by finish turning and grinding where required. Each process in the chain requires a different machine tool tailored to the individual job for successful completion. If the machine tool used for finish grinding could also be used for the stock removal process, several

stages could potentially be removed from the process chain. Figure 1.1 demonstrates this idea schematically.

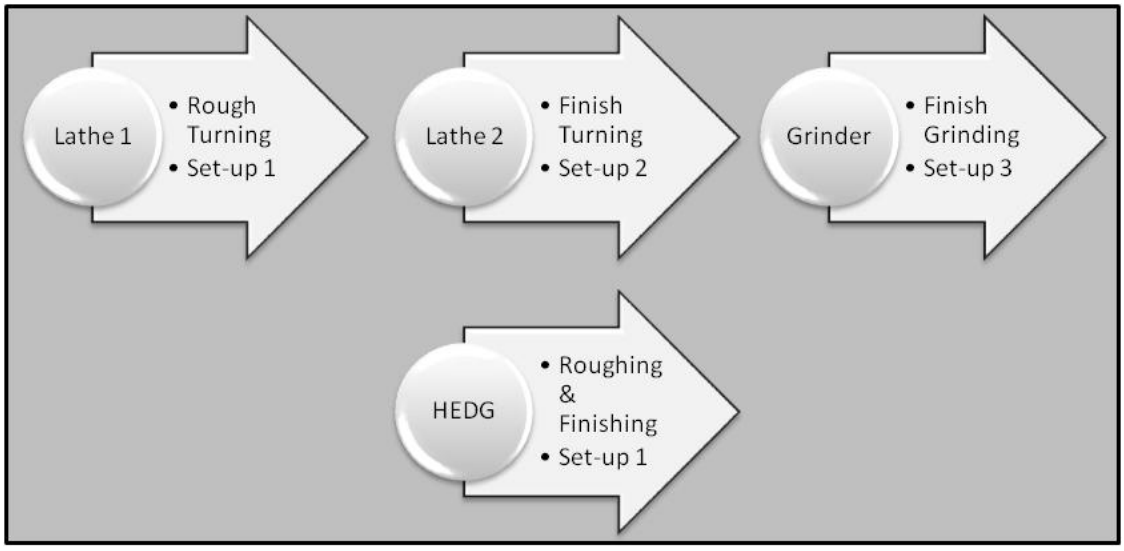

Figure 1.1 Comparison of the process chain for a cylindrical process using High Efficiency Deep Grinding versus a conventional process chain

The grinding process generates a high temperature in the workpiece as a result of the complex cutting action. High temperatures in the workpiece can result in subsurface damage. The effect of thermal damage on the life-cycle performance of a ground component is adverse. Whilst it is desirable to avoid thermally damaged components, it is also desirable to discard only those components which are truly damaged. Non-destructive testing methods detect only when the surface has already been damaged and they also require specialised equipment which may necessitate off-line testing of components. Non-destructive testing is therefore a non value-added process.

Predictive models of grinding burn tend to overestimate the temperature achieved and hence the effects experienced in the ground surface. Overestimation of the surface temperature results in parts being unnecessarily discarded. In spite of this tendency to overestimation, predictive models can be incorporated into the machine control system giving immediate warning when damaging conditions are achieved. Further they can be used to optimise machining in the process design phase. There is therefore a strong case for the development of accurate models for the prediction of thermal damage in ground surfaces.

The Superabrasive Turning process creates complex contact geometry during grinding. By both rotating and traversing the workpiece the process produces a helical form. This generates a heat flux from the side of the wheel in addition to that from the wheel periphery. This effect is similar in surface profile grinding where a shoulder feature is also generated. Whilst it is possible to measure the power consumption and hence indirectly estimate the grinding temperature, it is not possible to distinguish how that thermal energy is distributed around the profile generated. There is therefore a need for research to further the understanding of the energy partitioning and temperatures in profile grinding.

1.2 Research Objectives

Given the background to the research, it is clearly desirable to be able to predict and control grinding temperatures in real time in order that industry might take advantage of the HEDG process for conditions where a profile or shoulder is required. In order to achieve this, an understanding of the temperature profile at varying locations around the profile was required. Thus the aim of the research is:

- *To further our knowledge of the thermal characteristics of High Efficiency Deep Grinding for conditions which include a profile or grinding shoulder*

This led to the following objectives:

- *To provide data on the thermal profile formed during simple surface profile and cylindrical traverse grinding*
- *To provide data on the effect of the shoulder on the workpiece surface temperatures, grinding energies and grinding power.*
- *To create a burn threshold diagram suitable for HEDG grinding and appropriate to the removal rates to be experienced in SATURN*
- *To provide data on the behaviour of the grinding energy with increasing specific material removal rate*

These objectives have been achieved with a combination of surface and cylindrical grinding trials. These trials have focussed on those relationships which are essential to the development of a set of tools for the prediction of temperatures in High Efficiency Deep Grinding.

1.3 Structure of the Thesis

This thesis presents work aimed at an improved understanding of temperature prediction in High Efficiency Deep Grinding. The work begins by considering background material pertinent to the measurement and prediction of grinding temperatures and thermal damage. This is presented in the literature review of chapter 2. The review initially considers the grinding process as a background to the development of the High Efficiency Deep Grinding process such that the relative behaviour of this compared to other processes can be understood. This is followed by a study of temperature measurement techniques suitable for the machine tool environment. The literature review finishes with an overview of grinding burn and our ability to predict its occurrence. Prediction of grinding burn leads directly to a review of the prediction of grinding temperatures.

Chapter 3 presents details of the experimental methodology, establishing trials with a view to an understanding of the thermal characteristics of the process. Trials designed to highlight the trends in specific grinding energy are presented. These were used to assist the development of more accurate grinding temperature prediction from given process parameters. Details of the temperature measurement trials are also described in this chapter. This considered both the method of temperature measurement and its application to the processes under consideration.

Chapters 4 and 5 present the results of the experiments outlined in Chapter 3. Relationships between specific material removal rate and specific grinding energy and grinding powers are demonstrated leading to an example burn threshold diagram in Chapter 4. This is followed by the results presented in Chapter 5, which consider the temperature measurement process and the resulting thermal profiles generated during the grinding process. Surface grinding, simple surface profile grinding and cylindrical traverse grinding are also considered.

Chapter 6 is a discussion of the results of chapters 4 and 5 and provides examples of the new approach to the burn threshold diagram. The discussion also presents a study of the energy partitioning in the profile grinding process. Finally the conclusions of the thesis and recommended further work are presented in Chapter 7.

2 Review of the Literature

Manufacturing industry has experienced significant changes in recent years as increasing material and labour costs have taken a necessary toll on its competitiveness. Thus a drive exists for significant reductions in product touch and process time. An effective response to these constraints in the metal cutting field can be to reduce processing times with the use of advanced machining technologies.

Several emergent technologies exist in this field, based around the principle of single set-up, high performance machining; examples of which would include Viper Grinding, Prismatic Machining and High Efficiency Deep Grinding (HEDG), the latter being the focus of this particular thesis.

The literature review will consider the fundamentals of the HEDG process and its predecessors, creep and high speed grinding, as a precursor to the HEDG technology. Following this, temperature measurement techniques employed in both grinding and where relevant alternative metal cutting processes will be considered as a precursor to understanding the development of a temperature measurement methodology for an aggressive environment. Finally the review will consider models of burn threshold applied to the process in terms of the development of the residual stress profile and its prediction via thermal modelling techniques.

2.1 The Grinding Process

According to the U.S. Census Bureau (2006), 2005 saw the shipment of some 792 external cylindrical grinding machines and 564 surface grinding machines with individual values of over $3,025 and a total combined value of over $80 million. Grinding is a major aspect of the production industry, meeting the expectations of Merchant (1971) in terms of both the requirement for grinding processes and the technological advancements attained.

Broadly described by Armarego & Brown (1969), grinding is one of a number of abrasive processes including honing, lapping and superfinishing. The authors describe the abrasive process as a metal cutting process involving hard, sharp and friable abrasive grains, which as a result of their ability to produce a fine surface finish are often considered as finishing processes. It is stated that there are many instances in which grinding is used for stock removal with the example of rough grinding in foundry

work being presented. They go on to consider the earliest forms of abrasive process, which it is suggested began with the use of sandstone for the shaping of tools followed by the use of emery which was found to be more efficient. Emery is suggested to have been originally used as a loose material before it was eventually bonded with clay to form a wheel.

Armarego & Brown (1969) discuss grinding in its role as the most common and best known of the abrasive processes, abrasives are bonded to a wheel or cup, which is power driven. The process consists of a random dispersion of grains in the wheel, taking very small but frequent cuts and producing very small chips. The authors divide grinding operations into three major types as shown in figure 2.1. This should be considered in addition to the specialised regimes described in the following pages, which include creep feed, high speed and high efficiency deep grinding primarily utilised in the broad cylindrical and surface grinding operations.

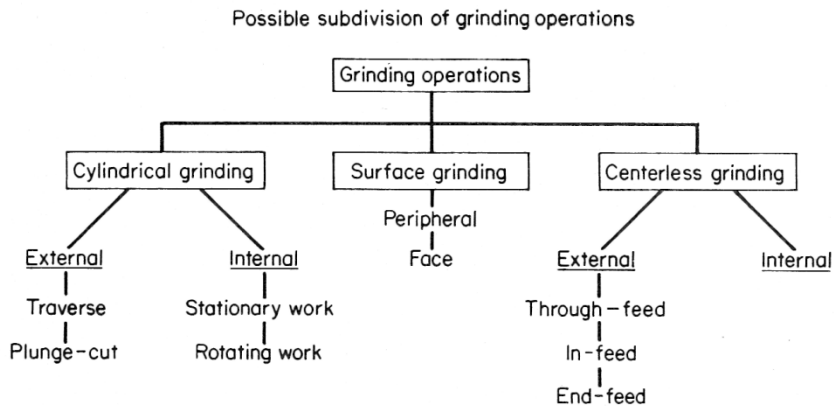

Figure 2.1 Suggested subdivision of grinding operations after Armarego & Brown (1969)

2.1.1 Creep Feed Grinding

Creep feed grinding exhibits a number of benefits over traditional grinding processes. Slow rates of feed with large depths of cut and high levels of coolant application promote a low temperature at the contact and a high quality finished surface.

The creep feed grinding process is described by Malkin (1989) as being characterised by the use of slow workpiece velocities combined with large depths of cut. He describes

the increase in depth of cut as a factor of a hundred or thousand times those encountered in regular grinding processes. Shaw (1996) describes the creep feed grinding process in comparison to the conventional pendulum grinding process and presents the schematic comparison of figure 2.2. The author comments on the processes ability to remove the required material in a single pass, when compared to the multiple passes of pendulum grinding and highlights its use in the production of deep slots in hydraulic pumps and fir tree patterns in turbine blade roots. Shaw (1996) continues to state that the most important aspect of a successful creep feed grinding process is the application of coolant. Coolant must be applied such as to provide uniform coverage of the wheel – work contact zone in order to reduce the high contact zone temperatures generated. The wheel is required to have an open structure such that pockets of fluid can be carried into the contact zone, whilst the use of an air scraper to prevent the boundary layer of air around the wheel deflecting the coolant is advised.

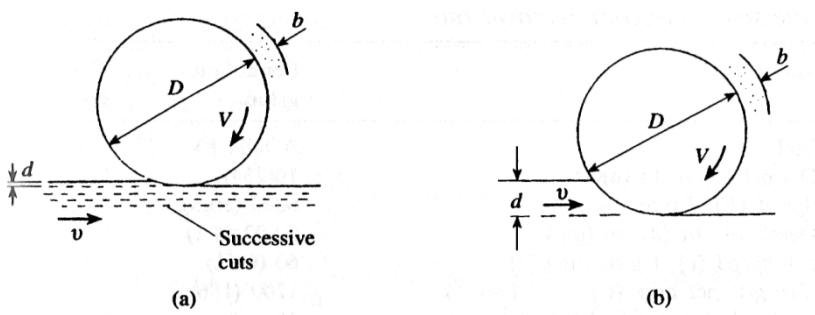

Figure 2.2 Comparison of pendulum and creep feed grinding processes after Shaw (1996)

Describing the process Werner (1979) distinguishes creep feed grinding from conventional grinding regimes by four characteristic features. The total grinding force and wheel-work contact zone temperatures are increased, whilst the individual grit force and work surface temperature are decreased. The increase in total grinding force is described as the result of the increased depth of cut, this increase results in a contact length which increases by a factor of 30 to 100 times. This results in an increased number of grits in the contact zone and hence a decrease in the individual grit force. The greater energy requirement of the creep feed process results in an increased heat influx per unit contact area. However, the larger contact zone and low heat source velocity result in a greater time for heat dissipation into the work surface, the greater volume yielding a lower overall temperature. The author concludes that the creep feed process

can be used to dramatically increase productivity when large amounts of stock have to be removed and the surface requirements are high. It should be noted that in some instances creep feed grinding does not create a greater energy requirement and the slow movement of the heat source can also result in elevated temperatures if uncontrolled.

2.1.2 High Speed Grinding

For the purposes of this thesis, high speed grinding refers to those grinding processes in which a wheel speed of 60 m/s is exceeded. Increasing the speed of the grinding wheel for a given grinding process produces a number of desirable effects. König et al. (1971) presents an early overview of work in the field compiling results from several authors and presenting evidence (figure 2.3) of the decreasing cutting force, surface roughness and wheel wear as a result of increasing wheel speeds.

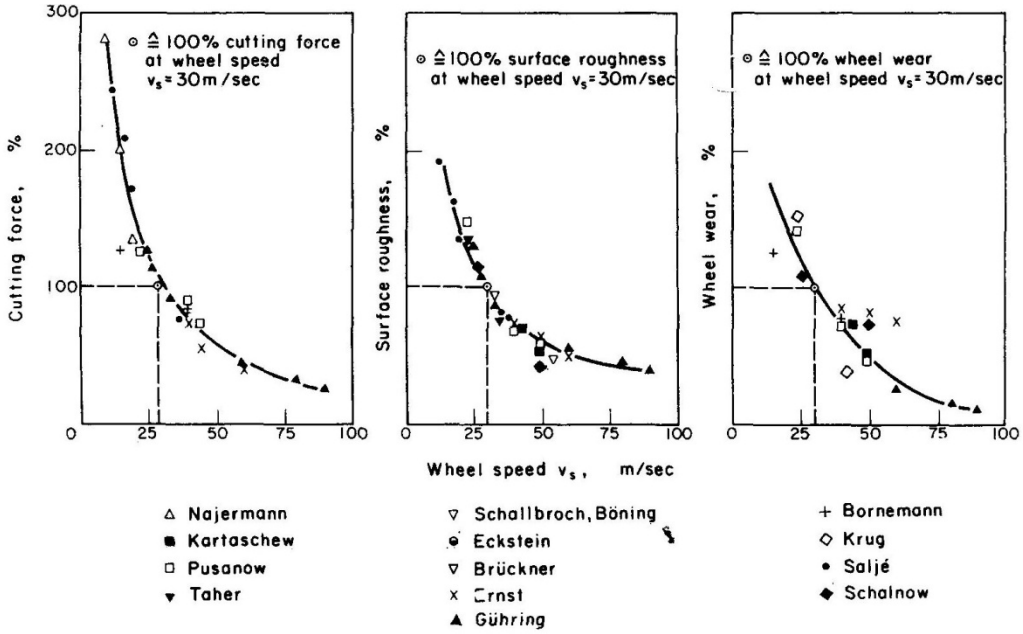

Figure 2.3 Changes in cutting force, surface roughness and wheel wear with increasing wheel speed after König et al. (1971)

High wheel speeds in modern grinding applications are largely the result of improvements in grinding wheel technology. Wheel requirements for successful high speed grinding are described by Jackson et al. (2001). The authors suggest a wheel exhibiting good damping characteristics, high rigidity and good thermal properties having a thin layer of abrasive material attached to a body of high mechanical strength. The most suitable abrasive for high speed grinding applications is cubic boron nitride (CBN), Tawakoli (1993) for example highlights the use of electroplated CBN steel

wheels, allowing wheel speeds to exceed 200m/s. Jackson et al. (2001) also comment on the suitability of CBN considering its high hardness and thermal and chemical stability to result in an ideal product for high speed ferrous machining. The authors continue to describe the application of electroplating as the preferred bonding system with steel wheels and consider cutting speeds in excess of 280m/s to be possible.

2.1.3 High Efficiency Deep Grinding

The High Efficiency Deep Grinding (HEDG) regime is the result of the development of wheel and machine technologies capable of delivering both high wheel and workpiece feedrates with a large depth of cut. The process is the product of the high speed and creep feed grinding regimes utilising the benefits of high wheel speeds at large depths of cut and feedrates to achieve high stock removal rates.

Described by Tawakoli (1993), the process readily achieves specific stock removal rates in excess of 50mm^3/mm·s whilst improving tool wear, specific energy requirement and surface integrity. Table 2.1 demonstrates typical values associated with common grinding techniques when compared to the HEDG regime.

	Method		
Machine Settings	**Reciprocating Grinding**	**Creep-feed Grinding**	**HEDG**
Depth of Cut a_e	Low 0.001 – 0.05mm	High 0.1-30mm	High 0.1 – 30mm
Workpiece Speed v_w	High 1 – 30m/min	Low 0.05 – 0.5m/min	High 0.5 – 10m/min
Wheel Speed v_s	Low 20 – 60m/s	Low 20 – 60m/s	High 80 – 200m/s
Specific Removal Rate	Low 0.1 – 10mm^3/mm·s	Low 0.1 – 10mm^3/mm·s	High 50 – 2000mm^3/mm·s

Table 2.1 Typical grinding parameters for common grinding techniques after Tawakoli (1993)

Tawakoli (1993) also highlights the low workpiece surface temperatures resulting from the HEDG process. The beneficial contact conditions, high angle of inclination and high wheel and workpiece speeds result in a low workpiece surface temperature and the

temperature trend presented in figure 2.4. It is to be questioned whether the same profile would exist in the sidewall, where no benefit from an angle of inclination is to be found.

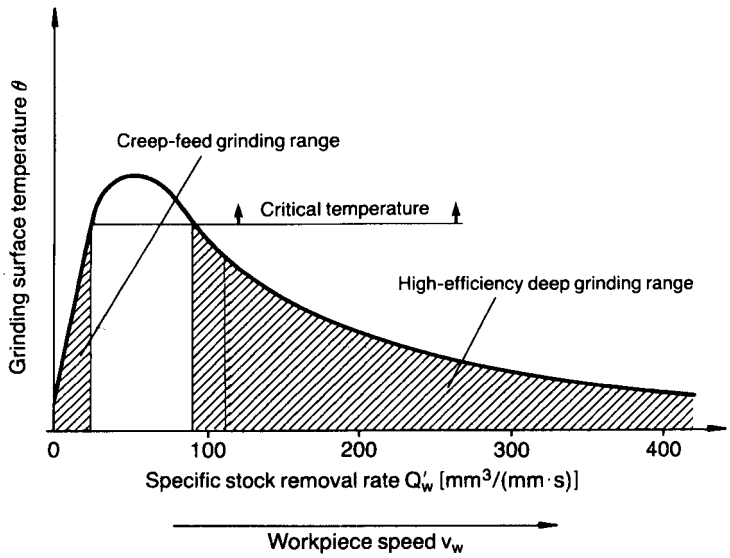

Figure 2.4 Surface temperature trend in HEDG after Tawakoli (1993)

Research in the field of High-performance profile grinding by Werner and Tawakoli (1988a), presents an example of the machine requirements for the HEDG process. The higher grinding forces described call for a machine exhibiting:

- A rigid machine bed
- Strong and powerful spindle drives and bearings
- Guide members of adequate dimensions
- A good coolant supply and filtering system
- Suitable grinding wheels and dressing devices where applicable

Further, wheel requirements are specified for high wheel speeds (greater than 125m/s), the high centrifugal forces requiring an electroplated steel wheel as the risk of wheel burst with conventional abrasives is too high. Rowe and Jin (2001) support the use of electroplated wheels describing the high wheel wear rate encountered during HEDG trials with an alumina wheel and calling for the future use of stronger wheels at higher wheel speeds.

Tawakoli (1993) considers the high speed grinding process as a prelude to the high efficiency deep grinding process. Further to the demonstration of König (1971) (figure

2.3), Tawakoli (1993) demonstrates the thermal benefit of high wheel speeds. Figure 2.5 shows the author's work with increasing wheel speed on the workpiece surface temperature. As wheel speed increases, there is an initial increase in frictional energy resulting in a rise in surface temperature as a result of the wheel engaging the workpiece more frequently. Temperatures continue to rise up to a given wheel speed before decreasing with increasing wheel speed.

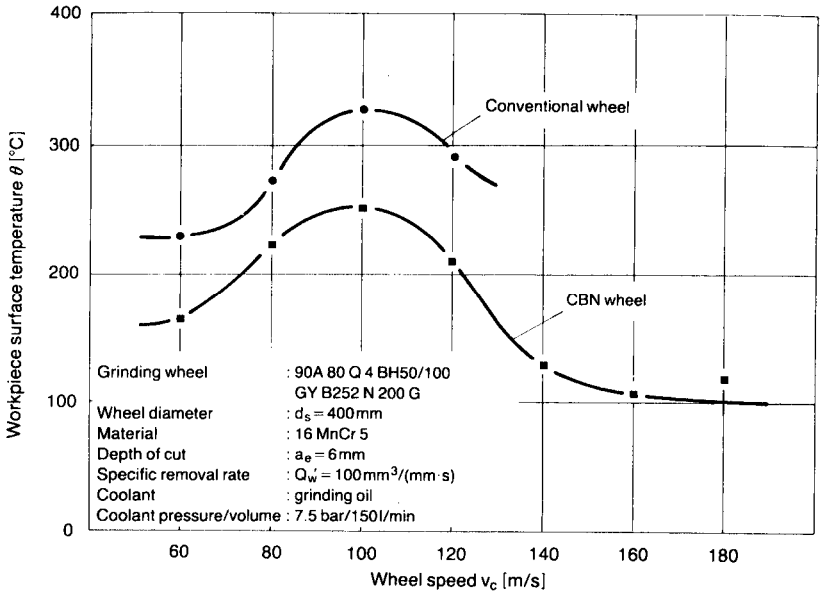

Figure 2.5 Surface temperature trends with increasing wheel speed after Tawakoli (1993)

Tawakoli (1993) describes changes in workpiece surface temperature as the result of the contact layer theory. The temperature at the cutting edge rises to a maximum (the chip-formation equilibrium temperature) as the cutting edge penetrates and moves through the contact zone. In HEDG, the high number of kinematic cutting edges and close proximity of cutting paths raises the contact surface temperature to the equilibrium temperature. The author goes on to describe the effects seen in pulse heating of surfaces with an electron beam. In this case the temperatures were shown to spread more rapidly across the surface than into the material core. As a result of this a rapid removal of the contact layer in HEDG, described as of the order of 0.5ms for a wheel speed of 100m/s at a specific material removal rate of 100mm^3/mm·s, removes heated material from the contact layer with the grinding chip. The high speed removal of the heated layer therefore prevents excessive thermal penetration into the workpiece surface.

The partitioning of heat energy in the HEDG regime plays a crucial role in the success of the process. Investigated by Jin & Stephenson (2003), a theoretical analysis of the heat partitioning shows the dominance of the grinding chip in heat removal from the workpiece. Increasing material removal rates were shown to result in an increasing heat partitioning ratio to the grinding chip (figure 2.6), with decreasing partition to the coolant, wheel and workpiece.

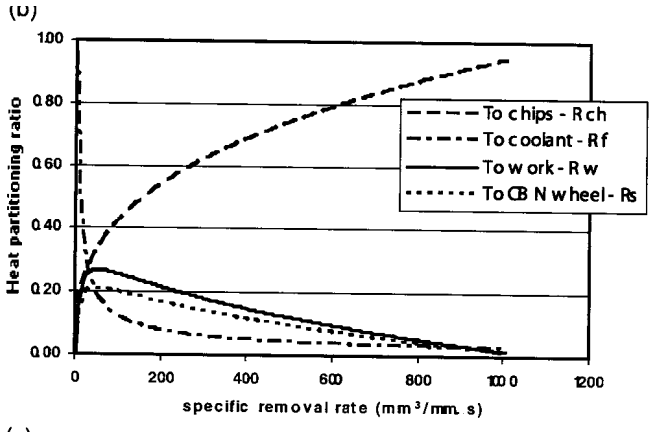

Figure 2.6 Heat partitioning in HEDG after Jin & Stephenson (2003)

Further, the authors make a useful assumption in the modelling of the process, demonstrating an exponential relationship between specific material removal rate (Q'_w) and specific grinding energy (e_c) of the type:

$$e_c = A \cdot Q'^{-t}_w$$

Where A and t are constants dependent on the workpiece material and grinding regime and noting that increases in both workpiece feedrate and depth of cut can increase the value of specific material removal rate. They reason that for similar wheel and coolant conditions an approximation of this nature can be used to predict the energy requirements. The valid range of this assumption may prove to be dependent on the concept of minimum grinding energy presented by Malkin (1989), given his demonstration that the minimum amount of energy required for material removal in grinding is dependent upon material property. This intimates that the power relationship would be limited to specific material removal rates where the minimum grinding energy had not been achieved and would be independent of the coolant supply conditions.

More recent attempts at modelling the specific grinding energy in the HEDG regime were made by Ghosh et al. (2008). The authors demonstrated a model of specific

grinding energy derived from the summation of the individual grit interactions at low values of specific material removal rate. This showed limited correlation between the measured and predicted values, with result scatter attributed to the complex grinding process.

Successful demonstrations of the use of HEDG in all the major grinding modes have been shown in the literature. Stephenson et al. (2002) demonstrate the application of the HEDG regime to the surface and cylindrical traverse grinding modes, presenting a theoretical discussion of the surface temperature trend with variation in work speed (figure 2.7) and also depth of cut (figure 2.8). The authors suggest that the increasing workpiece speed in HEDG acts to reduce temperatures at the contact and finished surface independently of coolant supply, with depths of cut beyond 2mm showing little variation in the temperatures generated. Their theoretical predictions thus assume that the effect of coolant for reducing grinding temperatures is in fact negligible at high work speeds. This is supported by results presented in the work, which demonstrate a limited variation in specific grinding energy with a decrease in fluid supply to the contact zone.

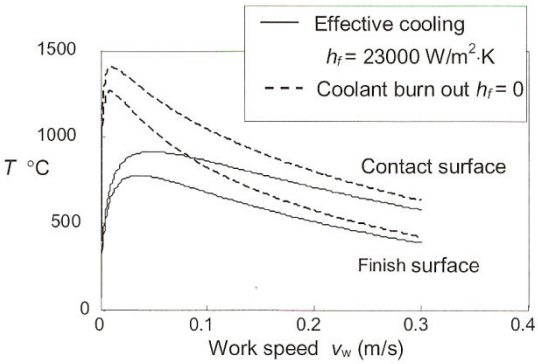

Figure 2.7 Temperature trends with work speed for HEDG conditions after Stephenson et al. (2002)

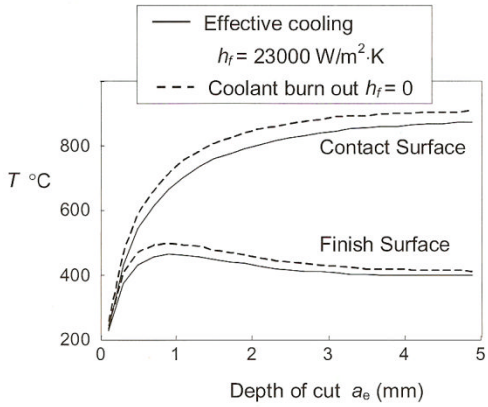

Figure 2.8 Temperature trends with depth of cut for HEDG conditions after Stephenson et al. (2002)

Comley et al. (2004) present a successful demonstration of the HEDG regime in the cylindrical plunge grinding mode. The authors present results to support the claim that high stock removal rates, in this case up to 2000mm^3/mm·s, are achievable without thermal damage. Comley (2005) again demonstrates the validity of the HEDG regime in the cylindrical plunge grinding mode. Here, it is also shown that the trend of surface temperatures with increasing removal rate is similar to that demonstrated for surface grinding by Tawakoli (1993). The work of Comley (2005) also shows a clear peak in temperature around values of specific material removal rate of 300 to 350mm^3/mm·s before falling away.

The integrity of a ground surface is primarily dependent on the thermal changes undertaken in the grinding process. The application of process control and predictive modelling to the HEDG regime is dependent on the successful modelling of the temperatures generated in the finished surface during processing. Jin et al. (2001) and Rowe (2001) presented the case for a moving inclined heat source for the modelling of the HEDG regime. However, current best practice in thermal modelling of the regime is presented by Rowe & Jin (2001) and describes a moving circular arc of heat source model. The work concludes that the reduction of temperature transmission to the finished surface in spite of high contact temperatures is the result of the large inclination angle of the contact, driven by the large depth of cut, and the high work speeds. Experimental data presented by the authors (figure 2.9) shows the high maximum contact temperatures achieved, approaching the melting temperature of the material.

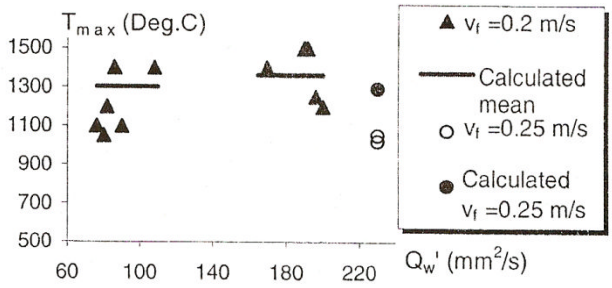

Figure 2.9 Measured maximum contact temperatures in HEDG during fluid burn-out after Rowe & Jin (2001)

A discussion of the results presented by Rowe & Jin (2001) suggests that the specific grinding energy approached the melting energy of the chip material, similar to the findings of Malkin (1989) for conventional grinding regimes. The concept of minimum or limiting specific grinding energy in the grinding process is also discussed by Morgan et al. (2004) and equated to the energy required to raise a grinding chip to the melting temperature. The authors state that for steel this value is approximately 6 J/mm^3, this is as compared to a value of minimum chip formation energy of approximately 10.4 J/mm^3 presented by Malkin (1989). If the minimum specific grinding energy is material dependent, a minimum grinding energy will be achieved independently of coolant supply and other factors and would be consistent for all applications.

2.1.4 Vertical Side Face Grinding

One of the most common applications for high performance grinding applications such as creep feed and high efficiency deep grinding is the production of deep slots and profiles. The production of a deep feature using the grinding process results in the development of a vertical sidewall. This sidewall can experience a differing wear and thermal profile to the axis parallel surface.

Both Mindek & Howes (1996) and Li et al. (1999) consider the effects of the presence of a sidewall during the grinding process. Mindek & Howes (1996) discuss the effect of the sidewall in creep feed grinding, they highlight the limitation of coolant access into the sidewall and the wear on the wheel edge radius as detrimental to the heat flux into the sidewall and the holding of tolerance in the bottom of the slot. The heat flux into the sidewall is considered to increase as the wheel begins to gather debris and worn wheel grits are not removed from the wheel.

Li et al. (1999) develop a model of the thermal and stress considerations in the sidewall for a creep feed grinding application. They suggest that for surface grinding conditions the peak temperature position in the wheel work contact zone will leave a burn strip on the sidewall. This is the result of the process not removing the sidewall material in subsequent passes as would be experienced in cylindrical traverse grinding. Figure 2.10 shows schematically the anticipated location of this burn strip in creep feed grinding. It may be expected that this burn strip exist in HEDG also, as a result of the similar depths of cut and the known high contact zone temperatures experienced.

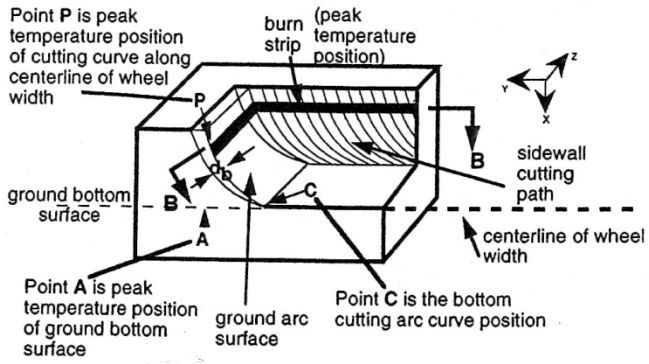

Figure 2.10 Anticipated location of burn in sidewall during creep feed grinding after Li et al. (1999)

The application of deep grinding of narrow slots in the HEDG regime is discussed by Werner & Tawakoli (1988b) and considers the application of an optimised wheel geometry for slot grinding. The authors developed a solid wheel, with partial electroplating of the CBN abrasive to the wheel flank or sidewall. This was shown to be the result of experimentation with a fully electroplated wheel and a slotted wheel and permits an improved flow of coolant into the sidewall and reduces sidewall friction. In addition to the benefits of the wheel geometry, a cleaning nozzle arrangement was added to the set-up to remove loaded metal particles from the wheel surface. The use of the optimised wheel geometry is shown to successfully produce slots of 25mm depth by 1.5mm wide in testing.

Snoeys et al. (1978) consider the thermal effects of cut-off grinding, during the cut-off process a vertical sidewall is created as the wheel penetrates the workpiece. The authors suggest that in this case the majority of heat is concentrated in the layer to be imminently ground away. Figure 2.11 shows a schematic of the theoretical heat flux into the sidewall, the temperature in the sidewall is suggested to be dependent on the

workpiece feedrate. The authors also present a theoretical analysis of the temperatures in the workpiece sidewall. Figure 2.12 demonstrates the temperature curves in the sidewall.

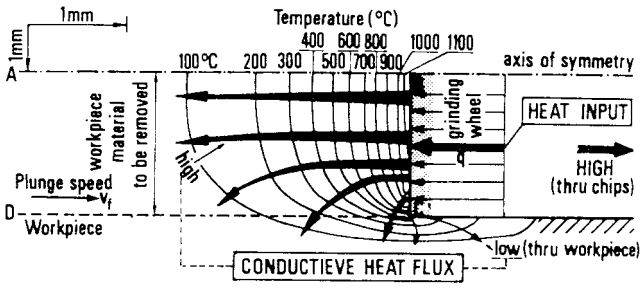

Figure 2.11 Theoretical heat flux to surface and sidewall during abrasive cut-off process after Snoeys et al. (1978)

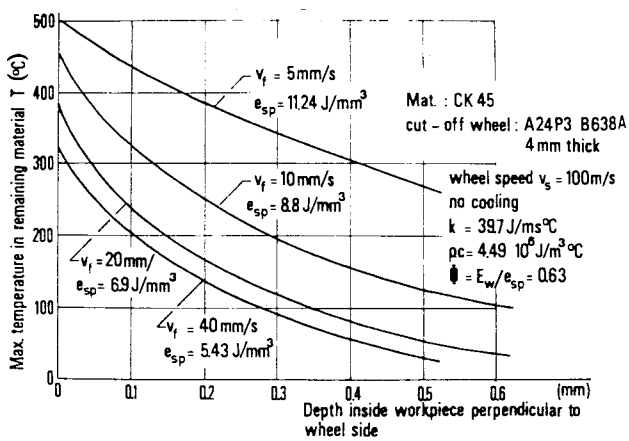

Figure 2.12 Sidewall temperature curves for the abrasive cut-off process after Snoeys et al. (1978)

Sainz (2005) made attempts to record the thermal profile where a vertical sidewall was present with the low melting point coating technique (discussed in section 2.3). He successfully shows the possibility of recording a complete isotherm in a profile using the technique with the grinding of thin samples and at small widths of cut in the HEDG regime. However the 2mm wide sample was insufficient to contain the entire sidewall isotherm and thermal gradients across the width of the sample due to the cooling at the sidewall face were higher than may be expected. The author concludes that the depth of cut increases the heat flux into the sidewall, with the trend similar for both creep and high efficiency deep grinding regimes. Further no effect on the heat flux to the sidewall as a result of changes in feed rate was found.

2.1.5 Cylindrical Traverse Grinding

Cylindrical traverse grinding is described by Malkin (1989) as grinding with the addition of a crossfeed motion of the workpiece relative to the grinding wheel in a direction perpendicular to the plane of wheel rotation. The author demonstrates the process schematically (figure 2.13) highlighting the issue of step wear in the wheel as progressive wear is encountered across the wheel width. This may result in a form error, which is cited as a primary reason for the preference of cylindrical plunge grinding in the production environment. The presence of step wear should be limited however by the application of advanced wheel technologies such as electroplated steel CBN wheels, which should exhibit negligible surface wear.

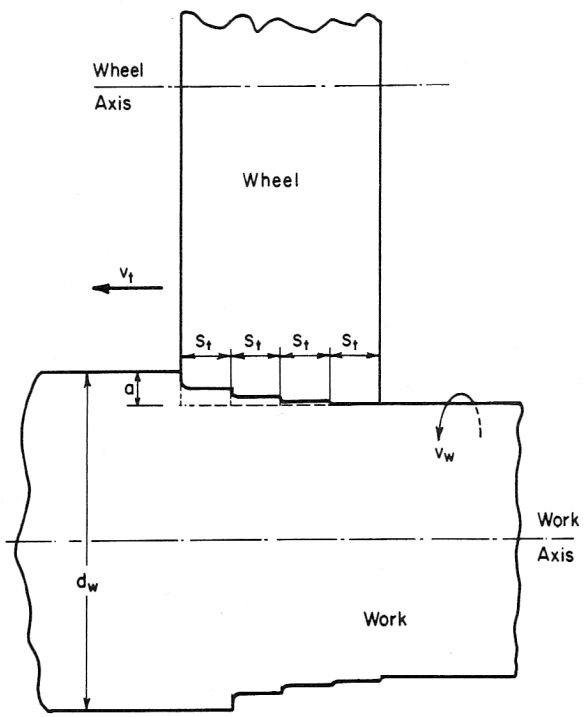

Figure 2.13 Schematic of the cylindrical traverse grinding process after Malkin (1989)

Nakayama et al. (2004) describe a ultra-high speed cylindrical traverse grinding process using CBN wheels. The authors show by experimentation that reducing the traverse feed per workpiece revolution improves the surface roughness. Increasing workpiece speed was shown to suppress the effect of heat in the ground subsurface and could generate compressive residual stress profiles. In conclusion the authors recommend that

the increase in work speed allows higher traverse feeds with a small effective width of cut providing an optimised solution for cylindrical traverse grinding. In keeping with results for surface grinding with high wheel speeds, both surface roughness and grinding forces are reduced in cylindrical traverse grinding. The work of Nakayama et al. (2004) is limited to a maximum depth of cut of 0.3mm, this delivers a specific material removal rate of 2600mm^3/mm·s and is within the range of high efficiency deep grinding. The work leaves scope for the investigation of larger depths of cut in keeping with stock removal techniques and does not consider temperatures in the surface or sidewall.

Further work in the field of cylindrical traverse grinding has been demonstrated by Weck et al. (2001), Capello & Semeraro (2002) and Bianchi et al. (2003). These reviews consider the application of the cylindrical traverse grinding process to the finish grinding process and do not consider stock removal applications. Stephenson et al. (2002) did however successfully demonstrate the application of the process in the HEDG regime. They considered the use of high rotational speeds with low cross feeds, suggesting that this resulted in a face grinding mode with grinding primarily occurring at the shoulder face of the grinding wheel.

2.2 The Application of Grinding Fluid

In grinding, grinding fluids perform a number of functions within the process. Figure 2.14, presented by Brinksmeier et al. (1999) demonstrates the primary effects of lubrication and cooling in the machining process, further to this however it is commonly accepted that coolant also assists in the removal of grinding chips from both the grinding wheel and grinding zone.

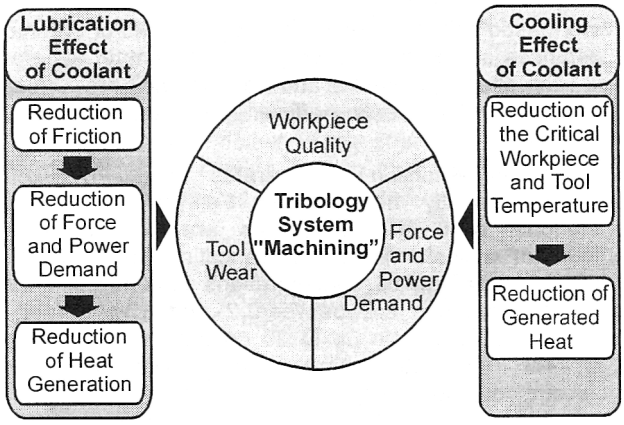

Figure 2.14 Primary effects of lubrication and cooling in the machining process after Brinksmeier et al. (1999)

Ye & Pearce (1984) consider the effect of the type of coolant in the creep feed grinding of a Nickel-base alloy. They demonstrate through experimentation the benefit on surface roughness and profile retention with the use of oil as a cutting fluid. However it is suggested that in this process the use of oil is more likely to result in workpiece burn and therefore if this is a primary consideration, water based coolants are preferred. Further, it is commented that neat oil permitted a greater production rate; this is relevant to the HEDG process as the high production rates possible with the process could be facilitated by the coolant selection.

For the application of grinding fluid to be successful, the coolant must be able to reach the required area of the grinding zone where its functionality is most required. Both Brinksmeier et al. (1999) and Ebbrell et al. (1999) consider the application of coolant into the grinding zone. Of particular importance to the HEDG regime is the boundary layer of air, which occurs around the wheel periphery as a result of high wheel speeds. Discussed by Ebbrell et al. (1999), conventional methods of fluid delivery are thought to fail to penetrate the boundary layer, resulting in insufficient cooling in the grinding zone. The authors suggest the use of a jet nozzle to avoid this problem, however the application of coolant tangential to the wheel surface is suggested to result in deflection by the boundary layer and thus an angular application of coolant is required, further benefits may also be achieved with the use of a scraper plate to spoil the air flow and minimise the effect of the boundary layer. Further to work relating to coolant selection, Carmona Diaz (2002) presented an optimised geometry for nozzle positioning in the HEDG regime using the Edgetek SAM at Cranfield University. The author suggests that

the leading edge nozzle should be inclined at a shallow angle to the horizontal for surface grinding, which ensures good application of coolant to the contact zone.

Considering high performance grinding, Brinksmeier & Minke (1993) suggest the braking effect of the grinding fluid on the grinding wheel is a major limiting factor on the process. When wheel speeds approach 180m/s, the authors note that only 25% of the total grinding power is actually being used for cutting, the remainder being utilised to drive the coolant (figure 2.15). The authors also demonstrate the effect of grinding fluid supply on grinding force (figure 2.16), concluding that the application of coolant in the high performance grinding process is a trade off between the reduction in coolant supply to minimise grinding forces and the minimum quantity of coolant required to cool and lubricate the process.

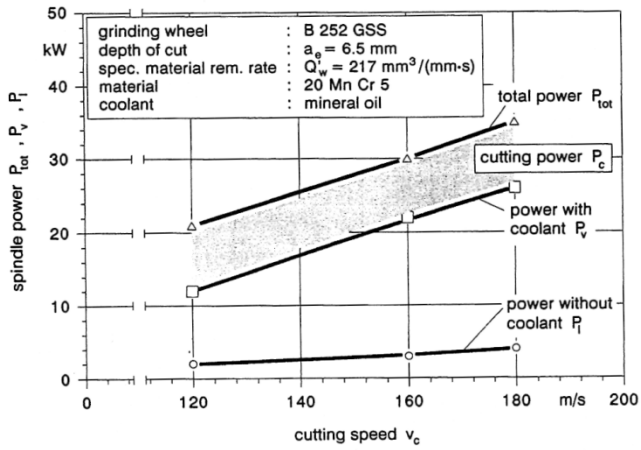

Figure 2.15 The effect of grinding fluid on grinding power after Brinksmeier & Minke (1993)

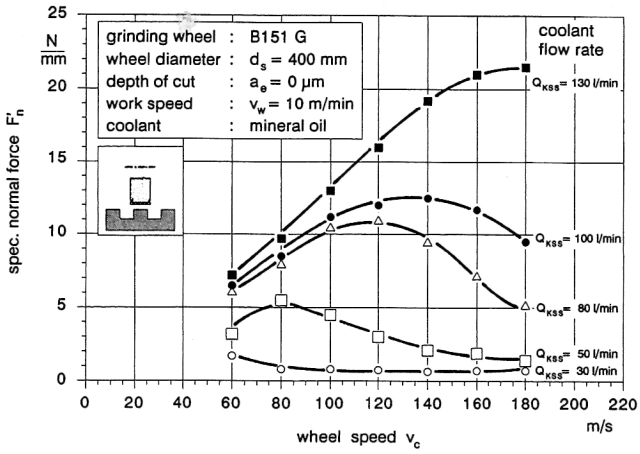

Figure 2.16 The effect of grinding fluid on grinding forces after Brinksmeier & Minke (1993)

Carmona Diaz (2002) studied the influence of grinding fluids on HEDG with a 51CrV4 low alloy steel. His research concluded that the most appropriate selection of grinding fluid for the HEDG regime was neat or synthetic oil. This supports the work of Ye & Pearce (1984), who, working in the creep feed regime, intimated the suitability of neat oil for high stock removal rate processes. It is accepted that this would be true for cylindrical grinding also, as the benefit appears to be the result of the favourable lubrication qualities of oil.

2.3 Temperature Measurement

The measurement of temperature in any manufacturing process is complicated by issues of accessibility to and the dynamics of the process in question. When considering machining processes, the accurate measurement of temperature is further frustrated by the addition of lubrication to and the removal of swarf from the cutting zone. This is of particular concern for the grinding process, which in many cases floods the wheel workpiece interface with coolant as in the creep feed grinding process or produces high volumes of waste material as found in stock removal processes.

Reviewed by Komanduri and Hou (2001), a variety of temperature measurement techniques are presently available to the researcher. The authors consider the application of thermocouples, infra-red photography and optical pyrometry, thermal paints, materials of known melting temperature and microstructural change. They conclude that the application of a given temperature measurement technique is dependent on the

situation considered. Issues include accessibility, heat source size, dynamics of the process, required accuracy, cost implications, sensor technology and data collection.

The use of thermocouples for temperature measurement in grinding is commonplace. Several examples are available of literature presenting results developed from the process, for example temperature measurements in Rowe et al. (1998) and Rowe & Jin (2001) utilised this method for verification of thermal models of HEDG. Tawakoli (1993) presents an example of the use of thermocouples for the development of surface temperatures in grinding regimes. He describes advantages including accuracy, a wide temperature range and the ability to place them in or just below the contact zone via drilled holes. It is also noted that the thermocouples require a reference temperature for set-up. The author provides a schematic (figure 2.17) of a thermocouple technique for extrapolating surface temperatures via a series of thermocouples placed at varying depths from the contact surface.

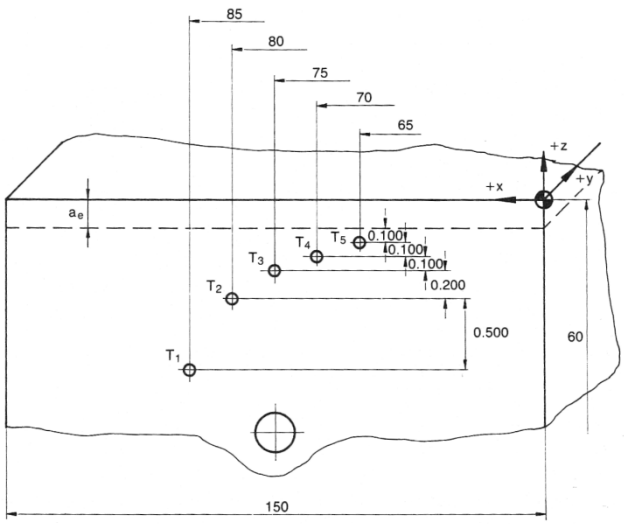

Figure 2.17 Schematic of thermocouple technique for measurement of surface temperatures during grinding after Tawakoli (1993)

Komanduri & Hou (2001) describe the embedded thermocouple technique process as requiring elaborate preparation, given the requirement for accurate drilling of holes in the surface of an often difficult to machine material. Further, they comment on the disturbance of the heat flow when placed close to the contact surface. They consider that the principal benefits of the system are the ease with which thermocouples can be used and the relatively low cost of the sensors. Kato & Fujii (1997) agree that the

thermal distortion around the embedded thermocouple may be an issue for the measurement of temperatures at the contact surface in grinding.

Hwang et al. (2003) present an example of the application of an infra-red imaging system to the measurement of temperatures in the grinding process. Trials were performed without the application of coolant by focusing the system onto the sidewall of the grinding sample (figure 2.18). The authors suggest significant benefits are offered as a result of the ability to consider temperature measurements over a broader area than the wheel workpiece contact zone; this is highlighted as distinct from other techniques which consider localised temperature measurement only. Issues raised by Komanduri & Hou (2001) relating to the use of infra-red and its requirements for elaborate instrumentation and the possibility of special environments, with the exception of an intolerance for coolant application during trials, appear to have been resolved with technological advancements.

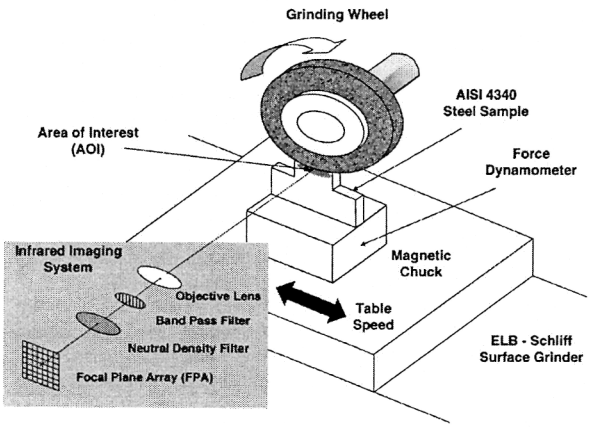

Figure 2.18 Schematic of infra-red temperature measurement system for measurement of grinding temperatures after Hwang et al. (2003)

Earlier measurements of grinding temperature with the use of an infrared radiation pyrometer are presented by Ueda et al. (1986). An optical fibre is positioned such as to record temperatures at the workpiece surface (figure 2.19), transferring the data to a remotely located infra-red pyrometer. An experimental set-up utilising a thermocouple for temperature measurement verification was also applied. The chief benefits of the approach are described as the response time and the ability to accurately determine peak temperatures. Response times of the pyrometer are sufficient to respond to the rapid changes in temperature experienced and thus pick up peak temperatures as well as the

average background temperature. More recent work by Müller & Renz (2003) considers the application of an infra-red pyrometer with an optical fibre to a conventional turning process. They agree that the speed of response and the accuracy of the technique are of significant benefit.

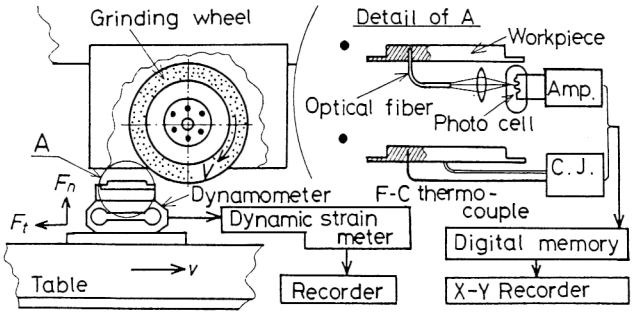

Figure 2.19 Schematic of infra-red pyrometer with local optical fibre temperature measurement system for measurement of grinding temperatures after Ueda et al. (1986)

Wright & Trent (1973) describe a metallographic method for determining the temperature gradient in a high speed steel cutting tool. The authors claim that the use of thermocouples and infra-red pyrometry can only provide an indication of the character of the temperature distribution in the tool and that this is inadequate. The use of the metallographic technique allows for a complete temperature distribution (figure 2.20) to be developed where applied. By the application of knowledge of the phase transformation temperatures and hence metallographic changes in the material, the temperature gradient can be determined. Figure 2.21 represents this process schematically, demonstrating the structural changes in high-speed steel as a function of tempering temperature and time. Komanduri & Hou (2001) highlight the limitations of the technique as being the requirement for a suitable material and the increased processing parameters to produce a suitable metallurgical isotherm.

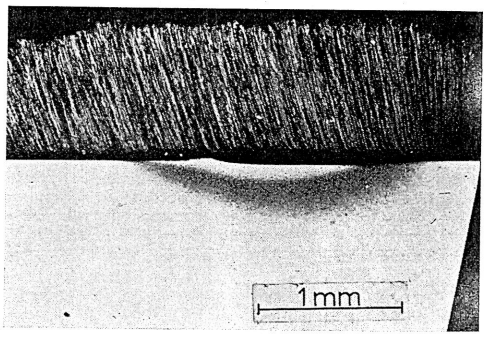

Figure 2.20 Complete temperature distribution shown in metallography of a cutting tool after Wright & Trent (1973)

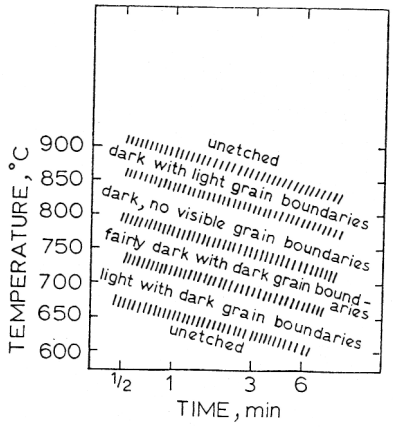

Figure 2.21 Sample time temperature transformation lines for analysis of cutting tools with metallography after Wright & Trent (1973)

Materials of a known melting point have been applied to machining processes for the measurement of the temperature distribution in cutting tools and surface temperatures in grinding. Kato et al. (1976) present the use of powders of a constant melting point to measure tool temperature distribution. The cutting tool was split parallel to the chip flow direction, with the powder applied to the mating surfaces using an aqueous solution of sodium silicate to aid adhesion. The authors conclude that the temperature distributions were measured easily and accurately, with processing resulting in a typical isotherm (figure 2.22) when surface temperatures were raised as a result of the cutting process. Measurements were recorded graphically as depicted in figure 2.23, with the technique demonstrated being typical for both powders and pure metals.

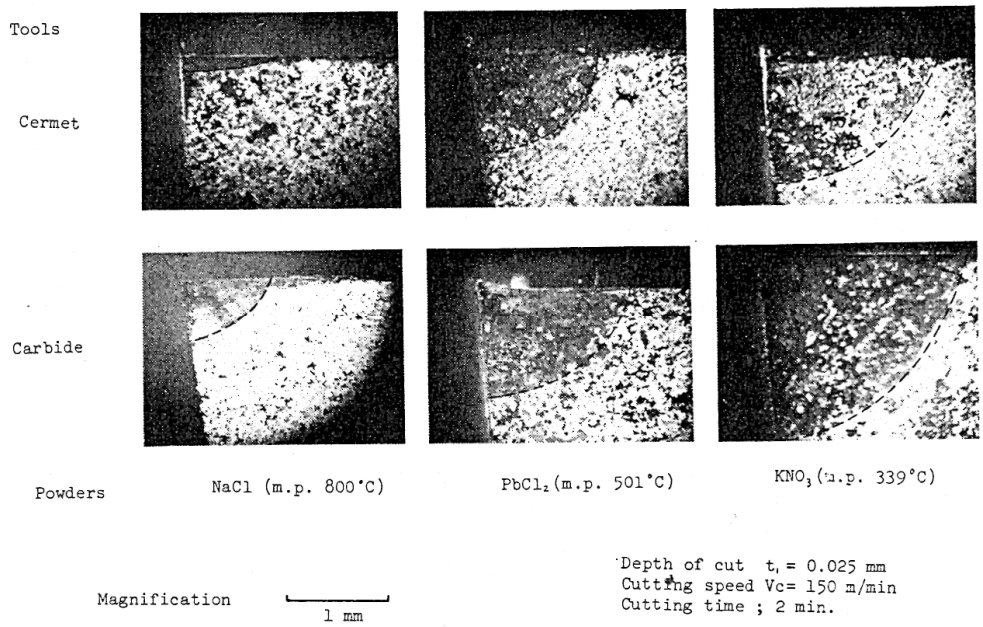

Figure 2.22 Typical isotherms in cutting tools using powders of known melting point after Kato et al. (1976)

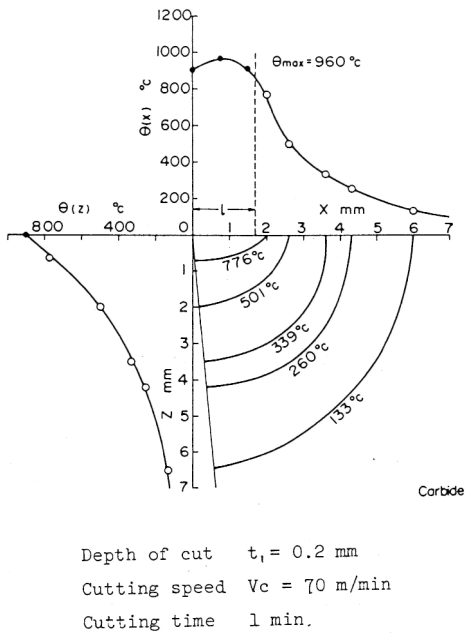

Figure 2.23 Graphical representation of isotherms shown in figure 2.22 after Kato et al. (1976)

Later work by Kato & Fujii (1996) highlighted the limitations of the powder route suggesting the thickness of the powder resulted in a poor thermal response and formed a thick layer preventing close contact with the surface. Again the split tool technique of Kato et al. (1976) was employed with a coating applied by the Physical Vapour

Deposition (PVD) technique and utilising the same measurement process. Varieties of pure metals were used as depicted in table 2.2 and can be considered typical of those used for these applications.

PVD Film Material	Symbol	Melting Point (K)	Purity %
Germanium	Ge	1211	99.999
Antimony	Sb	904	99.999
Tellurium	Te	723	99.999
Lead	Pb	601	99.999
Bismuth	Bi	545	99.999
Indium	In	429	99.999

Table 2.2 Typical pure materials used by Kato & Fujii (1996) for development of cutting tool isotherms

Kato & Fujii (1997 & 2000) present the use of a thin film deposited between mating surfaces of a sample workpiece by the PVD process. Figure 2.24 describes the experimental work undertaken by the authors, showing the relative location of the coated surface to the grinding parameters. The benefits of the technique are described as its applicability to any workpiece material without requirement for the drilling of holes for the embedding of sensors. Further the technique is capable of profiling the temperature at various depths from the surface. The work of Komanduri & Hou (2001) considers the PVD process as an inexpensive and simple method of providing information on the complete temperature distribution.

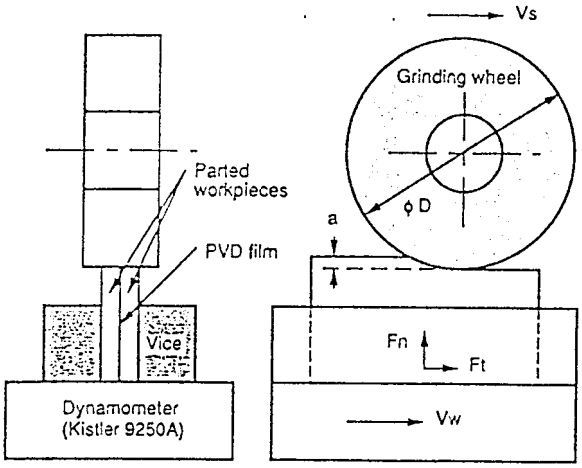

Figure 2.24 Schematic of the PVD method of temperature measurement technique for surface grinding after Kato & Fujii (2000)

The measurement of temperatures in the HEDG regime is complicated by the high feeds and speeds and the aggressive coolant supply. Walton et al. (2005) presents the case for the low melting point coating technique. The authors compare temperature and subsurface hardness profiles to demonstrate changes in hardness at temperatures critical to the phase transformation of the material. They conclude from experimentation that the low melting point coating technique is a robust method of temperature measurement. The high coolant pressures experienced had no detrimental effect on the temperature measured and the thinness of the coating promoted an undisturbed thermal field.

Batako et al. (2005) present a study of temperature measurement techniques in the HEDG regime. Experimental data collected here presents a case for the use of grindable thermocouples, concluding that the single pole grindable thermocouple technique was the simplest and most reliable. This is as compared to the findings shown in previous paragraphs considering low melting point coatings; the review does not consider the effect of the excessive electrical noise experienced during the HEDG process.

2.4 Grinding Burn

Surface integrity is described by Field & Kahles (1971) as the study and control of both surface roughness and surface metallurgy. They comment that conditions for developing surface integrity need not be imposed unless the service requirements dictate. When considering stock removal processes the issue of surface integrity is of lesser

importance, particularly the generated surface roughness as subsequent finishing passes of the grinding wheel at more conventional rates can remove undesirable surface effects. The depth of a surface effect is therefore critical if it is to be successfully removed. This is particularly significant in the HEDG regime where very high temperatures are generated during the process.

Grinding burn makes broad reference to the effects of temperature on the surface integrity of the workpiece material; this terminology will be used throughout the thesis to refer to these issues. Several degrees of grinding burn are noted in the literature from oxidation to rehardening burn. Badger & Torrance (2000) demonstrate schematically the varying levels of burn experienced against a relative temperature profile (figure 2.25) the onset of oxidation burn occurring at relatively low temperatures. The authors consider oxidation burn to be largely cosmetic; however it is clear that the presence of oxidation burn may imply a deeper level of damage.

Figure 2.25 Schematic of degrees of grinding burn after Badger & Torrance (2000)

The importance of damage resulting from the grinding process, grinding burn, cannot be underestimated. Field & Kahles (1971) comment on the importance of dynamic loading as a principal factor for engineering design, where fatigue life failures initiate on or near the surface. Further it is suggested that the surface condition is a primary factor in stress corrosion problems. The author demonstrates the effect of grinding on the fatigue life for three commonly employed engineering materials, summarised in table 2.3, and highlights significant reduction in fatigue life with abusive grinding conditions.

Alloy	Machining Operation	Endurance Limit in Bending 10^7 Cycles (psi)
4340 Steel, 50 R_c	Gentle grinding	102,000
	Abusive Grinding	62,000
Titanium 6Al-4V 32 R_c	Gentle grinding	62,000
	Abusive Grinding	13,000
Inconel 718, Aged, 44 R_c	Gentle grinding	60,000
	Conventional Grinding	24,000

Table 2.3 Effect of grinding processes on fatigue life of common engineering materials after Field & Kahles (1971)

The detrimental effect of a poorly controlled grinding process is qualified by Silva (2003) describing the failure of a vehicle crankshaft due to thermal fatigue cracking, whilst Eliaz et al. (2005) described the discovery of a crack in the main landing gear of a cargo aircraft as a result of abusive grinding. Whilst both events will result in a significant financial impact for the manufacturer, the failure described by Eliaz et al. (2005) is of particular importance as landing gear are a safety critical element of the aircraft. Their failure could have fatal implications.

Brinksmeier et al. (1982) demonstrate schematically the primary effects of residual stresses (figure 2.26). They consider the residual stresses to be the result of combined thermal and mechanical effects also discussed by Mahdi and Zhang (1999a & b) and Snoeys et al. (1978). Further, consideration of residual stress as the result of phase transformation is presented by Brinksmeier et al. (1982) Mahdi & Zhang (1999b) and Snoeys et al. (1978). Brinksmeier et al. (1982) consider some of the elements which result in a residual stress in the surface including machining conditions, wheel wear behaviour and the type and construction of the wheel. The author also demonstrates the beneficial effect of oil over emulsion on the residual stress; figure 2.27 shows results after Althaus (1982) presented by Brinksmeier et al. (1982) where residual stress is significantly reduced when using oil. Further the figure demonstrates the benefit of using a CBN wheel, here in grinding with both oil and emulsion, CBN produces a consistently lower residual stress than its corundum counterpart. Brinksmeier concludes

that whilst the cooling effect of emulsion is significantly greater, oil has the more beneficial effect on the tensile residual stress profile.

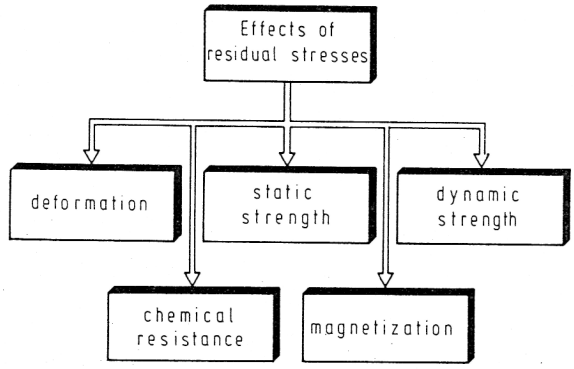

Figure 2.26 Primary effects of residual stress after Brinksmeier et al. (1982)

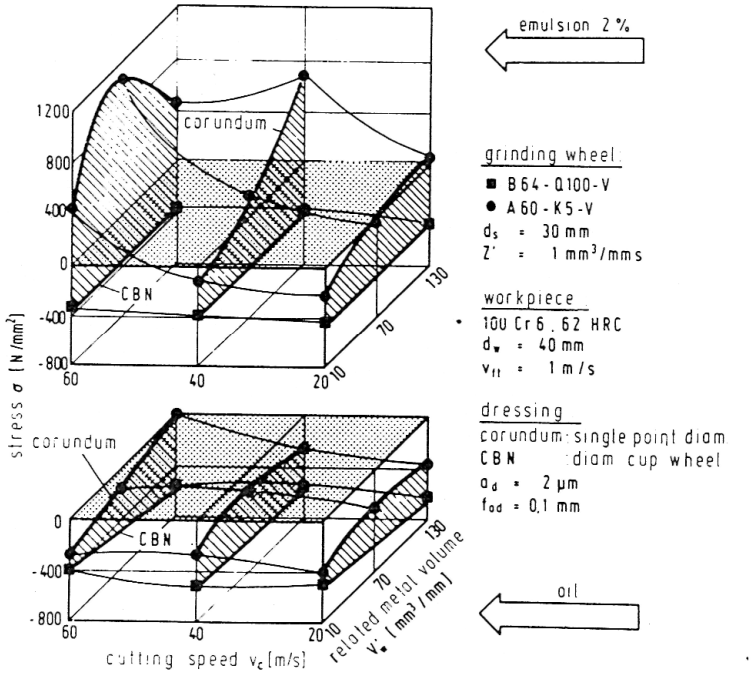

Figure 2.27 Effects of oil as a grinding fluid and the use of CBN wheels on residual stress in the as ground surface after Althaus (1982) cited Brinksmeier et al. (1982)

Of the forms of grinding burn commonly encountered, tensile residual stress is considered to be the most significant. The presence of tensile residual stress will promote fatigue failures, crack initiation and crack propagation. Chen et al. (2000) describe the origins of residual stress as the result of three effects during the grinding

process; thermal expansion and contraction, phase transformations when high temperatures are encountered and plastic deformation due to the abrasive grains of the wheel. They suggest that the most significant element in the generation of residual stress is the effect of thermal expansion and contraction and that this allows the process of predicting residual stress to be simplified to the prediction of temperature.

The focussing of the grinding burn problem on the generation of residual stress allows for the application of several commonly available technologies for burn detection. The effect of residual stress condition on hardness measurements has been demonstrated in the literature. Frankel et al. (1993) show an example of autofrettaged cylinders exhibiting a compressive internal diameter and a tensile outside diameter. Using Rockwell C hardness measurements, the authors show a decreasing hardness value with increasing tensile residual stress. This effect is also seen in the work of Blain (1957) in which Rockwell C measurements of surface hardness were seen to be similarly reduced by the presence of a tensile residual stress. The use of surface hardness as an indicator of a residual stress profile should be easily established and with the use of non-destructive ultrasonic contact impedance equipment can be tested in-situ.

Shaw et al. (1998) and Desvaux et al. (1999) show good results for the detection of grinding burn with Barkhausen noise analysis. Both sets of authors comment on the usability of the process, with Desvaux et al. (1999) commenting on its value as a replacement for the existing x-ray diffraction technique, which is considered lengthy, expensive and relatively inflexible for a more complex geometry. The authors agree that the Barkhausen technique demonstrates a correlation to the residual stress condition; however it is highlighted by Shaw et al. (1998) that the results require quantification against actual material properties developed. More recently, Comley (2005) utilised the Barkhausen technique for the detection of grinding burn, concluding that the set-up, whilst comparative, provides a quick non-destructive method suitable for industrial application.

The appearance of oxidation burn, i.e. the presence of temper colours on the workpiece surface has been used by Johnstone (2002) as a simple method of detecting grinding burn. McCormack et al. (2001) consider the use of temper colours for determination of grinding burn claiming that temperatures at which oxidation occurs are increased as a

result of the unusually short thermal pulse time in grinding. They consider the presence of surface oxidation in a critical component to be completely unacceptable due to the risk of sub-surface metallurgical damage, although comment on its acceptability on non critical surfaces where it may be polished out.

2.4.1 Burn Threshold Studies

Given the relationship between thermal effects and tensile residual stress presented in the literature, residual stress may be predicted by knowledge of the temperatures generated in the finished surface. Work in the field is in agreement that the onset of burn occurs at some critical surface temperature related to material properties. Therefore several attempts have been made to produce a diagram, which presents a constant line of temperature against grinding parameters and forms the basis of a threshold or limit of grinding burn.

Malkin (1974) equates the onset of grinding burn with the austenite formation temperature; however this approach does not consider the occurrence of tensile residual stresses at lower temperatures. McCormack et al. (2001) present a critical damage temperature, this is the temperature at which tensile residual stresses are formed in the surface and is lower than the temperatures of temper burn and phase transformation. The authors highlight that the critical damage temperature is dependent upon the type of material being ground, the heat treatment history and the value of yield stress and its relationship with temperature. Importantly for the HEDG regime, where feeds and speeds are particularly high (table 2.1), the authors point out that workpiece speed can affect the temperature of tensile residual stress onset.

The concept of a critical temperature for the onset of grinding burn gives the possibility of burn prediction via thermal modelling. Malkin & Lenz (1978) and Malkin (1989) demonstrates the application of this theory with the development of a burn threshold diagram. This develops from the consistent power law relationship between Peclet number and dimensionless temperature (figure 2.28) after Jaeger (1942) for Peclet numbers to 50 and is used in conjunction with energy partitioning theory for conventional grinding regimes. Peclet number can be considered as the ratio of the speed of the heat source across the surface to the rate of heat conduction into the surface.

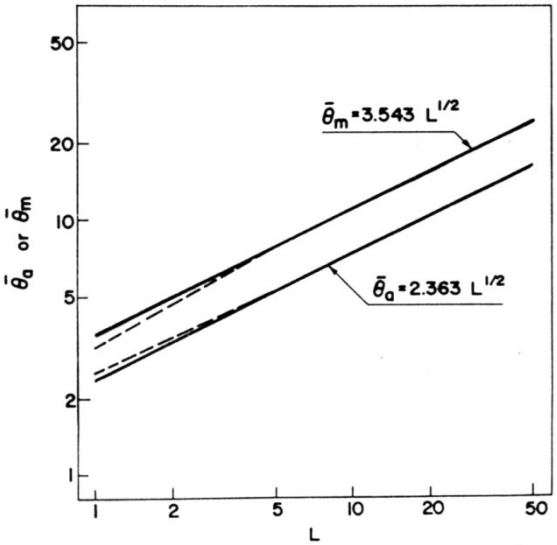

Figure 2.28 Power relationship between Peclet number and dimensionless temperatures in the workpiece after Malkin & Lenz (1978)

Malkin assumes that all grinding energy, except for approximately 55% of the chip formation energy is transferred to the workpiece. However section 2.1.3 has shown this to be inappropriate for HEDG given work in the field by Jin and Stephenson (2003), where as much as 95% of the total grinding energy can be removed by the grinding chip (figure 2.6). Furthermore, typical Peclet numbers in the HEDG regime would be likely to exceed the range considered by Malkin. The burn threshold diagram presented by Malkin & Lenz (1978) is a development of the relationship presented in figure 2.28, rearranging the equation of maximum dimensionless surface temperature where:

$$\bar{\theta}_m = 3.543 \cdot L^{1/2}$$

Malkin develops a relationship for the specific grinding energy required to develop a given temperature. Figure 2.29 shows a schematic after Malkin (1989) in which increasing temperatures increase the gradient of the threshold line. An example of a burn threshold diagram is presented in figure 2.30 after Malkin & Lenz (1978).

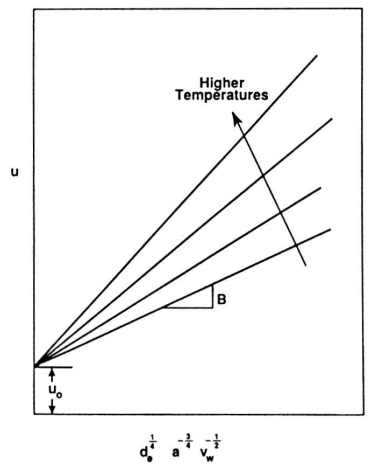

Figure 2.29 Schematic burn threshold diagram showing increasing gradient of threshold line with temperature after Malkin (1989)

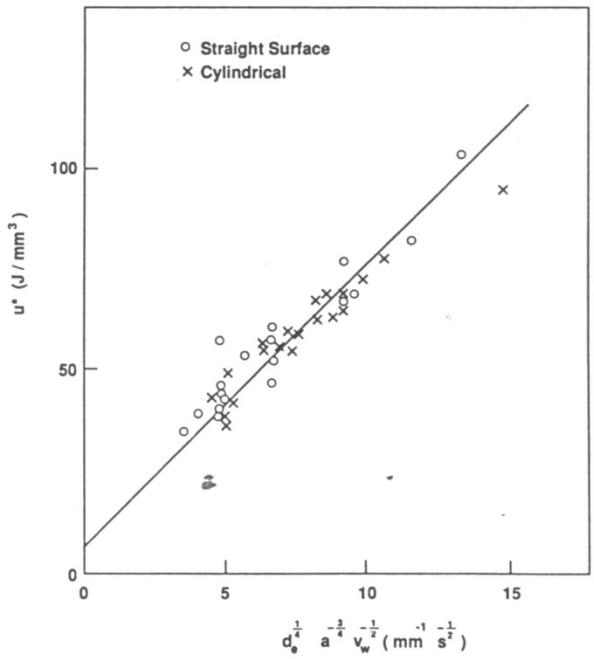

Figure 2.30 Example of a burn threshold diagram after Malkin & Lenz (1978)

An application of the conventional burn threshold diagram presented by Malkin & Lenz (1978) to the HEDG regime is presented by Stephenson et al. (2001). The authors plot a burn threshold diagram for a Nickel based superalloy (figure 2.31) which demonstrates a threshold temperature of greater than 2000°C. The unusually high threshold temperature is reasoned to be the result of the assumption by Malkin that the majority of the grinding energy enters the workpiece. In the HEDG regime it is known however,

that the primary heat removal mechanism is via the grinding chip and energy partition to the workpiece is low.

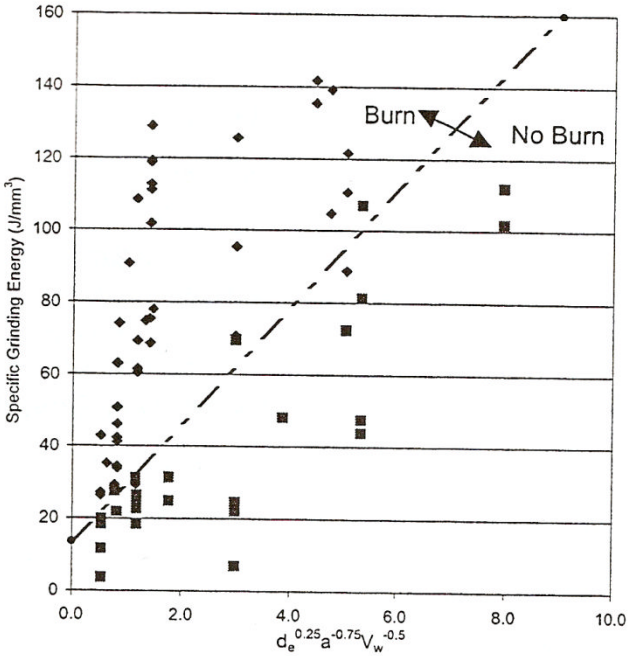

Figure 2.31 Example of a burn threshold diagram in HEDG with a threshold temperature line of 2000ºC after Stephenson et al. (2001)

Chen et al. (2000) discuss a transitional temperature for the onset of tensile residual stress in the workpiece. The authors show for grinding trials with EN9 medium carbon steel a transitional temperature occurring at values of 200 to 235°C, with trends being consistent for rectangular and triangular heat sources. A graphical representation of the transitional temperature is shown in figure 2.32, with an increasing feedrate decreasing the transition temperature.

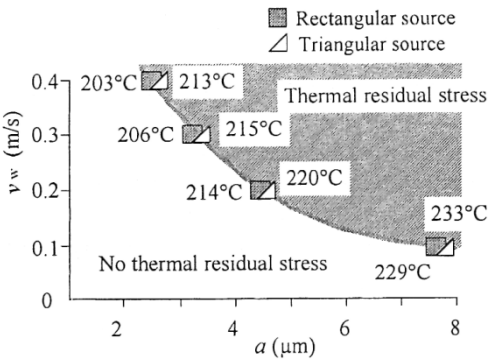

Figure 2.32 Burn threshold diagram based on the temperature for the onset of tensile residual stress after Chen et al. (2000)

Results for the threshold of grinding burn in HEDG are presented by Stephenson et al. (2002) for the surface grinding mode. The authors demonstrate an increasing burn threshold level with increasing specific material removal rate. The burn threshold diagram considered is presented in figure 2.33 and shows the described trend when considering the threshold as a function of the total heat flux generated during grinding. This trend is also presented by Jin et al. (2002); here high-carbon steel is subjected to the HEDG regime in the surface down grinding mode. The research concludes that in this case the onset of grinding burn is triggered by the film boiling of the coolant in the contact zone at temperatures in the region of 400°C. As with Chen et al. (2000) the threshold for grinding burn is suggested to occur over a range of temperatures.

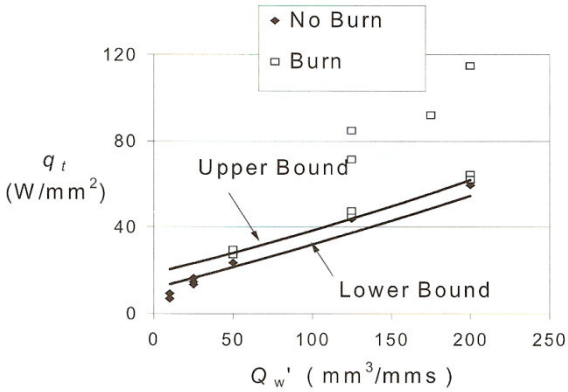

Figure 2.33 Burn threshold diagram for HEDG based on the heat flux at which grinding burn occurs after Stephenson et al. (2002)

Jones et al. (2004) present a statistical approach to the optimisation of the High Efficiency Deep grinding process. Utilising a fuzzy fitness function, the authors demonstrate three dimensional plots of feedrate and depth of cut against both specific grinding energy and surface temperature. The authors conclude that the use of a fuzzy expert system is an acceptable method for process optimisation. However, the use of this kind of statistical approach appears to be limited by the initial data set provided. When considering the HEDG regime in isolation, the system appears to suggest that grinding parameters known to produce a low temperature give high temperature values.

The thermal modelling approach is considered by Snoeys et al. (1978) who discuss a variety of grinding regimes and their thermal models. In consideration of cut-off grinding and creep feed grinding, the authors note that much of the heat is actually carried away with the grinding chip. The authors conclude that thermal damage in the

workpiece can be predicted with application of the appropriate thermal model, however it is noted that for applications such as cut-off and creep feed grinding the effect of heat removal with the grinding chip must be taken into account.

The mechanics of grinding burn are considered in the series of papers presented by Zhang & Mahdi (1995) and Mahdi & Zhang (1997, 1998 and 1999b). Utilising a combination of numerical and finite element modelling techniques, the authors present a description of the mechanism of phase transformation, thermal residual stress and the residual stress and surface hardening by coupled thermo-plasticity and phase transformation. Finally the process of residual stress formation as a result of mechanical and thermal deformation and phase transformation (Mahdi & Zhang 1999b) is considered. The authors conclude that the process of phase change results in all residual stress profiles becoming tensile and whilst coolant application has an effect, the process of phase transformation will be relatively unaffected by the presence of coolant.

2.4.2 Thermal Modelling as a Product of Burn Threshold Analysis

Given the relationship between the threshold of grinding burn and a threshold temperature, the strength of the burn threshold diagram or model must be dependent on the quality of the thermal model used to predict the grinding temperature.

The grinding process presents a moving heat source problem, considered by Jaeger (1942) a series of equations for assessment of the temperature with moving heat sources are presented. The author highlights the need for a series of equations to easily quantify the temperature resulting from a sliding contact. Grinding processes present an approximation of a rectangular or linear heat source moving across a surface and as such the models presented by Jaeger (1942) are utilised extensively in the literature as the basis of more recent thermal models.

Malkin & Anderson (1974) and Malkin (1974) present a model in which the total energy required for grinding is split into chip formation, sliding and ploughing energy. This follows on from Des Ruisseaux & Zerkle (1970) who calculated surface temperatures on the basis of the shear plane temperature. The authors conclude that calculating temperatures on the basis of chip formation is inhibited by the accuracy with which chip formation process and shear plane temperatures can be estimated. Further

they consider the effect of the grinding chip thermally insulating itself from the workpiece surface during removal, thus temperatures may be lower than calculated.

Malkin (1974) considers grinding temperatures as the effect of a peak temperature rise due to chip formation and an average grinding zone temperature due to the combined action of all abrasive grains. The average grinding zone temperature acts as a rectangular moving heat source with length equal to the contact length, width equal to the width of cut and velocity equal to the workpiece velocity. This analysis showed a peak temperature close to the melting point of the material at the cutting edge.

Models considering heat transfer to the wheel, workpiece and fluid are presented by Lavine & Jen (1991) and Guo & Malkin (1992). Considering the coolant as a convective heat transfer from the grinding interface, Lavine & Jen (1991) demonstrate the use of a model of maximum grinding zone temperature to predict the onset of fluid film boiling in the wheel workpiece contact occurring at some critical temperature. The authors conclude that upon achieving some critical temperature, the heat transfer to the grinding fluid becomes negligible and as such there is a sharp rise in workpiece background temperature, often resulting in grinding burn. Lavine & Jen (1991) make reference to the use of CBN grains on the grinding wheels, stating that their improved thermal conductivity over conventional abrasives results in a higher grinding power requirement to cause film boiling. This recognition of the improved thermal behaviour of the CBN grain is crucial to the development of more aggressive processes such as the HEDG regime.

Guo & Malkin (1992) also consider the application of CBN as a grinding medium and its benefits over conventional abrasives in creep feed grinding on the energy partition to the workpiece. Based on experimental data, the authors show a decreased energy fraction entering the workpiece being only 20% as compared to conventional wheels which experience between 70% and 90% energy fraction to the workpiece during grinding. In their consideration of the grinding fluid, Guo & Malkin (1992) highlight the fact that energy partition to the workpiece is greatly reduced when fluid boiling does not occur. It is fair to assume therefore that the combination of a good coolant supply with the use of CBN abrasives will give the most reduced heat partition to the workpiece for creep feed grinding conditions.

Given the extremely high contact temperatures in the wheel workpiece contact zone in HEDG at large depths of cut as presented by Stephenson et al. (2002) and the work presented by Lavine & Jen (1991) and Guo & Malkin (1992) a case is made for the use of CBN abrasives in the HEDG regime.

The large depths of cut in high efficiency deep grinding present an unusually large angle of inclination of the contact between wheel and workpiece. Rowe (2001) discusses the effect of the angle of inclination of the heat source from the finished surface on the temperature. Figure 2.34 demonstrates changes in the fraction of temperature in the finished workpiece surface to the maximum temperature occurring in the contact zone as contact angle is increased. This demonstrates that as the depth of cut and hence contact angle is increased the energy entering the finished surface is significantly reduced even at moderately low values of Peclet number.

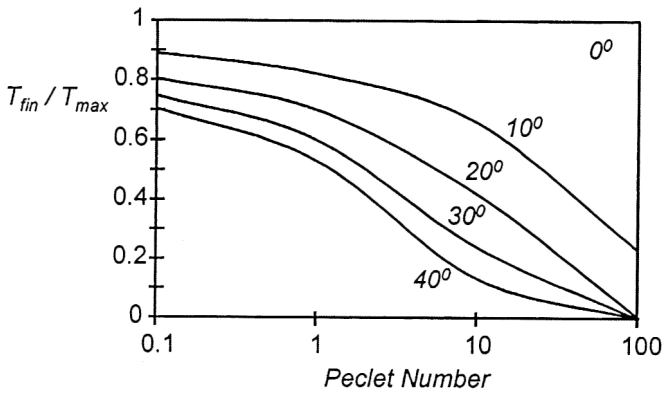

Figure 2.34 Effect of angle of inclination on energy partitioned to the finished workpiece surface from the wheel-workpiece contact after Rowe (2001)

Jin et al. (2001) consider an inclined moving heat source plane model for deep grinding conditions. The authors conclude that the angle of inclination of the heat source has a flattening effect on the temperature distribution in the wheel workpiece contact zone, which should be accounted for in modelling of the HEDG regime.

The circular arc of heat contact model presented by Rowe and Jin (2001) considers the thermal model in terms of heat flux partition to the various elements of the grinding process and is the most significant model for estimating grinding temperatures when considering the HEDG regime. The total heat flux to the workpiece (equation 2.1) is represented as the summation of the heat fluxes to the grinding chip q_{ch}, fluid q_f,

workpiece q_w and wheel q_s. A simplified equation for the total heat flux in terms of grinding parameters (equation 2.2) is presented by Rowe (2000).

$$q_t = q_w + q_s + q_{ch} + q_f \qquad \textit{Equation 2.1}$$

$$q_t = P_{net} / l_c \cdot b \qquad \textit{Equation 2.2}$$

Heat flux to the chip is presented in terms of a limiting chip energy e_{ch}, which is the energy required to elevate the grinding chip to its melting temperature. The heat flux to the grinding chips is represented by the following equation:

$$q_{ch} = e_{ch} \cdot a_e \cdot v_w / l_c$$

Where the limiting chip energy is described in terms of the workpiece material properties and an estimation of the maximum temperature achieved in the grinding chip, where:

$$e_{ch} = \rho \cdot c \cdot T_m$$

Heat flux to the fluid was estimated on the basis of experimental results, the following value of 290,000 W/m^{2}K for a water based fluid was used by Rowe & Jin (2001) however Stephenson & Jin (2003) present a table collated from previous works, summarised in table 2.4, in which a high degree of variation is experienced in the convection coefficient values.

Grinding Fluid	H_f (W/m^{2}K)	Data Sources
Mineral Oil	23,000	Rowe & Jin (2001)
Water Based	290,000	Rowe & Jin (2001)
Mineral Oil	100,000 – 160,000	Jin & Stephenson (2003)
Water Based	300,000 – 450,000	Jin & Stephenson (2003)
Water Based	15,000 – 20,000	Malkin

Table 2.4 Convection coefficients presented in the literature after Stephenson & Jin (2003)

The heat flux to the workpiece q_w is assessed in terms of the fraction of the maximum temperature generated entering the workpiece, where:

$$q_w = h_w \cdot T_{\max}$$

and

$$h_w = \frac{\beta_w}{C} \cdot \sqrt{\frac{v_f}{l_c}}$$

The factor C presented by Rowe & Jin (2001) represents the effects of the angle of inclination on the contact zone temperature. The C-factor quantifies the contact layer theory presented by Tawakoli (1993) for deep grinding. Figure 2.35 presents values of the C-factor with increasing Peclet number for varying angles of inclination.

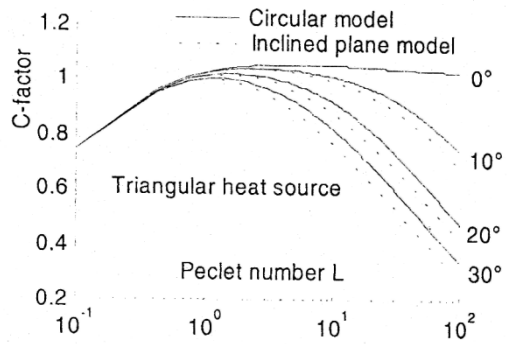

Figure 2.35 Sample C-factors for varying angles of inclination after Rowe & Jin (2001)

The heat flux to the grinding wheel has particular significance for processes utilising CBN wheels, due to their high thermal conductivity. Rowe & Jin (2001) assess the heat flux to the workpiece in terms of the maximum contact temperature as follows:

$$q_s = h_s \cdot T_{\max}$$

Where h_s is expressed as:

$$h_s = h_w \left[\frac{1}{R_{ws}} - 1 \right]$$

The factor Rws is the wheel workpiece partition ratio and is based on the model of Hahn (1962) for a grain sliding on a workpiece, where:

$$R_{ws} = \left[1 + \frac{0.97 k_g}{\beta_w \cdot \sqrt{r_0 \cdot v_s}} \right]^{-1}$$

The constants k_g, the thermal conductivity of the grain and r_0, the abrasive grain radius can have an effect on the error in the system, particularly the thermal conductivity. For HEDG with CBN wheels, Stephenson & Jin (2003) assume a value of 240 W/mK for k_g and 10µm for r_0.

The culmination of the model of Rowe & Jin (2001) is the development of the following equations for the maximum temperature in the contact zone both with and without the burnout of the grinding fluid. Equations 2.3 & 2.4 demonstrate the equations derived.

$$T_{\max} = \left. \frac{q_t - h_{ch} \cdot T_{mp}}{\frac{h_w}{R_{ws}} + h_f} \right|_{T_{\max} \le T_b} \qquad \textit{Equation 2.3}$$

$$T_{\max} = \left. \frac{q_t - h_{ch} \cdot T_{mp}}{\frac{h_w}{R_{ws}}} \right|_{T_{\max} > T_b} \qquad \textit{Equation 2.4}$$

The final aspect of the model presented by Rowe & Jin (2001) is to apply a factor relating the temperature in the inclined contact surface to the finished surface. The authors achieve this using a fractional factor presented in figure 2.36, which determines the fraction of energy which enters the finished workpiece. The experimental work is validated with a thermocouple test rig, showing good agreement between the theoretical work and the temperatures recorded.

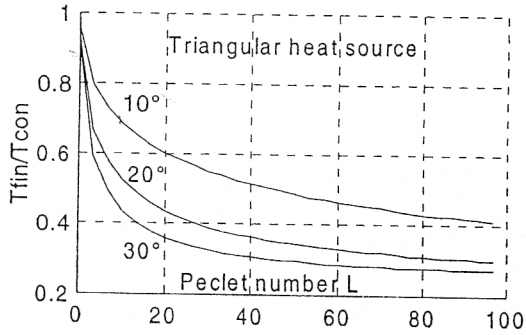

Figure 2.36 Fraction of energy partitioned to the finished workpiece surface after Rowe & Jin (2001)

Given that grinding presents a moving heat source and hence transient problem, Jin & Stephenson (2004) demonstrate the use of a finite elements (FE) approach for a transient 3D simulation. The authors consider the surface grinding of a thin steel plate and the effect of the presence of a shoulder in a simple profile grind. The application of HEDG conditions show a steady-state heat transfer condition after the wheel is fully engaged with the workpiece, whilst predicted temperatures showed similar values to the 2D circular arc of heat source model presented by Rowe & Jin (2001). It is also suggested that the use of an FE package can allow for 3D analysis of complex geometries.

2.5 Summary and Hypothesis

The literature review has raised a number of questions relating to workpiece temperatures and their prediction during High Efficiency Deep Grinding. Section 2.1.3 commented on the temperature profile with increasing specific material removal rates (figure 2.4) in the workpiece surface. Figures 2.7 and 2.8 also showed further temperature trends with workpiece speed and depth of cut again for the workpiece surface. These reviews do not consider the temperature in the sidewall, which for profile and cylindrical traverse grinding applications is a significant element.

Sainz (2005) successfully demonstrated the possibility of measuring the sidewall temperature for very thin deep cuts, and demonstrated a trend of increasing temperature in the sidewall with increasing depth of cut. However the limitations of the sample width prevented a complete collection of data on the subject. Further, no work has been found which considers the relationship between temperatures in the surface and those in the sidewall.

Section 2.1.3 also discusses the modelling of the specific grinding energy curve. Of particular reference is the work of Jin & Stephenson (2003), which considers a power law relationship between specific grinding energy and specific material removal rate. The question is raised of the large scale applicability of this relationship given the contention of Malkin (1989) and Morgan et al. (2004) that a minimum or constant value of grinding energy is ultimately achieved and that this is based on material properties.

The possibility of grinding without the application of grinding fluids was raised by both Jin & Stephenson (2003) and Stephenson et al. (2002) with the latter demonstrating limited variation in specific grinding energy with changes in fluid supply. Given the contention of a minimum specific grinding energy revisited in the previous paragraph, there exists the possibility that specific grinding energies would be identical irrespective of fluid supply strategy when minimum grinding energies have been achieved. This may be limited by the effects described in section 2.2, in which the work of Brinksmeier et al. (1999) considered the removal of grinding chips by the grinding fluid, thus preventing a build up of unwanted waste material in the wheel-workpiece interface which would increase workpiece temperatures

Burn threshold diagrams were considered in section 2.4.1 and highlighted the difficulties of predicting the threshold of grinding burn. Models presented by Malkin & Lenz (1978) and Malkin (1989) were applied by Stephenson et al. (2001) to the HEDG regime and whilst offering a distinct separation between burnt and unburnt samples, gave an inappropriately high temperature at which the onset of burn was to occur. This was discussed as being the result of the energy partitioning in the models being inappropriate to the HEDG regime. Whilst this model is not the only model available, the ability to translate it to the HEDG regime is desirable in light of the work presented by Jin & Stephenson (2003) in which specific grinding energies were predicted, thus making it possible to predict parameters likely to fall into burn regions from basic grinding parameters and knowledge of the phase change temperatures of the workpiece material.

This thesis therefore addresses 3 important research questions in reflection of the literature review, these are:

- Does specific grinding energy reduce to a constant value as specific material removal rates increase into the HEDG regime, and will this value be constant independent of coolant supply
- Can the burn threshold diagram first presented by Malkin & Lenz (1978) be adapted to the HEDG regime and hence be useful for process optimisation
- Will the temperature in the sidewall be linked to the temperature in the surface and will the temperature between profile surfaces exhibit a common trend.

3 Experimental Methodology

The experimental methodology describes the equipment, techniques and process undertaken to achieve an overview of the thermal properties of the HEDG regime during profile and cylindrical grinding. The research focuses on the development of four key areas of understanding:

- The asymptotic form of the specific material removal rate versus specific grinding energy curve, confirmation of its approximation with a power curve at extreme parameters and varying wheel condition and the value of minimum specific grinding energy determined
- The effect which coolant plays on the specific grinding energy and grinding power, with the concept of minimum grinding energy independent of coolant supply being explored in surface grinding and the effect of coolant type variation explored in cylindrical traverse grinding
- The application of the burn threshold diagram presented by Malkin (1978) when extreme parameters are used and aggressive specific material removal rates are achieved
- The behaviour of the thermal profile around the form generated during HEDG with the presence of a sidewall with recommendations for application to process design

3.1 Experimental Equipment

Section 3.1 considers the Edgetek machine tools used in the research, the Saint Gobain wheels and grinding fluid supplied for the grinding trials and the sources of error within and calibration of the equipment. The two Superabrasive Edgetek machines in the School of Applied Sciences (SAS) at Cranfield University are standard production machines, manufactured in the UK by Holroyd Precision Limited, a company within The Precision Technologies Group. The two machines are designed for the Superabrasive machining of hard to machine and exotic aerospace materials. They have the capability to achieve the aggressive removal rate characteristic of the HEDG condition and meet the HEDG machine requirements presented in section 2.1.3 of the literature review.

Grinding wheels were supplied by the Saint Gobain group and exhibited the requirements highlighted in section 2.1.3 and 2.4.2 of the literature review. Wheels had high thermal conductivity CBN grits with an electroplated bond to a strong steel wheel body. These were suited to the temperatures and aggressive grinding conditions experienced during the HEDG regime.

3.1.1 Edgetek SAM

The Edgetek SAM is a high performance, 4 + 1 axis surface grinding machine and the original machine with the capability for HEDG at Cranfield University. Figure 3.1 shows the Edgetek SAM with the standard twin nozzle coolant arrangement and workpiece fixture in place. These were used extensively throughout the course of this research for the surface grinding investigations.

Figure 3.1 Edgetek SAM 4 + 1 axis surface grinding machine

The machine specifications as published by the manufacturer are shown in table 3.1, the machine being capable of grinding at the rapid traverse rate and being set-up in metric units of measurement.

Edgetek SAM Machine Specifications	
Parameter	**Description**
X-Axis Travel	18.6” (472 mm)
Y-Axis Travel	12.8” (325 mm)
Z-Axis Travel	12.0” (305 mm)
B-Axis Rotary	12.59” (317.5mm) Diameter
5th Axis	A or rotary tilt version
Spindle HP	35 HP (27 kW)
Spindle RPM	14,000 RPM higher RPMs available
Way System	Schneeberger Hi-precision Linear Roller Bearing Ways
Position Feedback	Heidenhain Linear Scales on X,Y, Z
Feed Rate	To 157 IPM 66 mm/sec
Rapid Traverse	0 to 300 IPM (126 mm/sec)
Voltage	200 – 230 volts, 3 Phase 60 Cycle

Table 3.1 Specification of the Edgetek SAM machine tool

The Edgetek SAM was retrofitted with a motor load sensor to measure the power at the wheel spindle. Motor power was measured in preference to current drawn because of the linear nature of the relationship between motor load and power giving rise to a greater sensitivity at low load conditions (figure 3.2). The motor load sensor is described as accurate to 0.5% over the full load of the motor, a specification sheet is provided in Appendix A of the thesis. The output scale from the monitor was set to 150% of the full load; this could be achieved because of the linear nature of the relationship between load and power and allowed for instantaneous overloading of the motor up to approximately 40kW to be recorded.

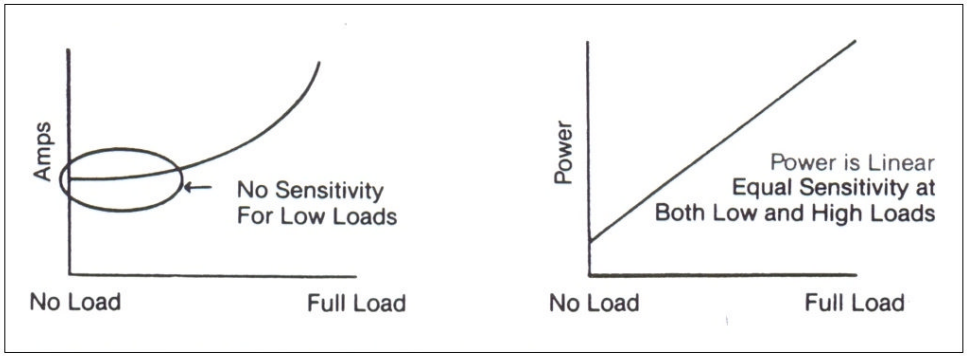

Figure 3.2 Comparison of curves for measurement of current versus measurement of power

The HEDG regime produces high temperatures in the wheel workpiece contact zone as well as a large volume of high temperature grinding chips. These may act as a source of ignition for the cutting oil and as such a fire protection system has been fitted to the machine. This system consists of an explosion vent to the roof of the machine to direct conflagrant material away from the area occupied by the operator and an argon fire suppression system. The argon system is designed to activate automatically upon a critical temperature being reached inside the machine, or to be activated manually with a simple glass-break switch by the operator.

3.1.2 Edgetek SAT

The Edgetek SAT (or SuperAbrasive Turner) is a purpose built cylindrical grinding machine designed for the application of superabrasive technologies and with sufficient capacity to achieve HEDG conditions. This was the second of the two machines suitable for the application of HEDG acquired by Cranfield University as part of the SATURN project. The SAT (figure 3.3) is shown here in standard cylindrical grinding configuration as used extensively throughout this research. The live tailstock is shown, with the later twin top nozzle and trough coolant system in place. This application was developed as part of the SATURN project by Massam (2008).

Figure 3.3 Edgetek SAT cylindrical grinding machine

The Edgetek SAT specifications as published by the manufacturer are shown in table 3.2. As for the Edgetek SAM the machine was capable of grinding at a rapid traverse rate and set-up in metric units of measurement.

Similarly to the Edgetek SAM, the Edgetek SAT was retrofitted with a motor load sensor for measurement of spindle power. Again this was set to measure to 150% of the full load allowing for instantaneous overload of the spindle. The system was therefore capable of recording power values up to a total of approximately 56kW. Further the Edgetek SAT was fitted with an identical fire suppression system to the Edgetek SAM. In spite of the improved coolant application possible with the cylindrical traverse grinding process, the preferred grinding fluid, oil, is still highly volatile and therefore requires the security of the fire suppression system.

Edgetek SAT Machine Specifications	
Parameter	**Description**
X-Axis Travel	472 mm
Z-Axis Travel	305 mm
B-Axis Rotary	12.59” (317.5mm) Diameter
5th Axis	A or rotary tilt version
Spindle Power	37 kW (50 hp)
Spindle Drive	Belt & Pulleys
Spindle RPM	9,000 RPM max.
CBN Wheel Dia.	250 mm – 355 mm
Swing	Per Application
Workhead	305 mm diameter workhead configured for chucking by fixture or chuck.
X – Z Feedback	Heidenhain MMS Linear Scales
Tailstock	Manual and automatic quill. Tailstock body manually positioned
Coolant Delivery	Two-Zone Programmable Valves
Voltage	200 – 230 volts, 3 Phase 60 Cycle

Table 3.2 Specification of the Edgetek SAT machine tool

3.1.3 Saint Gobain CBN Grinding Wheels

All grinding wheels used in the project were Saint Gobain electroplated CBN wheels. The wheel designation in all cases was B213, which is the CBN designation for a grit size of approximately 213µm. The grinding regimes of interest were simple surface grinding, grinding with the presence of a shoulder otherwise termed simple profile grinding and the cylindrical traverse grinding process. The presence of a shoulder in both regimes required the application of abrasive to the side face of the wheel.

Figures 3.4 & 3.5 describe the grinding wheel used for all surface grinding tests and present the terminology used for the surfaces under consideration in the thesis. This terminology will be used extensively throughout the work.

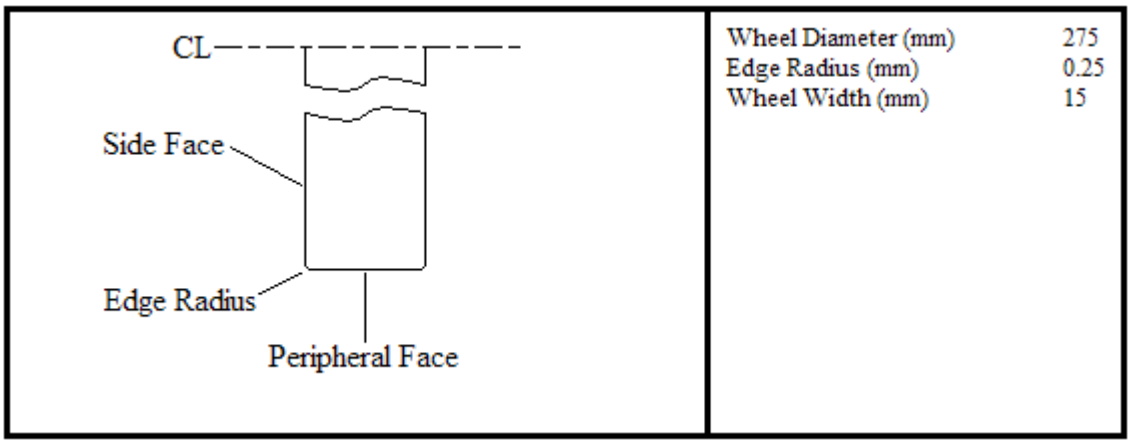

Figure 3.4 Schematic showing the geometry of the surface grinding wheel

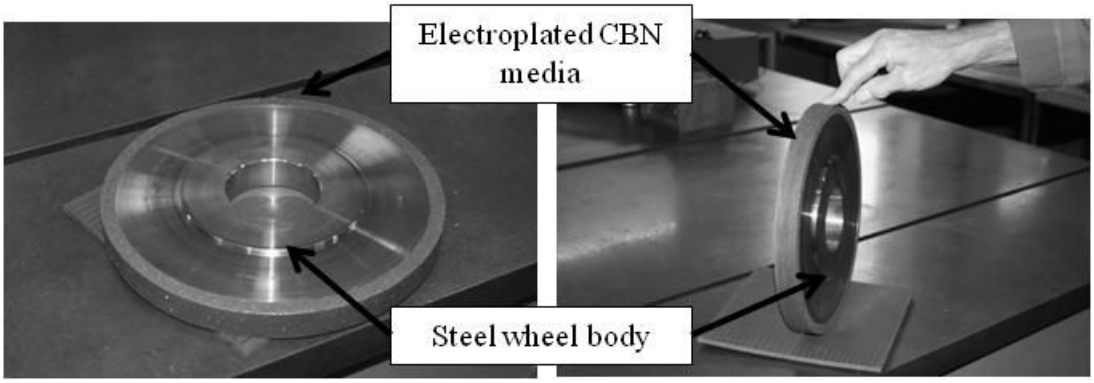

Figure 3.5 Photographs showing the typical surface grinding wheels used

Wheels for cylindrical traverse grinding operations were marked by the presence of significant leading and trailing edge radii. This was understood to facilitate the traverse of the wheel during grinding. Figure 3.6 shows the grinding wheel used for cylindrical traverse grinding schematically and its dimensions, with figure 3.7 showing the actual wheel used. Again the figures present the terminology used to describe the surfaces under consideration. Rudimentary measurements of the leading edge radius using a shadowgraph suggested that the designated dimension presented in figure 3.6 was accurate.

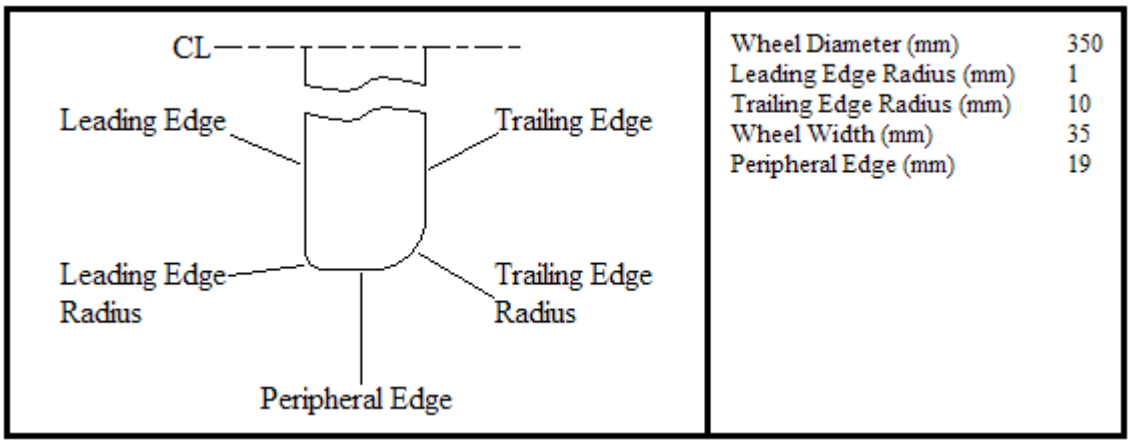

Figure 3.6 Schematic showing the geometry of the cylindrical grinding wheel

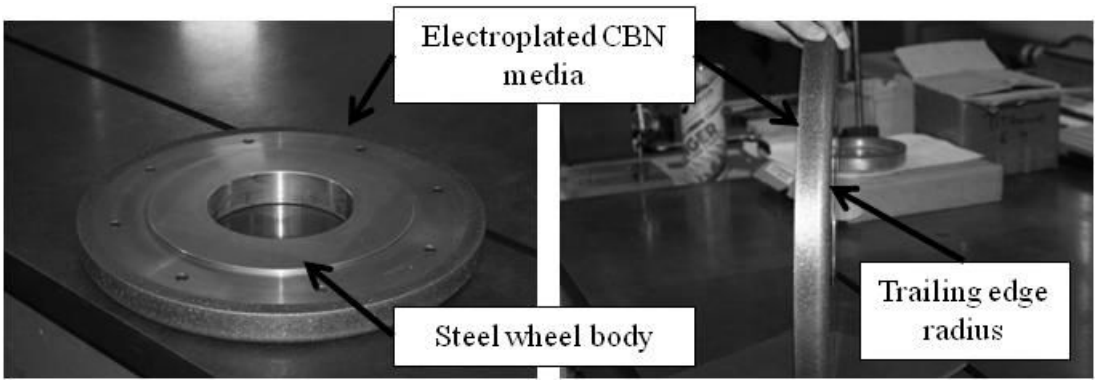

Figure 3.7 Photographs showing the typical cylindrical grinding wheels used

3.1.4 Grinding Fluids

Castrol provided two types of grinding fluid for use in the HEDG trials. These were Castrol Variocut G 600 SP neat grinding oil (referred to as oil based grinding fluid) and Hysol X Chlorine free soluble cutting fluid (referred to as water base grinding fluid). The Hysol X was diluted to 6% in water suitable for the high temperature application of HEDG. Details of the two grinding fluids can be found in data sheets in Appendix B of the thesis.

3.1.5 Calibration of the Machine Tool

The Edgetek machines were set-up by a trained machine setter for the trials undertaken. Measurements of finished samples confirmed that the cut dimensions were to within minus 10µm of the programmed value. This deviation was expected as a result of the

aggressive nature of the grinding parameters and as the process was stock removal was of no detriment to the results recorded.

Coolant supply was verified with the use of in-line volumetric flow metres with values set by the in-line flow metres attached to the coolant hose as distinct from the programmed value to ensure accurate and consistent coolant supply. Positions relative to the wheel were established with the use of a laser line to ensure consistent and accurate positioning.

The value of the power load sensor was set with 0V equal to no load and 10V equal to 150% of the motor power. The linear relationship described in figure 3.2 allowed for the calculation of set points along the power line. Thus voltages were verified by calculation against the motor power.

3.1.6 Sources of Error in the Equipment

All of the equipment required for the experimental phase exhibits some error in terms of accuracy of measurement and precision of the machine tool. The Edgetek machine tool slideways for example are accurate to ±0.005mm in every 300mm, with rotational axes to ±20 ARC seconds. This is combined with the error listed by the motor load sensor manufacturer and described as 0.5% over the full load of the motor. Additionally, machine tools such as the Edgetek series, whilst being highly rigid, do exhibit some flexibility under aggressive grinding conditions. As such the depth of cut, width of cut, workpiece feedrate and wheel speed may not be as prescribed by the programme adding further error to the system.

Given difficulties in the measurement of the error a 5% experimental error could be applied to results of specific grinding energy recorded. This allowed for variation in the system to be accounted for and deliver a result in which the author could be confident.

3.2 Assessment of the Specific Grinding Energy and Burn Threshold

Section 3.2 outlines the parameters and describes the methods used in the investigation of specific grinding energy trends. Assessment of the specific grinding energy and power curves was split into two sections, on the basis of verifying the asymptotic form of the specific grinding energy curve at high material removal rates:

- Surface grinding of profiles

- Cylindrical traverse grinding

Trials for the assessment of the burn threshold model were run concurrently with the specific grinding energy trials and utilised samples of Spheroidal Grey Cast Iron (SGCI) and 51CrV4, sourced from department stock. Cylindrical traverse grinding trials utilised samples of 51CrV4, again available as stock material in the department.

3.2.1 Surface Grinding Trials

The assessment of the total and net grinding powers, specific grinding energy and the application of HEDG parameters to the model of burn threshold presented by Malkin & Lenz (1978) were achieved via the following trials.

- Profile grinding with application of grinding fluid (51CrV4 and SGCI)
- Profile grinding without the application of grinding fluid (SGCI)

3.2.1.1 Set-up of the Edgetek SAM

For all surface grinding trials, the Edgetek SAM was set up with a configuration suitable for down grinding as shown in figure 3.8, which demonstrates the coolant nozzle arrangement, clamping set-up and grinding wheel in-situ. The photograph shows:

1) The rear coolant nozzle for spark suppression and cooling of the finished surface at the right hand side of the machine, the grinding direction for trials was from right to left
2) The front coolant nozzle for application of grinding fluid to the wheel – workpiece interface at the left hand side of the machine
3) The typical workpiece clamping solution (inset shows detail)
4) The grinding wheel as per the details shown in figure 3.4 & 3.5

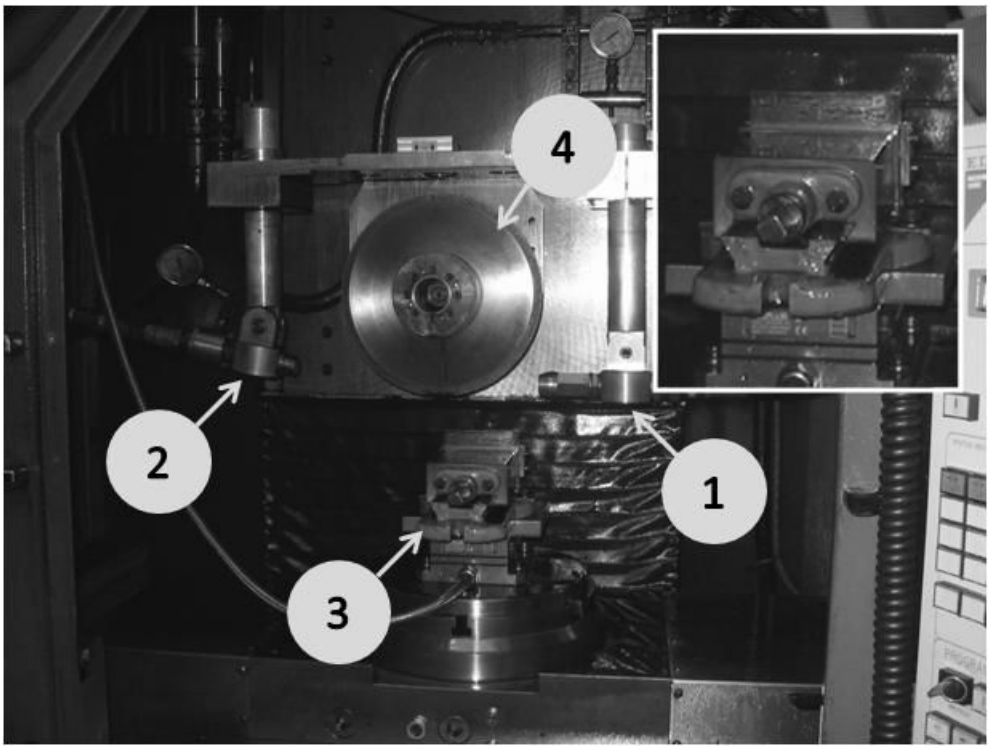

Figure 3.8 Photograph of Edgetek SAM set-up

Table 3.3 describes the key parameters and measurements in the setting of the machine tool fluid application, standard for all surface grinding trials.

	Left Nozzle (2)	Right Nozzle (1)
Height from horizontal tangent at wheel bottom	35mm	0mm
Angle from horizontal	11.5°	0°
Pressure at nozzle	6 Bar	6 Bar
Nozzle diameter	3 mm	3 mm

Table 3.3 Edgetek SAM fluid application set-up

3.2.1.2 Surface Grinding Sample Design and Preparation

The available SGCI was in the form of forged crankshaft sections as shown in figure 3.9. Samples were sectioned from the crankshaft to make surface grinding specimens typical of those shown in figure 3.10. Sample dimensions were typically 16mm wide by 70mm long, height varied dependent on material available.

Figure 3.9 Photograph of typical crankshaft section from which SGCI surface grinding samples were drawn

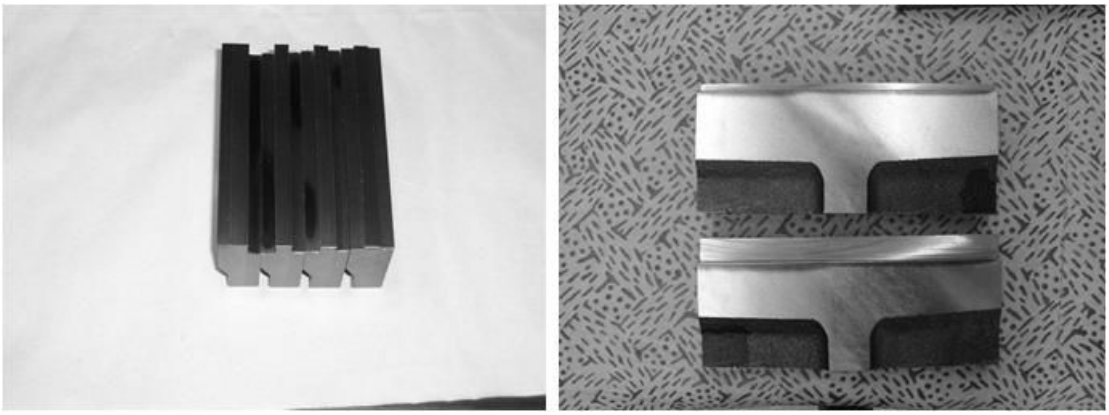

Figure 3.10 Photographs of typical SGCI samples in the as used condition noting dark surface marks indicating grinding burn

The 51CrV4 was of the form of untreated bar stock approximately 80mm in diameter. Samples were drawn from the bar stock following the schematic demonstrated in figure 3.11 below. Samples were surface ground on all faces to ensure square and parallel and measured 15mm wide by 50mm deep by 80mm long.

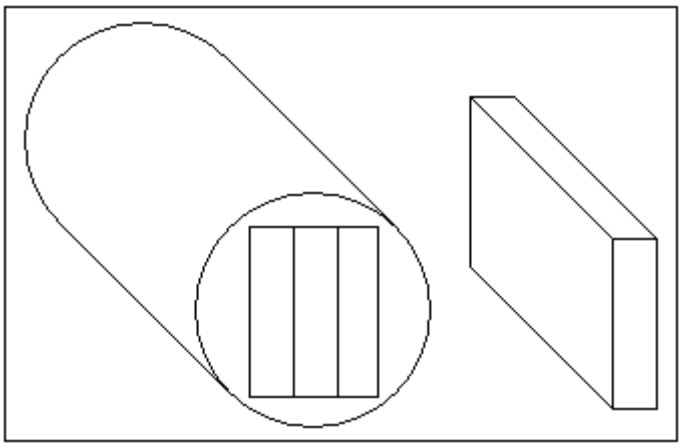

Figure 3.11 Schematic of sample extraction from 51CrV4 bar stock

3.2.1.3 Surface grinding parameters

Tables 3.4 to 3.6 detail the grinding parameters selected for the surface grinding trials, these trials were undertaken consecutively from low to high values of specific material removal rate. The selection of parameters is based on the onset of HEDG conditions around 50mm^3/mm·s (Tawakoli, 1993) and was designed to ensure results were available through the HEDG transition permitting the development of burn conditions.

Material	SGCI	
Fluid Application	Yes	
Grinding Direction	Down	
Parameter	**Symbol**	**Values**
Wheel speed (m/s)	v_s	50 – 150m/s
Workpiece speed (mm/s)	v_w	50 – 7500mm/min
Depth of Cut	a_e	0.5 – 9mm
Width of Cut	b	5 – 2mm
Specific Material Removal Rate	Q'_w	0.5 – 1125mm^3/mm·s

Table 3.4 Surface grinding parameters for trials in SGCI with grinding fluid application

Material	SGCI	
Fluid Application	No	
Grinding Direction	Down	
Parameter	**Symbol**	**Values**
Wheel speed (m/s)	v_s	50 – 150m/s
Workpiece speed (mm/s)	v_w	50 – 5000mm/min
Depth of Cut	a_e	0.5mm
Width of Cut	b	5mm
Specific Material Removal Rate	Q'_w	0.5 – 40mm^3/mm·s

Table 3.5 Surface grinding parameters for trials in SGCI without grinding fluid application

Material	51CrV4	
Fluid Application	Yes	
Grinding Direction	Down	
Parameter	**Symbol**	**Values**
Wheel speed (m/s)	v_s	50 – 200m/s
Workpiece speed (mm/s)	v_w	50 – 7500mm/min
Depth of Cut	a_e	0.5 – 4mm
Width of Cut	b	5 – 1mm
Specific Material Removal Rate	Q'_w	0.5 – 375mm^3/mm·s

Table 3.6 Surface grinding parameters for trials in 51CrV4 with grinding fluid application

3.2.1.4 Data Collection

Specific grinding energy e_c was estimated from the measured net grinding power P_{net} using the following equation:

$$e_c = P_{net} / Q'_w \cdot b$$

Where:

$$Q'_w = a_e \cdot v_w$$

The net grinding power was estimated via measurements from the motor load sensor described in section 3.1 and is the power absorbed during material removal from the surface of the workpiece. This was calculated by subtracting the measured sparkout power from the measured total power required by the spindle during grinding of a test piece.

The standard procedure for recording grinding power was as follows:

1. Hold the wheel at the end of the workpiece with test parameters applied, no contact to be made
2. Start recording power
3. Move the wheel through the workpiece at the desired feedrate
4. Stop recording power

A typical grinding power measurement is shown in figure 3.12 and demonstrates the region over which the measurement of grinding power actually takes place. Grinding power is averaged across the area marked 2 and labelled Grinding Zone inset. The figure demonstrates:

1) Ingress into the workpiece to full contact conditions
2) Full contact and area of grinding which can be used for measurement
3) Exit of the wheel from the workpiece

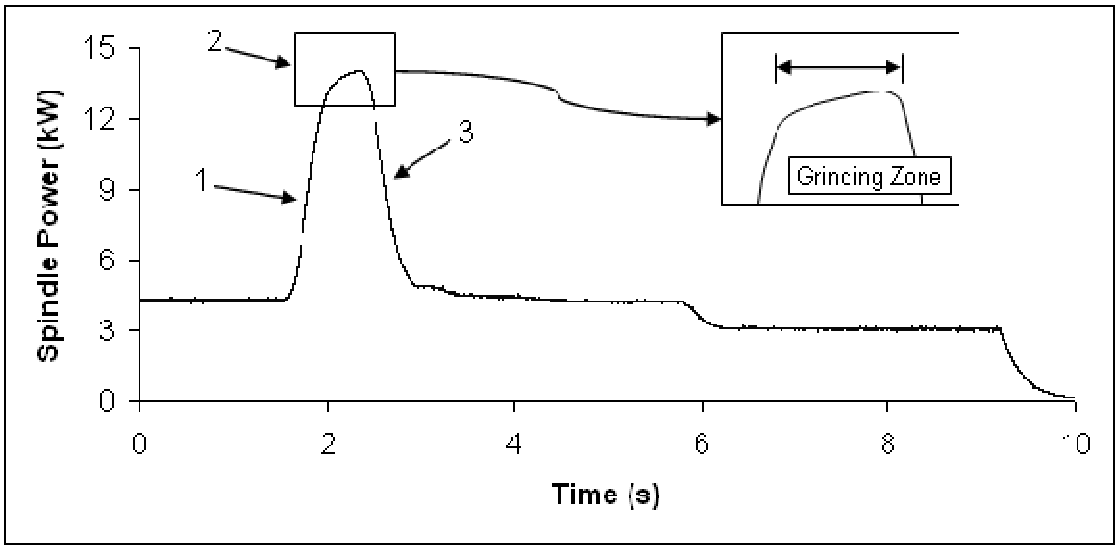

Figure 3.12 Typical grinding power curve for grinding power recorded at the spindle motor during surface grinding

The sparkout power is described as all power requirements of the grinding machine that do not directly contribute to material removal. Sparkout power was assessed prior to the machining trials with the following standard test procedure:

1. Form the wheel workpiece contact shape at the midpoint of the test block
2. Bring the wheel in to the contact zone
3. Start recording power
4. Move the wheel into the workpiece a further 0.5mm and dwell for 5 seconds
5. Extract wheel
6. Stop recording

This procedure resulted in a typical sparkout power graph, figure 3.13, of which a mean reading over section 3 of the curve resulted in the sparkout power for the particular condition. The figure demonstrates:

1) Build up of coolant pressure in the contact zone as full contact conditions are approached
2) Wheel contact with workpiece and 0.5 mm ingress
3) Sparkout power due to contact conditions
4) Power required for wheel and coolant outside of contact condition

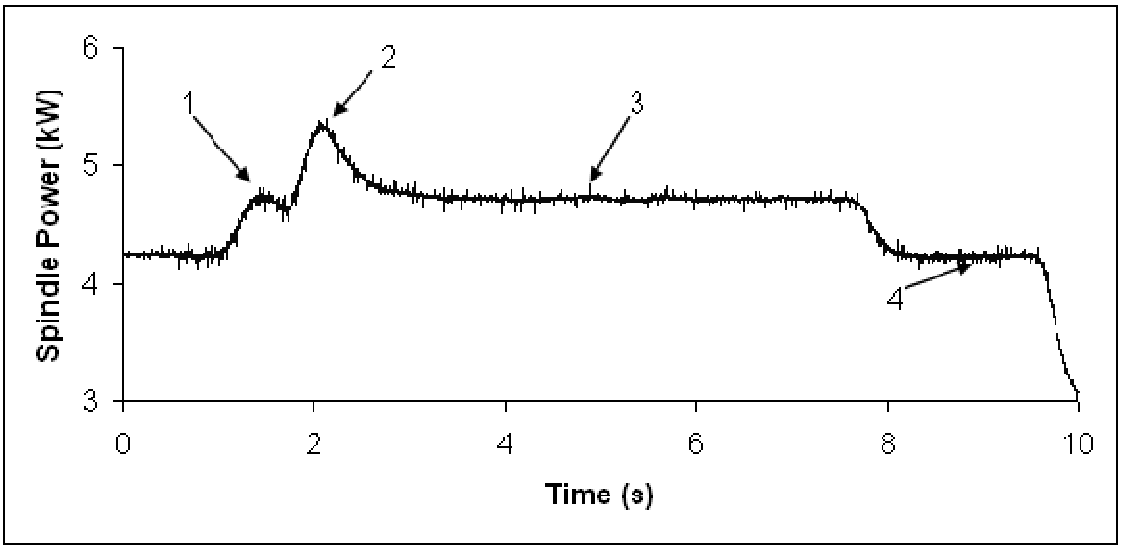

Figure 3.13 Typical sparkout power curve for grinding power as recorded at the spindle motor during surface grinding

Investigations of burn threshold were undertaken in the surface grinding mode to allow grinding burn to be verified visually. By taking a single pass, the workpiece surface was left in the as ground condition preventing deterioration of the temper colours characteristic of grinding burn by subsequent passes of the grinding wheel. Multiple passes of the grinding wheel in the cylindrical traverse grinding regime, the result of the feed per turn being less than the wheel width, resulted in the as ground surface being cleaned multiple times, removing temper colours. As such only the surface grinding regime was determined to be viable for assessment of the burn threshold.

The inspection of the surface was required to look for any discoloration from a very pale yellow to a pale blue[1], indicative of temperatures having reached a minimum of approximately 220°C at the surface for steel. Figure 3.14 demonstrates characteristic temper discoloration seen on the surface of an as ground 51CrV4 sample block. This discoloration was typically brown/black to blue/black and could be seen towards the end of the ground sample.

[1] For a full list of temper colours, see Machinery's Handbook, Oberg et al. (2000)

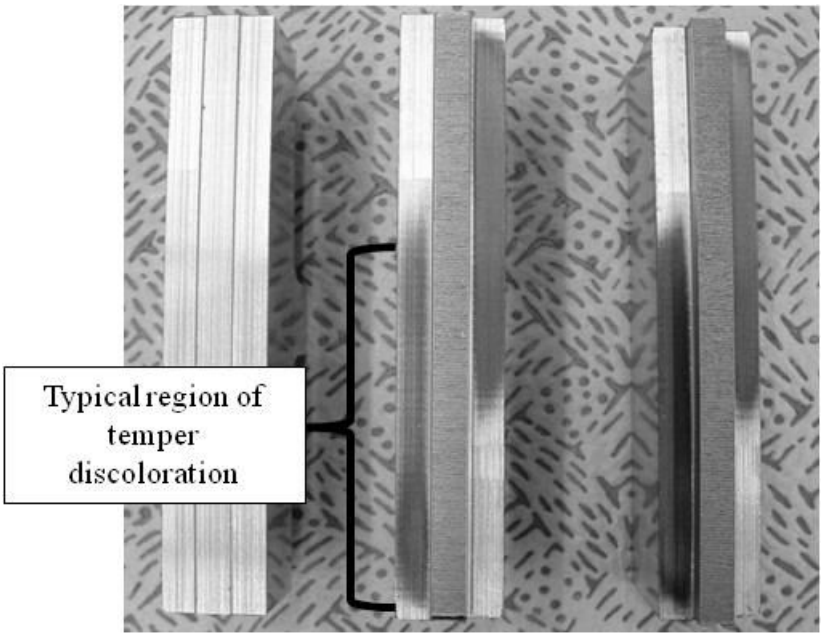

Figure 3.14 Regions of temper discoloration on the as ground surface in 51CrV4

3.2.2 Cylindrical Traverse Grinding

The 1000RPM workhead capacity of the Edgetek SAT allowed for the development of very high surface speeds. As such the assessment of the total and net grinding powers and the specific grinding energy curve could be expanded in the regime to very high and consistent stock removal rates. Further, this section provided the opportunity to explore the process parameters for very high removal rate trials with low melting point coatings. As previously stated, the interaction of the wheel and workpiece obliterating the initially ground surface prevented the use of cylindrical traverse grinding results in burn threshold analysis. The research strategy for cylindrical traverse grinding was therefore simply:

- Cylindrical traverse grinding with the application of water based and neat oil coolant to very high specific material removal rates with 51CrV4

3.2.2.1 Set-up of the Edgetek SAT

The Edgetek SAT was set up with a four jaw chuck and standard tailstock for the initial range of cylindrical traverse grinding experiments. Coolant application was via a small diameter convergent jet top nozzle, supplying grinding fluid directly into the nipping point of the interface between wheel and workpiece and a large diameter bottom nozzle

designed to suppress the grinding sparks. For grinding trials with water based coolant the bottom nozzle was removed as the grinding fluid was not flammable. Both nozzles were positioned such as the flow jet was centred on the wheel edge, figure 3.15 describes the machine set-up typical for the water based coolant with the blind arm for the bottom coolant nozzle shown, with table 3.7 and 3.8 detailing the chuck and tailstock type and the coolant parameters applied.

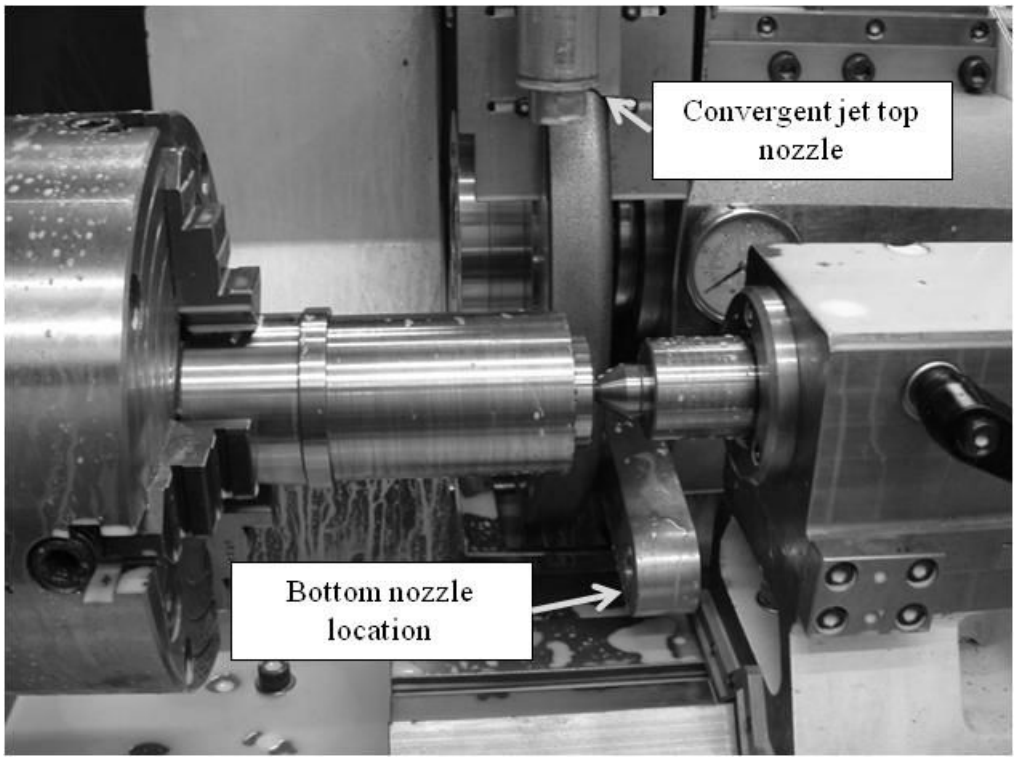

Figure 3.15 Detailed view of Edgetek SAT set-up for grinding with water based fluid, for early oil based fluid trials a bottom nozzle was used

	Top Nozzle	Bottom Nozzle
Pressure	10 Bar	12 Bar
Nozzle Diameter	3 mm	6 mm
Extension	Yes	N/A
Tailstock Type	Standard	
Chuck Type	4 - Jaw	

Table 3.7 Grinding fluid and machine tool parameters for trials with oil based fluid

	Top Nozzle	Bottom Nozzle
Pressure	4 Bar	N/A
Nozzle Diameter	3 mm	N/A
Extension	Yes	N/A
Tailstock Type	Standard	
Chuck Type	4 - Jaw	

Table 3.8 Grinding fluid and machine tool parameters for trials with water based fluid

The application of the cylindrical traverse grinding regime results in a load applied to the wheel sidewall. For this reason at large depth of cut there is a necessity for coolant to be applied to the wheel leading edge. The work of Massam (2008) considered the application of grinding fluid in the cylindrical traverse grinding regime, developing a combination of a top nozzle arrangement and a new design of spark arrestor to the bottom. The nozzle arrangement on the top featured two nozzles applying grinding fluid to the wheel edge radius and the leading edge and is shown in figure 3.16.

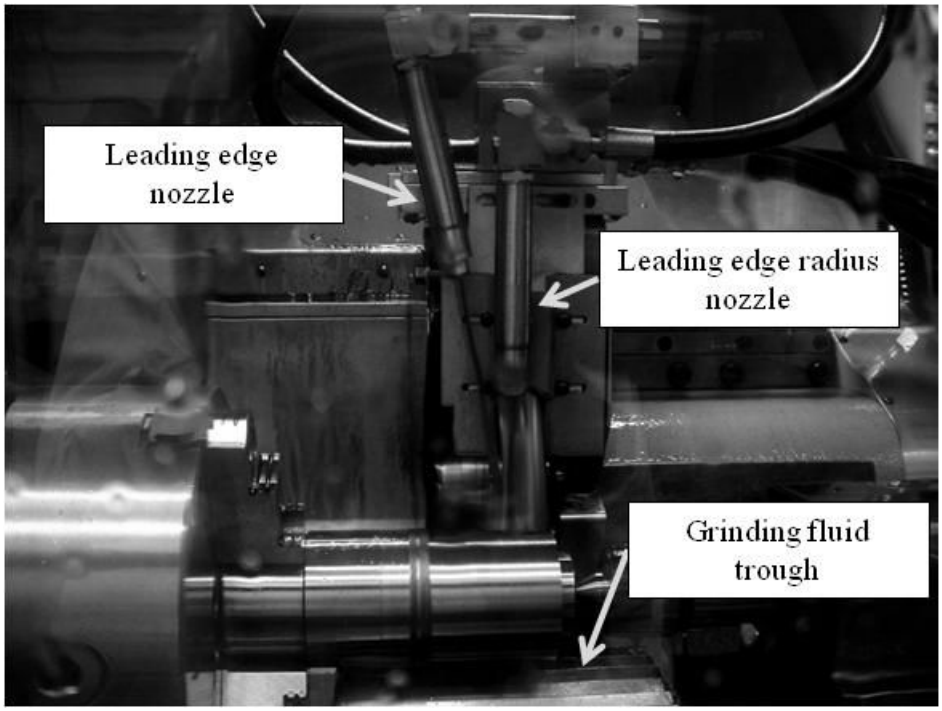

Figure 3.16 Detailed view of Edgetek SAT set-up for later cylindrical traverse grinding trials

The effect of the leading edge nozzle was measured by visual inspection. The inspector was required to look for a change in the volume and intensity of grinding sparks resulting from the application of the additional side nozzle. Power measurements were ruled out as the grinding parameters were too aggressive to be run for long periods prior to the operator becoming confident the machine could tolerate the aggressive cut with the coolant application. Figures 3.17 and 3.18 demonstrate the change in volume and luminosity of the grinding sparks with the change in grinding fluid application. Figure 3.18 shows a significantly reduced spark volume and luminosity with the application of a fluid jet to the wheel leading edge. Conversely the spark volume and luminosity demonstrated in figure 3.17 are shown to be higher. The results therefore show the requirement for the application of a leading edge nozzle when considering cylindrical traverse grinding in the high efficiency deep grinding regime.

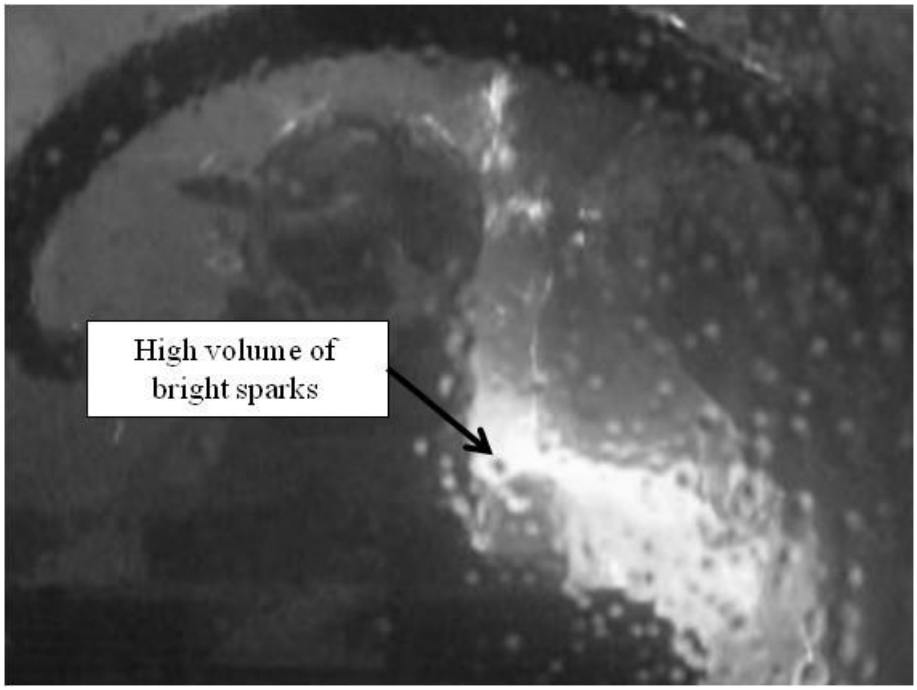

Figure 3.17 Photograph of spark generation without the application of a leading edge nozzle

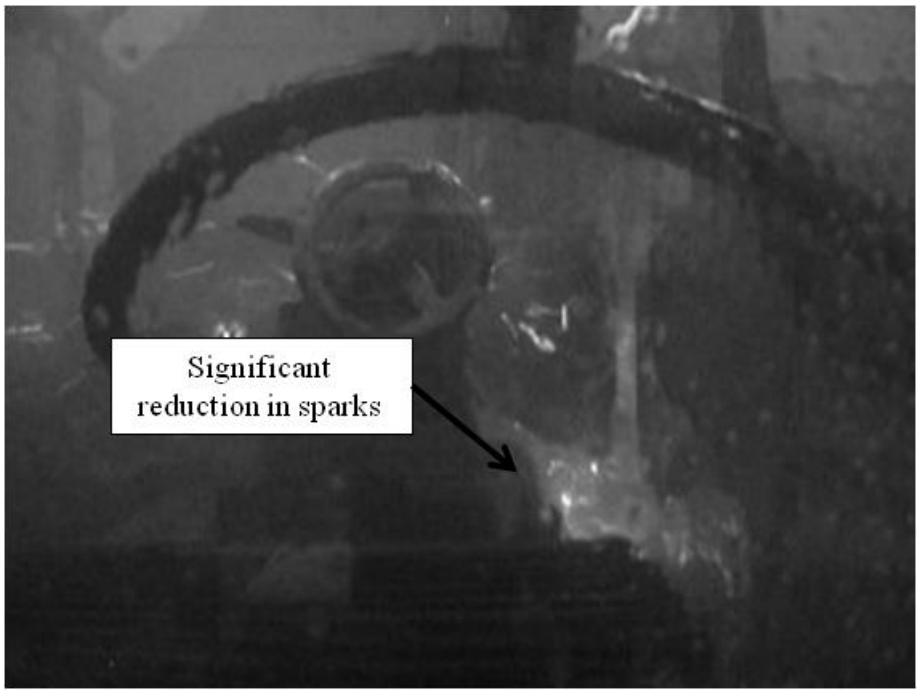

Figure 3.18 Photograph of spark generation with the application of a leading edge nozzle showing significant spark reduction

3.2.2.2 Cylindrical Traverse Grinding Samples

The investigation of the cylindrical traverse grinding regime was undertaken with 51CrV4 round bar available as department stock from a previous research programme. This untreated round bar was ground to a 79mm outside diameter to ensure concentricity with a small shoulder at 50mm outside diameter machined onto one end to facilitate a locating surface for the chuck attached to the workhead. A range of typical samples is shown in the as ground condition in figure 3.19 below.

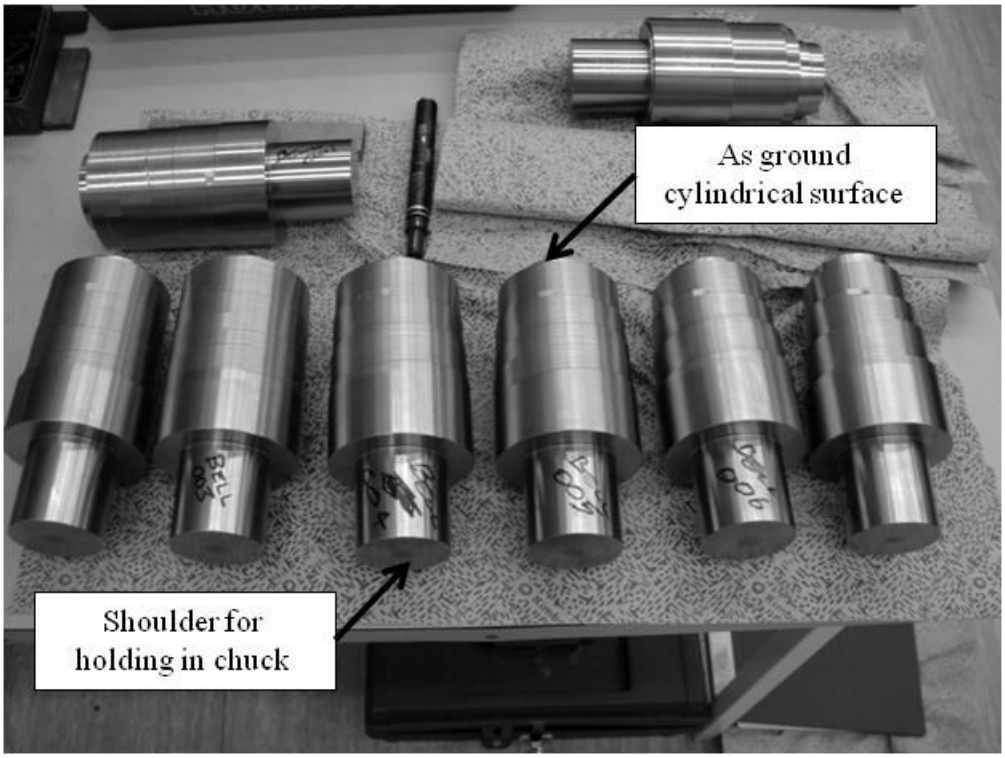

Figure 3.19 Photograph of typical cylindrical grinding samples in the as ground condition

3.2.2.3 Cylindrical Traverse Grinding Parameters

Experiments were undertaken following table 3.9 and 3.10, these were selected on the basis of providing a range of specific material removal rates at varying values of width of cut or feed per turn. Further the possibility of grinding at high removal rates with water based fluid was considered. An additional trial described in table 3.11 was made to study the capability of the machine at a high removal rate with the new twin top nozzle arrangement in place.

Parameter	Symbol	Values
Wheel speed	v_s	150m/s
Workpiece surface speed	v_w	2 to 96mm/s
Workpiece Traverse Speed	v_f	0.125 to 2 mm/s
Feed per Turn (mm)	b	5 to 15mm
Depth of Cut	a_e	0.5 to 3mm
Specific Material Removal Rate	Q'_w	1 to 120mm^3/mm·s
Nozzle Arrangement	Standard nozzles	
Grinding Direction	Up	

Table 3.9 Details of cylindrical traverse grinding trials with the application of oil based grinding fluid

Parameter	Symbol	Values
Wheel speed	v_s	150m/s
Workpiece surface speed	v_w	25 to 90mm/s
Workpiece Traverse Speed	v_f	1mm/s
Feed per Turn	b	2.5 to 5mm
Depth of Cut	a_e	0.5 to 6mm
Specific Material Removal Rate	Q'_w	18 to 415mm^3/mm·s
Nozzle Arrangement	Standard nozzles	
Grinding Direction	Up	

Table 3.10 Details of cylindrical traverse grinding trials with the application of water based grinding fluid

Parameter	Symbol	Values
Wheel speed (m/s)	v_s	150m/s
Workpiece surface speed (mm/s)	v_w	4085mm/s
Workpiece Traverse Speed (mm/s)	v_f	3.3mm/s
Feed per Turn (mm)	b	0.2mm
Depth of Cut	a_e	1mm
Specific Material Removal Rate	Q'_w	$4085mm^3/mm{\cdot}s$
Nozzle Arrangement	Twin nozzle and trough	
Grinding Direction	Up	

Table 3.11 Details of high material removal rate trial

3.2.2.4 Data Collection

Net Grinding power was estimated similarly to the surface grinding regime with measurements being taken via the motor load sensor described in section 3.1.1. As for surface grinding, the net grinding power is defined as the power required to remove material from the workpiece. This was estimated by subtracting the sparkout power from the total power required at the spindle during grinding. In cylindrical traverse grinding, the standard procedure for recording the total grinding power was:

1. Hold the wheel at the end of the workpiece with test parameters applied, no contact to be made
2. Start recording power
3. Move the wheel through the workpiece at the desired feedrate
4. Stop recording power

A typical grinding power graph is presented in figures 3.20. The power measurement described in figure 3.20 can be seen to be distinct from those recorded in surface grinding and demonstrates:

1) A slow ramp up to full grinding power as the wheel becomes fully engaged with the workpiece
2) A lengthy steady state grinding power region from which grinding power can be estimated

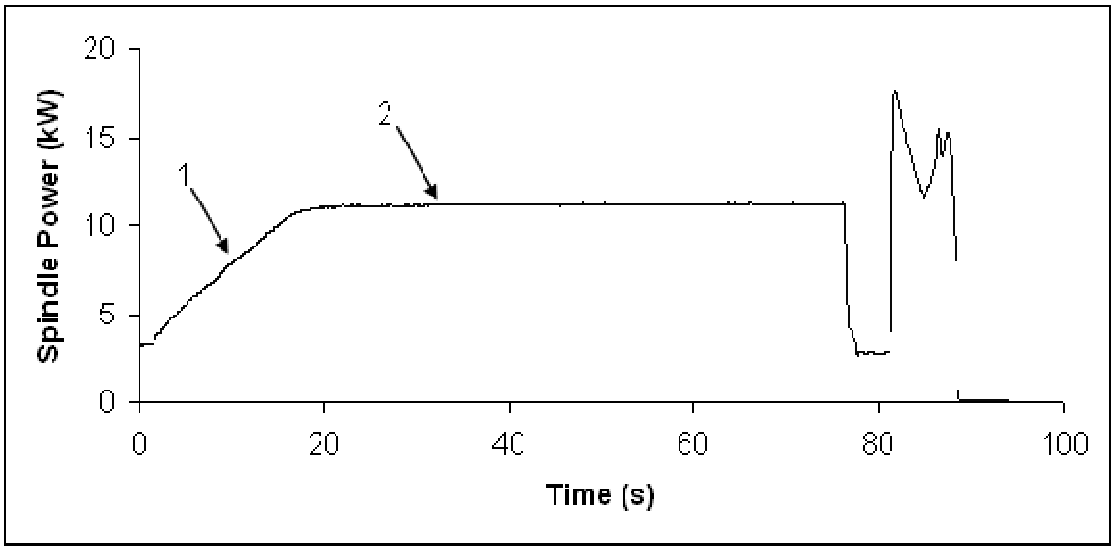

Figure 3.20 Typical grinding power curve for grinding power recorded at the spindle motor during cylindrical traverse grinding

As for surface grinding, the sparkout power was defined as the power requirements for all aspects of the grinding machine that do not contribute directly to material removal. Sparkout power was again assessed prior to the machining trials with the following test procedure:

1. Form the wheel workpiece contact shape at the midpoint of the test block
2. Bring the wheel in to the contact zone
3. Start recording power
4. Move the wheel into the workpiece 5 degrees and dwell for 5 seconds
5. Extract wheel
6. Stop recording

Figure 3.21 presents the typical sparkout power curve recorded and demonstrates:

1) A sharp increase in power similar to the surface grinding process as the wheel begins to interact with the workpiece
2) A steady state representing the power required to drive the coolant through the interface

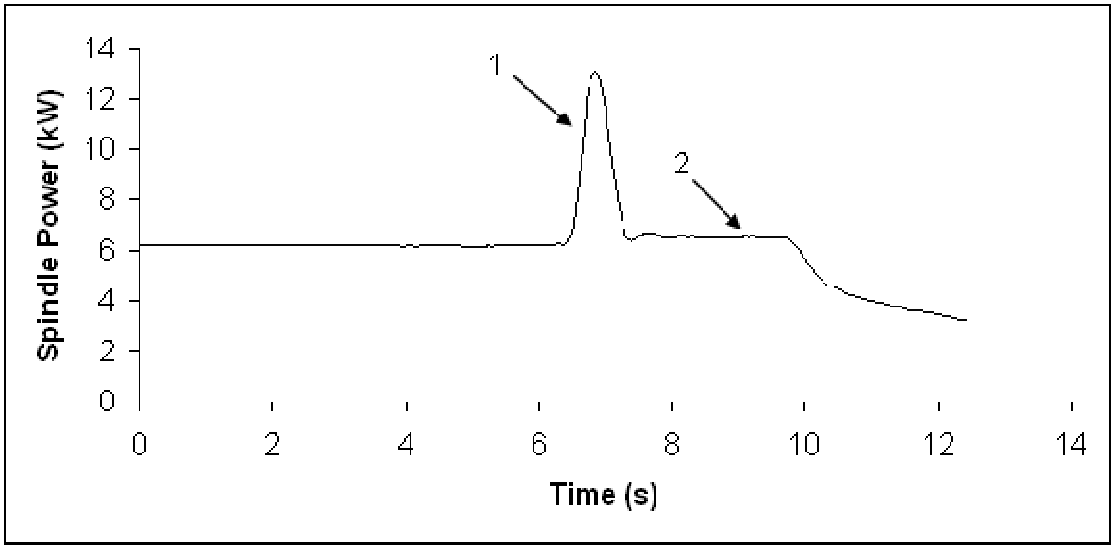

Figure 3.21 Typical sparkout power curve for grinding power recorded at the spindle motor during cylindrical traverse grinding

Forming of the contact shape in the cylindrical surface was achieved via the accurate control of the axes with the Edgetek SAT's capacity for complete CNC control of the workhead or C-axis. This full CNC control of the machine was accessed through the PLC and allowed the machine's C-axis to be moved by fractions of a degree, whilst traversing in the Z-axis. In this set-up the machine can be moved by a precise angle. The Z-axis must therefore be instructed to move a precise distance over the number of degrees rotated, in order that a desired feed per turn is maintained. To calculate the movement of the relative axes required, the following process was used.

The CNC command console of the Edgetek SAT is accessed through the M27 command, followed by the activation code G91 in order to instruct the machine that:

1) CNC control is active

2) All movements are incremental

The machine then calls for the parameters required for accurate machine movement, namely:

1) Z-axis movement in mm
2) C-axis movement in total number of degrees turned
3) An F command related to the C-axis and instructing the machine to operate at that value of degrees per min, the maximum available to the operator in CNC mode is 25,000°/min

The feed per turn was determined by the operator and a ratio of traverse rate (movement in the Z-axis) to rotational rate in the C-axis (RPM) was established in order to achieve that value. The feed per turn is a function of the traverse feedrate (movement in the Z-axis) and the RPM of the C-axis. The following formula allowed the feed per turn to be calculated and can be considered similar to the width of cut in surface grinding.

$$\text{Feed per turn} = \frac{Traverse}{RPM}$$

For a given RPM i.e. 100RPM and a required feed per turn of 0.2mm, the traverse rate in the Z-axis was calculated such that:

$$Traverse = 0.2 \times 100$$
$$Traverse = 20mm \cdot \min^{-1}$$

The workhead then required a distance of travel in the Z-axis and to know the time that this would take. Using an arbitrary value of 30mm required travel at 20mm/s to ensure the full engagement of the grinding wheel, the time of travel was calculated, where:

$$time = \frac{30}{20}$$
$$= 1.5 \min$$

At the given 100RPM, the total number of degrees turned 'C' is equal to:

$$C = RPM \times time \times 360$$
$$= 100 \times 1.5 \times 360$$
$$= 54000$$

The feedrate of the workhead in RPM, F, was calculated in °/min and was simply assessed using the following:

$$
\begin{aligned}
F &= RPM \times 360 \\
&= 100 \times 360 \\
&= 36000
\end{aligned}
$$

In real terms the feedrate cannot exceed 25,000°/min. The axis values were calculated dependent on the feed per turn of the experiment undertaken. Where possible the feedrate experienced in the trial was mimicked in the measurement of the sparkout power, however when this was not possible, the equivalent ratio of feed per turn was used.

3.3 Thermal Profiling with PVD Coatings

The selected parameters and methods used for the thermal profiling and temperature measurement of the grinding process with 51CrV4 grinding samples are outlined in this section. The investigation of the thermal profile formed around the wheel-workpiece contact considered two main areas as determined by the literature review. These were designed to reflect the need to understand the behaviour of the partition of heat flux around the sidewall with the experimental phase consisting of:

- Thermal profiles in surface grinding
- Thermal profiles in cylindrical traverse grinding

The details of the investigation are summarised in the following sections.

3.3.1 Surface Grinding

The thermal profile of the form grinding process under surface grinding conditions and the effect of the grinding parameters on the form were achieved with the following grinding trials:

- Grinding of PVD samples with and without a shoulder
- Grinding of PVD samples with a shoulder under varying levels of width and depth of cut and workpiece feedrate

3.3.1.1 Set-up of the Edgetek SAM

The surface grinding trials were performed on the Edgetek SAM. The machine was set up in the standard down grinding configuration presented in section 3.2.1.1 table 3.3. The vice used for the early surface grinding investigations was modified to accept an

end plate holding two M4 grub screws. These grub screws could then be used to provide additional clamping force and prevent undesirable movement of the split samples under grinding. Figure 3.22 shows the vice arrangement.

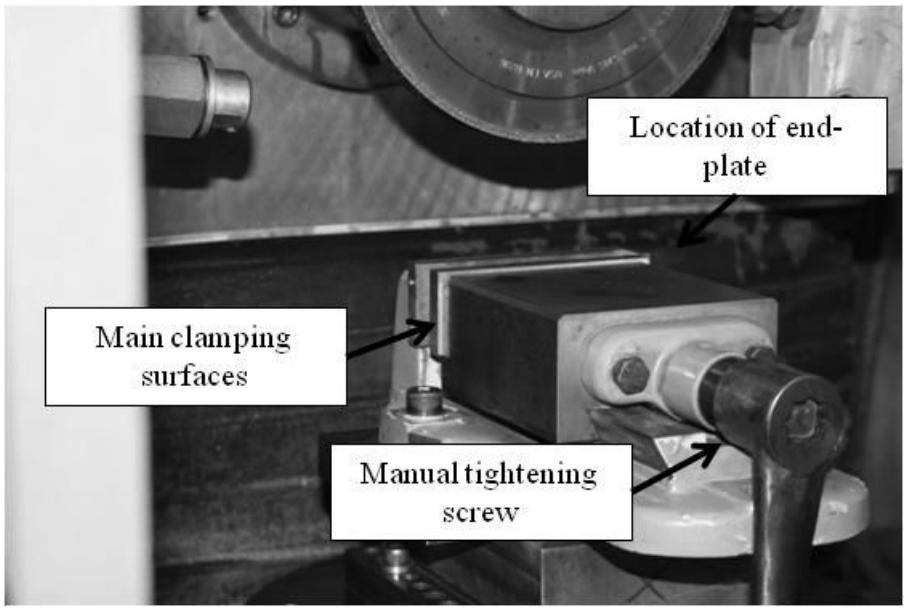

Figure 3.22 Photograph showing detailed view of work-holding arrangement for surface grinding trials

3.3.1.2 PVD Coated Surface Grinding Samples

Two test pieces were designed based on the work of Walton et al. (2005), the original example is shown in figure 3.23. New samples were designed to simulate the differences between basic surface and profile grinding. Thus samples were a combination of solid and castellated blocks, solid blocks simulating profile grinding and castellated blocks simulating surface grinding.

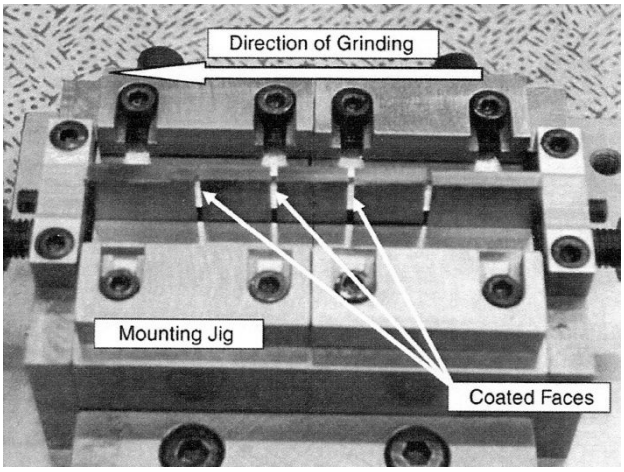

Figure 3.23 Photograph of test rig previously used for measurement of temperatures with PVD coatings after Walton et al. (2005)

Sample blocks are shown schematically in figure 3.24 and demonstrate:

1) Standard test block for profile grinding trials
2) Standard test block for surface grinding with no sidewall
3) Surfaces coated with low melting point coatings via the PVD method

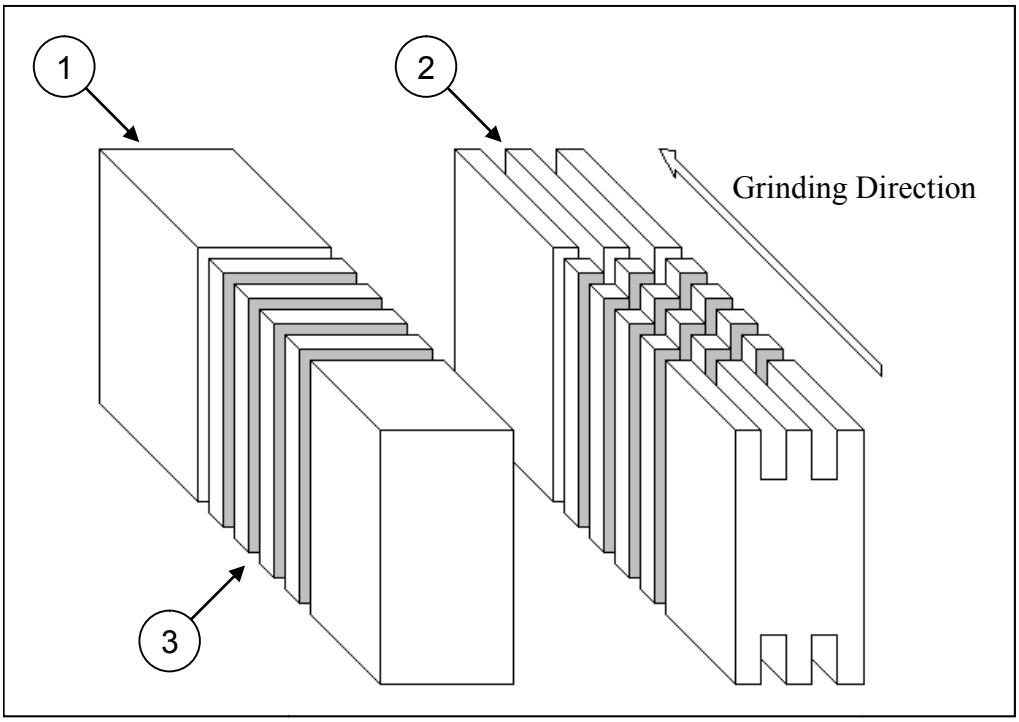

Figure 3.24 Schematic of PVD sample blocks

Coatings were aligned perpendicular to the grinding direction in order to produce an isotherm perpendicular to the grinding direction. The test block was manufactured with a large width of 15mm and hence surplus material was available in the sidewall

allowing a complete isotherm to form. This was in response to issues highlighted in the work of Sainz (2005) wherein isotherms had been drawn through the sidewall as a result of the thickness of the workpiece. Photographs of the two sample types are shown in figure 3.25 and 3.26 in the fully assembled condition.

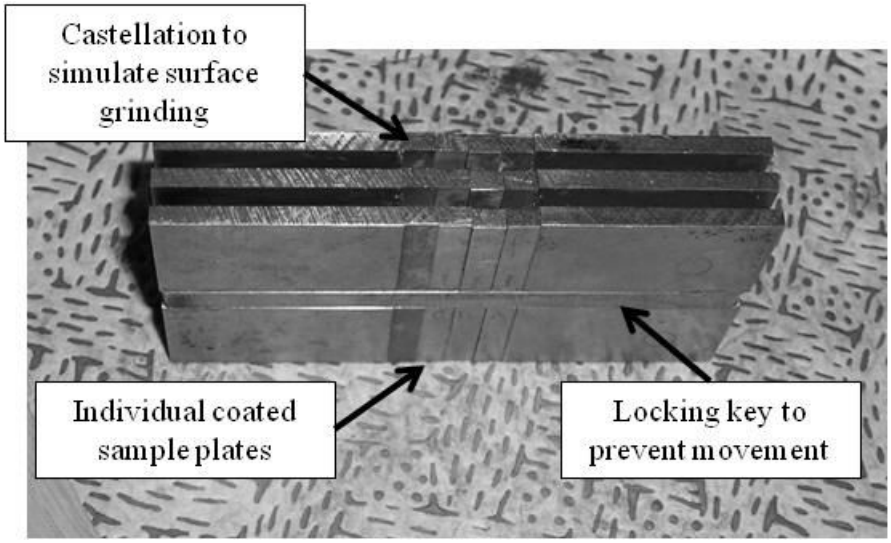

Figure 3.25 Photograph of surface grinding sample block

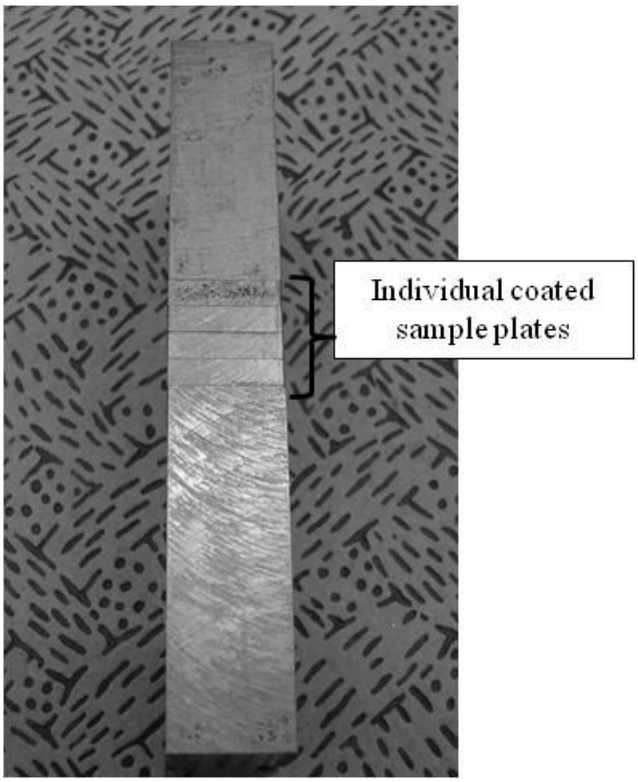

Figure 3.26 Photograph of profile grinding sample block

The sample blocks were secured with a 5mm wide by 3mm deep key and keyway to ensure the alignment and security of the separate test pieces. Detailed drawings of the sample blocks are shown in figure 3.27 and 3.28, with table 3.12 and 3.13 describing the values of the dimensions.

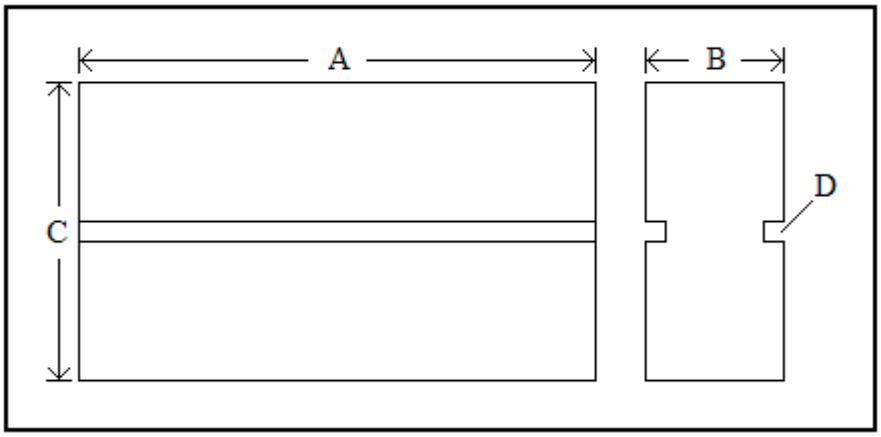

Figure 3.27 Detailed drawing of PVD coated profile grinding block

Section	A	B	C	D
Leading Edge	45	15	>35	To accept 5mm key
Trailing Edge	45	15	>35	To accept 5mm key
PVD section	5	15	>35	To accept 5mm key

Table 3.12 Table of dimensions for profile grinding blocks

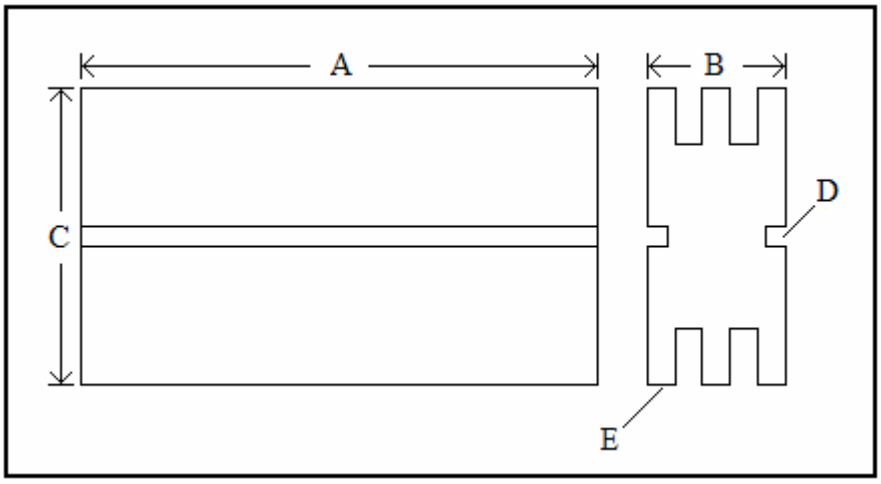

Figure 3.28 Detailed drawing of PVD coated surface grinding block

Section	A	B	C	D	E
Leading Edge	45mm	15mm	>35mm	To accept 5mm key	3 Equidistant lands, 3mm wide by 6mm deep
Trailing Edge	45mm	15mm	>35mm	To accept 5mm key	3 Equidistant lands, 3mm wide by 6mm deep
PVD section	5mm	15mm	>35mm	To accept 5mm key	3 Equidistant lands, 3mm wide by 6mm deep

Table 3.13 Table of dimensions for surface grinding block

Low melting point coatings were applied to the desired surfaces using a Physical Vapour Deposition technique. Described by Walton et al. (2005), the PVD technique deposits a 200nm thick layer of material onto the surface of the test piece. The deposition was achieved by a resistively heated thermal evaporation coating system and measured by the change in resonant frequency of a quartz crystal within the deposition chamber. The faces to which coatings were applied were prepared to a parallel mirror finish in order to minimise thermal distortion through the interface. The preparation of the surfaces was achieved with the Tetraform face grinding machine (figure 3.29) with samples checked visually for surface condition and physically by lapping together.

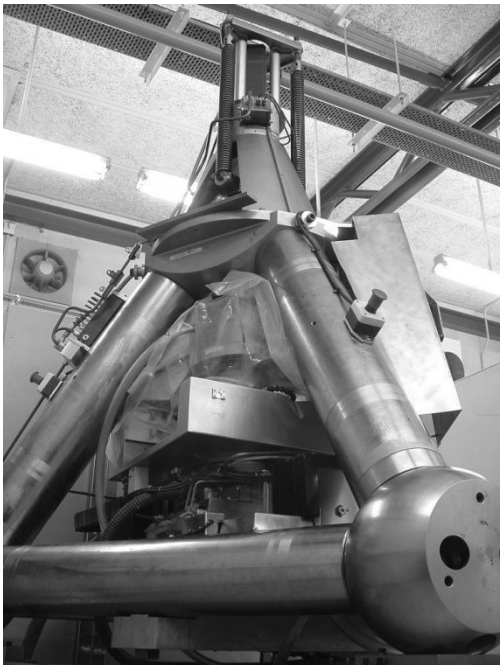

Figure 3.29 Tetraform face grinding machine as used in the preparation of surface and profile grinding samples

The low melting point coatings were selected on the basis of previous experience within the department to cover a range of possible temperatures. Coatings used are described in table 3.14 and achieve a range between 156 and 630°C.

Coating	Symbol	Melting Temperature °C
Indium	In	156
Bismuth	Bi	272
Zinc	Zn	419
Antimony	Sb	630

Table 3.14 Details of low melting point coatings applied to sample blocks for temperature measurement trials

3.3.1.3 Parameters for Thermal Profiling Trials

Grinding trials were separated into two phases, phase one focussed on the effects of the presence of a shoulder or profile on the thermal behaviour of the grinding process, table 3.15 depicts the experiments undertaken to achieve this. Tests were performed consecutively first without and then with a shoulder present in order to minimise variation in the wheel condition between trials.

Trial Number	Block type	a_e (mm)	v_w mm/s	v_s (m/s)	b (mm)	Q'_w ($mm^3/mm \cdot s$)
1	No Shoulder	1	125	200	3	125
2	Shoulder	1	125	200	3	125
3	No Shoulder	2	125	200	3	250
4	Shoulder	2	125	200	3	250
5	No Shoulder	3	125	200	3	375
6	Shoulder	3	125	200	3	375
7	No Shoulder	4	125	200	3	500
8	Shoulder	4	125	200	3	500

Table 3.15 Parameters for trials measuring the effect of the presence of a shoulder on the thermal profile

The second stage of the experimental phase considered a basic experimental design to study the effect of the three major grinding parameters, width of cut, depth of cut and workpiece feedrate on the maximum temperature into the sidewall and surface during grinding. These experiments were randomised in order to minimise the effects of variation in the wheel condition with details presented in table 3.16.

Trial Number	Block type	a_e (mm)	v_w mm/s	v_s (m/s)	b (mm)	Q'_w ($mm^3/mm{\cdot}s$)
9	Shoulder	4	75	200	3	300
10	Shoulder	2	75	200	1	150
11	Shoulder	4	125	200	1	500
12	Shoulder	2	125	200	3	250
13	Shoulder	2	125	200	3	250
14	Shoulder	4	125	200	1	500
15	Shoulder	4	75	200	3	300
16	Shoulder	2	75	200	1	150

Table 3.16 Parameters for the exploration of the effects of grinding parameters on the thermal profile

For the above described trials 1 to 16, the parameters were selected in order to maximise temperatures. In this way the isotherm was anticipated to be large and therefore ease of measurement would be facilitated with a good contrast at the melt interface of the PVD coating.

3.3.1.4 Collation of PVD Results

Temperature estimations based on the low melting point coating technique were realised with the application of the exponential relationship demonstrated by Kato & Fujii (2000) citing the approximation presented by Takazawa (1966). The approximation of surface temperature is dependent upon the measured boundary of the isotherm falling within the limits of the approximation described by Takazawa (1966) where:

$$z_{\lim} = \frac{8\alpha}{v_w}$$

Figure 3.30 shows the limits of application for the temperature measurement, calculated for the selected 51CrV4 alloy. To simplify the calculations, the assumption was made that specific heat capacity and thermal conductivity will remain constant through the various temperatures the material is exposed to.

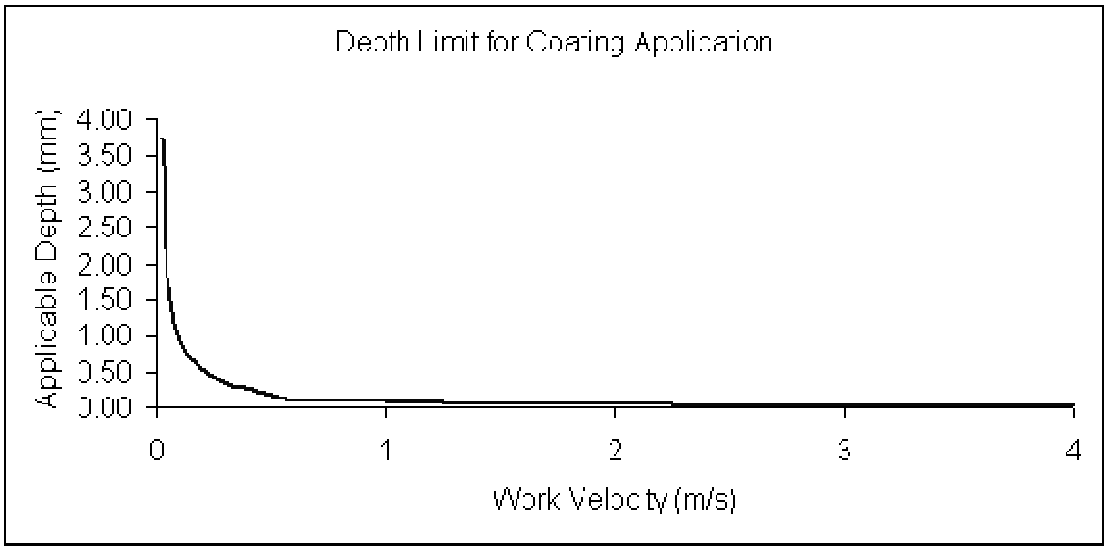

Figure 3.30 Graphical representation of the limiting depth of the PVD isotherm in 51CrV4

Isotherms formed on the mating surfaces of the sample block described in section 3.3.1.2 were examined under a Nikon stereo-microscope and photographed with the microscopes digital camera attachment. Figure 3.31 shows the style of microscope used with the digital camera attached. Software included with the digital camera was utilised to deliver a composite image of the complete isotherm. A typical composite isotherm is shown in figure 3.32, the level of magnification was dependent upon the individual circumstances, however a 10× magnification was typically used.

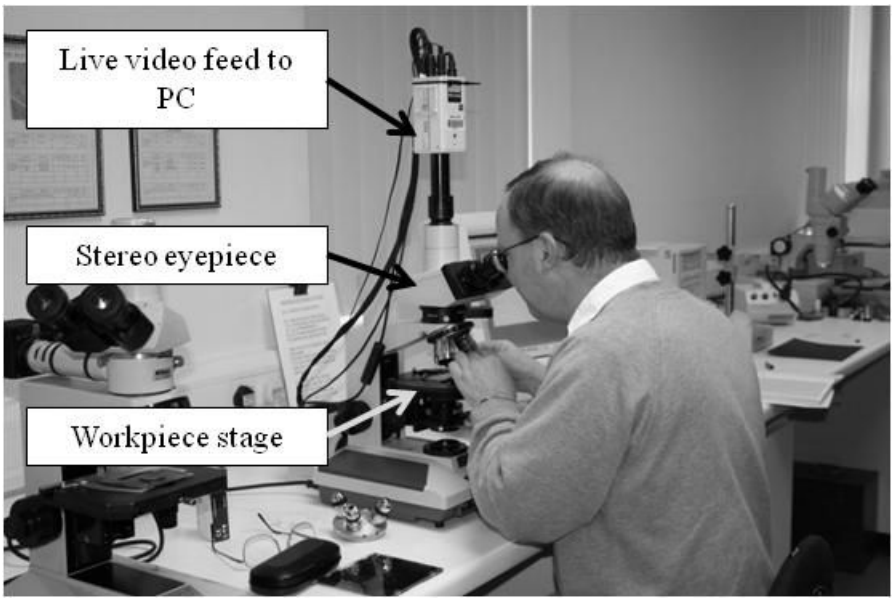

Figure 3.31 Photograph of microscope set-up

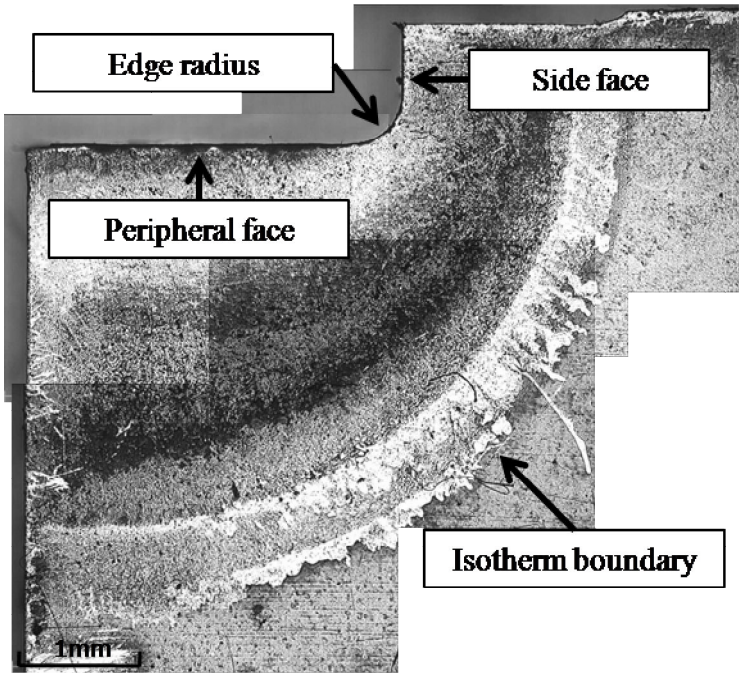

Figure 3.32 Typical surface grinding composite PVD micrograph

A Cartesian co-ordinate system was overlaid onto the composite micrograph in order to facilitate measurement of the isotherm, the x and y-axes being the horizontal and vertical as ground surfaces respectively. Information collated in this way was applied to a graphical representation of the isotherm with graphs adjusted to show the approximate depth of penetration perpendicular to the as ground surface. A typical graph of

penetration depth is shown for surface gridning in figure 3.33, highlighting the variation in melt depth around the profile consisting of:

A) Side face
B) Edge Radius
C) Peripheral face

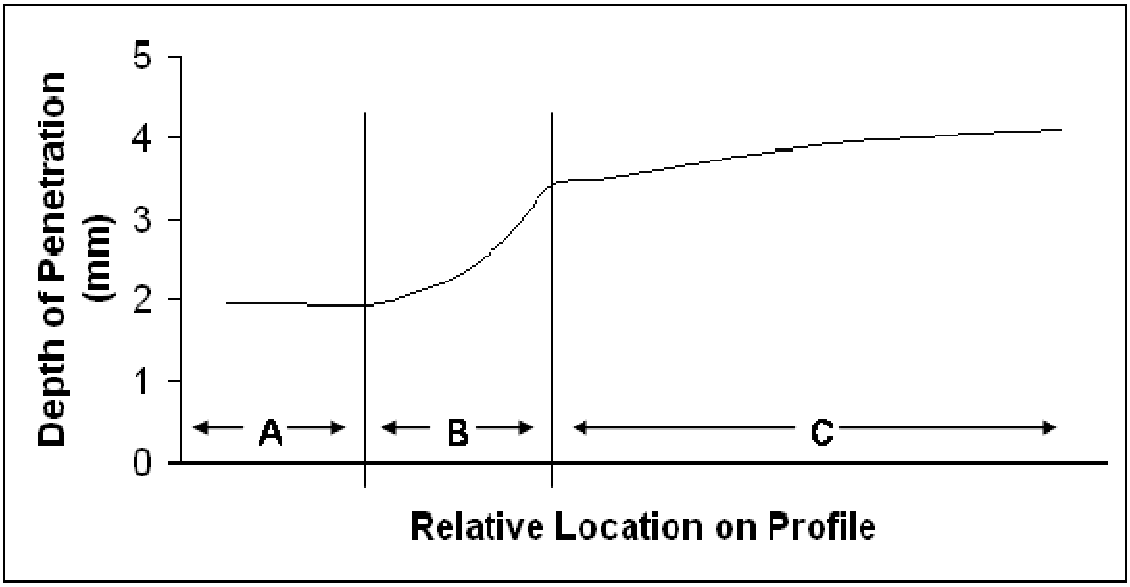

Figure 3.33 Typical graph of melt depth versus relative location on ground profile surface

3.3.2 Cylindrical Traverse Grinding

The assessment of the thermal profile and temperature in the cylindrical traverse grinding process was achieved with a series of axially split PVD coated samples. These were then subjected to the following trials.

- Trials at low specific material removal rates and large values of feed per turn for purposes of profiling the heat flux form
- Trials at high specific material removal rates and low values of feed per turn to study the temperatures at the high removal rates reported by Nakayama et al. (2004)

3.3.2.1 Machine Set-up

For temperature measurement in the cylindrical traverse grinding regime, the Edgetek SAT was set up with the earlier trialled twin nozzle and trough configuration described in section 3.2.2.1 and figure 3.16. Nozzles were located using a laser pointing device, and targeted such that they impacted on the centre of the leading edge radius (Nozzle B) and touching the outer diameter of the leading edge (Nozzle A). Table 3.17 demonstrates the parameters used for the machine set-up.

Nozzle A Target Position	Workpiece centre axis + 70 mm
Nozzle A Pressure	6 Bar
Nozzle B Target Position	Workpiece centre axis
Nozzle B Pressure	6 Bar
Nozzle A Diameter	3 mm
Nozzle B Diameter	3 mm
Trough Pressure	To maintain trough fill
Tailstock Type	Live
Chuck Type	3 Jaw self-centring

Table 3.17 Table of machine tool parameters for temperature measurement grinding trials

Figure 3.34 shows the fluid application set-up schematically demonstrating:

A) Leading edge nozzle
B) Leading edge radius nozzle
C) Coolant trough

Fluid application was designed to maintain a good flow of grinding fluid into the wheel leading edge and wheel-workpiece contact zone.

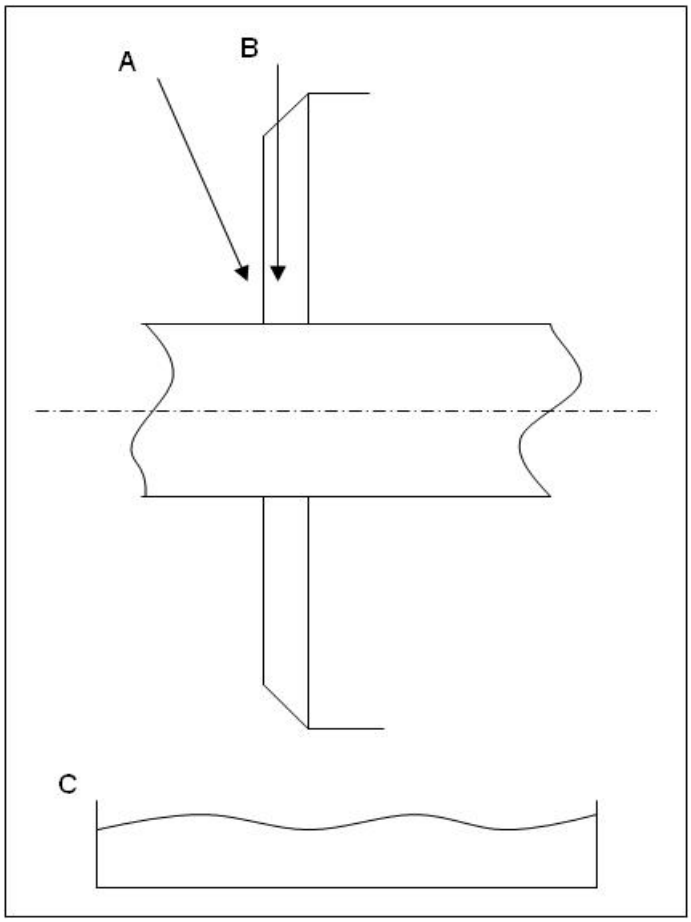

Figure 3.34 Schematic of the Edgetek SAT twin nozzle fluid application system for temperature measurement

3.3.2.2 Preparation of Cylindrical Traverse Grinding Low Melting Point Coating Samples

Low melting point coatings were aligned perpendicular to the principal grinding direction as for surface grinding, again developing an isotherm perpendicular to the principal grinding direction. For cylindrical traverse grinding, perpendicular to the principal grinding direction is defined as perpendicular to the direction of rotation of the workpiece. This equates to the coating lying parallel to the central axis of the workpiece as described in figure 3.35 which demonstrates:

A) PVD coated mating faces
B) Recessed central section to improve parallelism of mating faces
C) Outer diameter turned to 79mm
D) Sample length of 100mm

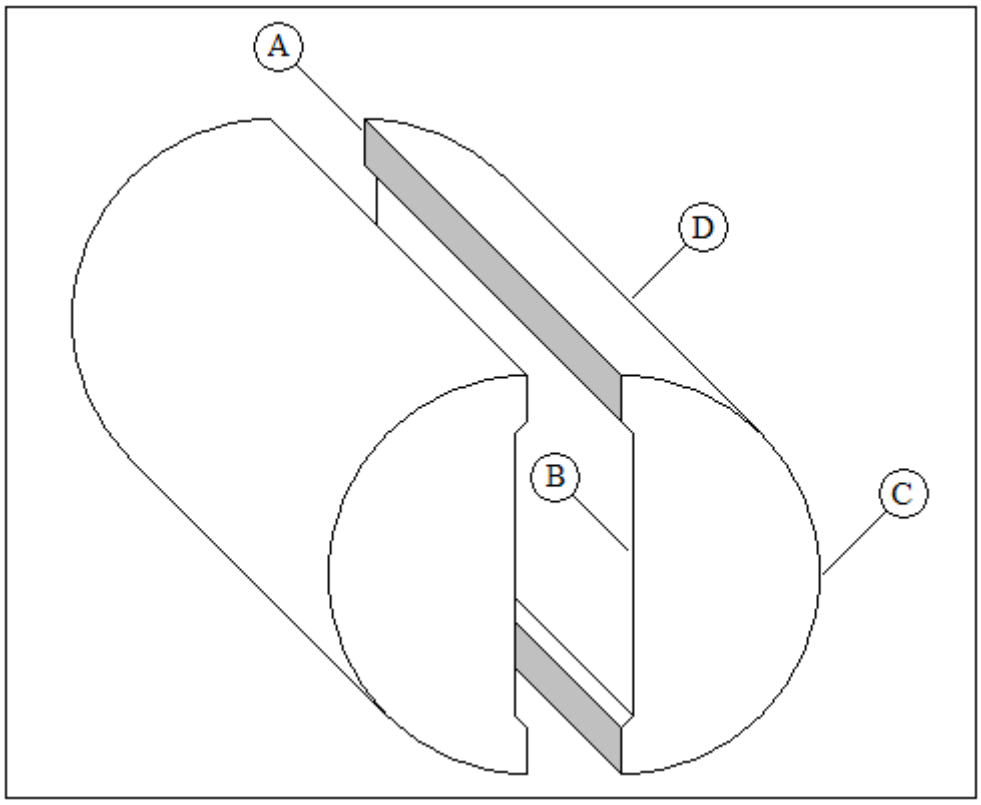

Figure 3.35 Schematic of the cylindrical traverse grinding temperature measurement block

Figure 3.36 shows an image of the cylindrical traverse grinding temperature measurement sample used.

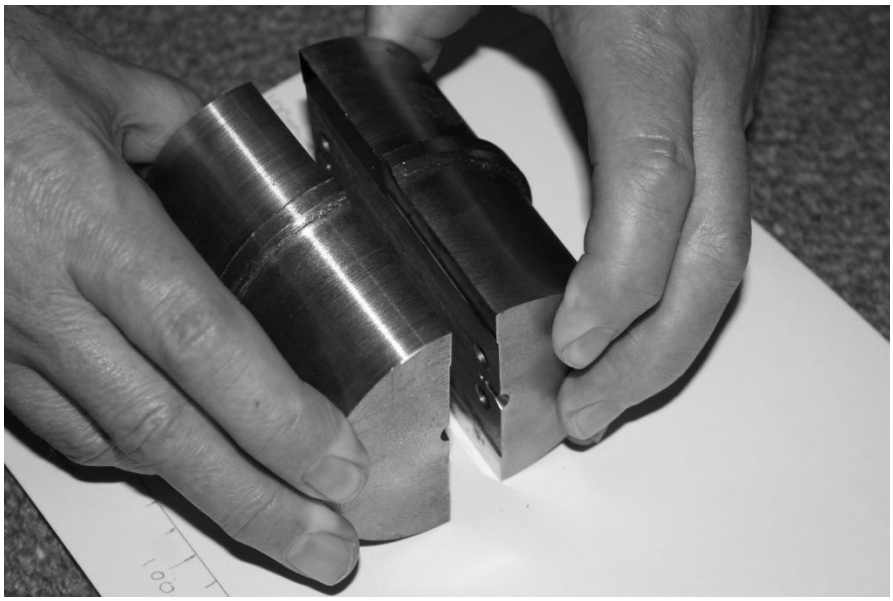

Figure 3.36 Photograph showing the axially split temperature measurement sample in the as ground condition

The cylindrical PVD samples were prepared by a specialist flat lapping provider, Opus Metrology[2], who finished the samples by hand in pairs to fit. Finished pairs were checked visually for a mirror finish and a sample touched together with engineer's blue to ensure good pick up and hence good surface mating. Once a good surface contact was assured, the samples were coated with a variety of low melting point coatings as per the description in section 3.3.1.2.

3.3.2.3 Parameters for Thermal Profiling of Cylindrical Traverse Grinding

The selection of grinding parameters was assisted with the use of a 2-dimensional finite element analysis. The grinding process demonstrates an increase in power requirement and hence heat flux with increasing specific material removal rate. Conversely there is a beneficial effect to increasing the speed of a heat flux across a surface, which acts to reduce thermal penetration. Given the very high workpiece feeds planned for the cylindrical traverse grinding trials, an investigation of the dominant effect was undertaken by simulation.

The simulation called for an investigation of the thermal penetration into the workpiece surface to ensure temperatures were controlled and with a view to preventing damage to the system; to achieve this a heat flux increasing with workpiece speed was applied. A macro written in the ANSYS Parametric Design Language (APDL) was developed using a cylindrical co-ordinate system to produce a two-dimensional moving heat source model. The heat flux was applied to the surface lines.

The trend of the increasing heat flux to the workpiece was estimated from grinding trials presented in section 3.2.2.3 tables 3.9 and 3.11 by estimation of the linear relationship between specific material removal rate and total heat flux to the workpiece. An increasing workpiece velocity was approximated by increasing the velocity of the heat source over the surface. The programme was set in the cylindrical coordinate system such that a two-dimensional circular object could be created with the heat flux moving along the edge. The velocity of the heat source was calculated from the workhead RPM, with the programme requiring the time frame for dwell on the surface nodes. Given knowledge of the number of surface nodes, the velocity was readily translated into dwell time and the velocity approximated.

[2] Details of the services provided can be found at http://www.opus.co.uk/

Figures 3.37 to 3.39 show the resulting 2D basic FEA models for an 80mm diameter disc, predicting a very low thermal penetration despite high heat flux application.

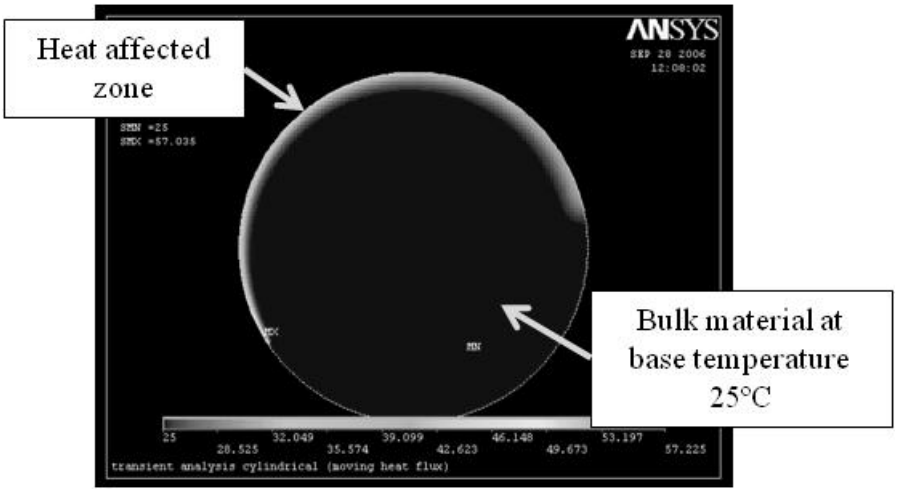

Figure 3.37 Thermal profile estimation with FEA for a heat source of 200W/mm^2 at 250RPM

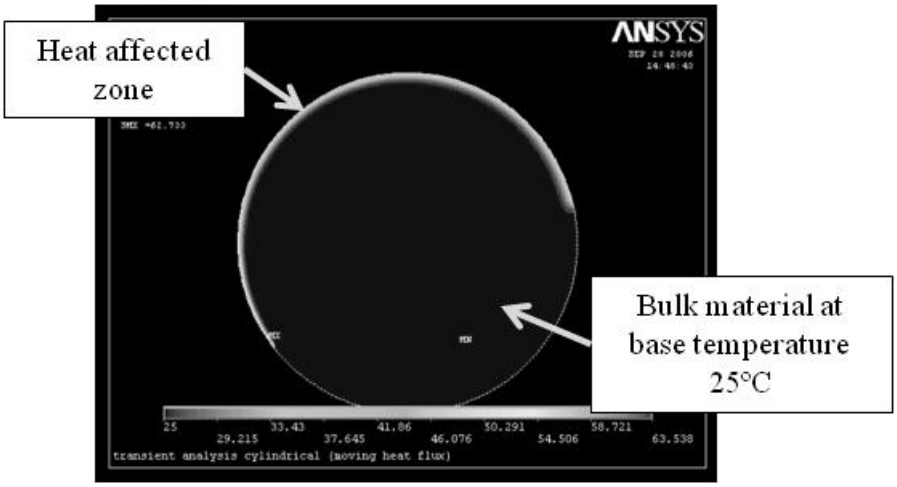

Figure 3.38 Thermal profile estimation with FEA for a heat source of 900W/mm^2 at 1000RPM

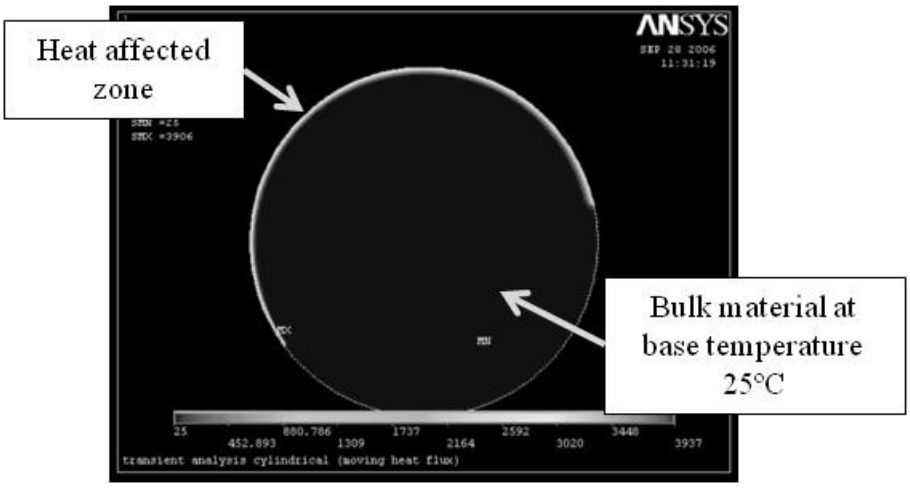

Figure 3.39 Thermal profile estimation with FEA for a heat source of 360500W/mm^2 at 4000RPM

For a given specific grinding energy and specific material removal rate, reducing the width of cut reduces the net power requirement proportionally according to the specific grinding energy equation where:

$$e_c = \frac{P_{net}}{Q'_w \cdot b}$$

In order to minimise the power requirement on the machine at the planned very high removal rates, it was suggested that the feed per turn (width of cut) was minimised. By reducing the feed per turn in this way, the power available for grinding was maximised.

Feedrates for experiments investigating changes in the width of cut were significantly reduced in order to allow large variations in width of cut to be considered. At the extremely high removal rates this would not have been possible as a result of the limitations of the table feed. The parameters used for the cylindrical traverse grinding trials are presented in table 3.18.

v_w (RPM)	v_t (mm/min)	b (mm)	a_e (mm)	D_w (mm)	Q'_w ($mm^3/mm \cdot s$)
6	60	10	3	79	72
12	60	5	3	79	143
24	120	5	3	79	287
24	60	2.5	3	79	287
250	50	0.2	1	75	969
500	100	0.2	1	75	1937
750	150	0.2	1	75	2906
1000	200	0.2	1	75	3875

Table 3.18 Table of grinding parameters for temperature measurement trials in cylindrical traverse grinding

3.3.2.4 Collation of Cylindrical Traverse Grinding Results with Low Melting Point Coatings

Cylindrical traverse grinding samples were handled similarly to the surface grinding samples described in section 3.3.1.4, using the same methodology to produce composite micrographs. Again images were collated with the Nikon microscope photographing images with the attached digital camera to produce the composite micrographs typical of figure 3.40. Overlaying a Cartesian co-ordinate system in the cylindrical traverse grinding trials was complicated by the flexibility in the grinding system. The grinding wheel was found to lean over in the traverse direction, thus the axis parallel surface was established as the x-axis with the y-axis drafted perpendicular to the x-axis at the approximated intersection of the vertical and horizontal surfaces. Where multiple isotherms were overlaid as in figure 3.40, the initial isotherm alone was considered.

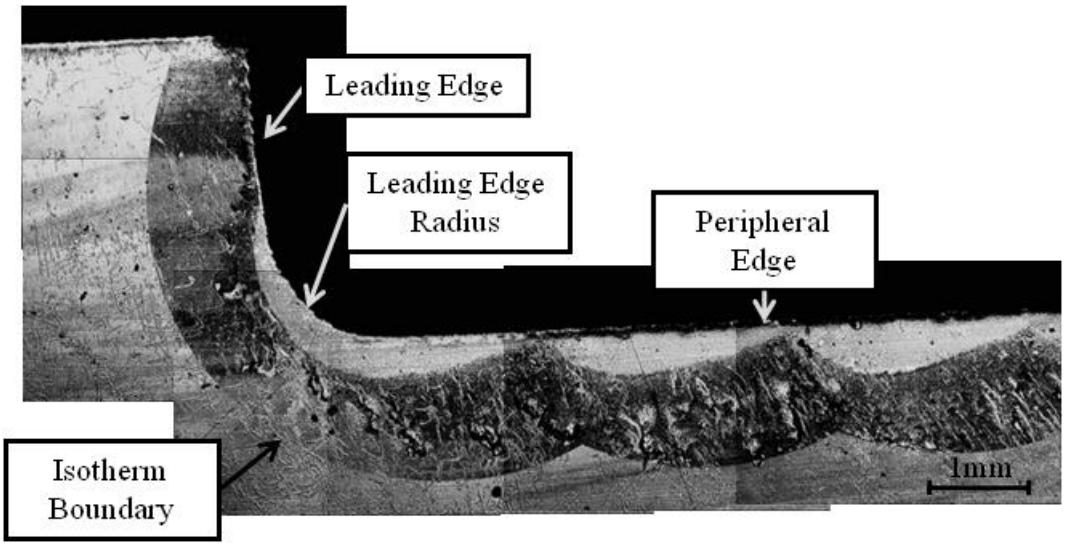

Figure 3.40 Typical cylindrical traverse grinding composite PVD micrograph

4 Investigation of Specific Grinding Energy and Burn Threshold

Chapter 4 of the thesis shows the results of experiments detailed in section 3.2. These trials considered the effect of high removal rates and contact conditions consistent with the HEDG regime on the specific grinding energy, grinding power and burn threshold diagram.

4.1 Trends in Specific Grinding Energy and Grinding Power

Stephenson and Jin (2003) suggested that the specific grinding energy can be approximated given knowledge of the specific material removal rate by a power law equation. Section 4.1 considers the fitting of a power law approximation to the specific grinding energy curves over large ranges of specific material removal rate. By predicting specific grinding energy from the grinding parameters, estimation of the grinding power and hence heat flux and temperature from the same becomes possible.

This section also considers the trends of both net and total grinding powers for the grinding parameters tested. The grinding power plays a pivotal role in the specification of the grinding machine, by understanding the power trends for various grinding parameters the optimum machine set-up can be highlighted.

4.1.1 Surface Grinding

Initial results for surface grinding experiments detailed in tables 3.4 & 3.6 of section 3.2.1.3 with the application of oil based grinding fluid showed an asymptotic form and the achievement of a constant value of specific grinding energy as specific material removal rates increased. Figure 4.1 shows the specific grinding energy curve for SGCI trials with grinding parameters summarised in table 4.1, the power law curve was fitted in Excel. It can be seen that the predicted power law curve deviates from the results set. This deviation of the power law curve is greater than the potential error in the system, assuming an experimental error of 5%. We could therefore be confident that a single power law approximation was unsuitable in this instance.

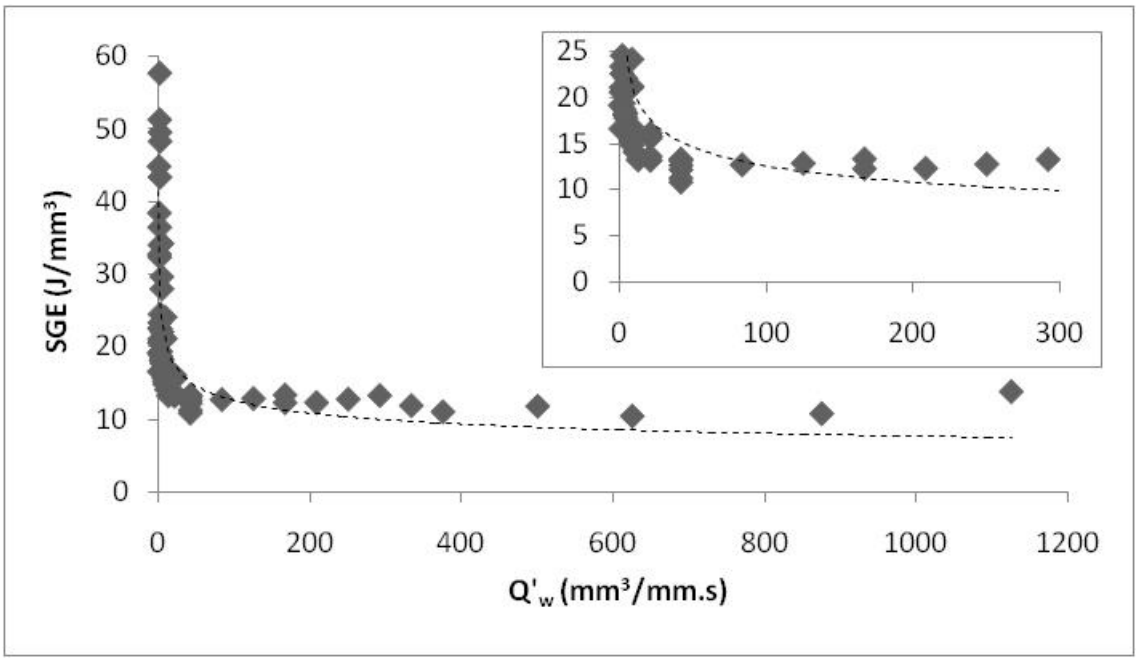

Figure 4.1 Specific grinding energy curve for simple surface profile grinding of SGCI showing detailed view of low values of specific material removal rate inset

a_e (mm)	b (mm)	v_w (mm/min)	v_s (m/s)
0.5 – 9	5 – 2	50 – 7500	50 – 150

Table 4.1 Summary of grinding parameters for results presented in figure 4.1

Figure 4.2 shows the specific grinding energy curve for trials with 51CrV4, grinding parameters are presented in table 4.2, the power law curve was again fitted in Excel. In this case the deviation of the power law approximation was more noticeable at lower values of specific material removal rate. The direct fitting of a power law curve is perhaps inappropriate, the accuracy of the approximation is critical given that small changes at low values of specific grinding energy can result in large changes in the finished temperature. Additionally, the tail of the specific grinding energy curve appears to hold a constant value in both instances considered. This suggested that a split relationship between specific material removal rate and specific grinding energy would be more appropriate. Possible reasons for a constant specific grinding energy are discussed in Chapter 6.

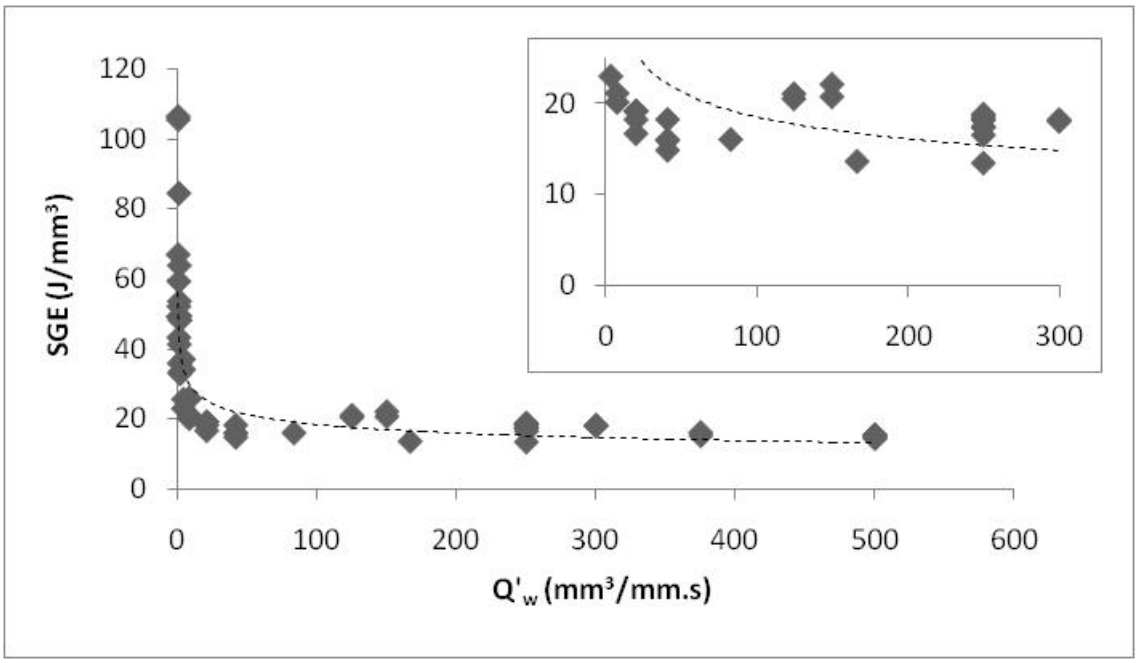

Figure 4.2 Specific grinding energy curve for simple surface profile grinding of 51CrV4 with zoomed section showing low specific material removal rates

a_e (mm)	b (mm)	v_w (mm/min)	v_s (m/s)
0.5 – 4	5 – 1	50 – 7500	50 – 200

Table 4.2 Summary of grinding parameters for results presented in figure 4.2

Deviation of the results recorded from the approximation proposed can have a significant effect on the temperatures experienced in the finished workpiece surface. At high values of specific grinding energy small increases in value give small variations in temperature as the percentage rise is small. Approaching the HEDG regime when specific grinding energies are reduced to low values, small variations in specific grinding energy can result in a large change in the finished surface temperature. Thus the case is made for a more accurate predictive tool when considering HEDG results.

Visual inspection of figures 4.1 and 4.2 demonstrated a constant value of specific grinding energy from specific material removal rates of approximately 50mm^3/mm·s. These values were 13J/mm^3 for SGCI and 16J/mm^3 for 51CrV4. The power law approximation was reapplied for values of specific material removal rate less than 50mm^3/mm·s. Results in the range 0 to 50mm^3/mm·s showed excellent agreement with a power law approximation, where:

$e_c = A \cdot Q'^{-t}_w$ *Equation 4.1*

Figures 4.3 to 4.5 show curves of specific material removal rate (Q'_w) versus specific grinding energy (SGE) for specific material removal rates to 50mm^3/mm·s with grinding parameters summarised in table 4.3. The results demonstrated a small increase in specific grinding energy for SGCI and 51CrV4 (figures 4.3 and 4.5) with the application of grinding fluid at low specific material removal rates with increasing wheel speed. Results for grinding without fluid application are included here after trials detailed in table 3.5 of section 3.2.1.3 (figure 4.4) and showed an indeterminable change in the specific grinding energy curve. It is possible that increases in specific grinding energy with wheel speed were a result of the braking effect of the grinding fluid or possibly an effect of wheel wear. The limitation of the curve to values of specific material removal rate to 50mm^3/mm·s greatly improved the fit of the power law approximation.

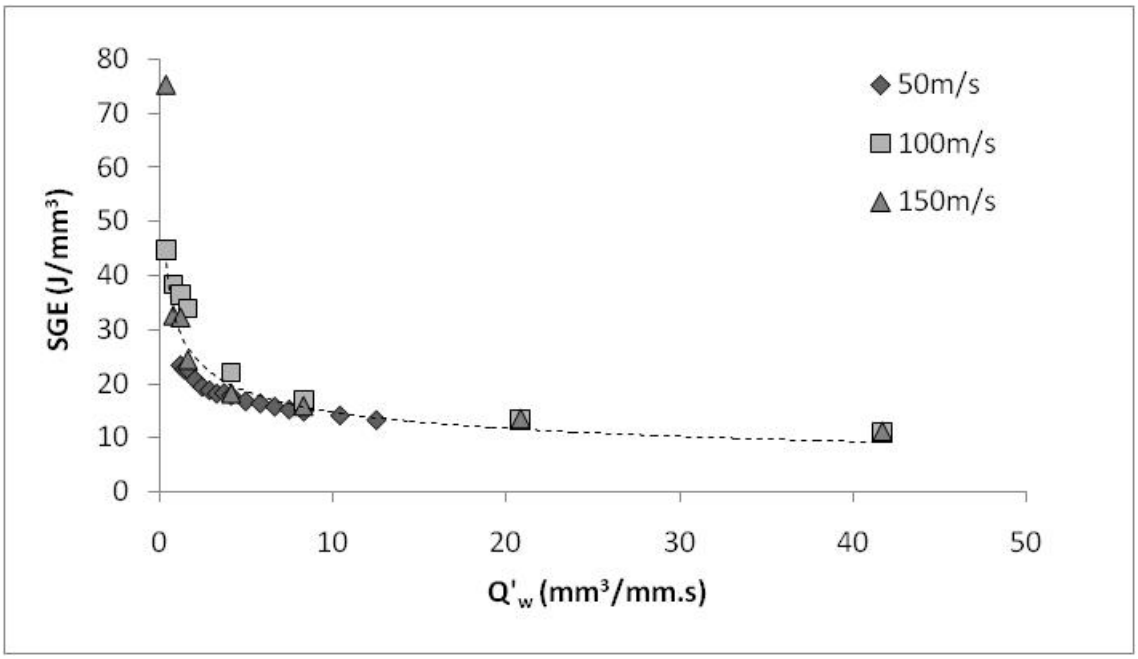

Figure 4.3 Trends in specific grinding energy for specific material removal rates up to 50mm^3/mm·s for trials in SGCI with the application of grinindg fluid

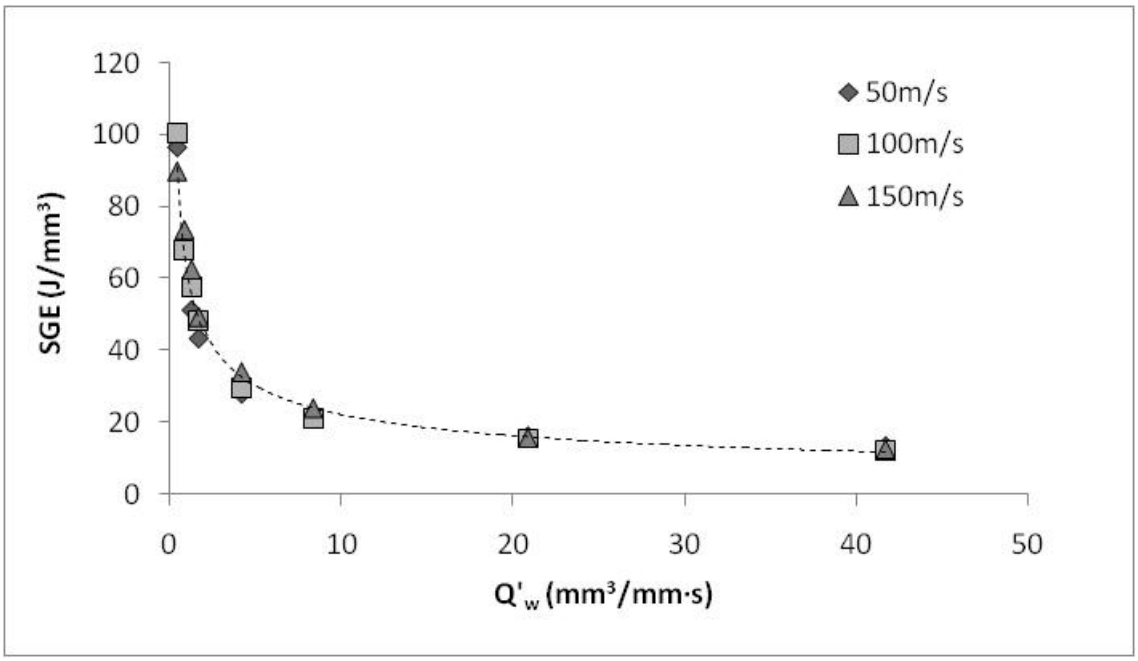

Figure 4.4 *Trends in specific grinding energy for specific material removal rates up to 50mm^3/mm·s for trials in SGCI without the application of grinding fluid*

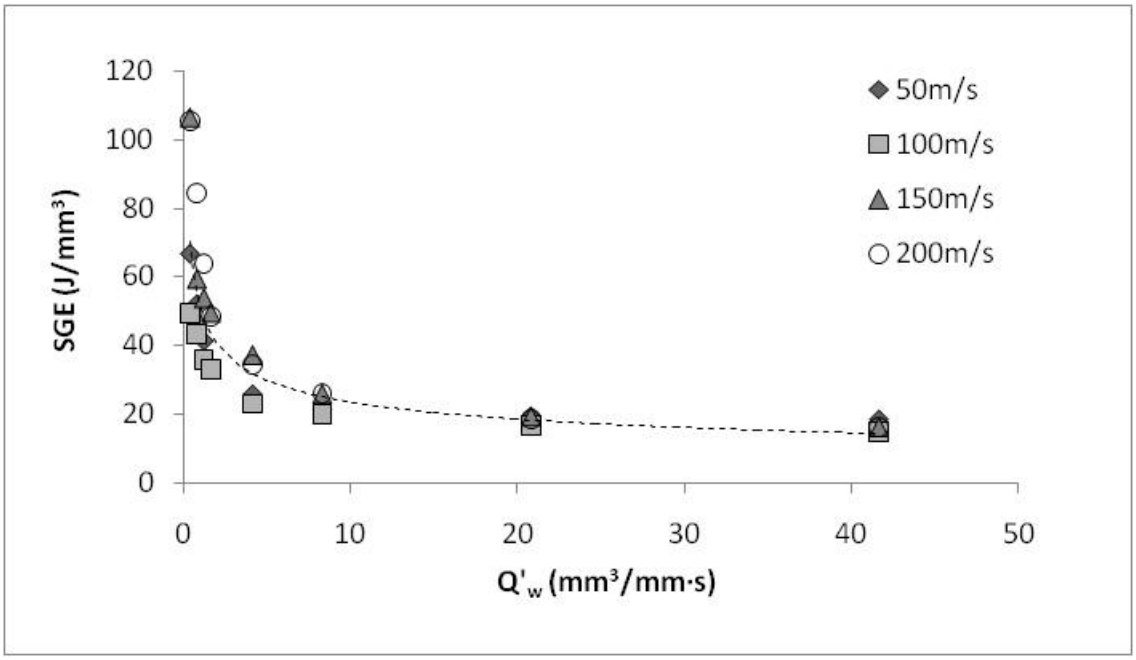

Figure 4.5 *Trends in specific grinding energy for specific material removal rate up to 50mm^3/mm·s for surface grinding trials in 51CrV4 with the application of grinding fluid*

Figure	a_e (mm)	b (mm)	v_w (mm/min)	v_s (m/s)
4.3 SGCI with grinding fluid	0.5 – 1	5	50 – 5000	50 – 150
4.4 SGCI without grinding fluid	0.5	5	50 – 5000	50 – 150
4.5 51CrV4 with grinding fluid	0.5	5	50 – 5000	50 – 150

Table 4.3 Summary of surface grinding parameters

Values for the constants A and t (equation 4.1) ascribed to the specific grinding energy curves demonstrated in figures 4.3 to 4.5 by the Excel line fitting function are presented in Table 4.4.

Material	Grinding Fluid Application	A	t
SGCI	Yes	32	0.33
SGCI	No	62	0.45
51CrV4	Yes	52	0.34

Table 4.4 Values of A and t for trials in spheroidal grey cast iron

Figure 4.6 combines results for the grinding of SGCI with the two fluid applications at a wheel speed of 150m/s. The results showed that application of grinding fluid to the grinding zone reduced the specific grinding energy when at low specific material removal rates. As the removal rate tended towards $50mm^3/mm{\cdot}s$ results for trials with and without the application of grinding fluid achieved a common value.

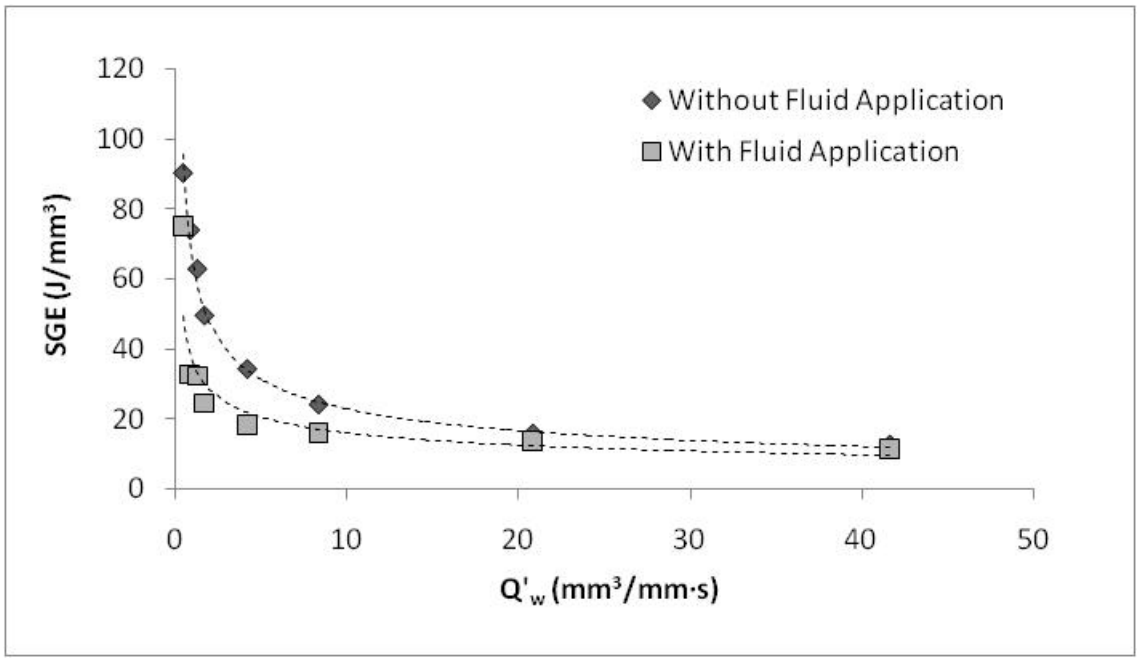

Figure 4.6 Comparison of specific grinding energy curves for grinding of SGCI with and without the application of grinding fluid for a constant wheel speed of 150m/s

The effect of grinding fluid application on the total and net grinding power for the specific grinding energy curves presented in figure 4.3 and 4.4 is demonstrated in figures 4.7 and 4.8 for a wheel speed of 150m/s. The results show a consistently higher net grinding power requirement for trials where no grinding fluid was applied. Conversely the application of grinding fluid increases the total power requirement for the machine tool.

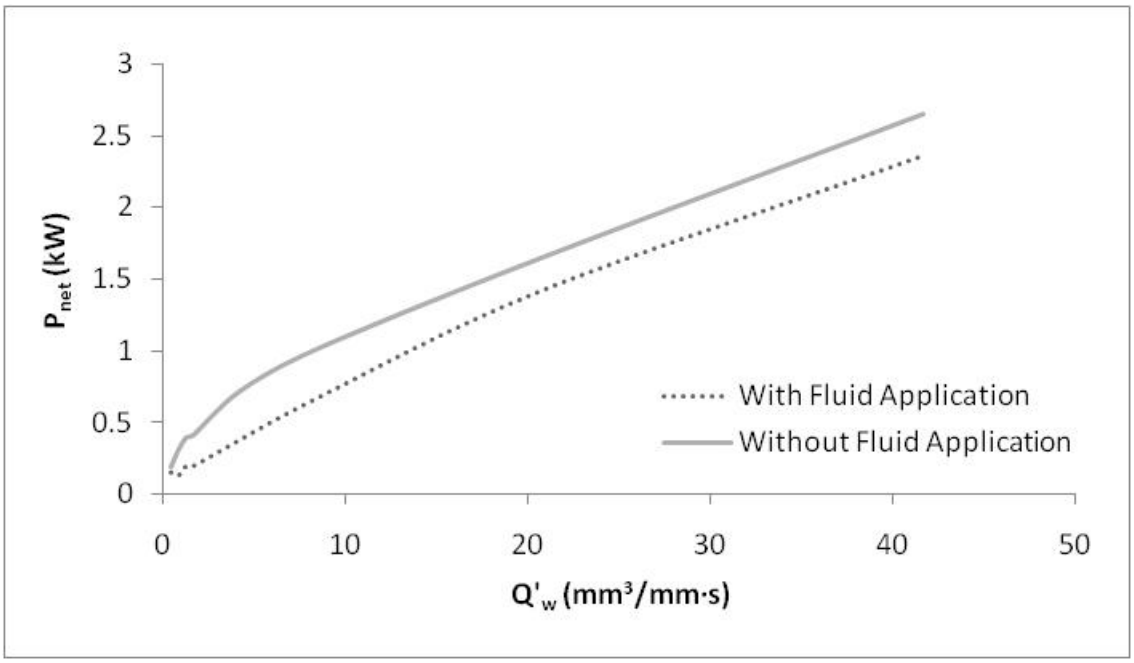

Figure 4.7 Change in net grinding power requirement with specific material removal rate dependent on fluid application

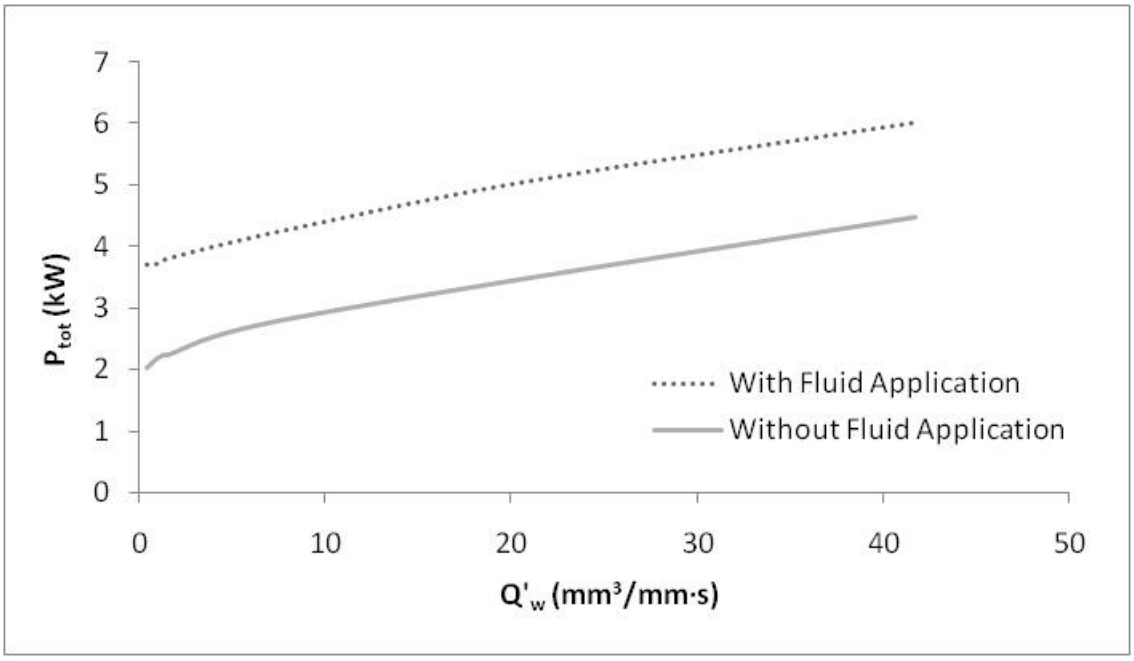

Figure 4.8 Change in total grinding power requirement with specific material removal rate dependent on fluid application

The results confirmed that the application of grinding fluid has a beneficial effect on the energy consumed in the grinding process, particularly at low removal rates. However, the grinding fluid application reduced the power available to the machine tool for the

process. It is suggested that a high specific material removal rate is theoretically achievable when no grinding fluid is applied, without detrimental effect to the specific grinding energy.

4.1.2 Cylindrical Traverse Grinding

Cylindrical traverse grinding trials were undertaken with 51CrV4 sample blocks exclusively and both oil and water based grinding fluids. As for surface grinding, values of specific grinding energy achieved a constant value and had an asymptotical form with increasing specific material removal rate.

The specific material removal rate for cylindrical traverse grinding was calculated using the same methodology as for surface grinding, where:

$$Q'_w = a_e \cdot v_w \qquad \textit{Equation 4.2}$$

Equation 4.2 refers to a straight surface grinding cut, however the cylindrical traverse grinding process forms a helical path during the grinding process. To verify that the equation was applicable to the cylindrical traverse grinding process, the specific material removal rate was calculated geometrically from the contact conditions. This suggested that a negligible difference existed between the two trials and as such the approximation of equation 4.2 was acceptable for purposes of the calculations undertaken.

Figure 4.9 shows a plot of specific material removal rate versus specific grinding energy for trials with the two grinding fluid types, grinding parameters are summarised in table 4.5. The results showed that a constant value of grinding energy was rapidly approached with the oil based Castrol Variocut G 600 SP. However the rate for the water based Hysol X 6% suspension is seen to be more gradual and a constant value was not fully achieved until specific material removal rates in excess of 175mm^{3}mm·s were achieved.

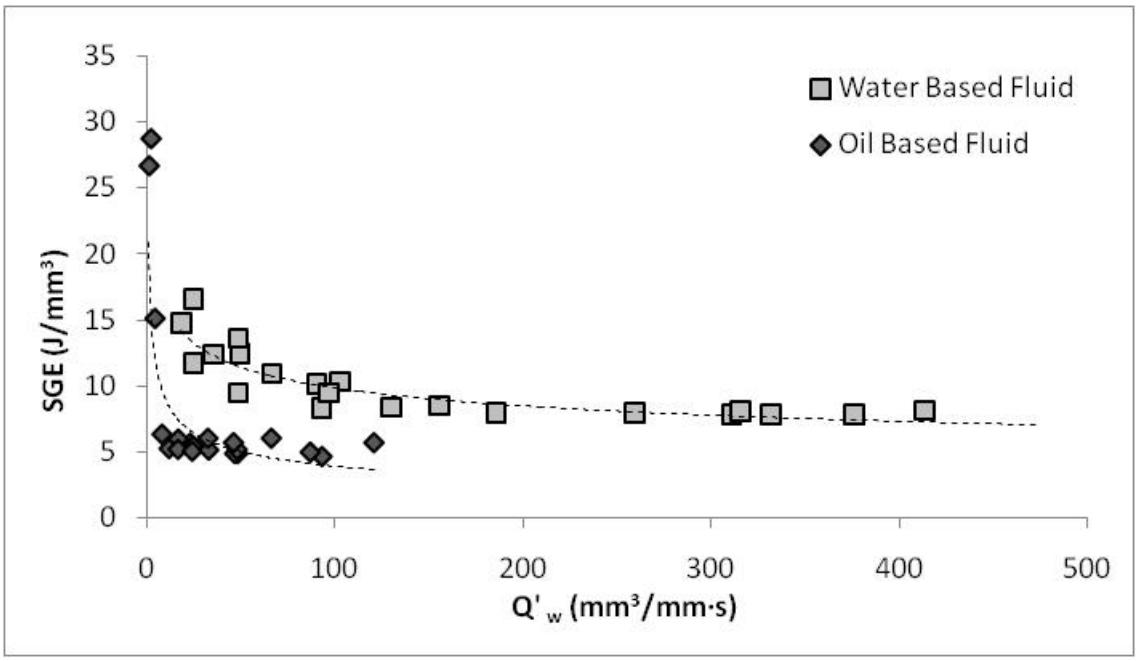

Figure 4.9 Comparison of specific grinding energy curves for oil and water based grinding fluid application

Fluid Type	a_e	v_t	v_w	b	v_s
Water	0.5 – 6mm	60mm/min	12 – 24RPM	2.5 – 5mm	150m/s
Oil	0.5 – 3mm	7.5 – 120mm/min	0.5 – 24RPM	5 – 15mm	150m/s

Table 4.5 Summary of cylindrical traverse grinding parameters for results shown in figure 4.9

Recalling the relationship between specific grinding energy and specific material removal rate shown in equation 4.1, table 4.6 presents values of the constants A and t assigned by the Microsoft Excel line fitting function. It should be noted that initial trials with oil based grinding fluid were performed with a new wheel, which was in an unused and unconditioned state at the start of grinding trials.

Vs (m/s)	Valid Range	Grinding fluid Type	A	t
150	0 – 20 mm^3/mm·s	Oil: Castrol Variocut G600 SP	33	0.67
150	0 – 175 mm^3/mm·s	Water: Hysol XH 6%	34	0.28

Table 4.6 Values of A and t for approximation in cylindrical traverse grinding

Figure 4.9 also demonstrates the variation in specific grinding energy with specific material removal rate for those trials undertaken with oil (Castrol Variocut G 600 SP) and water (Hysol X 6%). Values of specific grinding energy for Hysol X 6% are significantly higher than for the Castrol Variocut G 600 SP over the range of specific material removal rates considered. Unlike for trials in surface grinding, the minimum specific grinding energy for the two grinding fluid applications does not appear to tend to the same minimum value. It should be noted that the grinding wheel was in an unconditioned state for the grinding trials with oil and thus was sharper than would necessarily be the norm. The wheel had developed a normal grinding condition for the water based grinding fluid experiments. Given opportunity to repeat experiments and sufficient time to run trials, the wheel would have undergone a prolonged period of conditioning and the experiments between grinding fluid types in this instance would have been randomised. Figure 4.10 presents later results taken with oil based grinding fluid after the grinding wheel had undergone significant conditioning. It should be noted that the constant value of specific grinding energy is now more appropriate to the results recorded with the water based grinding fluid with values tending towards 10.5J/mm^3.

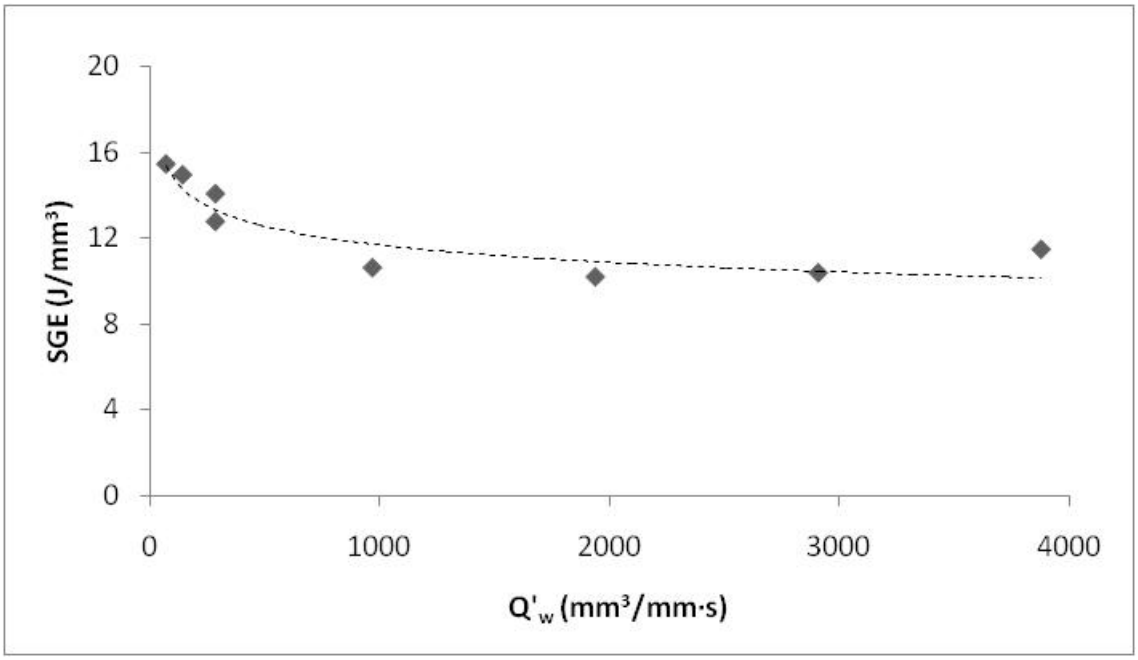

Figure 4.10 Specific material removal rate versus specific grinding energy for grinding trials with oil based grinding fluid

Figures 4.11 and 4.12 demonstrate the effect of grinding fluid choice on the total and net grinding powers developed during the grinding process for a value of feed per turn of 5mm with parameters summarised in table 4.7. The results show an insignificant change in the total grinding power for trials undertaken. The net grinding power is however shown to be reduced by the application of oil as the grinding fluid choice. This trend in net grinding power is similar to that demonstrated for the surface grinding trials, understanding that water has a lower lubricity than oil as dry grinding exhibits no lubrication. However this benefit must be contrasted against the higher convection coefficient of water based fluids, removing greater quantities of heat energy at its operational temperatures than oil.

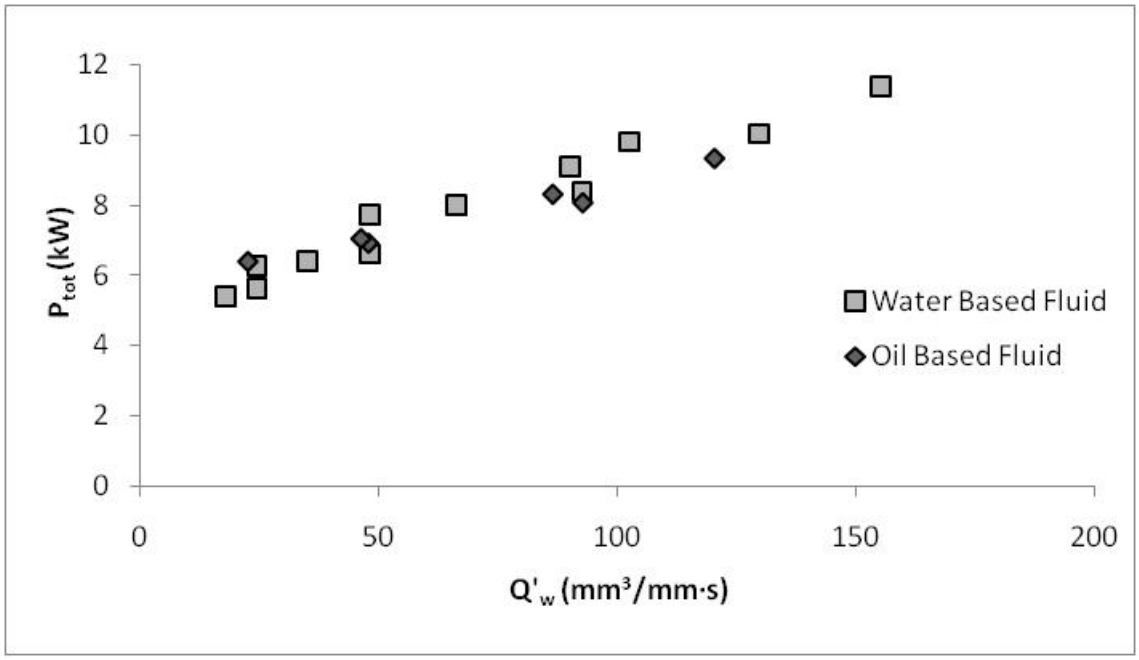

Figure 4.11 Trends in total grinding power with fluid type for increasing specific material removal rate

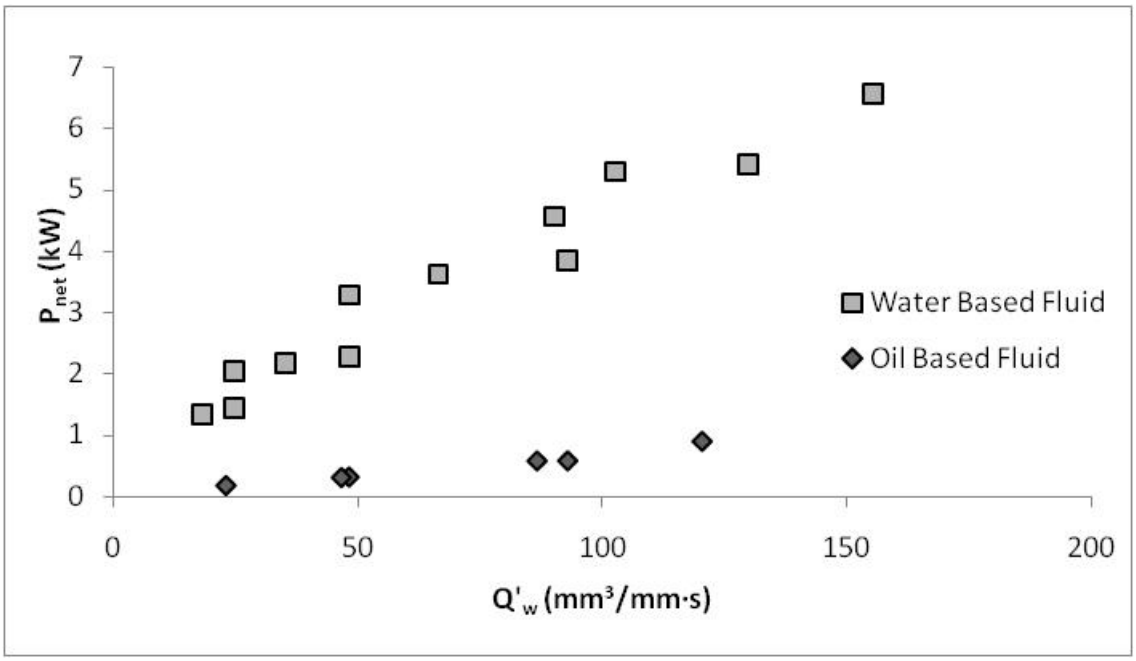

Figure 4.12 Trends in net grinding power with grinding fluid type

Fluid Type	a_e (mm)	v_t (mm/min)	v_w (RPM)	v_s (m/s)
Water	0.5 – 4	60	12	150
Oil	0.5 – 3	60 – 120	12 – 24	150

Table 4.7 Summary of grinding parameters for results shown in figures 4.11 and 4.12

Figure 4.13 demonstrates the effect of the feed per turn or width of cut on the total grinding power. These results, recorded during both water oil based fluid trials described in table 4.8, show a clear benefit to reducing the feed per turn to a small value, effectively reducing the total power requirement for the grinding operation for an equivalent specific material removal rate.

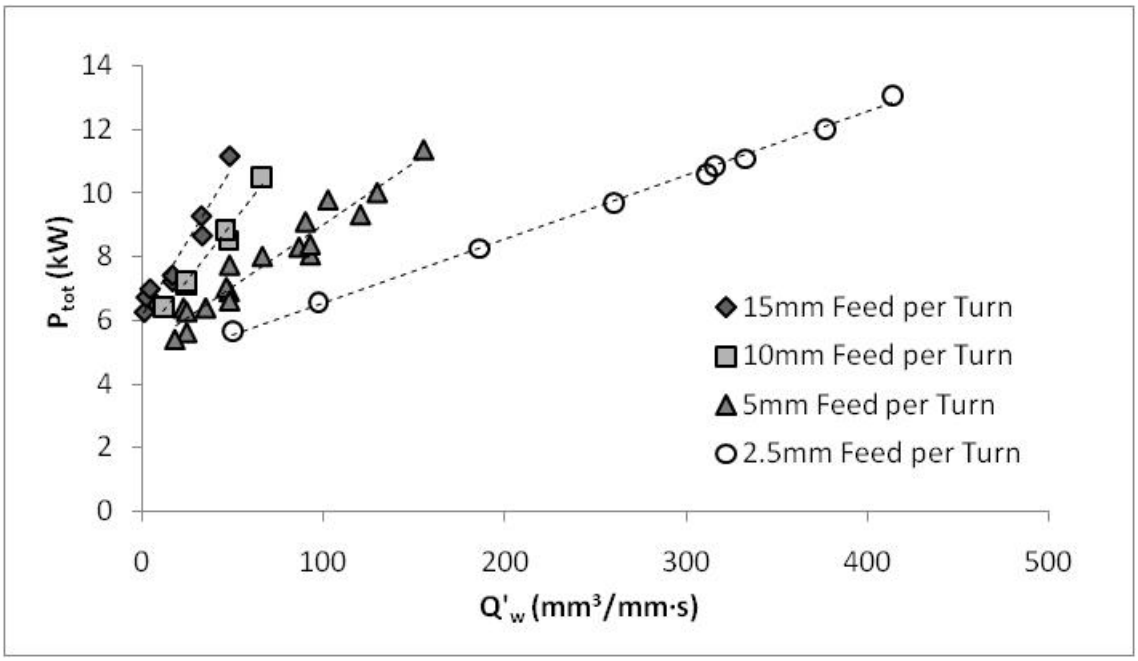

Figure 4.13 Total power requirements with change in feed per turn with increasing specific material removal rate for oil and water based grinding fluids

Fluid Type	a_e (mm)	v_t (mm/min)	v_w (RPM)	v_s (m/s)
Water	0.5 – 6	60	12 – 24	150
Oil	0.5 – 3	7.5 – 120	0.5 – 24	150

Table 4.8 Summary of grinding parameters for feed per turn comparison of figure 4.13

Decreasing the feed per turn by increasing the rotational velocity of the workpiece leads to an increased chip thickness and hence lower grinding power. However this is not the only mechanism at work here, with both traverse rate and workpiece speed being adjusted within the same results set. Figure 4.14 shows a linear relationship between the volumetric removal rate and the total grinding power for all values of feed per turn considered. A high volumetric removal rate requires a high total grinding power. Figure 4.13 shows that for a given grinding power the reduction in the feed per turn permits a higher specific material removal rate. The HEDG process is driven by achieving high specific material removal rates which have been shown to reduce finished surface temperatures. The results imply that a small feed per turn at a high total grinding power will result in the highest possible volumetric removal rate with the highest possible specific material removal rate and hence the best possible HEDG conditions.

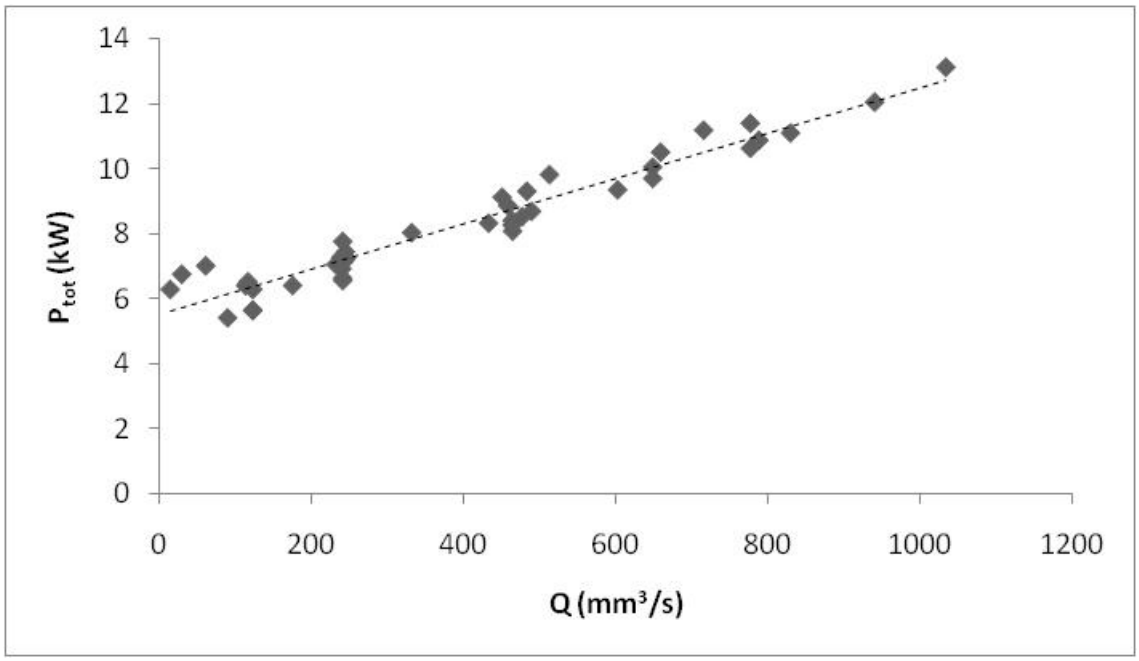

Figure 4.14 Volumetric removal rate versus total grinding power for cylindrical traverse grinding with oil and water based grinding fluids

The results for surface and cylindrical traverse grinding have shown trends between the specific material removal rate and the specific grinding energy and grinding powers. These trends make it possible to predict the specific grinding energy and grinding power given knowledge of the specific material removal rate. In this way the temperature at the workpiece surface can ultimately be estimated and the burn threshold established.

4.1.3 The Effect of Wheel Wear on Results

The effect of wheel wear was considered at various stages of the experimental phase with the addition of trials at constant grinding parameters to measure the changes in the grinding powers and specific grinding energy that resulted. Figure 4.15 and 4.16 show trends in specific grinding energy for surface and cylindrical traverse grinding for the parameters summarised in table 4.9. It can be seen that the process of grinding has resulted in wear of the wheel, which in turn has increased the specific grinding energy required by the process.

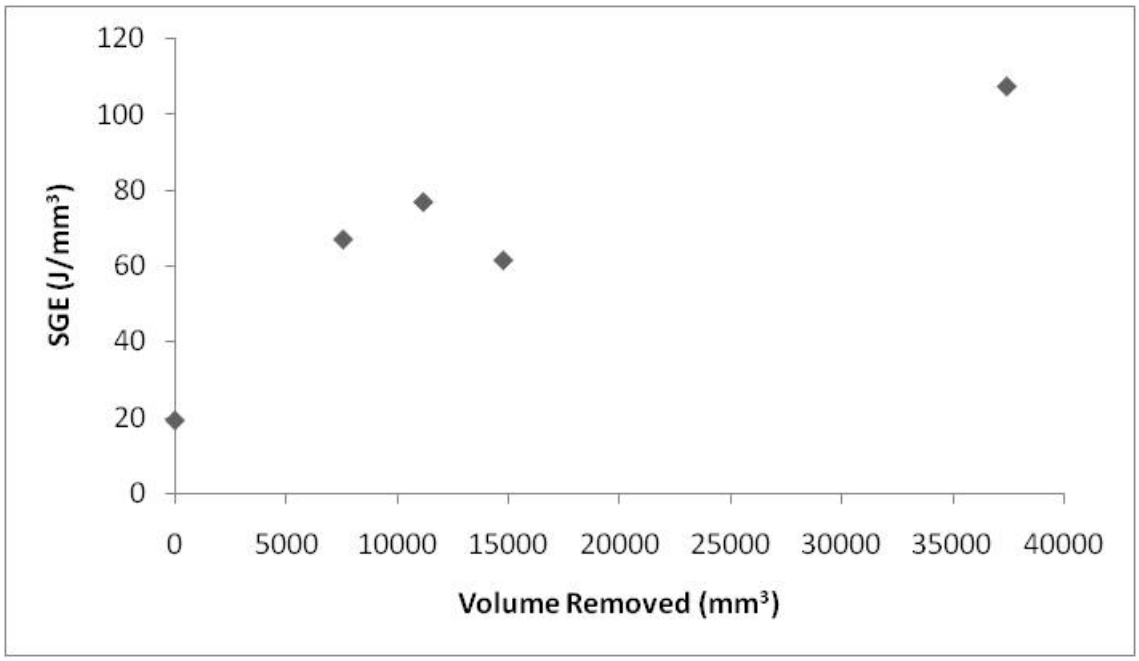

Figure 4.15 Effect of wear on the specific grinding energy over the course of surface grinding with SGCI

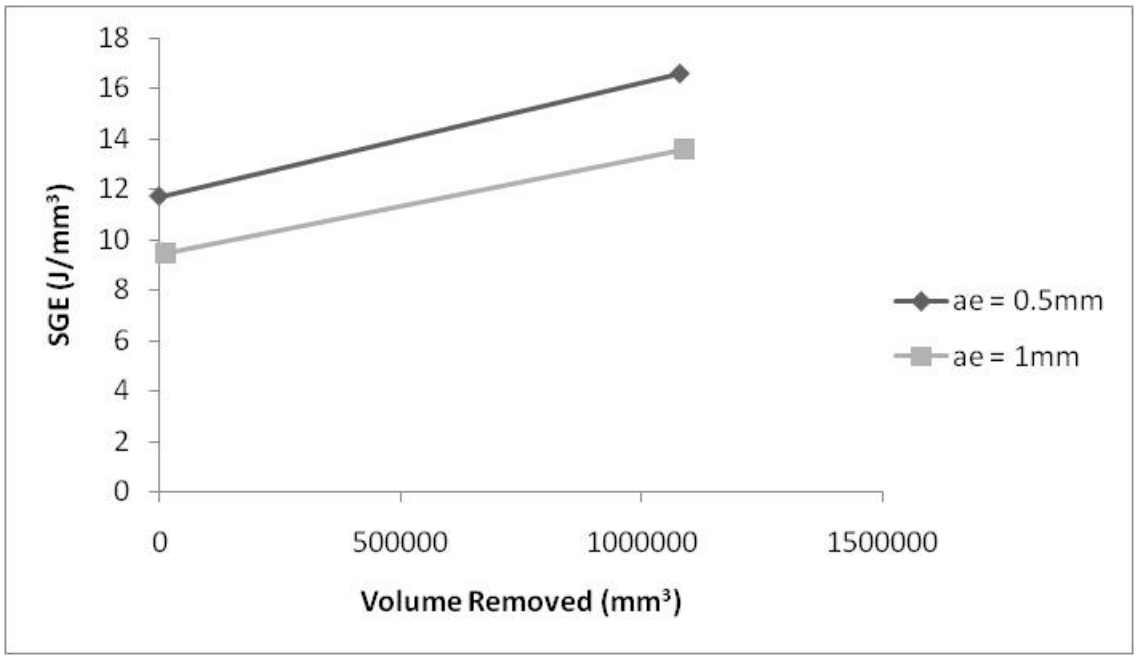

Figure 4.16 Effect of wear on the specific grinding energy over the course of cylindrical traverse grinding with 51CrV4

Figure number	a_e (mm)	v_w	b (mm)	v_s (m/s)
4.15	0.5	50mm/min	5	50
4.16	0.5/1	12RPM	5	150

Table 4.9 Summary of grinding parameters for wear trials

The changes in specific grinding energy over the course of the grinding trials undertaken are significant to the development of the process. However, given that grinding burn is expected to occur at a level of specific grinding energy does not create issue with the analysis of the results.

4.2 Application of the Burn Threshold Diagram

Results demonstrating the effect of HEDG conditions on the process of burn threshold analysis developed by Malkin & Lenz (1978) are presented in this section. The results show the effect of the contact conditions and feedrates consistent with the HEDG regime on plots of Peclet number versus maximum dimensionless temperature rise. This section will show the results of a burn threshold diagram plotted using the results from the HEDG trials and demonstrate how the diagram is affected by the HEDG process.

4.2.1 Evaluation of Peclet Number versus Maximum Dimensionless Temperature Rise

Malkin & Lenz (1978) expressed the relationship between Peclet number and maximum dimensionless temperature rise with the following relationship:

$$\bar{\theta}_m = 3.543 \cdot L^{1/2} \qquad \textit{Equation 4. 3}$$

This relationship forms the basis of Malkin's burn threshold diagram allowing the derivation of the burn threshold relationship. The maximum dimensionless temperature rise for the results set was calculated using equation 4.4, where:

$$\bar{\theta}_m = \left(\frac{\pi \cdot k \cdot v_w}{2 \cdot \alpha \cdot q_w} \right) \theta_m \qquad \textit{Equation 4.4}$$

Using the circular arc of heat contact model for the estimation of the maximum temperature rise θ_m and heat flux partitioned to the finished workpiece surface q_w values of maximum dimensionless temperature rise were estimated.

For the grinding fluid application parameters summarised in table 4.3, plots of Peclet number versus maximum dimensionless temperature rise for SGCI and 51CrV4 are shown in figures 4.17 and 4.18 respectively. This relationship is a fundamental derivation of the moving heat source equations presented by Jaeger (1942). At a Peclet number of approximately 40 the results deviate from the relationship expected, recalling that equation 4.3 refers to a sliding heat contact which is not inclined. Separated by common feedrate the onset of deviation appears to move to the right with increasing feedrate. This effect was notably less when grinding 51CrV4, however lower Peclet numbers were achieved with the material choice.

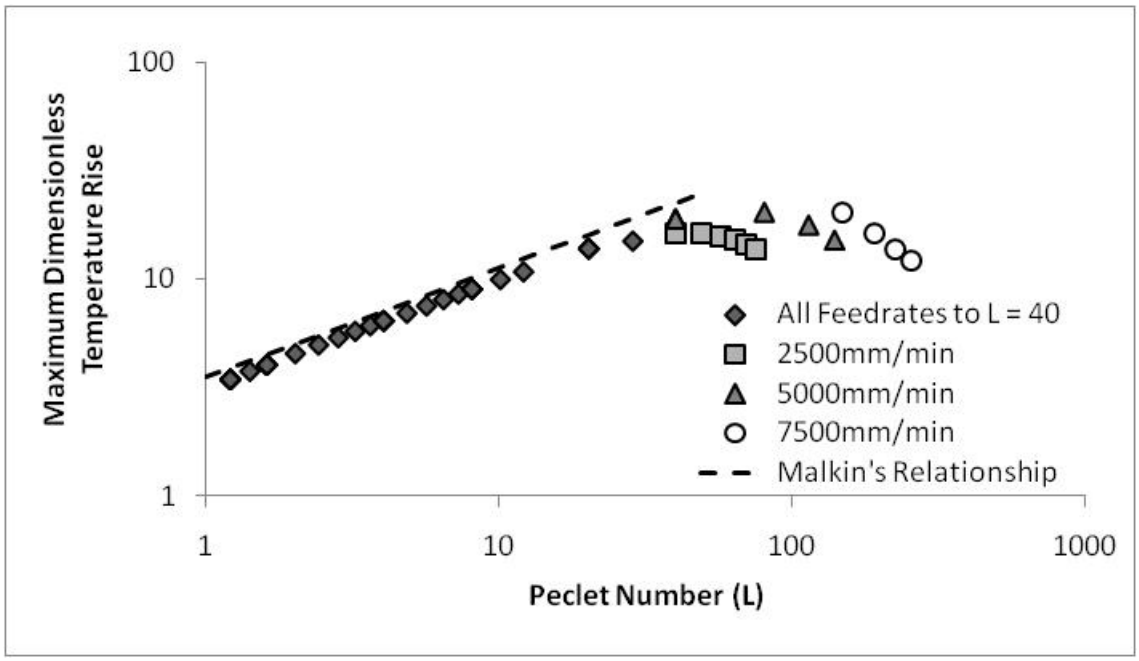

Figure 4.17 Deviation from predicted limit for SGCI

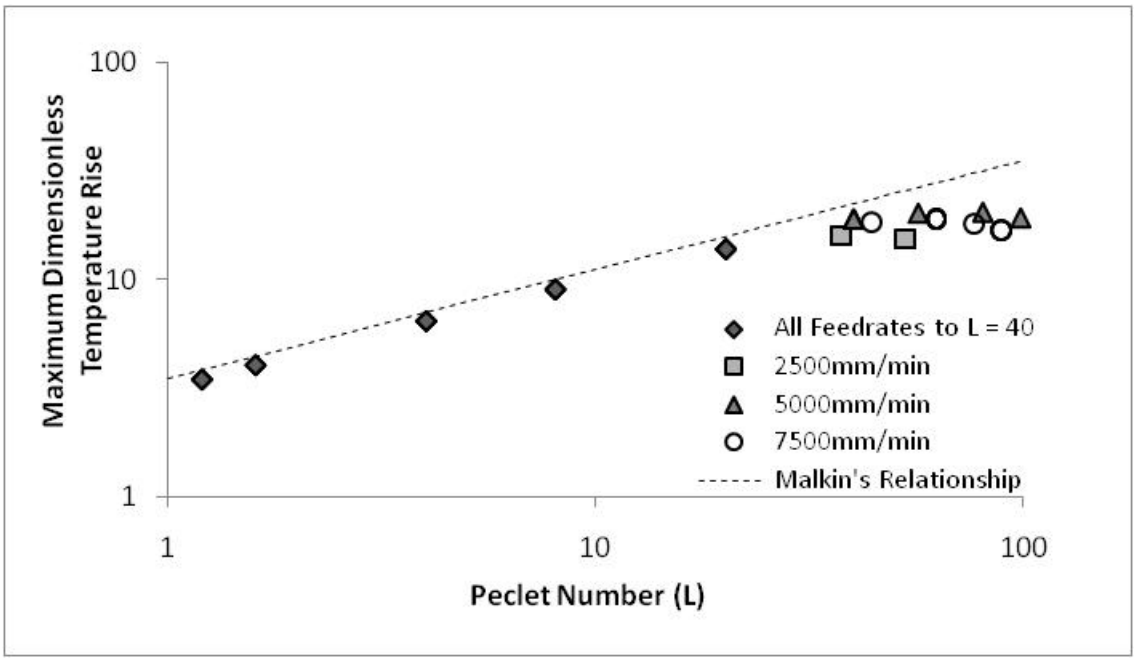

Figure 4.18 Deviation from predicted limit for 51CrV4

4.2.2 Example Burn Threshold Diagram

Using the visual inspection method for detection of grinding burn as described in figure 3.14 of section 3.2.1.4, a sample burn threshold diagram was developed with a visually determined limit. Figure 4.19 demonstrates the burn threshold diagram for SGCI with a limit of grinding burn of 750°C, a similar demonstration with 51CrV4 was not possible as all results presented a burnt surface. The limit of grinding burn was developed by calculation using visual inspection to confirm the fit to the data set in the burn threshold diagram as the threshold temperature increased. This methodology was adapted from figure 2.29 of section 2.4.1. The minimum specific grinding energy from results is estimated to be approximately equal to 13J/mm^3, giving a value of specific grinding energy transferred to the workpiece[3] u_0 equal to 5.85J/mm^3. The burn threshold diagram therefore shows a much higher temperature for the limit of grinding burn than was experienced in practice.

[3] Malkin & Lenz (1978) and Malkin (1989) assume that all specific grinding energy is transferred to the workpiece except for 55% of the chip formation energy during optimal cutting conditions

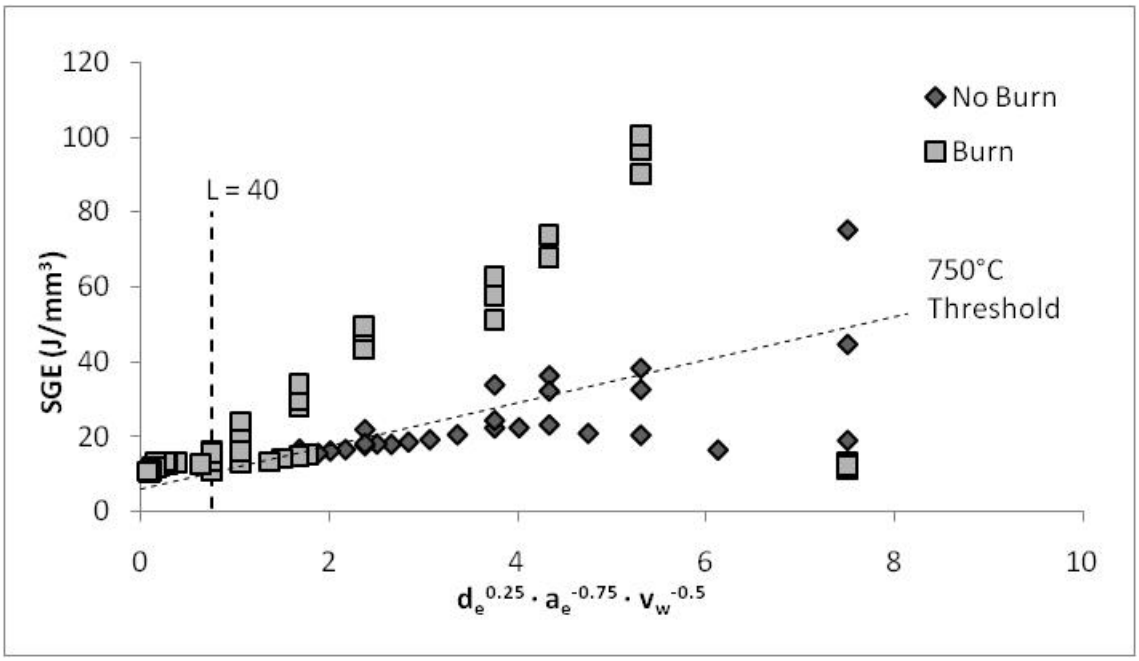

Figure 4.19 Burn threshold diagram limit 750°C

Table 4.8 demonstrates the range of temperatures over which thermal damage occurs based on temperature estimations calculated using the circular arc of heat contact model of Rowe & Jin (2001). The results show that grinding burn in the finished surface appears to occur over a range of temperatures, specifically an estimated temperature rise between 75 and 120°C, which should be considered low for the onset of physical or metallurgical change.

Surface Condition	Estimated Temperature Rise
Unburnt	0 - 120°C
Burnt	75 - 950°C

Table 4.10 Typical surface temperature ranges for burnt and unburnt surface condition with oil based grinding fluid

The burn threshold model of figure 4.19 is therefore shown to give some distinction between a good surface and a burnt surface, however the temperature calculated as required to achieve that limit is significantly larger than that determined by the circular arc of heat contact model of Rowe and Jin (2001). The same results set of figure 4.19 are presented in figure 4.20 with the vertical axis replaced by the maximum surface temperature rise. This results in a clear boundary at the lower end of the specific

material rempoval rate spectrum towards the right of the horizontal axis, however as specific material removal rates increase, the boundary is less clear.

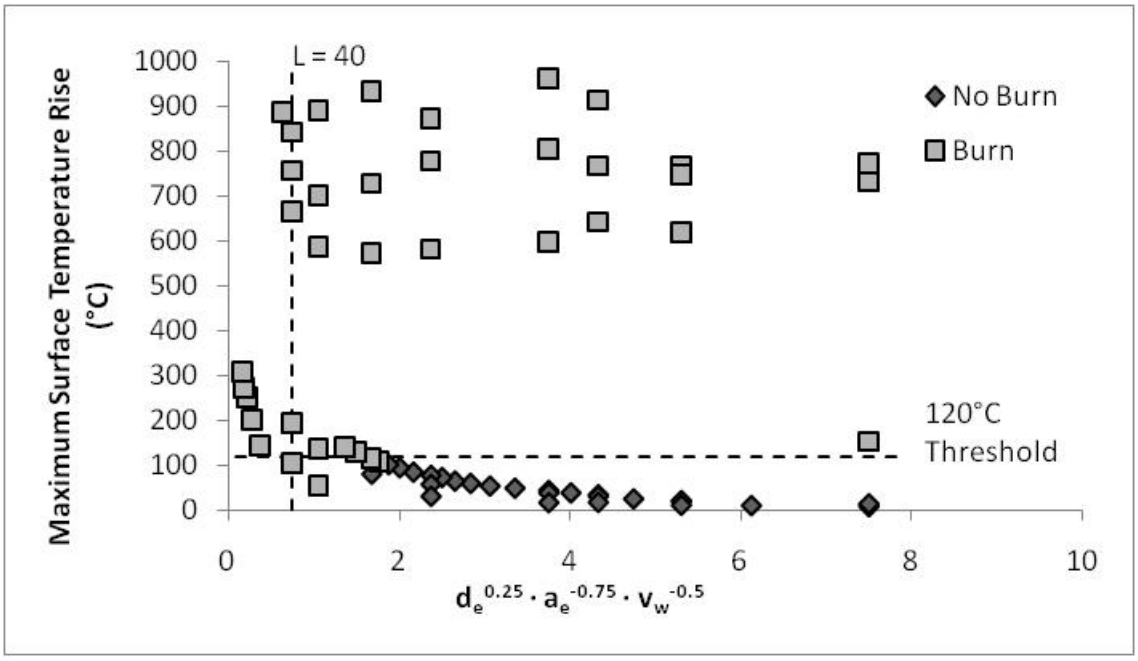

Figure 4.20 Burn threshold with temperature

4.3 Summary

The results of the investigation of trends in specific grinding energy have shown an asymptotic form of the specific grinding energy versus specific material removal rate curve. However the approximation of a power law curve to the results sets recorded was found to be inappropriate as results of specific grinding energy appeared to tend to some constant value under increasing specific material removal rate. This constant value of specific grinding energy was found to be consistent with or without the application of grinding fluid for the limited results set considered.

The supply of grinding fluid to the workpiece has been shown in surface grinding to result in an increased total power requirement. The net grinding power requirement is however reduced when grinding fluid is supplied. For cylindrical grinding, the differences between oil and water based grinding fluids showed a similar effect on the total grinding power, yet the net grinding power was significantly reduced with the use of oil based grinding fluid.

In cylindrical traverse grinding, the tendency to a constant value of specific grinding energy has been shown similarly to surface grinding. However the constant value for cylindrical grinding was shown to occur at much higher values of specific material removal rate than for the surface grinding process with the same material. This suggests that the constant specific grinding energy is not material driven. Results recorded at varying values of feed per turn have shown the benefit of reducing this value to a minimum in terms of total grinding power and hence power available to the machine tool.

Finally the application of the results recorded to a burn threshold diagram typical of Malkin & Lenz (1978) showed an inappropriately high burn threshold temperature. The threshold line was estimated visually so as to lie between burnt and unburnt samples recorded during grinding trials and gave a value of 750ºC, a factor of 5 greater than the predicted values of temperature calculated from the circular arc of heat contact model.

5 Thermal Profiling in High Efficiency Deep Grinding

Chapter 5 presents the thermal profiles and associated data from trials with low melting point coatings in both surface and cylindrical traverse grinding, building a picture of the thermal profile around the contact surface. The results also consider variations present in the thermal profile when a shoulder is present as in profile grinding when compared to the identical parameters for a conventional surface grind.

5.1 Surface Grinding

Section 5.1 considers the effect of the change from surface to profile grinding on the thermal profile in the contact surfaces. The section compares the estimated surface temperatures to those measured by the low melting point coating technique where possible.

Finally the results will consider the response of the thermal profile to changes in the grinding parameters. This will involve a basic look at the effect of changing the three significant process parameters, width and depth of cut, and workpiece velocity.

5.1.1 Comparison of Temperatures in Surface and Profile Grinding

Composite micrographs for surface and profile grinding were collated as per the description in section 3.3.1.4 for the trials summarised in table 5.1. During this process it was found that a number of isotherms had failed to form in completion. As a result of this, comparisons between surface and profile grinding focussed on the Bismuth isotherm, which was seen to form successfully in all cases. Figure 5.1 shows a typical Bismuth micrograph for surface grinding.

Trial Number	a_e (mm)	b (mm)	v_w (mm/s)	v_s (m/s)
1	1	3	125	200
2	2	3	125	200
3	3	3	125	200
4	4	3	125	200

Table 5.1 Summary of surface and profile grinding parameters, trials were repeated for both surface and profile grinding

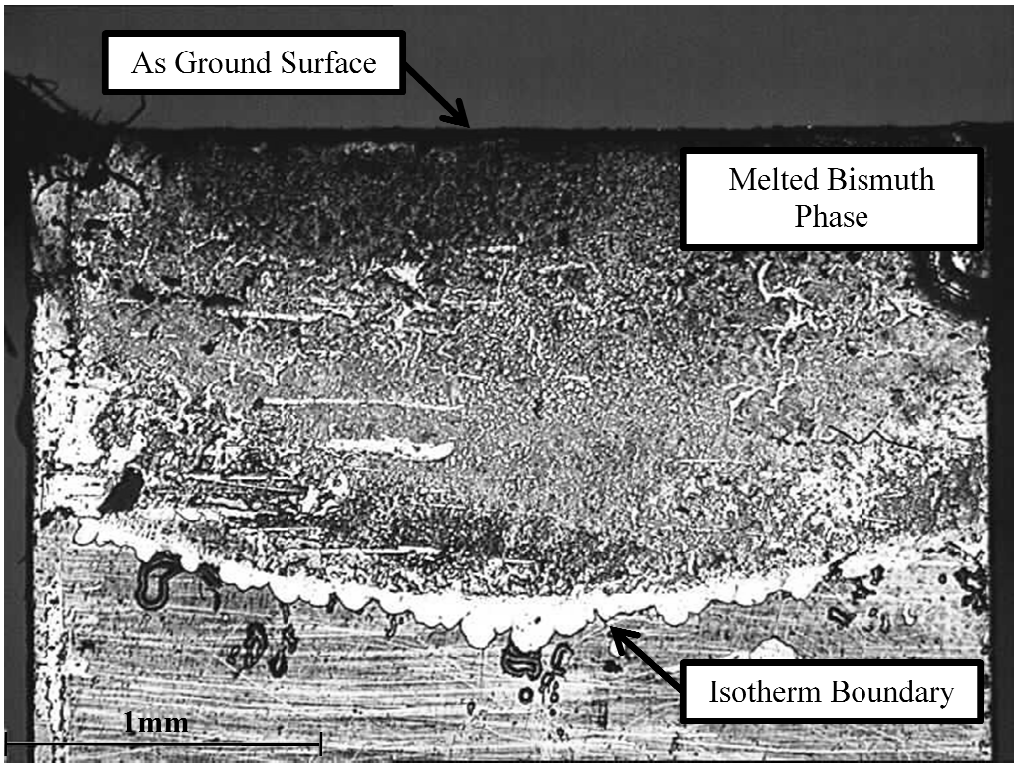

Figure 5.1 Example of a Bismuth isotherm for trial 3 from table 5.1 the grinding direction is away from the reader

Figure 5.2 presents the surface grinding isotherms as plots of relative position versus melt depth. The results show little variation in the value of melt depth as the depth of cut increases from 1mm to 4mm; this is in agreement with results demonstrated by Sainz (2005) who also showed a limited variation in melt depth with increasing depth of cut. The isotherms should be noted to be asymmetric, having a melt depth which increases slightly from left to right. This is likely to be the result of the positioning of the fluid application nozzle, which as described in section 3.2.1.1, was targeted at the wheel edge radius. As a result of this, the coolant application was offset to the left of the sample (left of the x-axis in figure 5.2) as looking along the direction of the grind.

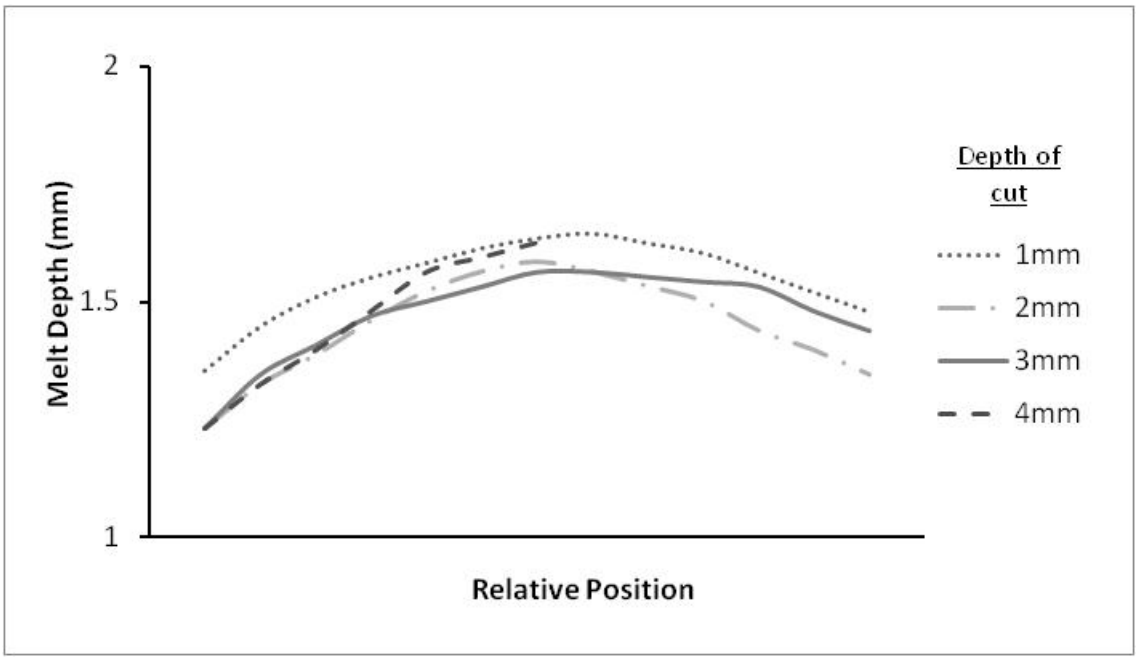

Figure 5.2 Plot of relative position versus melt depth for Bismuth isotherm (parameters); the limiting depth for Takazawa's approximation is 0.75mm

A typical composite micrograph for profile grinding trials is presented in figure 5.3 and demonstrates the form of the isotherm recorded. To recall, measurement was achieved via the overlay of a Cartesian co-ordinate system with the axis parallel surface selected as the x-axis and the sidewall as the y-axis. The corner radius required a method of measurement which would allow for the melt depth perpendicular to the surface to be measured. This was achieved by geometrically estimating the centre point of the wheel edge radius and developing a series of straight lines at 22.5º, 45º and 67.5º from the vertical as shown in figure 5.3. These lines were perpendicular to the wheel edge radius surface and their intersection with the isotherm provided the melt depth required.

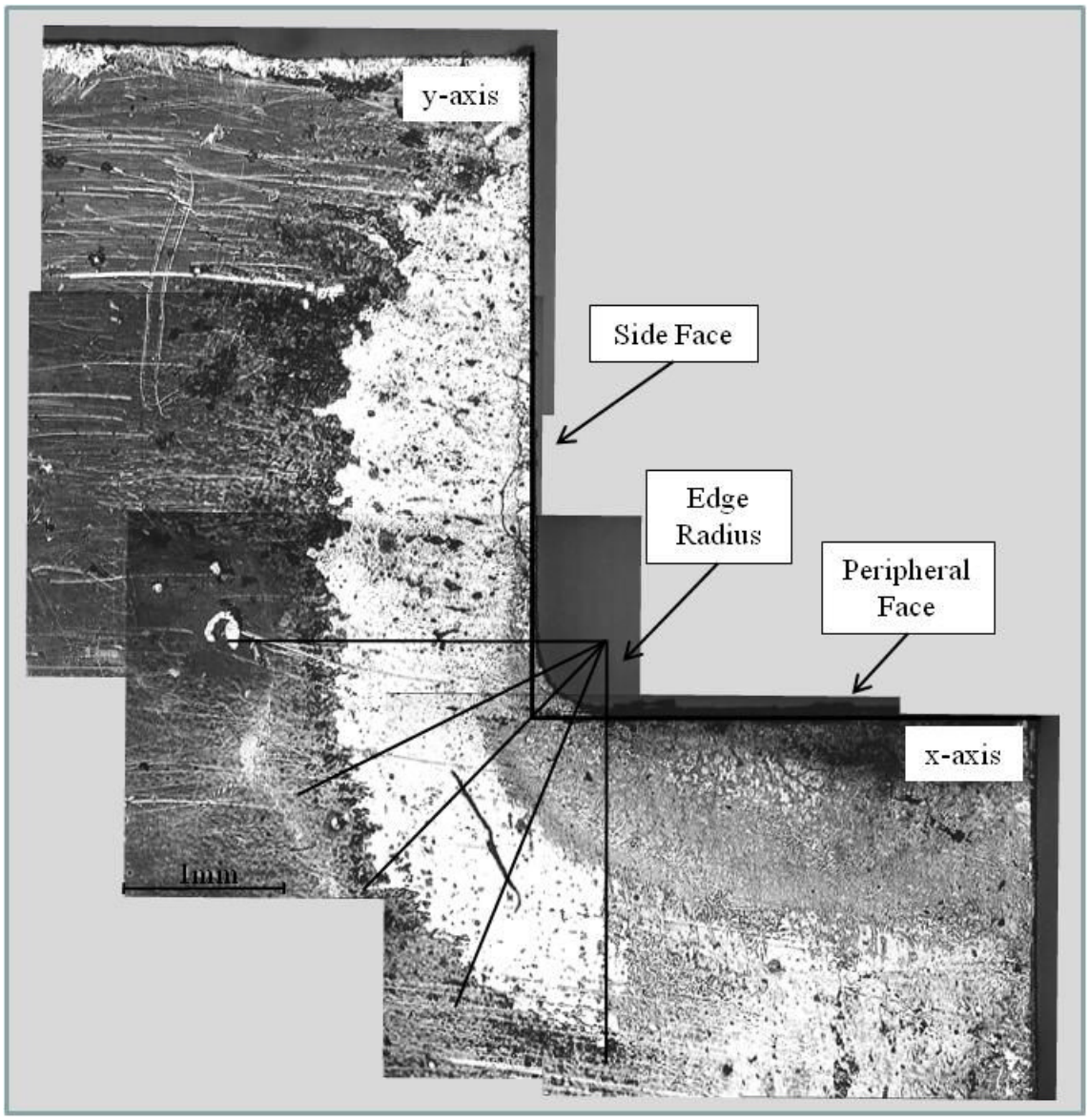

Figure 5.3 Typical Bismuth isotherm with Cartesian grid overlaid and highlighting the method used for measurement of the isotherm perpendicular to the corner radius

Profile grinding trials were again recorded as plots of relative position versus melt depth of the isotherm. Figure 5.4 shows results for the Bismuth isotherms for trials summarised in table 5.1. Results presented in this way are divided into the three sections as marked. The plot shows an increasing melt depth as the relative position moves down the side face contact surface, and approaches the edge radius contact surface. The melt depth can then be seen to increase sharply around the edge radius as the relative position moves towards the peripheral face contact surface before showing a steady increase in melt depth as the edge of the sample is approached.

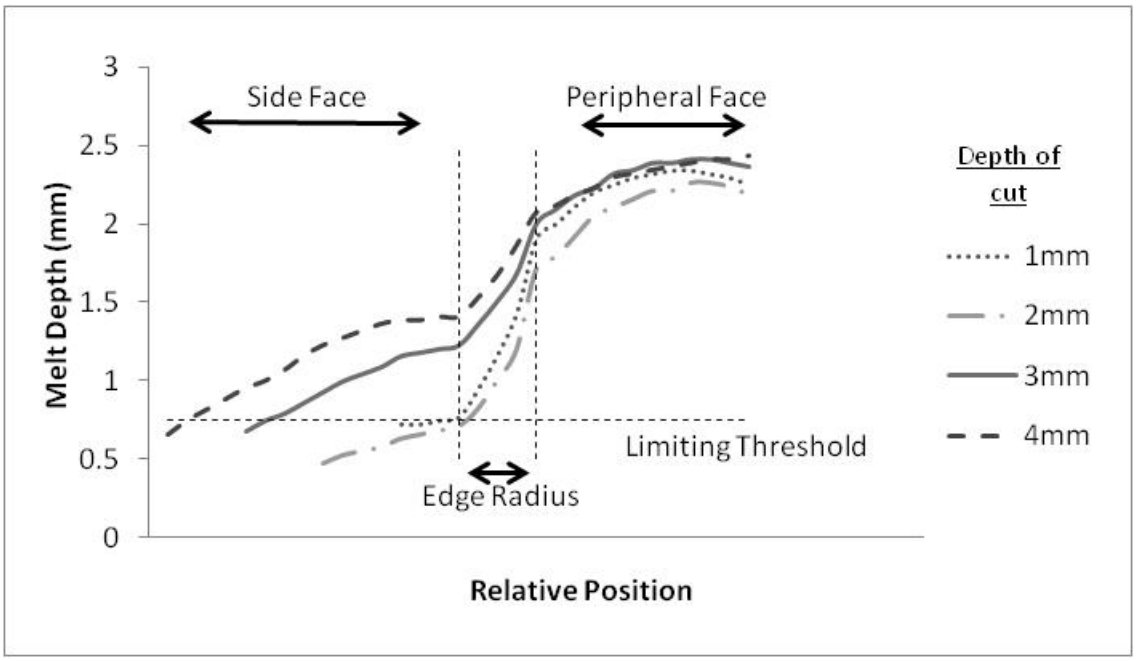

Figure 5.4 Relative position versus melt depth for Bismuth isotherms recorded in profile grinding of 51CrV4 with increasing depth of cut

Figures 5.5 to 5.8 combine results for surface and profile grinding trials for the grinding parameters summarised in table 5.1. The results show there is an effect on the peripheral face temperature when profile grinding compared to surface grinding with the same grinding parameters. The melt depth of the Bismuth isotherm is seen to consistently increase as a result of the presence of the profile or grinding shoulder. The increase in melt depth between plain surface and profile grinding shown in figure 5.5 to 5.8 also appears to be relatively consistent, ranging between 0.5mm towards the corner radius to 0.9mm at the sample side. This increase can be wholly attributed to the presence of the shoulder as the effect of depth of cut on the axis parallel surface is understood to be negligible with increasing depth of cut. However it is not possible from this trial to determine whether there is an effect of coolant deflection and positioning.

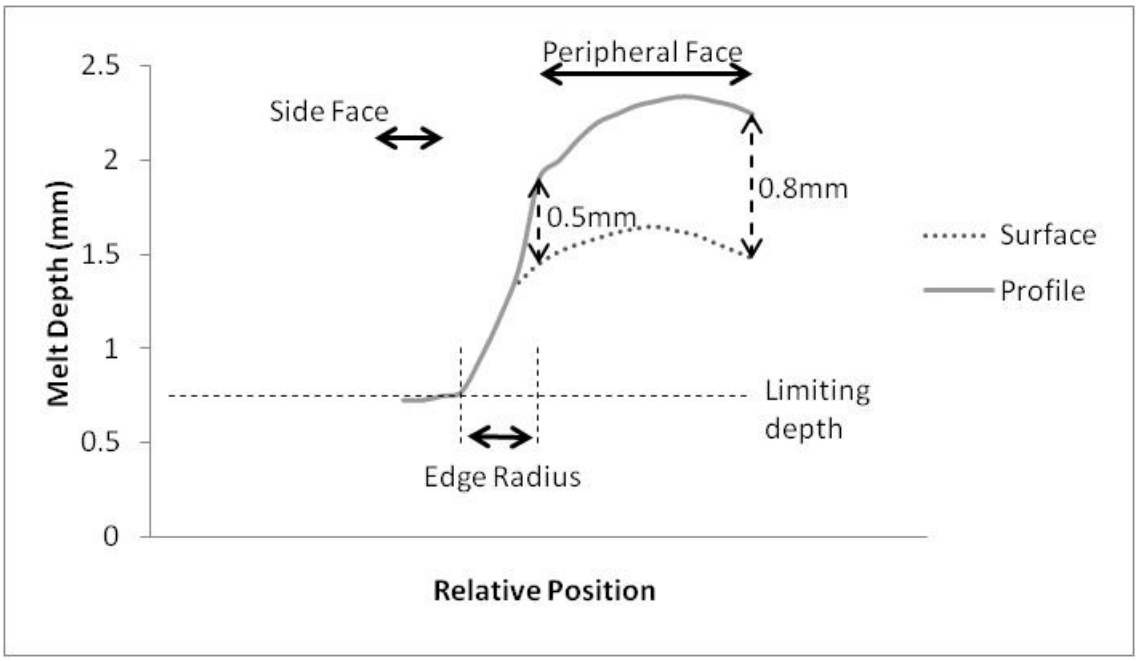

Figure 5.5 Comparison of changes in the Bismuth isotherm as a result of the grinding shoulder for 1mm depth of cut

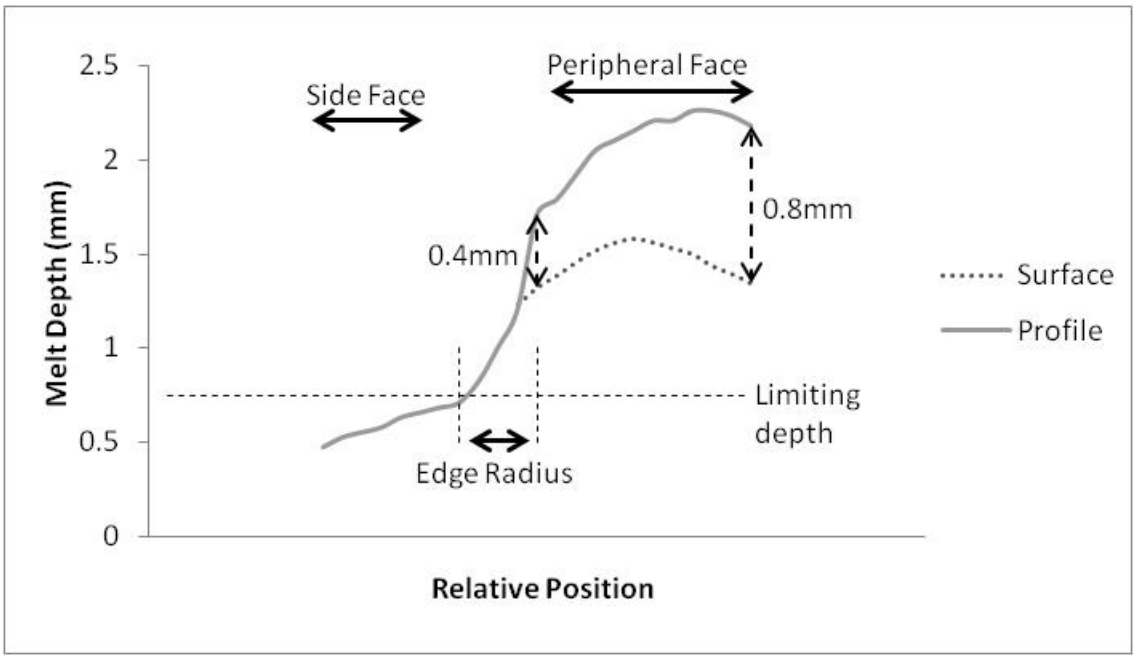

Figure 5.6 Comparison of changes in the Bismuth isotherm as a result of the grinding shoulder for 2mm depth of cut

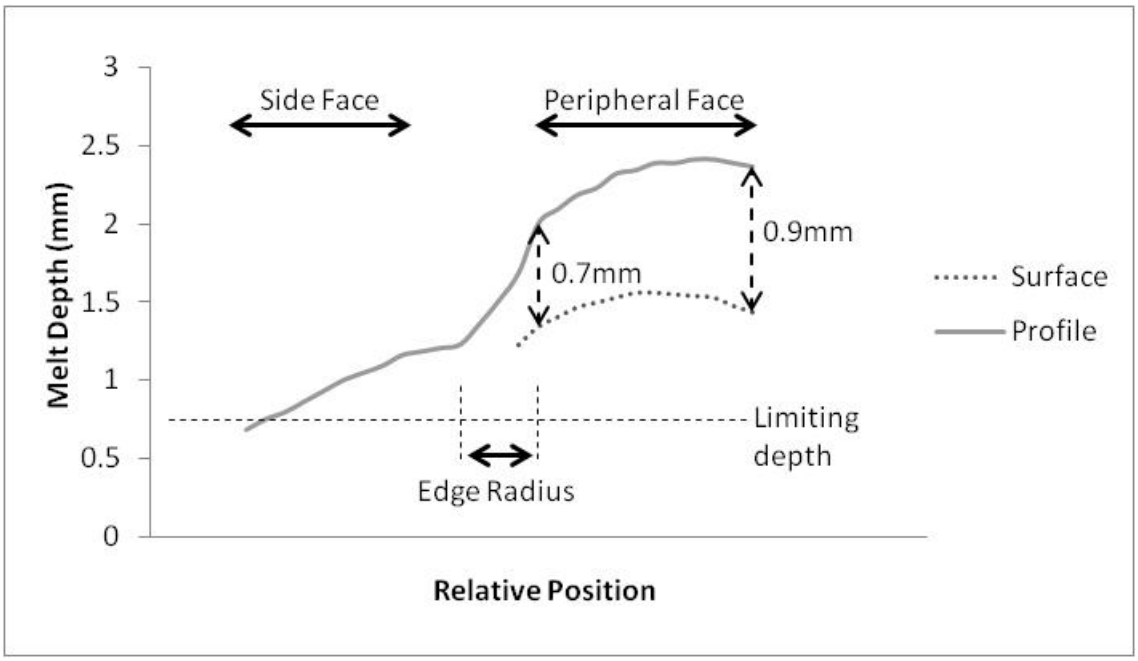

Figure 5.7 Comparison of changes in the Bismuth isotherm as a result of the grinding shoulder for 3mm depth of cut

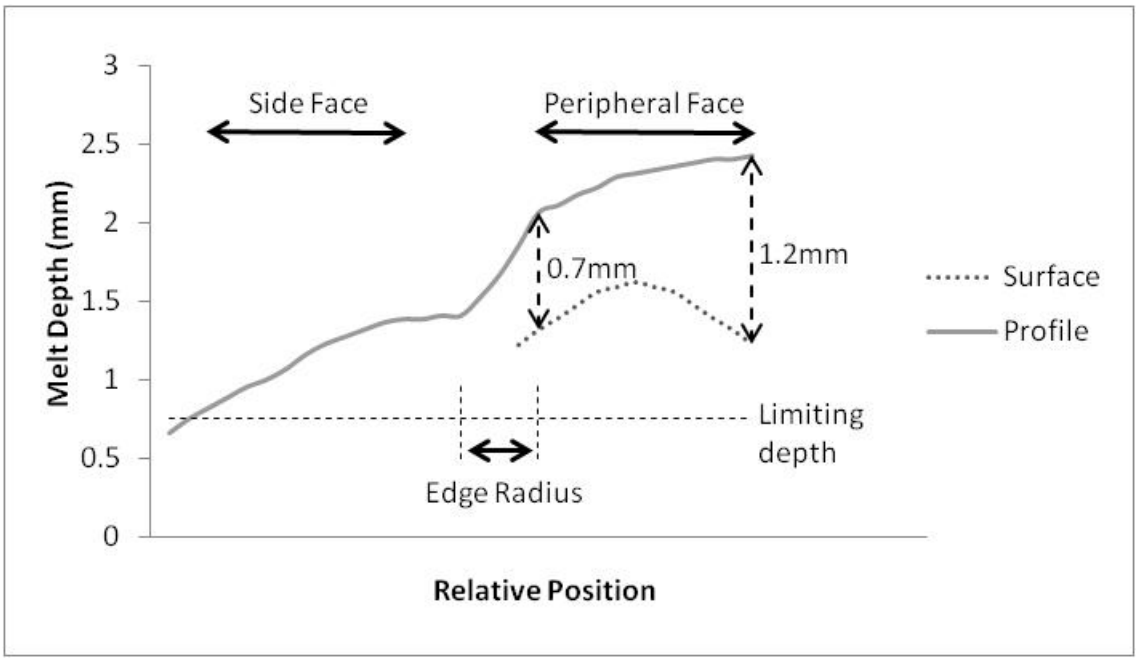

Figure 5.8 Comparison of changes in the Bismuth isotherm as a result of the grinding shoulder for 4mm depth of cut

The results presented in figures 5.6 to 5.8 also demonstrated the limited effect of depth of cut on the surface temperature (by proxy of the melt depth). Shown in figure 5.9, the depth of cut can be seen to increase the specific material removal rate whilst having a

negligible effect on the maximum melt depth of the isotherm in surface grinding and the peripheral face in profile grinding. For the side face in profile grinding, the increase in depth of cut is shown to increase the melt depth in the side face.

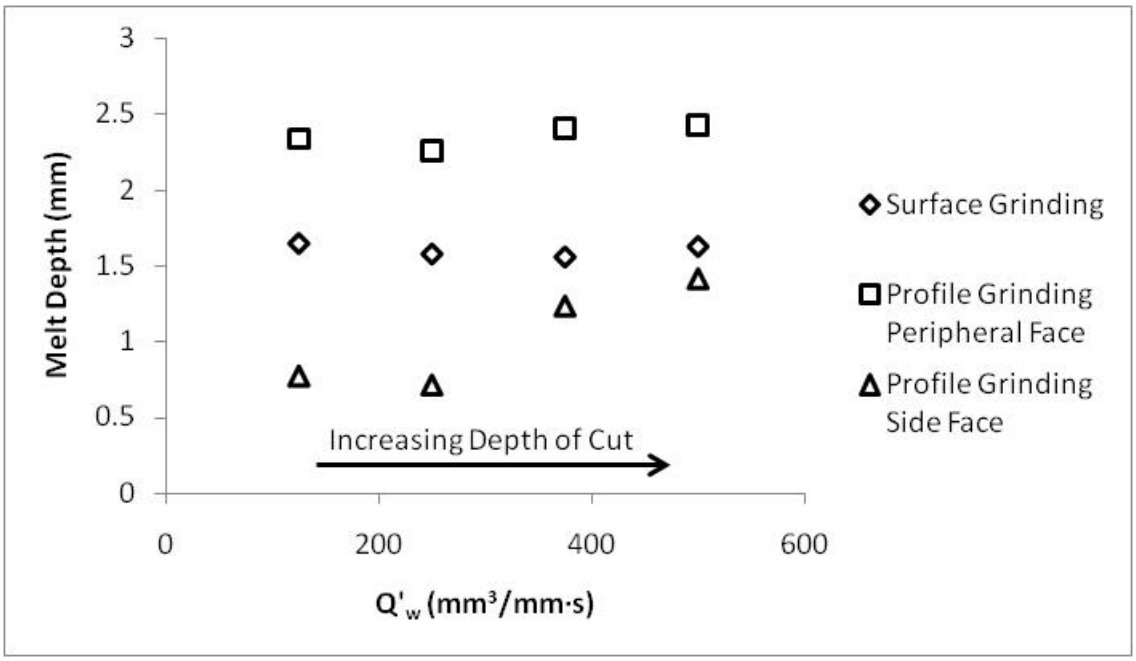

Figure 5.9 Comparison of the surface and profile melt depths with increasing depth of cut

Figures 5.10 to 5.12 consider the variation in the measured power and specific grinding energy corresponding to the temperature measurement trials summarised in table 5.1. Figure 5.10 shows a plot of specific material removal rate versus the total power requirement of the grinding process. As specific material removal rates increase, the shoulder appears to exert a consistent increase in power requirement on the machine tool. The small variation in total grinding power between surface and profile grinding at a value of 125mm^3/mm·s is thought to be the result of the small depth of cut encountered and hence minimal coolant deflection by the body of the workpiece.

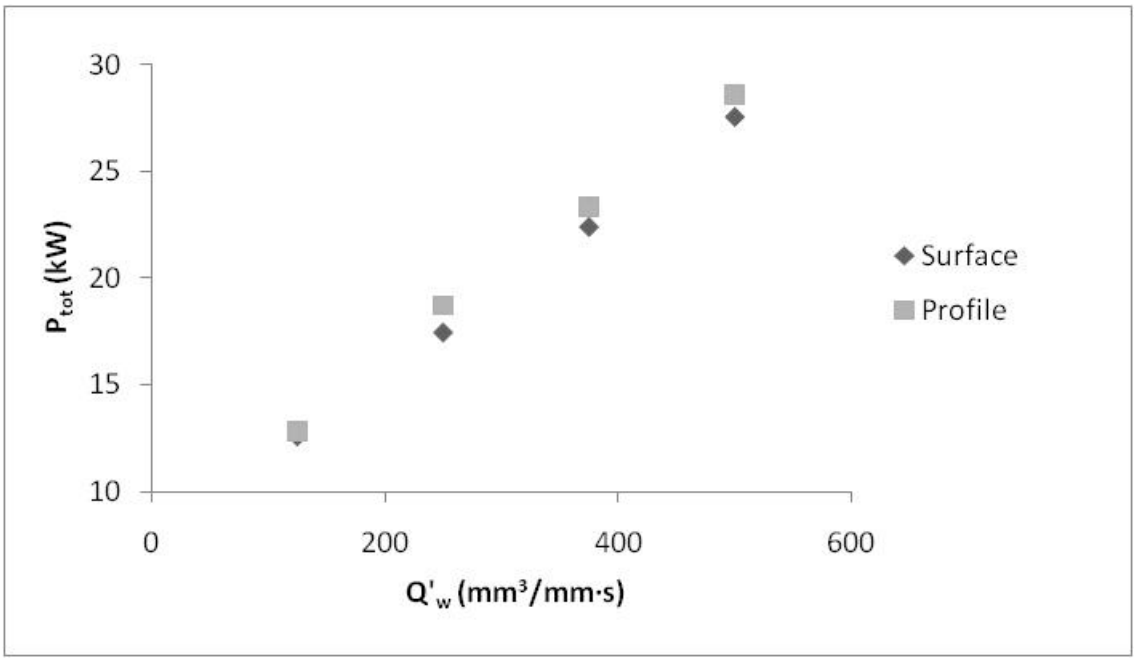

Figure 5.10 Specific material removal rate versus total power showing variation between surface and profile grinding

Figure 5.11 shows a plot of specific material removal rate versus net grinding power. The trend is similar to that shown for total grinding power in figure 5.10, again the small variation in net grinding power at a value of 125mm^3/mm·s is thought to be the result of limited coolant deflection by the shoulder.

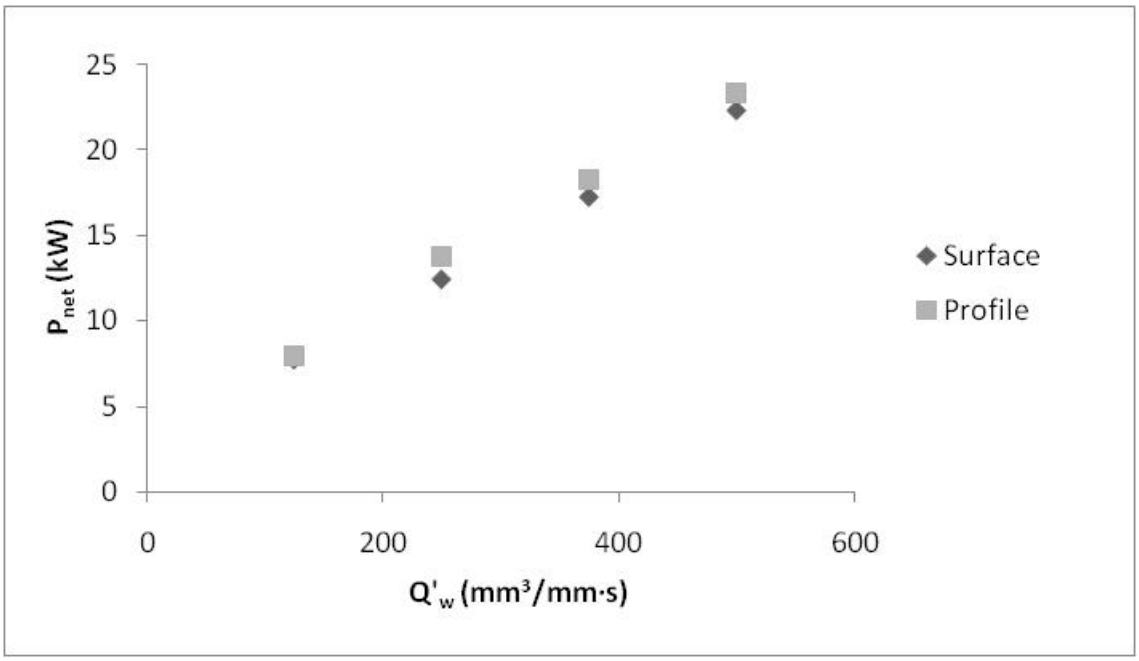

Figure 5.11 Specific material removal rate versus net grinding power showing variation between surface and profile grinding

The resulting plot of specific material removal rate versus specific grinding energy is shown in figure 5.12. As may be expected the specific grinding energy requirement is increased for profile grinding as compared to surface grinding. However the change in specific grinding energy is only small varying between 3% to 10% and could fall within the error of the system or be the result of wheel wear. It should be noted that this curve differs from that presented in figure 4.2 showing a series of much higher specific grinding energies. This is thought to be the result of wheel wear.

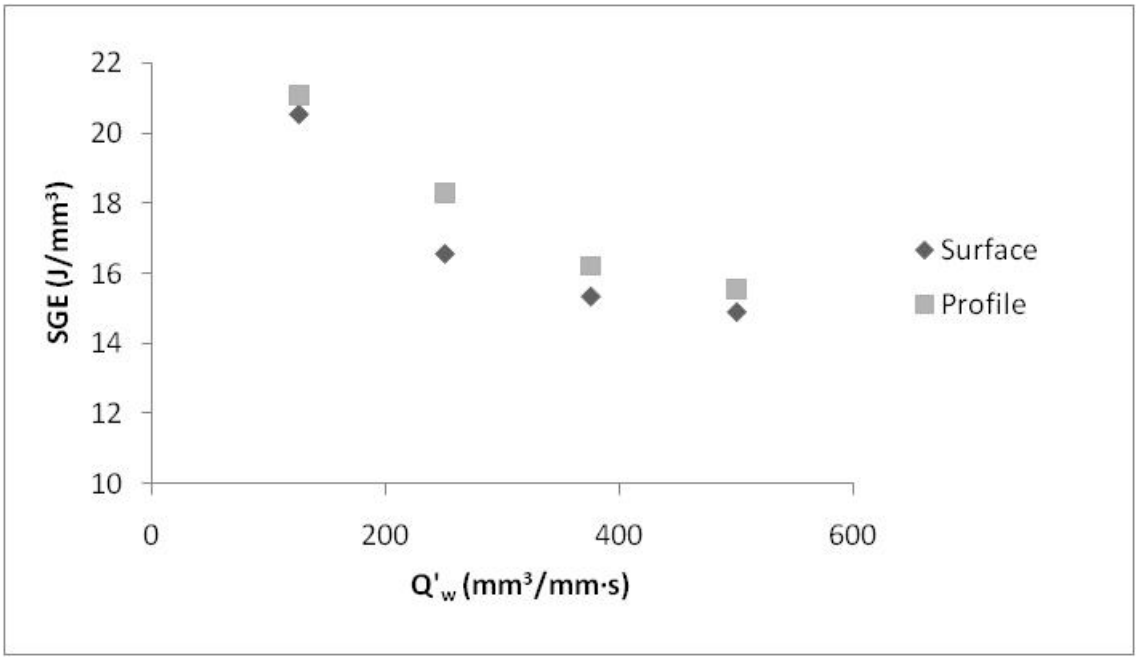

Figure 5.12 Specific material removal rate versus specific grinding energy for surface and profile grinding

Figure 5.13 shows the estimated temperatures from the circular arc of heat contact model and those estimated from the low melting point coatings. A clear increase in temperature in the peripheral face surface is present in profile grinding when compared to surface grinding. This is expected from the melt depth variation in figures 5.5 to 5.8 and the trends of the specific grinding energy curve of figure 5.12. A single line represents values predicted from the circular arc of heat contact model. The model consistently predicted temperature rises greater than the melting temperature of the material. In this case the temperature was estimated to be close to the melting temperature of the material at 1350ºC. This resulted in the temperature being equivalent in both surface and profile grinding and further shows a temperature reduction as a

result of the energy partitioned to the finished workpiece surface decreasing with the increasing depth of cut.

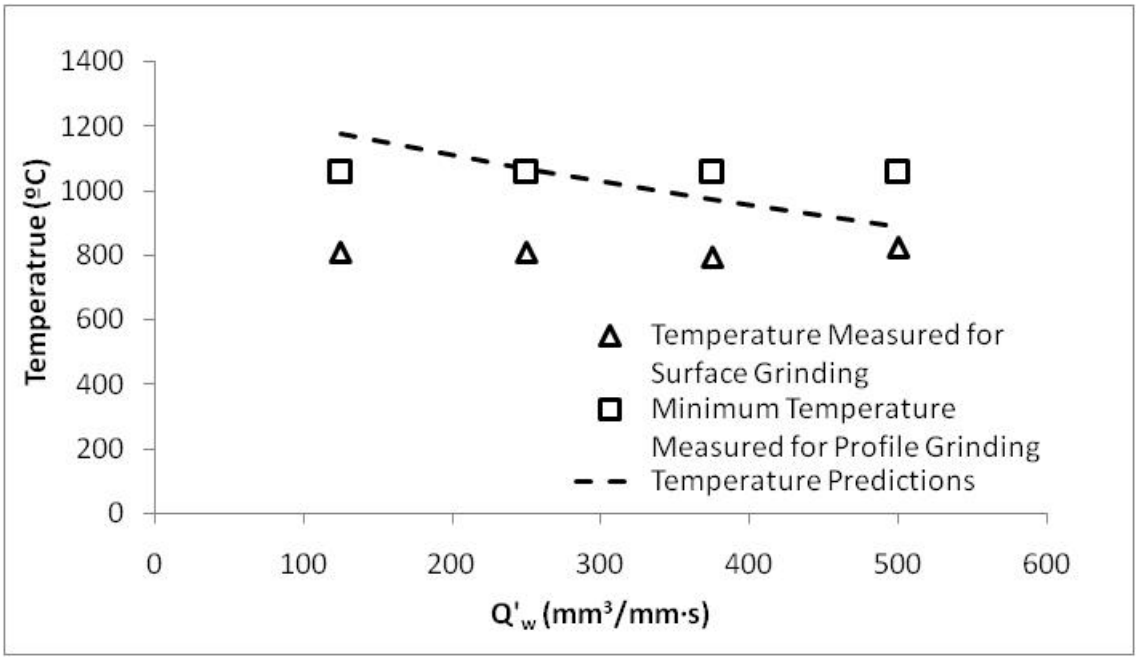

Figure 5.13 Temperatures in the finished peripheral face surface for surface and profile grinding and as predicted from the circular arc of heat contact model

5.1.2 The Effect of Grinding Parameters on Temperatures around the Profile

Section 5.1.2 shows the effect of changes in grinding parameters on the temperature around the profile, table 5.2 summarises the parameters used. Graphs of relative position versus melt depth are shown in figure 5.14 to 5.17 with trial numbers corresponding to table 5.2. These demonstrated the similarity between the forms for similar parameters with the Indium low melting point coating. The results showed an increase in the melt depth between the first (dotted line) and second (solid line) of the repeat runs shown in the individual figures which is thought to be the product of wheel wear. The results show that the trend of the isotherm is similar for similar grinding parameters and also exhibits a series of similar trends between grinding parameters for the three sections highlighted.

Trial Number	a_e (mm)	b (mm)	v_w (mm/s)	v_s (m/s)
1	4	3	75	200
2	2	1	75	200
3	4	1	125	200
4	2	3	125	200
5	2	3	125	200
6	4	1	125	200
7	4	3	75	200
8	2	1	75	200

Table 5.2 Summary of profile grinding trial parameters

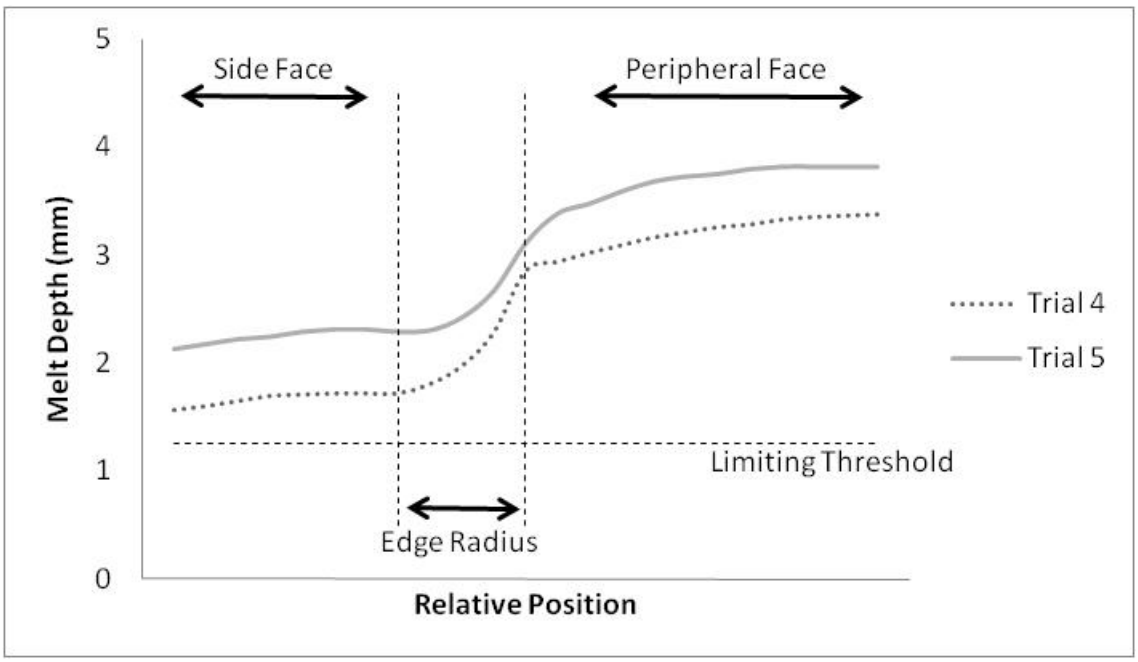

Figure 5.14 Relative position versus melt depth for trial 4 & 5

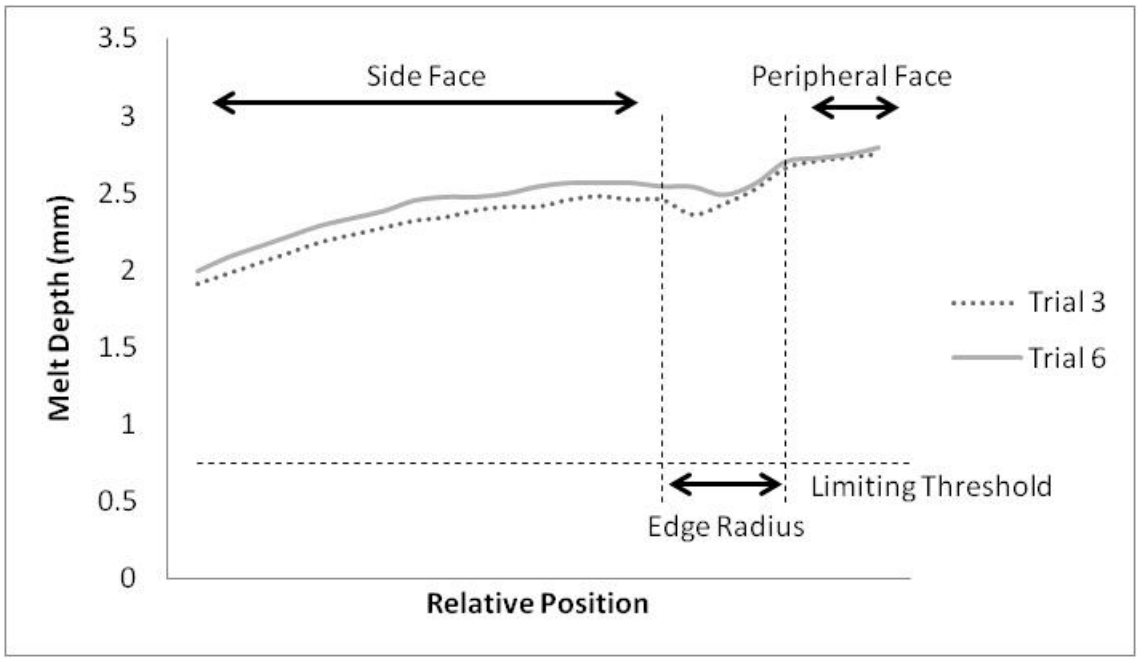

Figure 5.15 Relative position versus melt depth for trial 3 & 6

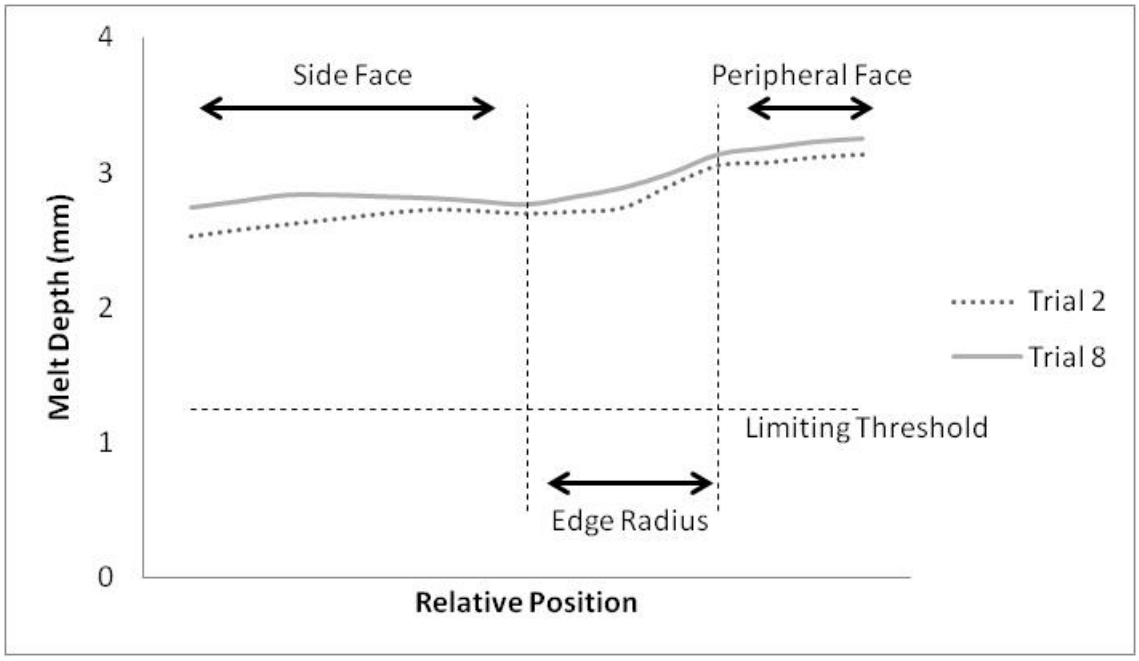

Figure 5.16 Relative position versus melt depth for trial 2 & 8

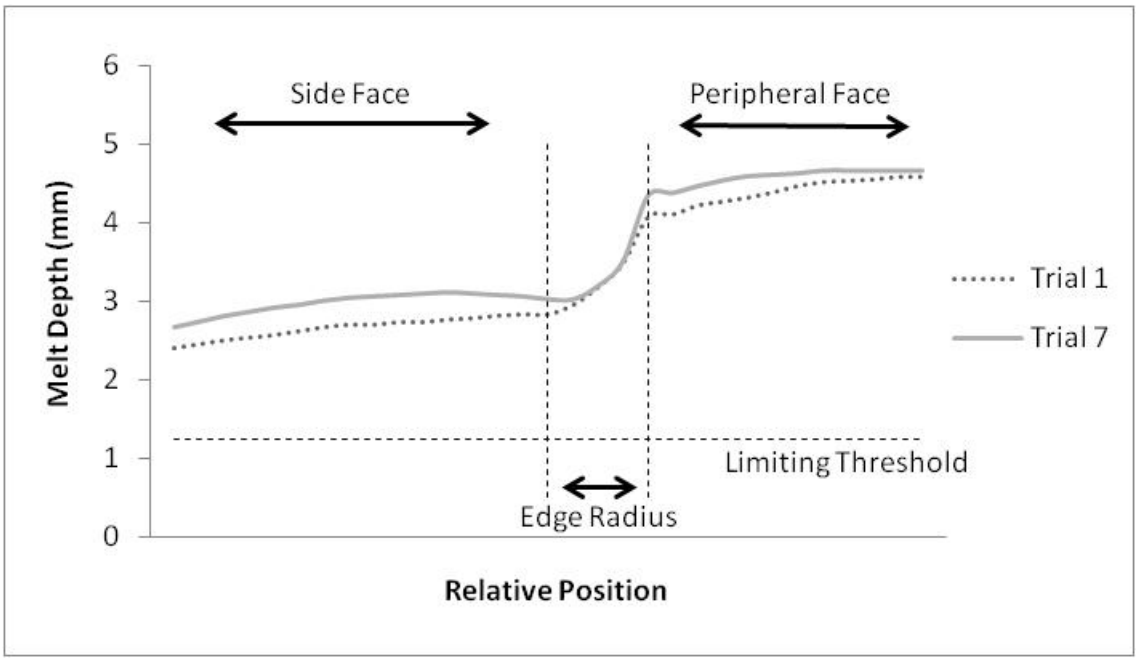

Figure 5.17 Relative position versus melt depth for trial 1 & 7

Figures 5.18 and 5.19 show a basic study of the effects of the selected grinding variables on the melt depth of the isotherm. Given the limited number of test pieces available, a statistical validation of the results was not achievable, requiring a minimum of 3 samples at each of the levels of the trial. However, the results do indicate the trend established by changing the particular variable. For both the side face and the peripheral face contact surfaces, the workpiece feedrate reduced the thermal penetration during grinding contrary to the findings of Sainz (2005). The increase in the width of cut resulted in an increase in the thermal penetration into the peripheral face contact surface, whilst at the same time having no significant effect on the thermal penetration into the sidewall. The depth of cut can be seen to produce a limited increase in the thermal penetration into the sidewall; however there is no significant change in the thermal penetration into the axis parallel surface.

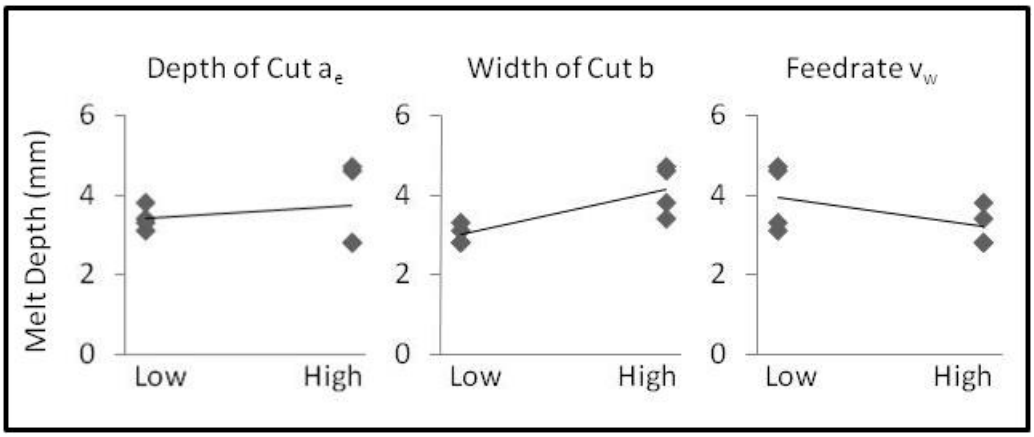

Figure 5.18 Effects of the variables on the melt depth in the peripheral face contact surface during simple surface profile grinding

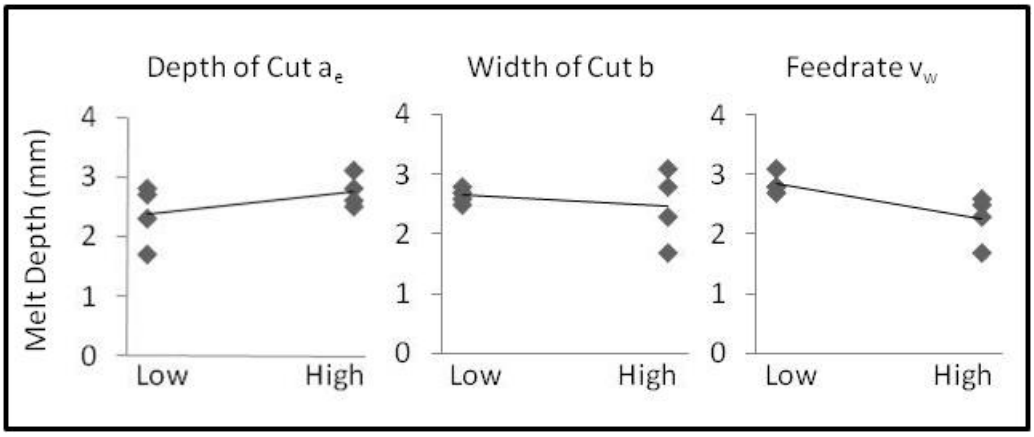

Figure 5.19 Effects of the variables on the melt depth in the side face contact surface during simple surface profile grinding

The effect of the width of cut is seen to increase the temperature in the peripheral face contact surface. This can be considered significant when taken in conjunction with results from section 4.1.2, which suggested lower total grinding power requirements with decreasing feed per turn in cylindrical traverse grinding. This confirms that a small width of cut or feed per turn is desirable in the selection of grinding parameters for processing at high specific material removal rates.

Results from the trials summarised in table 5.2 were also used to develop figures 5.20 to 5.22 considering the effects of the variables on the total and net grinding powers and the specific grinding energy. Both figures 5.20 and 5.21 present similar forms and suggests increases in power requirements for increasing both the depth of cut and the workpiece feedrate. The width of cut suggests a neutral effect; however there is evidence of a high

level of interactivity between the high and low values. This requires further analysis before a conclusion can be drawn.

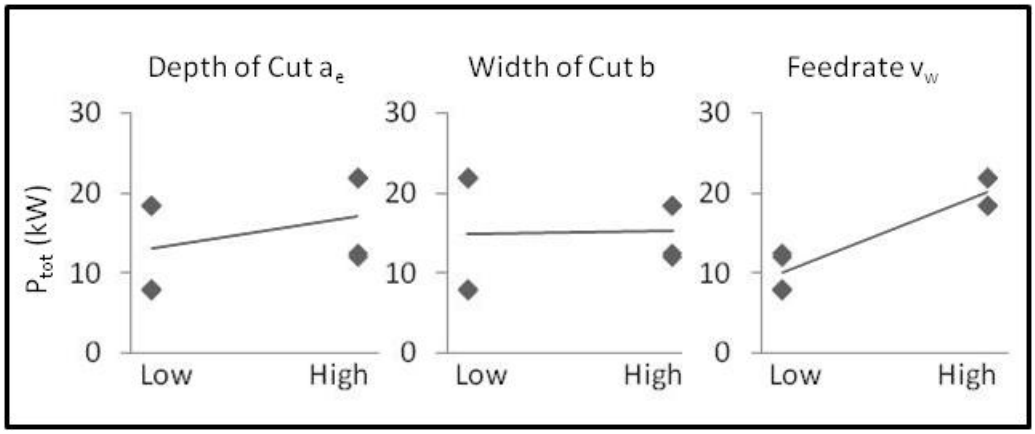

Figure 5.20 Effects of the variables on the total grinding power

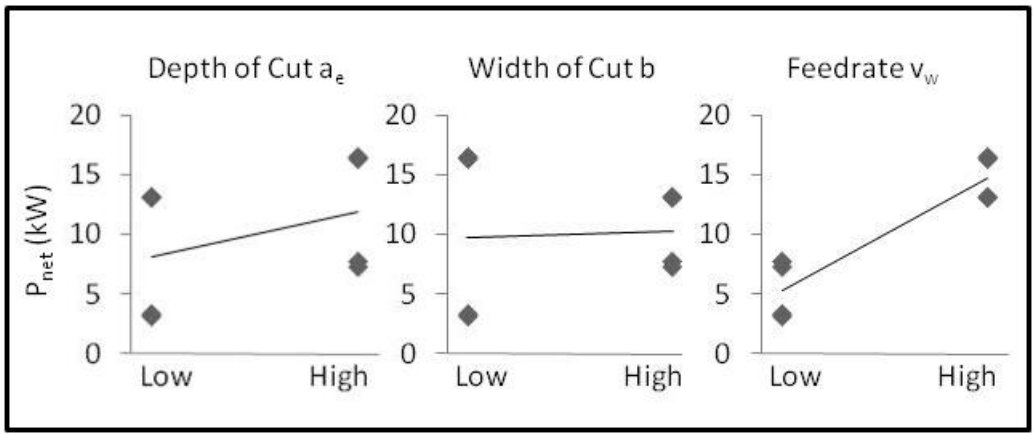

Figure 5.21 Effects of the variables on the net grinding power

Figure 5.22 shows that increasing the workpiece feedrate resulted in a neutral effect on the specific grinding energy although there is the potential for some interaction here. The width of cut and depth of cut showed a reduction in specific grinding energy as values were increased.

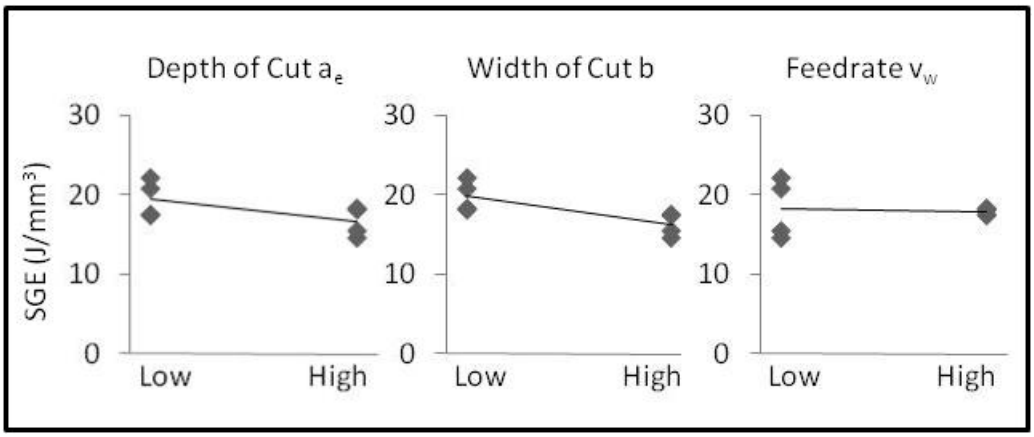

Figure 5.22 Effects of the variables on the specific grinding energy

During the testing of the variables on temperatures around the profile, a series of wear tests were interspersed to test the effect of the wheel wear on the temperature profile. Tests were standardised with the following parameters:

v_w = 125mm/s

a_e = 2mm

b = 2mm

v_s = 200m/s

Figure 5.23 shows results for the melt depth for the Bismuth low melting point coating in both the peripheral and side faces and suggests a negligible changes in the melt depth in both surfaces. However, this requires further investigation to validate as results fall within the error range of the system and the test range was small. Further it would appear to contradict the changes in melt depth witnessed in figures 5.14 to 5.17, where increases in melt depth were experienced as a result of wheel wear.

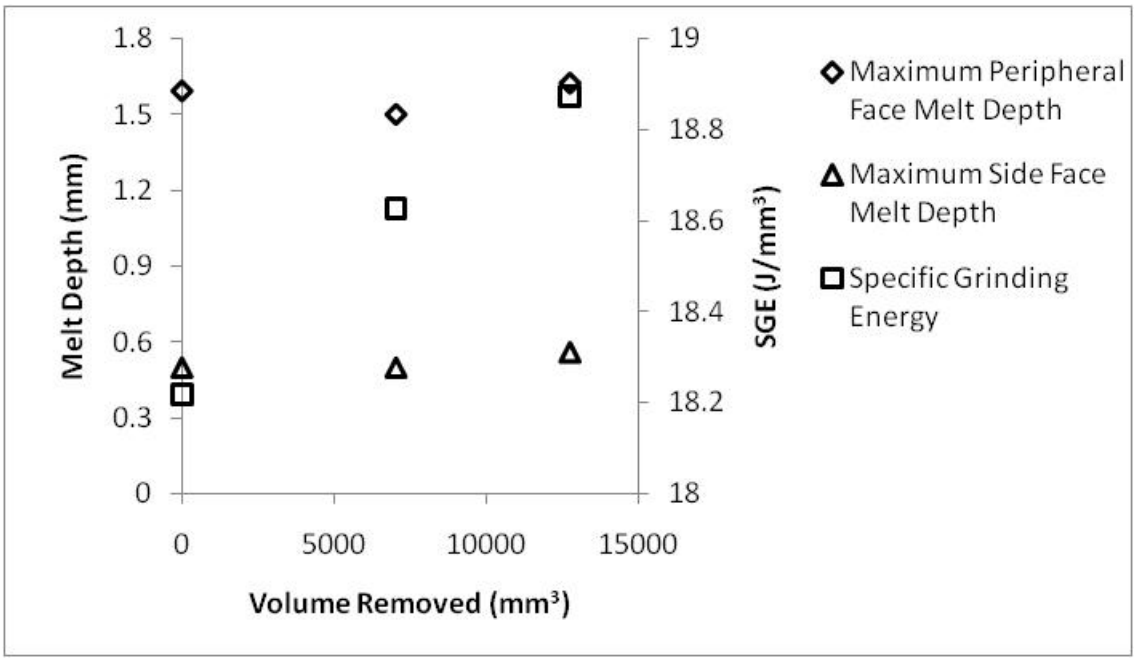

Figure 5.23 Effect of wear on the temperature profile in surface grinding

5.2 Cylindrical Traverse Grinding

The study of cylindrical traverse grinding initially considered a high feed per turn under conditions designed to generate a high grinding temperature with parameters summarised in table 5.3. Composite micrographs for these conditions are presented in figure 5.24 to 5.27 for the Indium low melting point coating isotherms. Unlike the profile grinding trials presented in section 5.1.1, the continuation of the axis parallel surface shows the isotherm in near completion.

Trial Number	a_e (mm)	v_t (mm/min)	v_w (RPM)	b (mm)	v_s (m/s)
1	3	60	6	10	150
2	3	60	12	5	150
3	3	120	24	5	150
4	3	60	24	2.5	150

Table 5.3 Summary of cylindrical traverse grinding parameters

The profile of the isotherm in cylindrical traverse grinding was measured similarly to the surface grinding trials. Results were again measured by overlaying a Cartesian coordinate system, with the peripheral edge surface taken as the x-axis. There is evidence of wheel lean shown under microscopy in figures 5.24 to 5.27. This effect was

incorporated by measuring the surface in conjunction with the isotherm to allow an accurate measure of depth from the ground surface.

Figure 5.24 demonstrates a complete isotherm in the ground surface for a feed per turn of 10mm using the grinding parameters summarised in table 5.3. The length of the isotherm was measured at approximately 12mm compared to the 10mm width of cut specified by the grinding parameters. This is thought to be the effect of the wheel contact being greater than the width of cut, thus the tail of the isotherm is extended slightly beyond the width of cut.

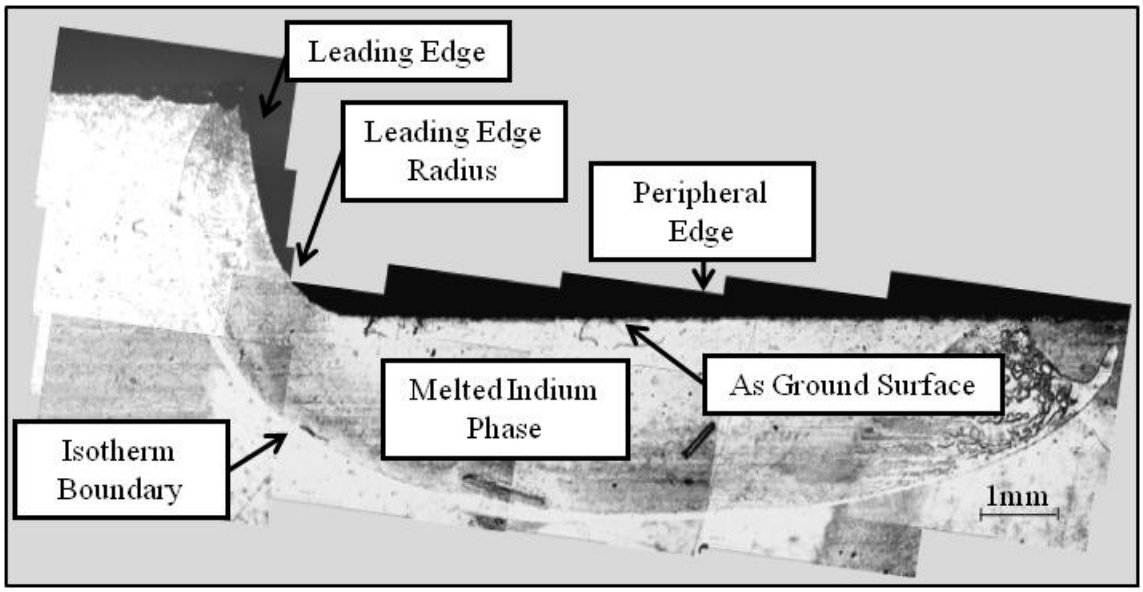

Figure 5.24 Indium isotherm for trial 1

The isotherms presented in figures 5.25 and 5.26 show a width of cut of 5mm and demonstrate the first instance of the isotherms appearing to form a string of beads along the workpiece surface.

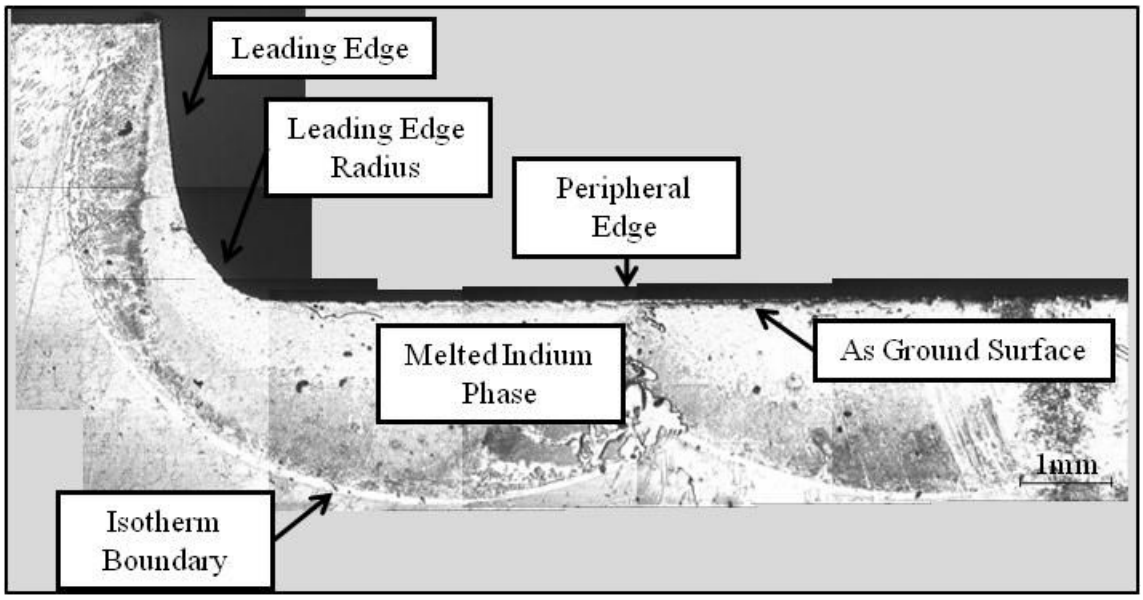

Figure 5.25 Indium isotherm for trial 2

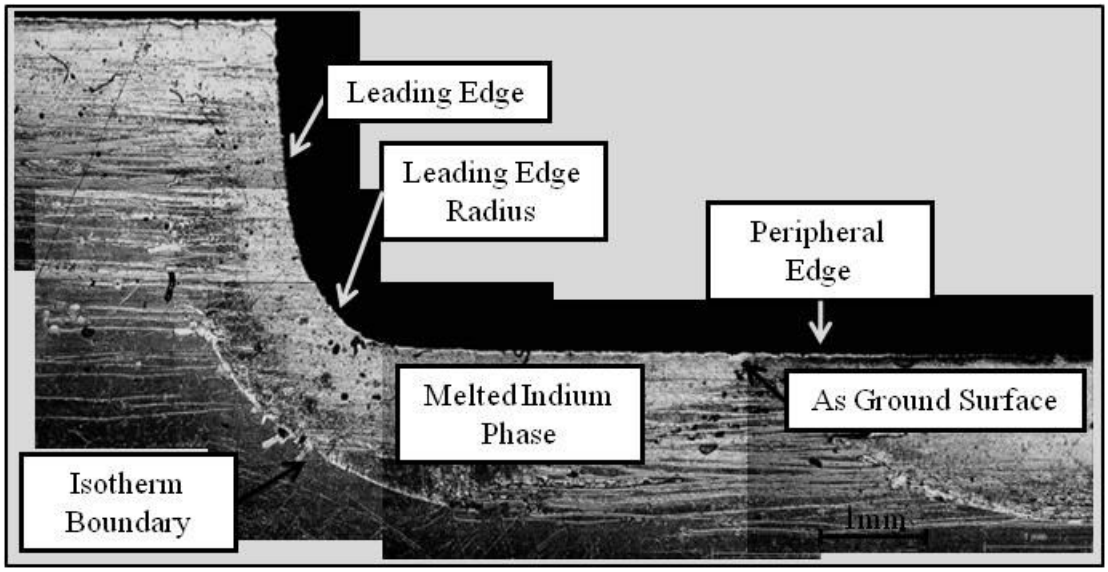

Figure 5.26 Indium isotherm for trial 3

The composite image shown in figure 5.27 demonstrates a series of well defined, complete isotherms. Measuring between the intersections of the isotherms demonstrates a length equivalent to the feed per turn or width of cut. In the case of figure 5.27, this length is equal to 2.5mm. When considering cylindrical traverse grinding with a high

feed per turn, this effect could be significant for non-destructive testing methods. The variation in temperature across the finished surface may mean the temperature peak and hence greatest damage level may not be fully detected.

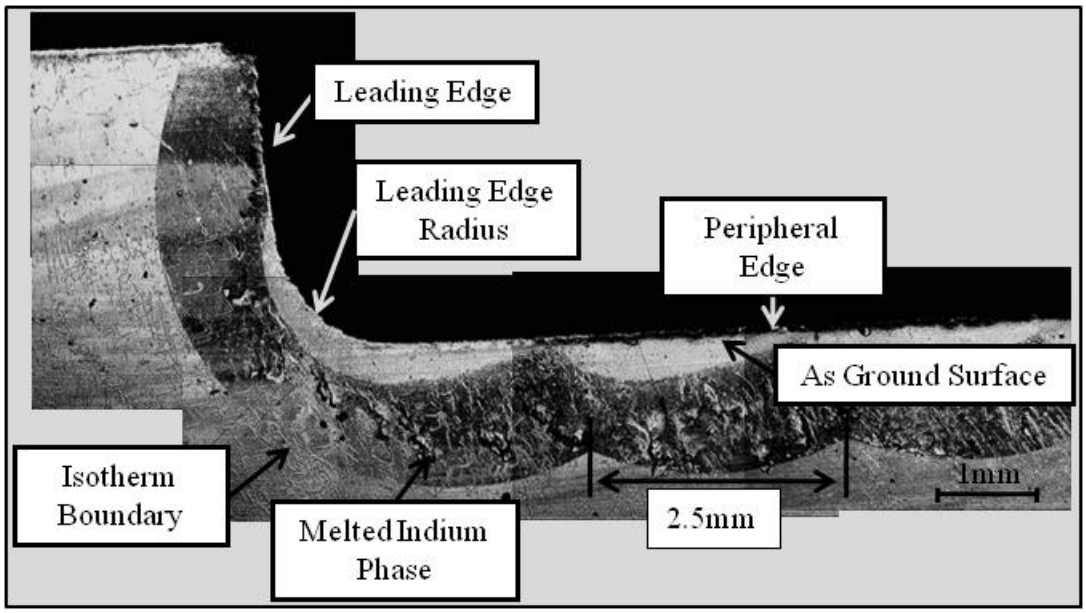

Figure 5.27 Indium isotherm for trial 4

Figure 5.28 demonstrates a plot of relative position versus melt depth for trials in cylindrical traverse grinding. As for surface grinding the depth of penetration into the sidewall increases towards the leading edge radius, however the melt depth transitions much more smoothly into the peripheral edge than for surface grinding. The smoother transition from leading edge to peripheral edge is likely to be the result of both the increased corner load and the apparent lean of the wheel. At this stage the highest heat flux is still seen to be into the peripheral edge contact surface, indicating that the traverse may not be creating the primarily face grinding conditions expected.

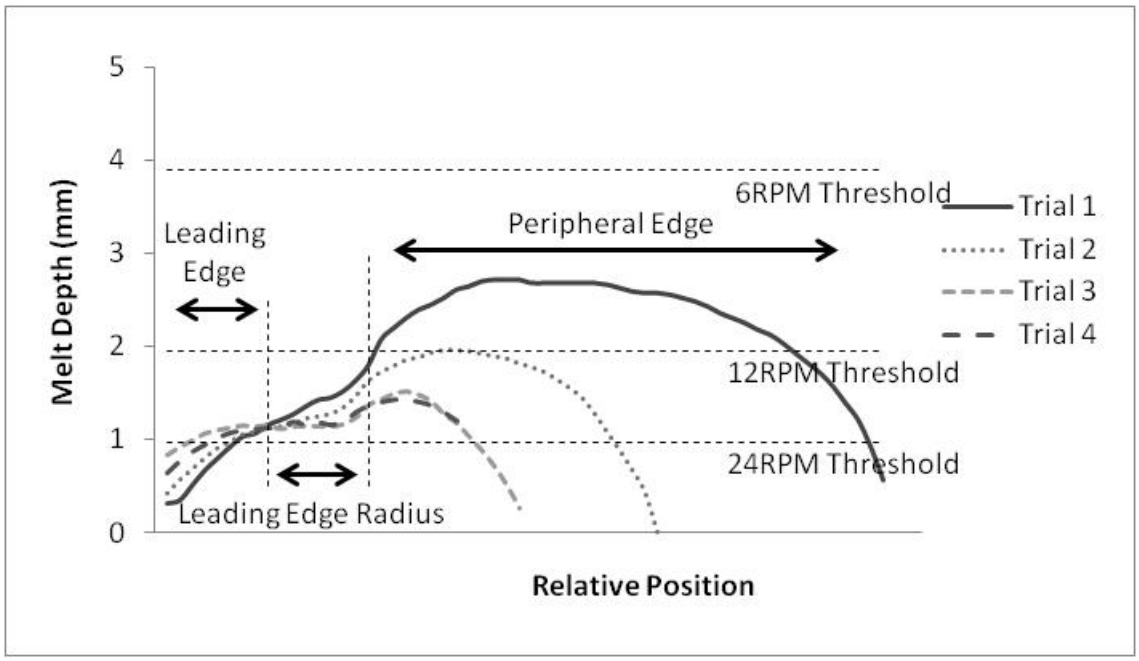

Figure 5.28 Plot of relative position versus melt depth

The second stage of the study of cylindrical traverse grinding considered processing at high RPM with the low widths of cut recommended from results in section 4.12. Figure 5.29 shows a typical isotherm for these high RPM trials with a Bismuth low melting point coating. This was typical of the isotherms recorded throughout the high RPM trials and is significant in the fact that the melt depth is extremely small, being of the order of 50 to 200µm.

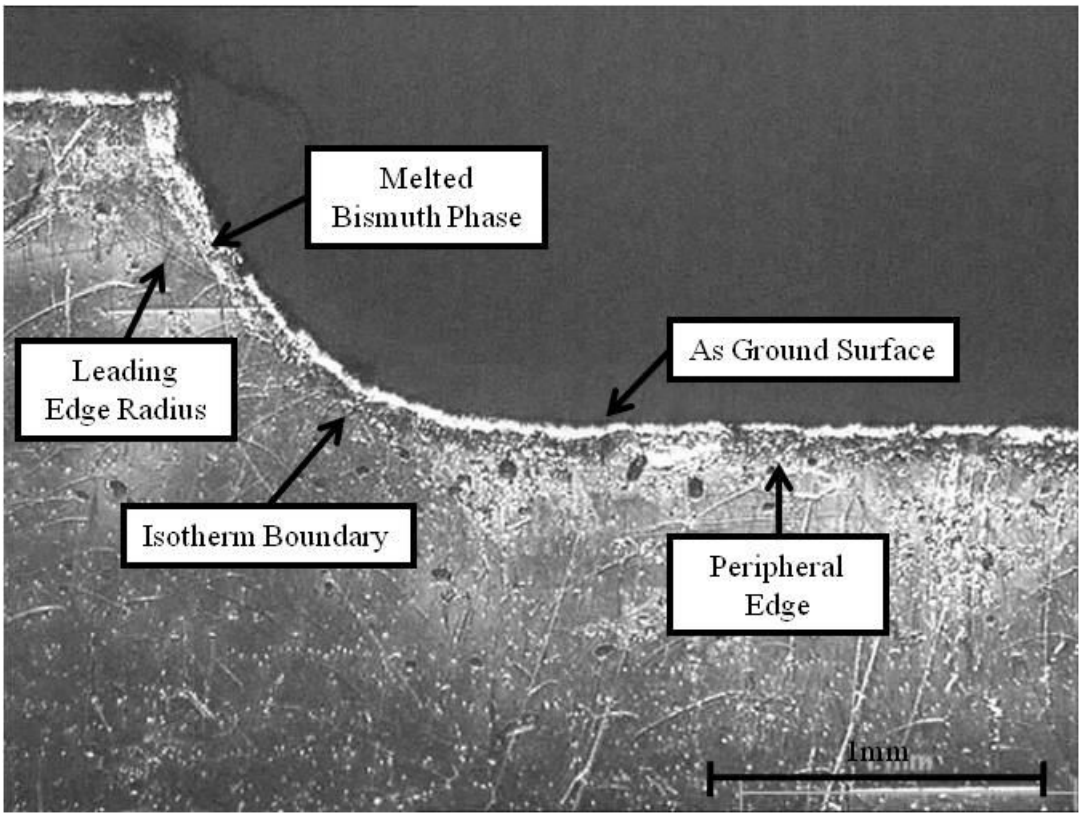

Figure 5.29 Typical Bismuth isotherm taken during Superabrasive Turning process

Figure 5.30 shows a plot of relative position versus melt depth with the Bismuth isotherm for parameters summarised in table 5.4, this demonstrates a small variation between the leading edge radius and the peripheral edge. The melt depth in the leading edge radius is also higher in value than the peripheral edge unlike previous results where the trend was for an increase in the melt depth from sidewall to surface in both simple surface profile grinding and cylindrical traverse grinding.

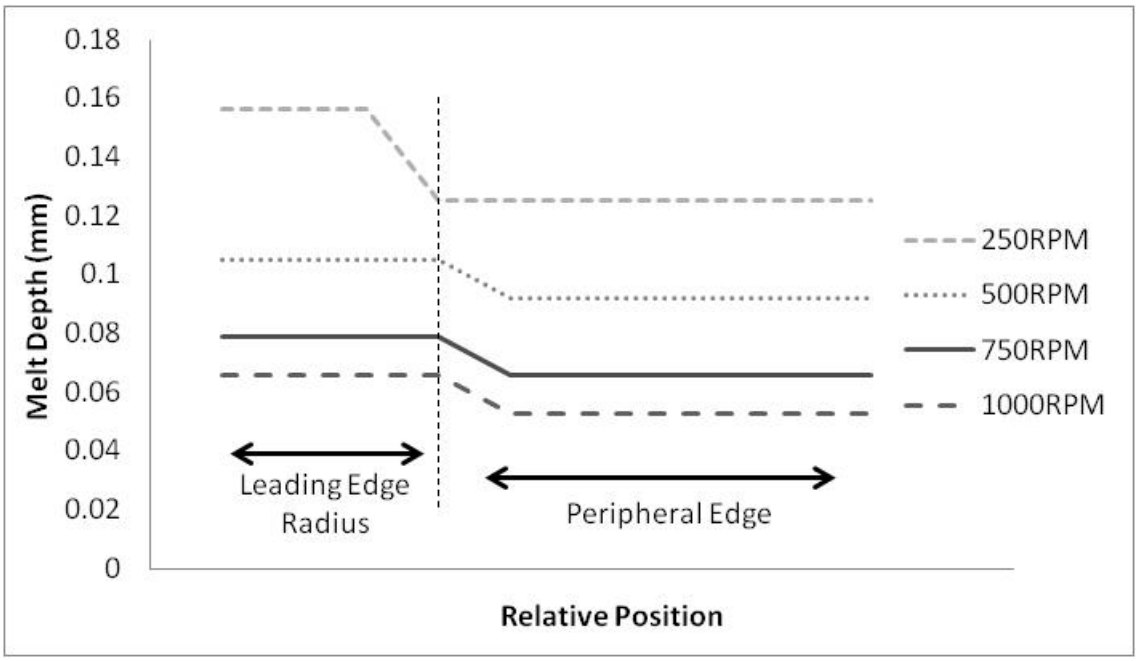

Figure 5.30 Relative position versus melt depth

Trial Number	a_e (mm)	v_t (mm/min)	v_w (RPM)	b (mm)	v_s (m/s)
1	1	50	250	0.2	150
2	1	100	500	0.2	150
3	1	150	750	0.2	150
4	1	200	1000	0.2	150

Table 5.4 Summary of grinding parameters at high values of RPM

Table 5.5 shows the maximum measured and predicted surface temperature rise (T_s) where possible for the peripheral edge contact surface for all cylindrical grinding trials undertaken. The results show a significant discrepancy in the value recorded and that predicted with the circular arc of heat contact model for trials at specific material removal rates between 70 and 300 $mm^3/mm{\cdot}s$. This is thought to result from the assumption in the circular arc of heat contact model that the whole of the heat flux, derived from the net grinding power, is passing through the axis parallel interface between the wheel and workpiece.

Q'_w ($mm^3/mm \cdot s$)	P_{tot} (kW)	P_{net} (kW)	e_c (J/mm^3)	T_s (ºC) Estimated	T_s (ºC) Measured
970	9.2	2.1	10.6	N/A	720min
1940	11.0	3.9	10.2	N/A	670min
2910	13.0	6.0	10.4	N/A	650min
3870	15.5	8.9	11.5	N/A	640min
72	19.0	11.1	15.5	870	1040
143	18.1	10.7	15.0	1080	420
287	25.8	18.3	12.8	990	460
287	17.4	10.1	14.1	990	550

Table 5.5 Comparison of measured and calculated temperatures for CTG

Section 3.3.2.3 considered the effect of high workpiece speeds with large heat fluxes on the thermal profile in the surface using the ANSYS suite of software. This was undertaken primarily to ensure that trials at high specific material removal rates were viable. The trend of the thermal profile in this principal study suggested that although heat fluxes and temperatures at the surface could be very high, the overriding effect of the high workpiece speeds was to reduce the penetration of thermal effects into the surface.

As predicted by the ANSYS software and shown in figure 5.30 above, the typical melt depth is low in spite of a high heat flux across the section. Given the heat flux is a derivative of the net grinding power and that the contact area and feed per turn remain constant, figure 5.31 shows a plot of the net grinding power versus the maximum melt depth in the peripheral edge contact surface. Whilst the net grinding power and hence heat flux to the surface continue to increase, the melt depth is shown to decrease with increasing specific material removal rate. Net grinding power was used here in favour of heat flux as the precise partitioning of heat flux to the surface was unknown.

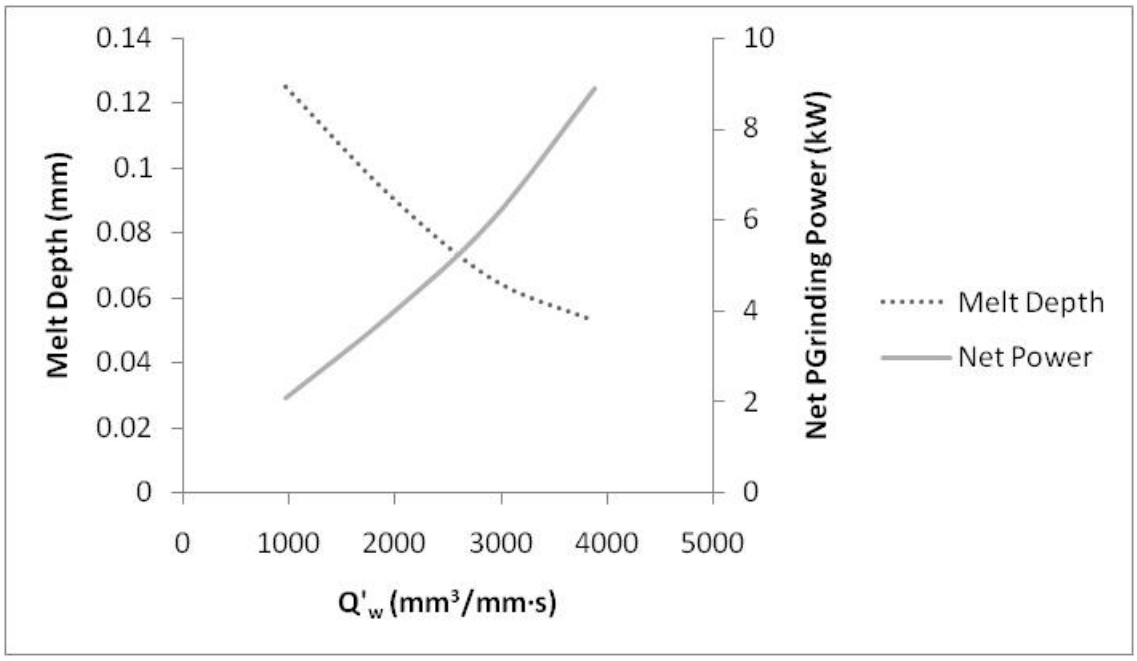

Figure 5.31 Trends in melt depth in Bismuth with net grinding power

The resulting melt depth in the surface can be thought to represent the temperature gradient in the workpiece surface, with low melt depths representing a high temperature gradient. Table 5.4 highlighted high values of minimum surface temperature measured in the peripheral edge contact surface at stock removal rates between 970 and 3870mm^3/mm·s. These temperatures would undoubtedly result in grinding burn of the workpiece surface. Figure 5.32 shows the melt depth achieved with the Indium low melting point coating as specific material removal rates increase. As high specific material removal rates are achieved, the melt depth becomes significantly reduced, with actual values approaching 100µm. Given the melting temperature of the Indium isotherm is 156ºC, the surface would be in excellent condition, with the full possibility of damaged material being removed in subsequent finishing passes.

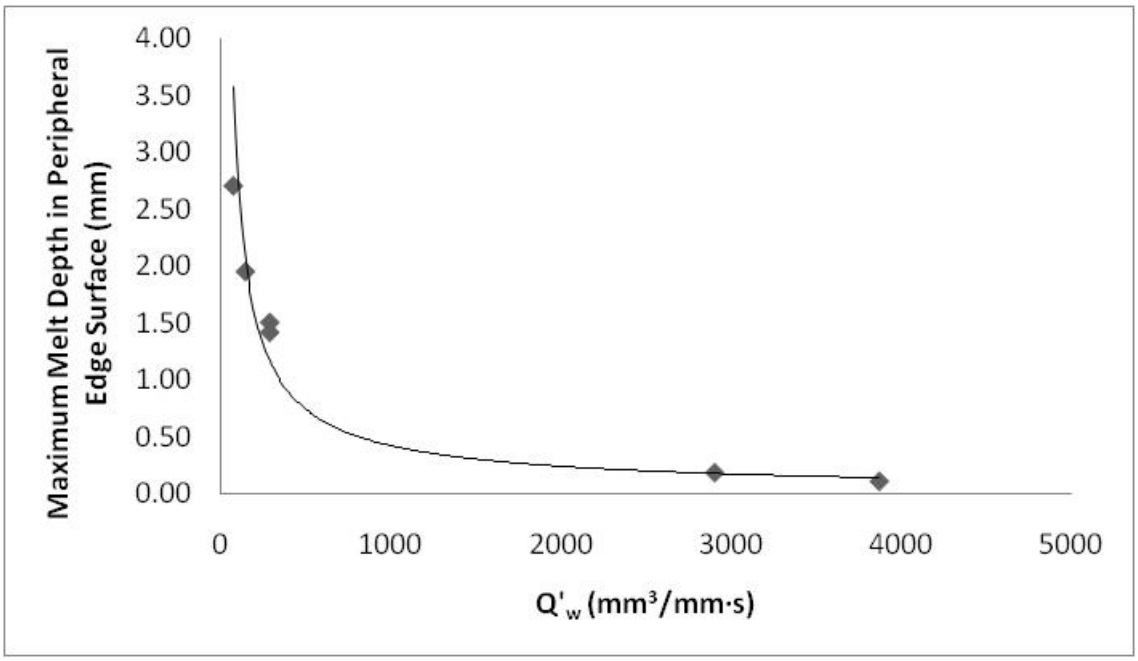

Figure 5.32 Typical melt depth in surface with Indium isotherm for CTG showing a power law relationship between specific material removal rate and melt depth

5.3 Summary

The results for surface grinding trials have shown that the effect of the change from surface to profile grinding is to increase the temperature in the peripheral face contact surface. The surface grinding trials also compared the estimated surface temperatures to those measured by the low melting point coating technique where applicable. Shown in figure 5.13 the circular arc of heat contact model does not adequately differentiate between surface and profile grinding. This is thought to be the result of the lack of knowledge of partitioning between side face, edge radius and peripheral face contact surfaces of the total grinding powers and energies.

The thermal profile responds to changes in the grinding parameters. Although requiring further investigation, the results have demonstrated that the peripheral face contact surface may be significantly affected by both the width of cut and the workpiece feedrate. The side face contact surface appears to be affected by the feedrate alone.

It is unclear what effect the coolant plays on the variation in temperature between the surface and shoulder grinding conditions. The changes in temperature can be attributed

to the addition of a shoulder and the coolant is believed to be at a sufficient temperature to have boiled out. The possibility must therefore be acknowledged that some of the effect may have resulted from the deflection of the coolant from the contact zone when grinding profiles.

The temperature at the finished surface appears to be no indicator of the depth of the thermally affected layer. Results in section 5.2 have demonstrated that whilst temperatures at the finished surface can be high, the penetration can be sufficiently low for subsequent removal of the affected layer, recalling that the HEDG process is a stock removal process and not a finishing process.

6 Discussion

Chapter 6 provides analysis of the results presented in chapters 4 and 5 of the thesis. The objective of this analysis was to demonstrate those trends and relationships which would further the understanding of the temperatures and energy partitioning in the process. The results of chapters 4 and 5 highlighted 3 key areas for further analysis, these were:

1. Application of the power law relationship considered by Stephenson & Jin (2003) to the results presented in chapter 4
2. Modelling of the threshold of grinding burn via a modification of the Malkin & Lenz (1978) model
3. The relationship of the thermal effects between the sidewall and wheel-axis parallel surface

6.1 Application of Power Law Relationships between Specific Material Removal Rate and Specific Grinding Energy

Chapter 4 of the thesis demonstrated the application of a power law approximation to graphs of specific material removal rate versus specific grinding energy after Stephenson & Jin (2003). The power relationship for the limited specific material removal rates demonstrated did not hold well for values outside the range of specific material removal rates specified. This analysis will consider all values of specific material removal rate, discussing methods of approximation for large removal rate ranges.

6.1.1 Surface Grinding

Surface grinding trials considered the machining of two materials, a spheroidal grey cast iron (SGCI) and a low alloy steel (51CrV4). Recalling results presented in section 4.1.1, figures 4.1 & 4.2 showed the relationship between specific material removal rate and specific grinding energy for SGCI and 51CrV4 and the tendency towards a constant specific grinding energy.

A constant value of specific grinding energy was present beyond specific material removal rates of approximately 50mm^3/mm·s where the minimum specific grinding energy for the process was achieved and therefore a different kind of approximation was

required. Separating results for both SGCI and 51CrV4 by a specific material removal rate of 50mm^3/mm·s and applying results for all wheel speeds a new approximation was proposed. Table 6.1 demonstrates that when constant values are present above 50mm^3/mm·s, the specific grinding energy could be equated to a simple value.

Q' range	Type	Material	Approximation
0 – 50	Power law	SGCI	A= 38 t=0.34
50 – max	Constant	SGCI	S.G.E.= 13
0 – 50	Power law	51CrV4	A=52 t=0.34
50 – max	Constant	51CrV4	S.G.E.= 16

Table 6.1 Approximation of the Specific Grinding Energy curve for surface grinding showing estimated constant values of Specific Grinding Energy

Analysis of the specific grinding energy curves suggested a constant grinding energy for SGCI of 13J/mm^3 and 16J/mm^3 for 51CrV4. Section 4.1.1 considered the specific grinding energy curves for the two materials and showed a difference in constant grinding energy with material choice. SGCI whose high carbon content results in a free cutting nature was shown to have a lower constant value of specific grinding energy than 51CrV4. Further, the power law relationship showed a similar value for the constant t, understood to be related to the chip formation process, and a variation in the value of the constant A, understood to be related to the workpiece material properties.

Section 4.1.3 highlights variation in specific grinding energy with wheel wear. Figure 4.16 showed increases in the specific grinding energy for cylindrical traverse grinding at values close to the constant specific grinding energy recorded. This supports the case for constant values of specific grinding energy being primarily driven by contact and cutting conditions rather than material property. The effect of the wheel wear moves the grit action towards ploughing and sliding and away from cutting as the contact becomes less sharp. This changes the cutting dynamic and increases the specific grinding energy required to remove material.

Constant values of specific grinding could be explained by the chip formation process theory. Shaw (1996) shows a relationship between the specific grinding energy e_c and the chip thickness t for metal cutting processes, where:

$$e_c = \frac{1}{t^n}$$

Where n is a constant between 0 and 1 dependent on the material removal regime under consideration.

If the removal rate has increased such that the abrasive grit achieves a full plunge depth on each grinding pass, then theoretically the chip thickness approaches a constant value. Thus the relationship shown in Shaw (1996) would tend to a constant value of specific grinding energy.

6.1.2 Cylindrical Traverse Grinding

Unlike surface grinding, cylindrical traverse grinding trials only considered the low alloy steel 51CrV4. A constant value of specific grinding energy was apparent for both oil and water based grinding fluids as specific material removal rates were increased. However, for cylindrical traverse grinding the change between power law and constant regions occurred at a greater value than for surface grinding. Table 6.2 demonstrates this transition occurring at a stock removal rate of approximately 175mm^3/mm·s with a constant specific grinding energy of 8J/mm^3 for water based grinding fluids and 1000mm^3/mm·s with a constant specific grinding energy of 11J/mm^3 for oil based grinding fluids. Values as low as 5J/mm^3 were recorded in initial investigations with oil based grinding fluid when wheel was very sharp.

Later results taken during the PVD coating trials, indicated a minimum specific grinding energy close to 10J/mm^3. This value is likely to be increased from earlier trials as a result of the wheel experiencing significant wear during aggressive processing.

Fluid Type	Q'_w (mm^3/mm·s)	Type	Material	Approximation
Water	0 – 175	Power law	51CrV4	A=34 t=0.28
Water	175 – max	Constant	51CrV4	S.G.E.= 8
Oil	0-1000	Power law	51CrV4	A=30 t=0.15
Oil	1000-max	Constant	51CrV4	10.7

Table 6.2 Approximation of the Specific Grinding Energy curve for cylindrical traverse grinding showing estimated constant values of Specific Grinding Energy

The apparent tendency to a constant value of grinding energy suggests that some limiting effect has been approached. Malkin (1986) suggests that this is the result of the shear energy during chip formation approaching the melting energy of the material. However melting energy for pure iron approaches 11J/mm^3, this would seem to contradict results found in this research with minimum values recorded approaching values as low as 8J/mm^3 and early tests achieving 5J/mm^3.

One possible explanation of this smaller than expected specific grinding energy is the behaviour of the abrasive grit and the interaction of sliding, ploughing and cutting or shearing energies at high removal rates. When moving towards high removal rates, the abrasive grits behave like micro cutting tools, primarily cutting or shearing material with less of the energy being consumed by ploughing and sliding. This allows a lower value of specific grinding energy than first postulated to be approached. The constant specific grinding energy is the result of the grit spacing on the surface. At high removal rates the voids between the grits can become clogged with material, reducing their ability to cut and increasing their tendency to plough and slide reducing wheel performance.

Prediction of the specific grinding energy curve from grinding parameters is not currently possible without the application of a series of trials to develop a grinding curve for the process. By undertaking preliminary trials with a conditioned wheel, the form of the curve can be established allowing the process developer to predict burn thresholds. Given the link between material properties, the chip formation process and the specific grinding energy, it is recommended that further investigation is undertaken into the development of the specific grinding energy from the chip formation process.

6.2 Model of Burn Threshold

Results in chapter 4 presented a burn threshold diagram based on the theory presented by Malkin & Lenz (1978) in which a limiting threshold temperature line was formed. The temperature of the limiting threshold for results in SGCI demonstrated in figure 4.17 of section 4.2.2 was estimated according to the model of Malkin & Lenz (1978) and assessed to be approximately 750°C. It is understood from the literature review that the onset of tensile residual stress can begin from much lower values with Chen at al. (2000) demonstrating values in EN9 between 200°C and 250°C.

The assumptions upon which this threshold model is based were discussed in the literature review and shown to be inappropriate for the assessment of the HEDG condition. Rowe & Jin (2001) amongst others demonstrated a model which, unlike Malkin & Lenz (1978), considered the effect of the wheel workpiece contact angle and also the contact layer theory presented by Tawakoli (1993) to the grinding process. These models demonstrated the possibility for a much higher quantity of energy to be distributed to the grinding chip, whilst the increasing contact angles can result in a lower than expected heat flux to the workpiece. It was therefore necessary to develop the model of burn threshold to account for this change in modelling theory.

Malkin & Lenz's (1978) modelling of the burn threshold demonstrated a relationship between the function of grinding parameters $d_e^{1/4} \cdot a_e^{-3/4} \cdot v_w^{-1/2}$ and the specific grinding energy. This relationship is derived from the model of Jaeger (1942) describing the relationship between the Peclet number and the dimensionless surface temperature for a sliding heat source. Using the model presented by Rowe & Jin (2001) the approach of Malkin & Lenz (1978) can be reconsidered to create a new model of burn threshold dependent on the easily measured and predicted parameters of speeds, feeds and specific grinding energy.

Following the equations presented by Malkin & Lenz (1978) and further in Malkin (1989), the maximum dimensionless surface temperature $\bar{\theta}_m$ is a function of the maximum surface temperature incurred, where:

$$\bar{\theta}_m = \frac{\pi \cdot k \cdot v_w}{2 \cdot \alpha \cdot \bar{q}_w} \cdot \theta_m \qquad \text{Equation 6.1}$$

Where α is the thermal diffusivity of the workpiece material and is defined by:

$$\alpha = \frac{k}{\rho \cdot c} \qquad \text{Equation 6.2}$$

The maximum surface temperature θ_m from the circular arc of heat contact model after Rowe & Jin (2001) is of the form:

$$\theta_m = C \cdot \frac{\overline{q}_w}{\beta_w} \cdot \sqrt{\frac{l_c}{v_w}} \qquad \text{Equation 6.3}$$

Where C is the temperature constant for workpiece conduction quantifying the effect of contact angle on the contact zone temperature and:

$$\beta_w = \sqrt{k \cdot \rho \cdot c} \qquad \text{Equation 6.4}$$

Equation 1 can be rearranged in terms of the maximum surface temperature such that:

$$\theta_m = \overline{\theta}_m \cdot \frac{2 \cdot \alpha \cdot \overline{q}_w}{\pi \cdot k \cdot v_w} \qquad \text{Equation 6.5}$$

Combining equations 6.3 and 6.5 to equate the maximum surface temperature equations produces the following relationship:

$$\theta_m = \overline{\theta}_m \cdot \frac{2 \cdot \alpha \cdot \overline{q}_w}{\pi \cdot k \cdot v_w} = C \cdot \frac{\overline{q}_w}{\beta_w} \cdot \sqrt{\frac{l_c}{v_w}} \qquad \text{Equation 6.6}$$

Equation 6.6 was then rearranged to give the dimensionless temperature in terms of the grinding variables and thermal properties of the workpiece, where:

$$\overline{\theta}_m = C \cdot \frac{\overline{q}_w}{\beta_w} \cdot \frac{\pi \cdot k \cdot v_w}{2 \cdot \alpha \cdot \overline{q}_w} \cdot \sqrt{\frac{l_c}{v_w}} \qquad \text{Equation 6.7}$$

Cancelling out like terms gives:

$$\overline{\theta}_m = C \cdot \frac{1}{\beta_w} \cdot \frac{\pi \cdot k \cdot v_w}{2 \cdot \alpha} \cdot \sqrt{\frac{l_c}{v_w}} \qquad \text{Equation 6.8}$$

Given that Peclet number L is defined as:

$$L = \frac{v_w \cdot l_c}{4 \cdot \alpha} \qquad \text{Equation 6.9}$$

Terms relating to thermal diffusivity α , workpiece speed v_w and contact length l_c were gathered inside the square root to give:

$$\bar{\theta}_m = C \cdot \frac{1}{\beta_w} \cdot \pi \cdot k \cdot \sqrt{\frac{l_c \cdot v_w^2}{4 \cdot \alpha^2 \cdot v_w}} \qquad \text{Equation 6.10}$$

The formula for dimensionless temperature could then be represented in terms of Peclet number L where:

$$\bar{\theta}_m = C \cdot \frac{1}{\beta_w} \cdot \pi \cdot k \cdot \sqrt{\frac{L}{\alpha}} \qquad \text{Equation 6.11}$$

Recalling equations 6.2 and 6.4 β_w was first expanded to give:

$$\bar{\theta}_m = C \cdot \frac{1}{\sqrt{k \cdot \rho \cdot c}} \cdot \pi \cdot k \cdot \sqrt{\frac{L}{\alpha}} \qquad \text{Equation 6.12}$$

Folowed by α to give:

$$\bar{\theta}_m = C \cdot \frac{1}{\sqrt{k} \cdot \sqrt{\rho} \cdot \sqrt{c}} \cdot \pi \cdot k \cdot \frac{\sqrt{L} \cdot \sqrt{\rho} \cdot \sqrt{c}}{\sqrt{k}} \qquad \text{Equation 6.13}$$

Finally equation 6.13 was reduced to give the dimensionless temperature in simplest terms corresponding to the relationship proposed by Malkin & Lenz (1978)

$$\bar{\theta}_m = C \cdot \pi \cdot L^{1/2} \qquad \text{Equation 6.14}$$

The relationship considered in equation 6.14 was compared to the graphical relationship presented by Malkin & Lenz (1978). Figure 6.1 shows the original relationship presented by Malkin compared to that newly developed in this thesis. Data points were taken from the results described in section 4.1.1 for workpiece feedrates of 2500mm/s and wheel speeds of 150m/s. It can be seen that the new model deviates from the original as a result of the inclusion of the C-factor; this deviation becomes more significant as the Peclet number is increased into the HEDG regime at values typically in excess of 40.

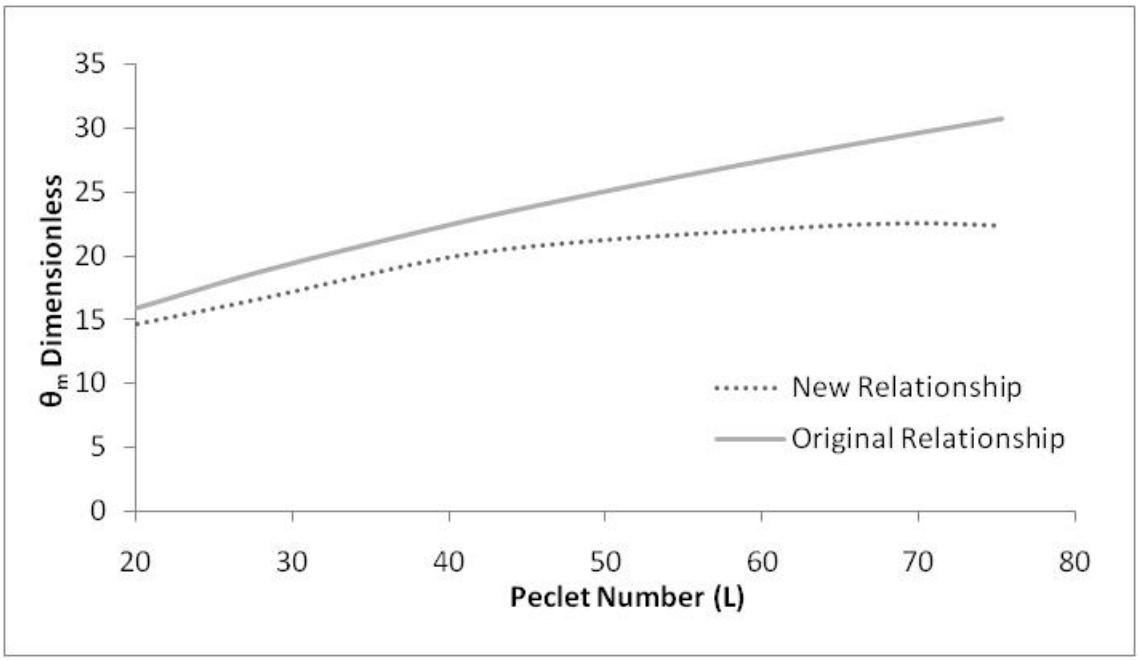

Figure 6.1 Comparison of the relationship between Peclet number and dimensionless temperature for the new relationship presented in equation 6.14 versus the original relationship considered by Malkin & Lenz (1978)

Following the methodology suggested by Malkin (1989), equations 6.1 and 6.14 were combined, such that:

$$\bar{\theta}_m = \frac{\pi \cdot k \cdot v_w}{2 \cdot \alpha \cdot \bar{q}_w} \cdot \theta_m = C \cdot \pi \cdot L^{1/2} \qquad \text{Equation 6.15}$$

This was rearranged to give the maximum contact temperature in terms of Peclet number L, where:

$$\theta_m = \frac{2 \cdot \alpha \cdot \bar{q}_w}{\pi \cdot k \cdot v_w} \cdot C \cdot \pi \cdot L^{1/2} \qquad \text{Equation 6.16}$$

$$\theta_m = \frac{2 \cdot \alpha \cdot \bar{q}_w}{k \cdot v_w} \cdot C \cdot L^{1/2} \qquad \text{Equation 6.17}$$

Expanding the Peclet number into simplest terms, gave the dimensionless temperature in terms of basic grinding parameters, where:

$$\theta_m = \frac{2 \cdot \alpha \cdot \overline{q}_w}{k \cdot v_w} \cdot C \cdot \left(\frac{v_w \cdot l_c}{4 \cdot \alpha} \right)^{1/2} \qquad \text{Equation 6.18}$$

Contact length was then expanded into simplest terms, to give:

$$l_c = (a_e \cdot d_e)^{1/2} \qquad \text{Equation 6.19}$$

And substituted such that:

$$\theta_m = \frac{2 \cdot \alpha \cdot \overline{q}_w}{k \cdot v_w} \cdot C \cdot \left(\frac{v_w \cdot a_e^{1/2} \cdot d_e^{1/2}}{4 \cdot \alpha} \right)^{1/2} \qquad \text{Equation 6.20}$$

Simplifying equation 6.20 θ_m can then be rewritten as:

$$\theta_m = \frac{C \cdot \alpha^{1/2} \cdot \overline{q}_w \cdot a_e^{1/4} \cdot d_e^{1/4}}{k \cdot v_w^{1/2}} \qquad \text{Equation 6.21}$$

The mean heat flux in the contact zone in the circular arc of heat contact model is described in terms of the total heat flux, where:

$$\overline{q}_w = R_w \cdot \overline{q}_t \qquad \text{Equation 6.22}$$

Where R_w is the wheel partition ratio and for purposes of this thesis is calculated using the ratio developed in equation 6.22, substituting equation 6.22 into equation 6.21 gives:

$$\theta_m = \frac{C \cdot \alpha^{1/2} \cdot R_w \cdot \overline{q}_t \cdot a_e^{1/4} \cdot d_e^{1/4}}{k \cdot v_w^{1/2}} \qquad \text{Equation 6.23}$$

The total heat flux $\overline{q}_t$ can be written in terms of the grinding parameters, where:

$$\overline{q}_t = e_c \cdot a_e \cdot \frac{v_w}{l_c} \qquad \text{Equation 6.24}$$

And recalling, that:

$$l_c = (a_e \cdot d_e)^{1/2}$$

substituting equation 6.24 into equation 6.23 gives:

$$\theta_m = \frac{C \cdot \alpha^{1/2} \cdot R_w \cdot v_w^{1/2} \cdot a_e^{3/4} \cdot e_c}{k \cdot d_e^{1/4}} \qquad \text{Equation 6.25}$$

Grinding burn takes place in the finished workpiece surface. The above gives details of equations leading to the maximum contact temperature, which is appropriate if assuming all energy in the contact surface is transferred to the workpiece. The circular arc of heat contact model assumes that there is a factor relating contact and finished surface temperatures, which accounts for the angle of inclination of the contact surface. Therefore the maximum surface temperature can be described as:

$$\theta_{ms} = \frac{{}^{fi}/_{co} \cdot C \cdot \alpha^{1/2} \cdot R_w \cdot v_w^{1/2} \cdot a_e^{3/4} \cdot e_c}{k \cdot d_e^{1/4}} \qquad \text{Equation 6.26}$$

Equation 6.26 was rearranged to give temperature changes in terms of specific grinding energy, where:

$$e_c = \frac{\theta_{ms} \cdot k}{A \cdot \alpha^{1/2}} \cdot d_e^{1/4} \cdot v_f^{-1/2} \cdot a_e^{-3/4} \qquad \text{Equation 6.27}$$

Where A is a dimensionless variable relating to contact and material condition and is equal to:

$$A = {}^{fi}/_{co} \cdot C \cdot R_w \qquad \text{Equation 6.28}$$

Values of C and ${}^{fi}/_{co}$ were calculated using a Matlab model for prediction of their values from the contact angle and Peclet number.

Recalling results for the comparison of Peclet number versus dimensionless temperature (figures 4.17 & 4.18 of section 4.1.1), a deviation from the linear relationship proposed by Malkin & Lenz (1978) occurs. The onset of deviation was determined by the workpiece speed as may be expected given the contact layer theory presented by Tawakoli (1993). However, the revised burn threshold diagram developed considers results by common wheel speed as this value is not accounted for in the relationship.

Figure 6.2 applies the new approach to results for SGCI summarised in Table 6.3 and demonstrates the variation between the two burn threshold processes for a limiting temperature rise of 150°C. A fundamental change in the threshold condition is experienced at the very high removal rates represented at the far left of the x-axis. This

form is the result of the energy partitioning theory associated with the HEDG regime, as specific material removal rates increase into HEDG conditions the temperature in the finished surface is reduced by a process of increasing heat flux to the chip and the favourable contact angle.

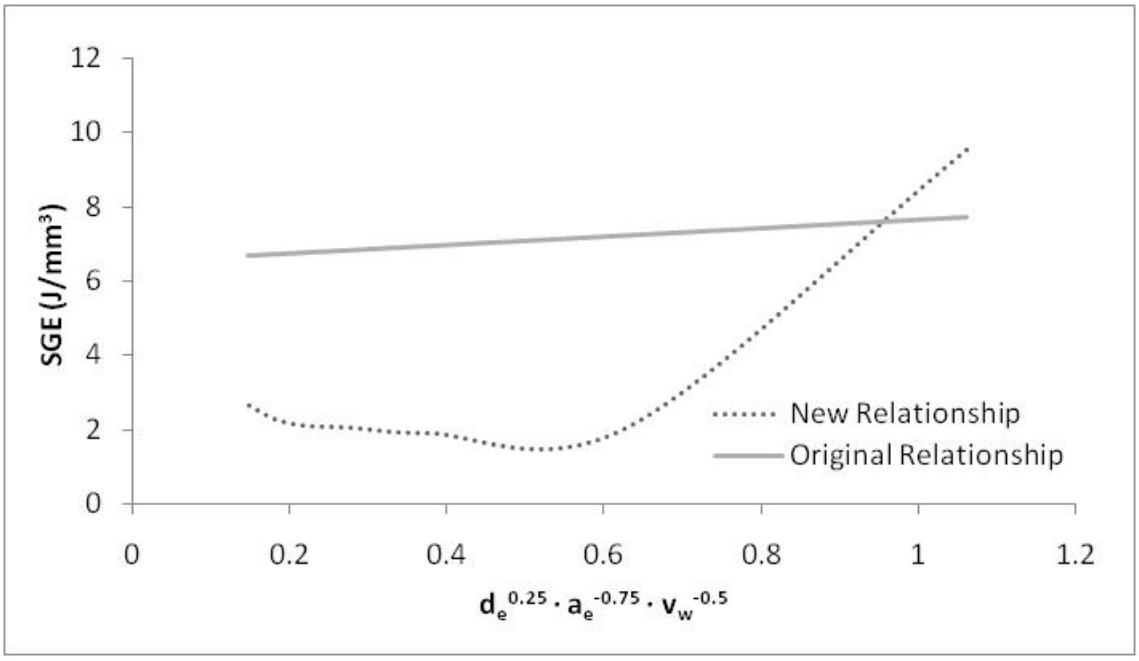

Figure 6.2 Limiting threshold curves for a temperature rise of 150ºC, comparing the original Malkin model to the model described in equation 6.27

Material	a_e (mm)	b (mm)	v_w (mm/s)	v_s (m/s)	Q'_w (mm^3/mm·s)
SGCI	0.5 – 7	5	2500	150	20 – 300

Table 6.3 Grinding parameters for plot of $d_e^{1/4} \cdot a_e^{-3/4} \cdot v_w^{-1/2}$ versus Specific Grinding Energy

Application of the new burn threshold methodology to results for the grinding of SGCI, revealed an excellent approximation of the burn threshold for a threshold temperature of 150°C. Figures 6.3 to 6.5 describe the burn threshold curve for values of grinding parameters at wheel speeds of 50ms/, 100m/s and 150 m/s for the parameters summarised in table 6.4. This demonstrates the curve separating the regions of burnt and unburnt samples offers an improved approximation at an appropriate temperature over the original straight line presented by Malkin & Lenz (1978).

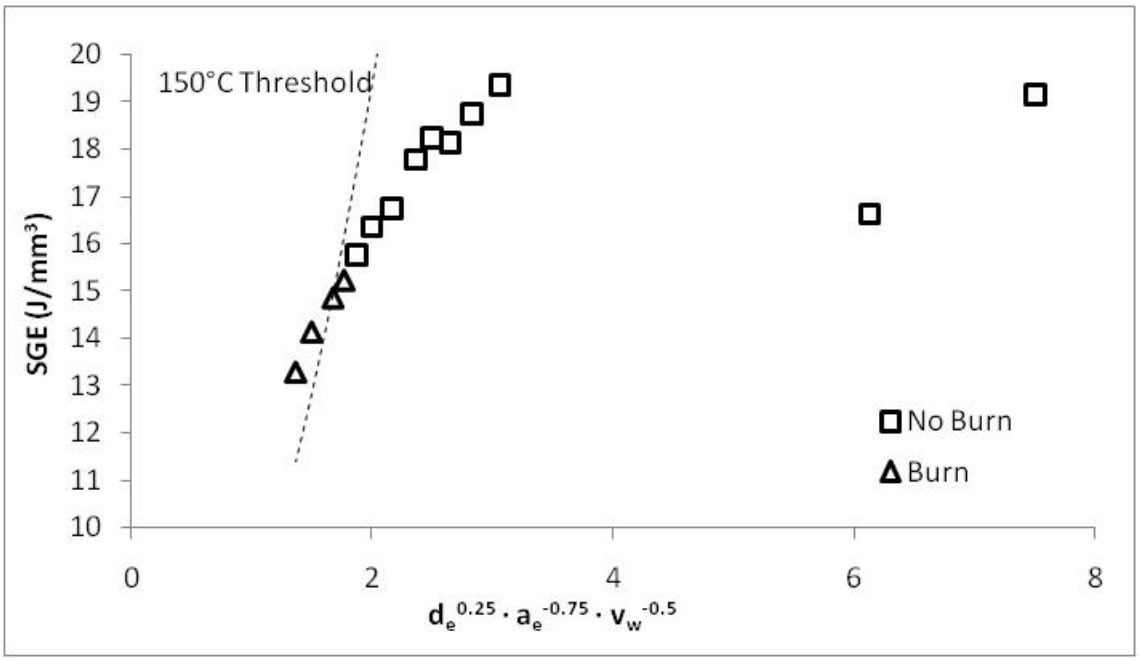

Figure 6.3 Burn threshold diagram demonstrating a limiting threshold for a temperature rise of 150ºC for wheel speeds of 50m/s

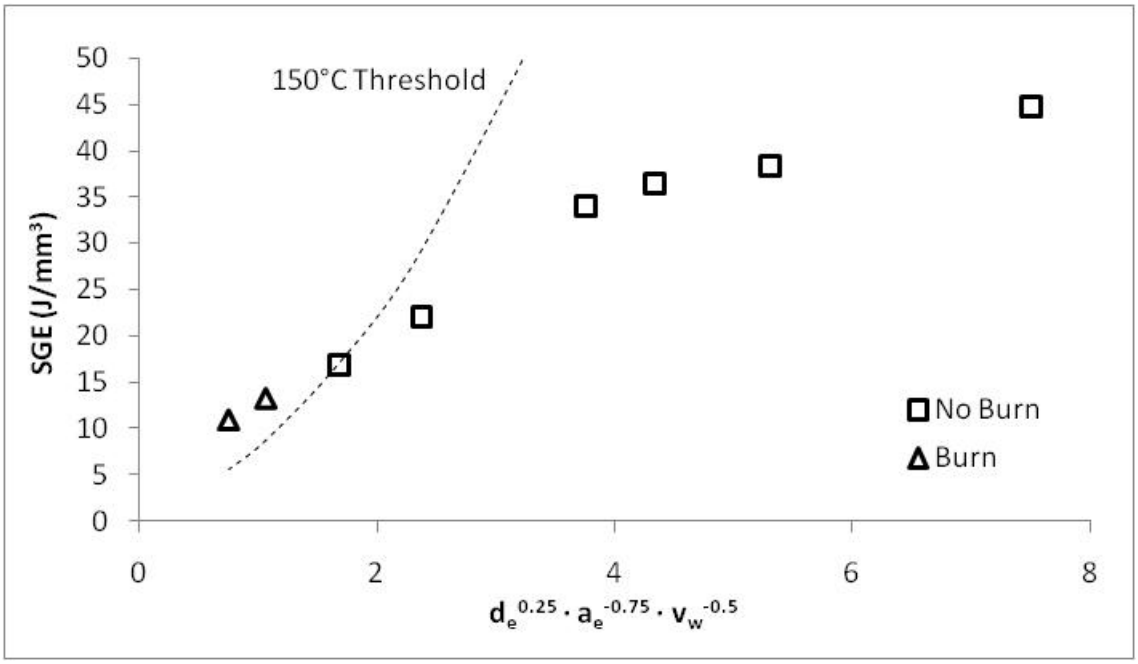

Figure 6.4 Burn threshold diagram demonstrating a limiting threshold for a temperature rise of 150ºC for wheel speeds of 100m/s

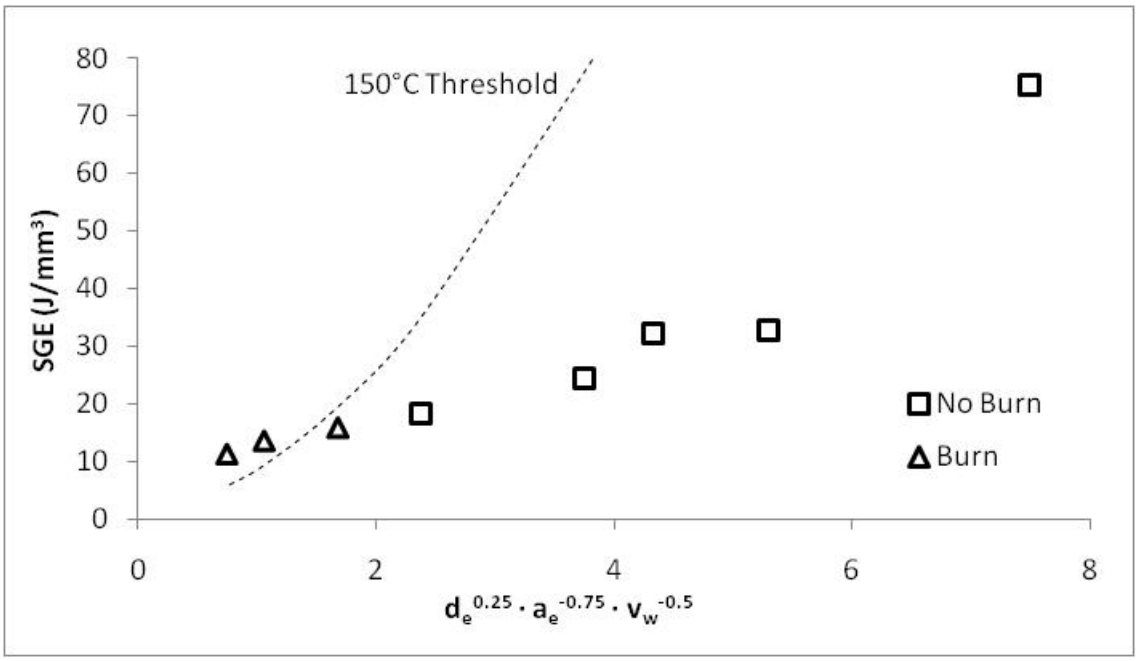

Figure 6.5 Burn threshold diagram demonstrating a limiting threshold for a temperature rise of 150ºC for wheel speeds of 150m/s

a_e (mm)	b (mm)	v_w (mm/min)	v_s (m/s)
0.5 – 9	5 – 2	0.83 – 125	50 – 150

Table 6.4 Summary of grinding parameters for burn threshold diagram trials

6.3 Temperature Ratios

Two analyses were undertaken relating to the low melting point coating results. These were designed to explore the feasibility of a common rule set for prediction of temperatures in the profile grinding process. This was initiated with an analysis of the melt depth in the sidewall and surface, considering how changes in one affect the other. The relative heat flux to the regions of the profile will also be considered, calculated from the temperatures recorded with the low melting point coatings.

6.3.1 Melt Depth Ratios

Variation in the melt depth between the vertical and horizontal surfaces of the grinding regimes considered in chapter 5 appeared to show a regular change in the melt depths with increasing specific material removal rates. The ratio of the maximum melt depth in the vertical surface to the horizontal was compared to selected grinding parameters in an

effort to clarify this relatioship. Table 6.5 summarises the grinding parameters considered.

	Material	a_e (mm)	b (mm)	v_w (mm/s)	v_s (m/s)	Q'_w (mm^3/mm·s)
Surface	51CrV4	2 – 4	1 – 3	75 – 125	200	150 – 500
Cylindrical	51CrV4	1 – 3	0.2 – 10	20 – 3900	196	70 – 3900

Table 6.5 Grinding parameters used in analysis of melt depth ratios

Results for surface grinding are shown in figure 6.6, demonstrating a plot of the ratio of width of cut to depth of cut versus the ratio of the maximum melt depth in the vertical surface to the maximum melt depth in the horizontal surface. This suggested that as the width of cut was reduced in comparison to the depth of cut, the ratio of melt depths followed a power law relationship. As such the possibility exists of predicting the partitioning of the temperatures from the grinding parameters. Furthermore if the temperature in one surface is known, the temperature in the second can be predicted.

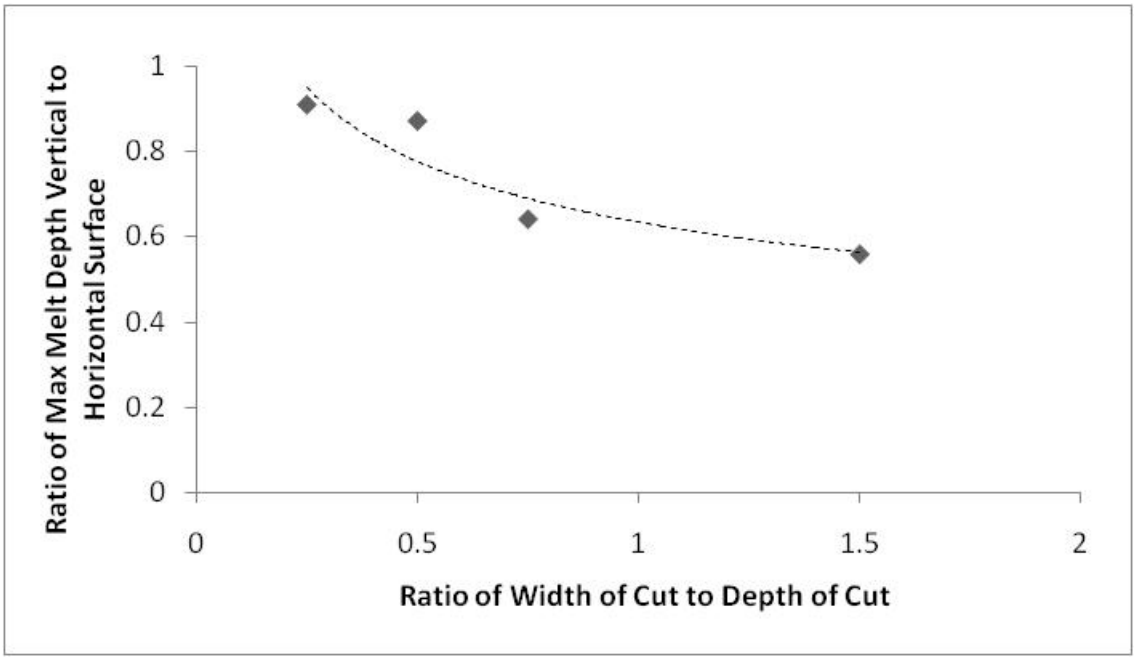

Figure 6.6 The ratio of width of cut to depth of cut versus the ratio of the maximum melt depth in the vertical surface to the maximum melt depth in the horizontal surface for surface grinding

Repeating the same analysis for the cylindrical traverse grinding results shown in figure 6.7, demonstrated a similar relationship to that shown in surface grinding. Again as

width of cut was reduced in relation to the depth of cut, the ratio of maximum melt depth in the vertical surface to the horizontal followed a power law relationship.

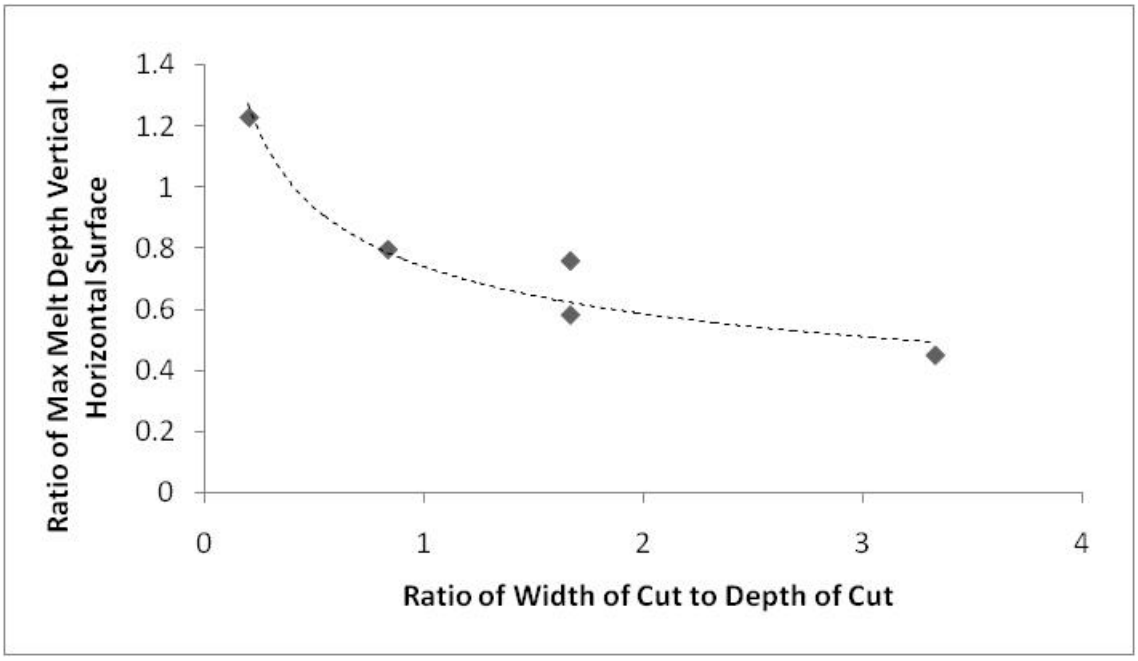

Figure 6.7 The ratio of width of cut to depth of cut versus the ratio of the maximum melt depth in the vertical surface to the maximum melt depth in the horizontal surface for cylindrical traverse grinding

Overlaying results for surface and cylindrical traverse grinding, figure 6.8 suggests that there is a relationship between the two ratios, independent of the grinding regime under consideration.

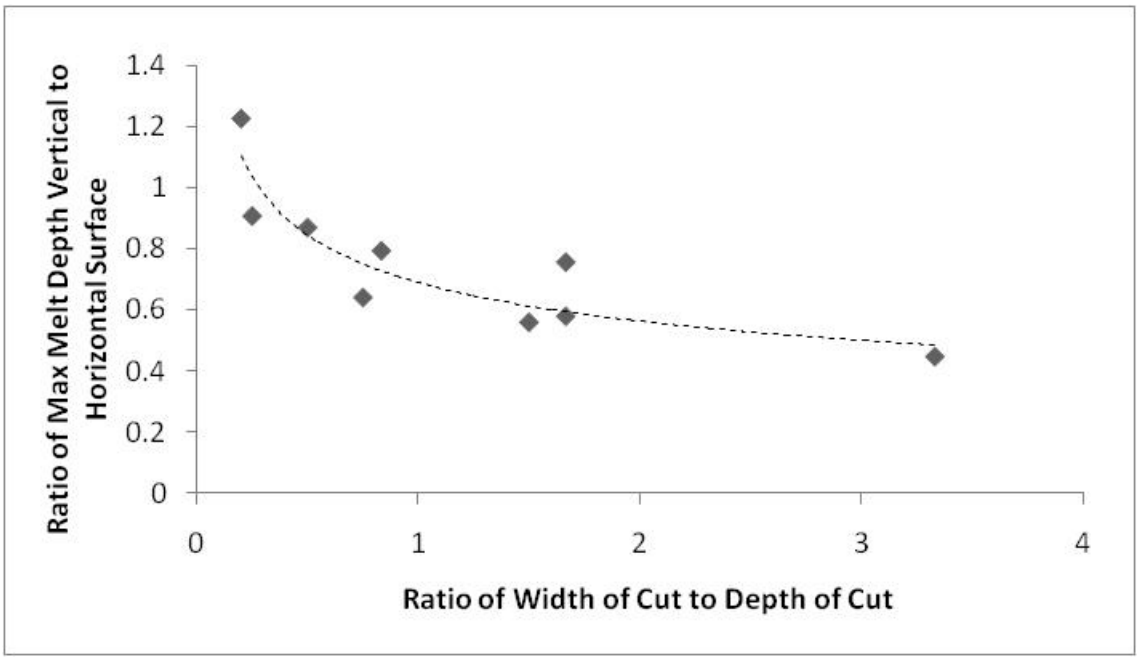

Figure 6.8 The ratio of width of cut to depth of cut versus the ratio of the maximum melt depth in the vertical surface to the maximum melt depth in the horizontal surface for all regimes

The power law approximation applied to the results in figures 6.6 to 6.8 follows the relationship:

$$y = M \cdot x^{-n}$$

Where M and n are constants as described in table 6.6. It can be seen that values of M and n fall within a similar range.

Figure Number	M	n
Figure 6.6	0.63	0.29
Figure 6.7	0.74	0.34
Figure 6.8	0.69	0.29

Table 6.6 Values of the constants M and n for the relationship between melt depth and grinding parameter ratios shown in figures 6.6 to 6.8

Recalling the discussion of cylindrical traverse grinding (section 2.1.5), Nakayama et al. (2004) suggested that a small width of cut at high work speeds presented an optimum solution for the process. The very small widths of cut demonstrated here suggest that the temperature in the leading edge and leading edge radius will be greater than the peripheral face. However depths of penetration are low and the expectation of the small

increase in leading edge and leading edge radius temperature can be easily predicted and hence controlled.

6.3.2 Energy Partitioning in Surface & Cylindrical Traverse Grinding

Results for temperature measurement with low melting point coatings suggested a significant surface temperature rise in the grinding profile. Hence contact temperatures and the heat flux to develop these could also be assumed to be large. However the variation in contact conditions between surface, corner and sidewall indicates that the heat flux may not be consistent over all surfaces. For example the contact angle varies from 0° in the sidewall to an inclined angle in the axis parallel surface dependent on the wheel radius and depth of cut.

The low melting point coatings also suggested that the change in heat flux with contact region was similar for trials in the same grinding regime. Given that contact areas change consistently with changes in grinding parameters, partitioning of the heat flux by percentage of contact area was considered. Figure 6.9 shows the areas in the wheel-workpiece interface for surface grinding, with nomenclature presented in figure 6.10. Areas represented may be calculated using the equations described in equations 6.29 to 6.31.

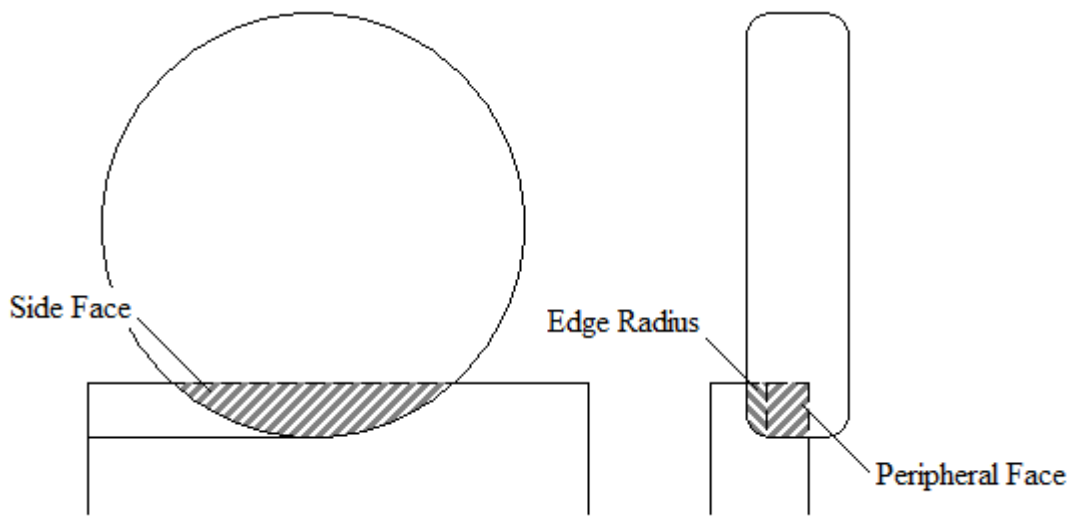

Figure 6.9 Areas of contact in surface grinding

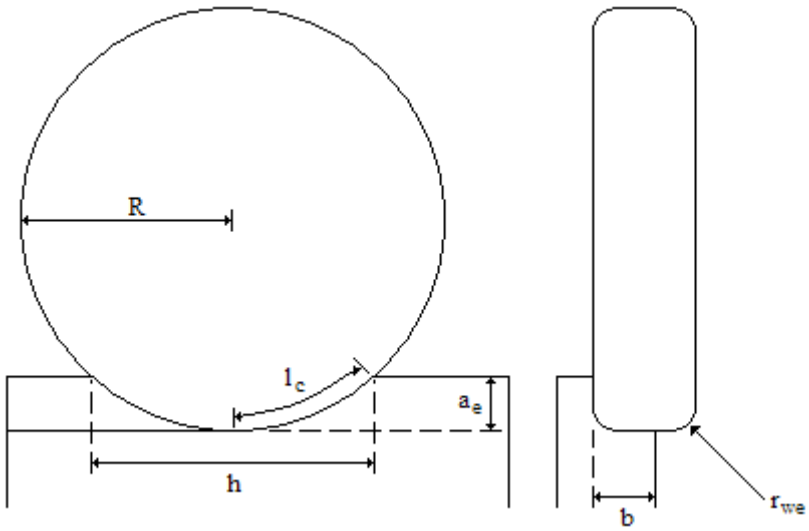

Figure 6.10 Nomenclature for surface grinding contact area calculations

$$A_{sidewall} = \frac{a_e - r_{we}}{6 \cdot h} \cdot \left[\left(3 \cdot \left(a_e - r_{we}\right)\right)^2 + \left(4h\right)^2 \right] \qquad \text{Equation 6.29}$$

$$A_{corner} = \bar{l}_c \cdot \pi \cdot \frac{r_{we}}{4} \qquad \text{Equation 6.30}$$

$$A_{surf} = l_c \cdot \left(b - r_{we}\right) \qquad \text{Equation 6.31}$$

Figures 6.11 and 6.12 and equations 6.32 to 6.34 show the methodology for calculating the contact areas in the profile in cylindrical traverse grinding. This is differentiated from the surface grinding process as a result of the geometric interaction between two cylinders, which forms an intersection of two arcs.

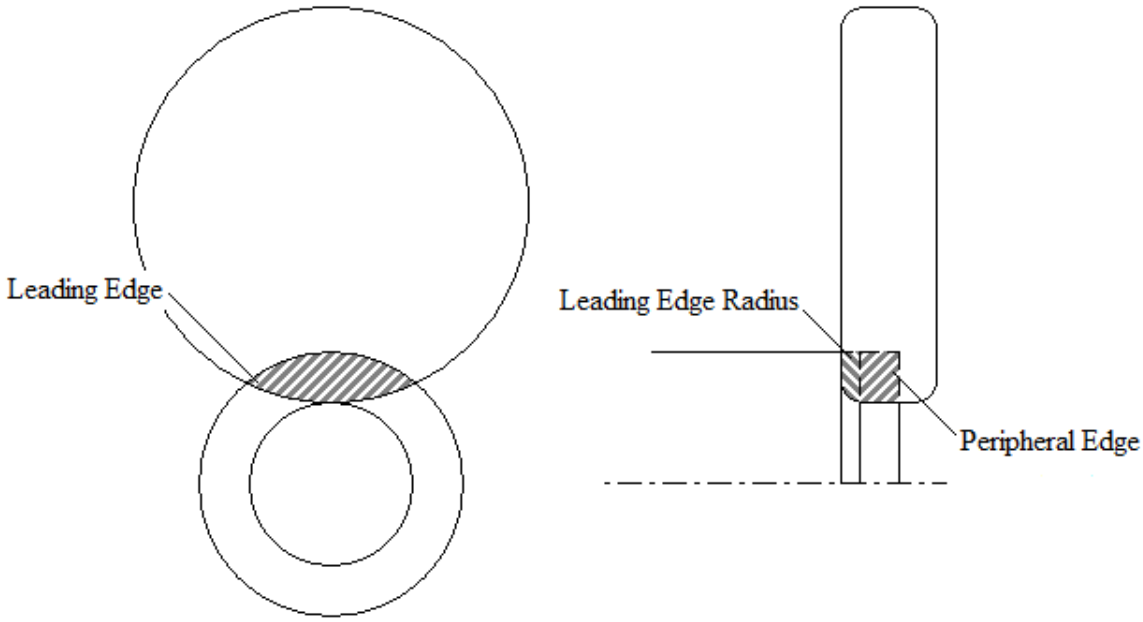

Figure 6.11 Areas of contact in cylindrical traverse grinding

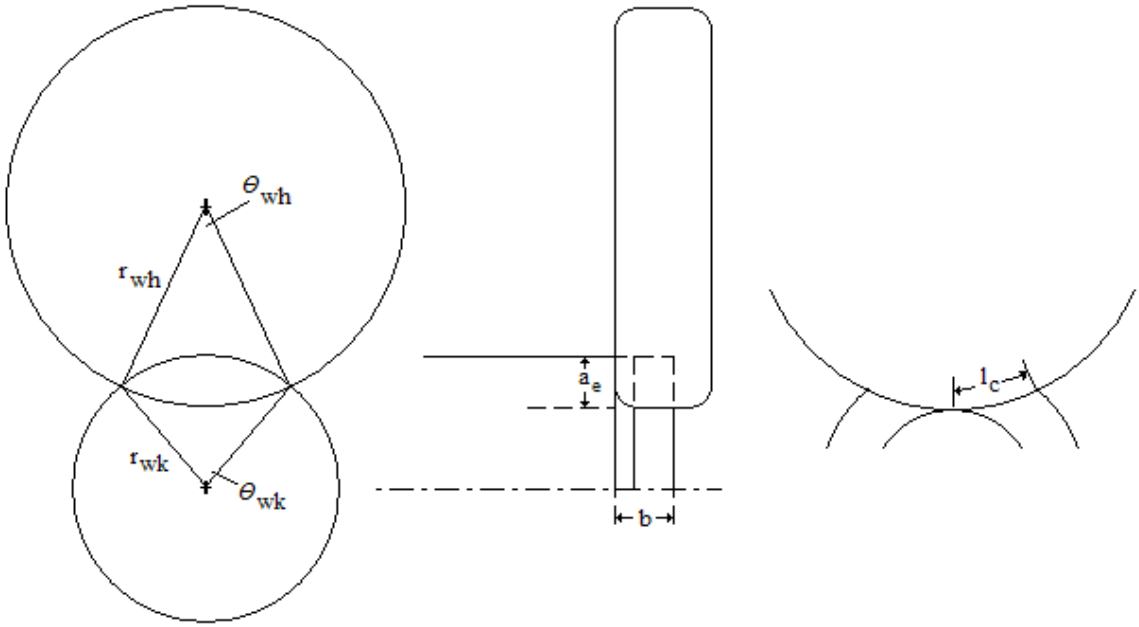

Figure 6.12 Nomenclature for cylindrical traverse grinding contact area calculation

$$A_{sidewall} = \left[\frac{r_{wk}^2}{2}\cdot\left(\theta_{wk} - \sin\theta_{wk}\right)\right] + \left[\frac{r_{wh}^2}{2}\cdot\left(\theta_{wh} - \sin\theta_{wh}\right)\right] \qquad \text{Equation 6.32}$$

$$A_{surf} = r_{wh}\cdot\frac{\theta_{wh}}{2}\cdot\left(b - r_{we}\right) \qquad \text{Equation 6.33}$$

$$A_{corner} = \pi\cdot\left(\frac{2\cdot r_{wh}}{4}\right)\cdot l_c \qquad \text{Equation 6.34}$$

Figure 6.13 shows the area by percentage in the sidewall, corner and surface of the wheel-workpiece contact zone for surface grinding. The results suggest the edge radius has the lowest percentage of heat partitioning, this does not agree with temperature measurement results shown in chapter 5. These demonstrate that the highest melt depth and hence temperature was in the peripheral face, followed by the edge radius and then the side face. Therefore it would be unlikely that the highest heat flux would be to the side face, in spite of having the largest contact area. For this reason, no further discussion was undertakne regarding cylindrical traverse grinding and its relationship to contact areas.

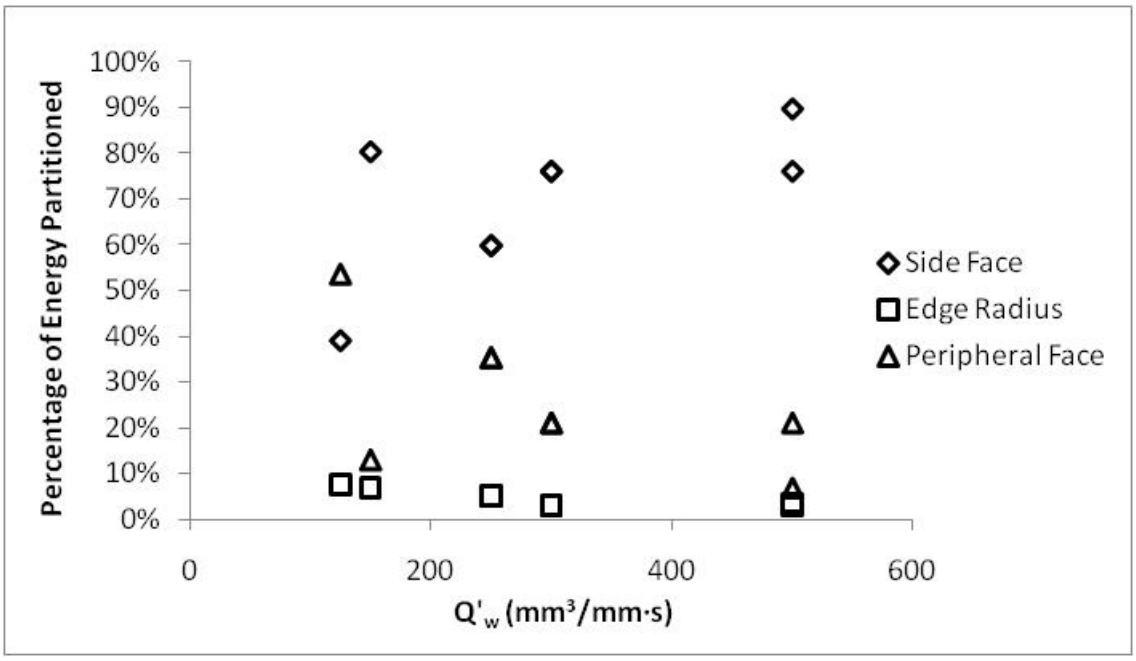

Figure 6.13 Percentage of energy partitioned to the contact surfaces of the workpiece as calculated from contact areas in the workpiece for surface grinding

In order to estimate the heat flux to the workpiece in the various contact regions, the measured temperature was used with the equations presented by Rowe & Jin (2001) to estimate the relative heat flux. Table 6.7 presents the grinding parameters used.

Trial Number.	a_e (mm)	b (mm)	v_w (mm/s)	v_s (m/s)	Q'_w (mm^3/mm·s)
S1	1	3	125	200	125
S2	2	3	125	200	250
S3	4	3	125	200	500
S4	4	3	75	200	300
S5	2	1	75	200	150
S6	4	1	125	200	500
S7	2	3	125	200	250
S8	4	3	75	200	300

Table 6.7 Grinding parameters selected for analysis of relative heat flux to the surface for surface grinding

Heat flux to the workpiece q_w is estimated from the maximum contact temperature rise T_{max} using equation 6.35, where:

$$q_w = h_w \cdot T_{\max} \qquad \text{Equation 6.35}$$

Given h_w can be calculated using equation 6.36, where:

$$h_w = \frac{\beta_w}{C} \cdot \sqrt{\frac{v_f}{l_c}} \qquad \text{Equation 6.36}$$

In the surface, the contact length can be considered consistent across the width of cut, however the sidewall and corner have a variable contact length. The contact length l_c was estimated geometrically using the knowledge of the peak temperature regions from the isotherms recorded in chapter 5. For the edge radius and the side face, the peak of the isotherm was the point closest to the surface.

Table 6.8 shows results for the heat flux to the workpiece for the surface grinding trials. Where temperatures could not be measured accurately estimations of the minimum temperature achieved were used. This was acceptable as the minimum temperature

predicted values close to the melting point of the material thought to be the limit of temperature in the workpiece, these results are marked with an asterisk. It should be noted that the total summation of heat flux to the workpiece was greater in value than that calculated from the net grinding power. This is thought to be the result of the maximum temperature points being used in the calculation of the heat flux as opposed to the average surface temperature. Further the analysis makes no account for the spread of energy from the peripheral face contact surface into the side face, given that energy is known to travel parallel to the ground surface, it is logical to assume that some heat generated in the edge radius and side face would be the result of the temperature in the peripheral face.

Trial Number	Side W/m^2	Corner W/m^2	Surface W/m^2	Total W/m^2
S1	16958000	30276000	*41145000	88379000
S2	15866000	33070000	*38102000	87038000
S3	*17902000	*38351000	*38351000	94604000
S4	14259000	*30912000	*30912000	76083000
S5	11123000	22261000	24381000	57766000
S6	17649000	35818000	*38351000	91818000
S7	12251000	33070000	*38102000	83423000
S8	12297000	*30912000	*30912000	74121000

Table 6.8 Heat flux to the relative surfaces as calculated from the surface temperature

Values for the relative heat fluxes as a percentage of the total estimated are shown in figure 6.14. The percentage of energy partitioned appears consistent by location and could therefore be considered independent of the grinding parameters used. As such, partitioning is thought to be the result of the contact and cutting conditions alone and being consistent by location on the contact surface.

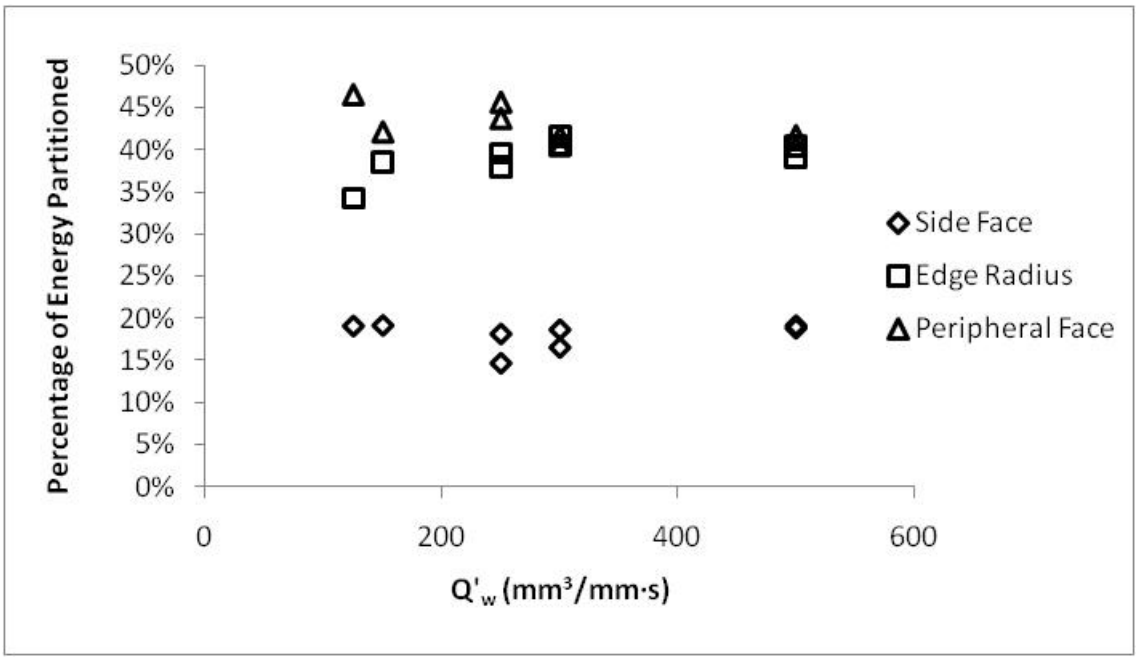

Figure 6.14 Percentage of energy partitioned to the contact surfaces of the workpiece as calculated from measured temperatures in the workpiece surface for surface grinding

Results recorded for temperatures in the surface grinding regime suggested that sufficient temperatures in the contact zone had been achieved to result in boil-out of the grinding fluid. Partitioning was therefore divided between the wheel, workpiece and grinding chip. Using the measured temperatures, the heat flux to the grinding chip and wheel were also estimated. Equation 6.37 shows the method of estimating the heat flux to the grinding chip whilst equation 6.38 shows the method of estimating the heat flux to the wheel given knowledge of the estimated heat flux to the workpiece.

$$q_{ch} = \rho \cdot c \cdot T_{mp} \cdot a \cdot {}^{v_w}\!/_{l_c} \qquad \text{Equation 6.37}$$

$$q_s = \left(\frac{q_w}{R_{ws}} \right) - q_w \qquad \text{Equation 6.38}$$

Assuming that:

$$q_t = q_w + q_s + q_{ch}$$

Figure 6.15 shows the percentage of energy partitioned to the wheel workpiece and chip for each of the regions of the profile combined. The trend was similar independent of the region under consideration. However, this assumes that the chip formation processes

are equivalent for all regions of the contact, even though contact conditions will vary dependent on relative position.

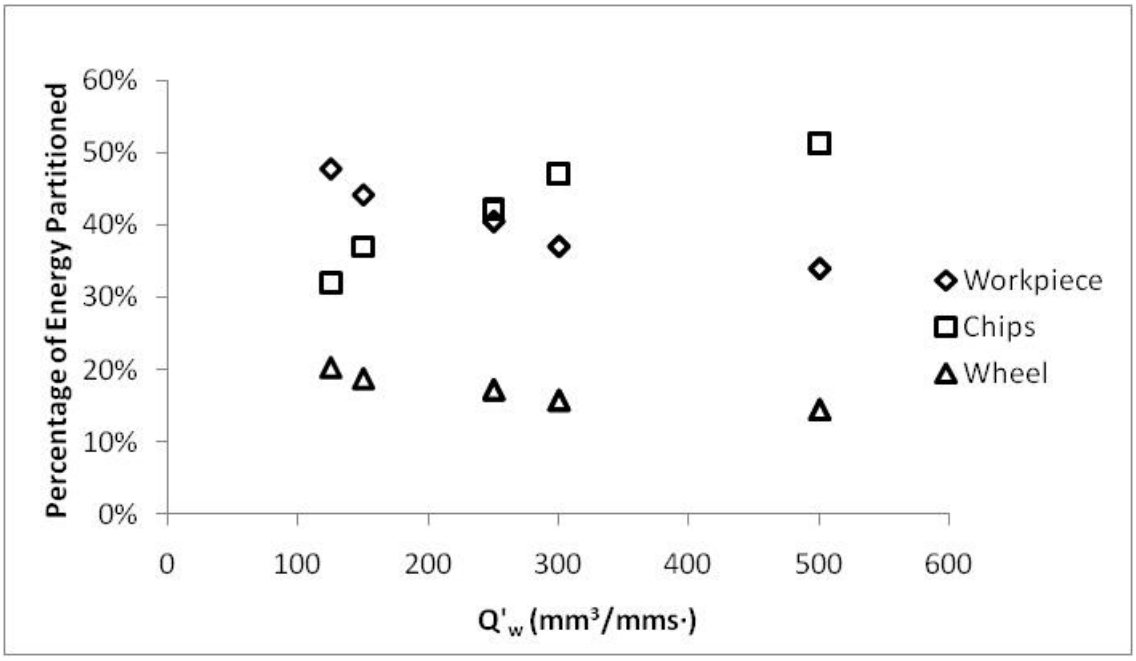

Figure 6.15 Percentage of energy partitioned to the workpiece, wheel and grinding chip as calculated from surface temperatures recorded in the workpiece surface for surface grinding

The cylindrical traverse grinding regime also generated high temperatures and hence high heat fluxes. Recalling equations 6.35 & 6.36, the energy partitioning for the profile in the cylindrical traverse grinding regime was estimated. Table 6.9 shows the experiments from which results were taken.

Trial Number	a_e (mm)	v_t (mm/min)	v_w (RPM)	b (mm)	v_s (m/s)	Q'_w (mm^3/mm·s)
C1	3	60	6	10	196	72
C2	3	60	12	5	196	143
C3	3	120	24	5	196	287
C4	3	60	24	2.5	196	287

Table 6.9 Grinding parameters selected for analysis of relative heat flux to the surface for cylindrical traverse grinding

Table 6.10 discusses the partitioning between the three regions of the contact for the results recorded. At the low values of RPM in cylindrical traverse grinding trials it was

possible to get acceptable temperature measurements for all results. Similarly to surface grinding the summation of the three regions leads to a higher value than that calculated from the net grinding power. Again this is thought to be the result of the maximum temperature points being used in the calculation of the heat flux.

Test no.	Side W/m^2	Corner W/m^2	Surface W/m^2	Total W/m^2
C1	6324000	10365000	13014000	29704000
C2	4142000	6379000	7862000	18383000
C3	7285000	11338000	13408000	32031000
C4	10014000	15870000	15681000	41565000

Table 6.10 Heat flux to the relative surfaces as calculated from the surface temperature for cylindrical traverse grinding

Figure 6.16 shows the partitioning for the three regions of the contact by percentage. Similarly to surface grinding the values appear to be relatively constant again leading to the assumption that the energy partitioned is linked to contact and cutting conditions.

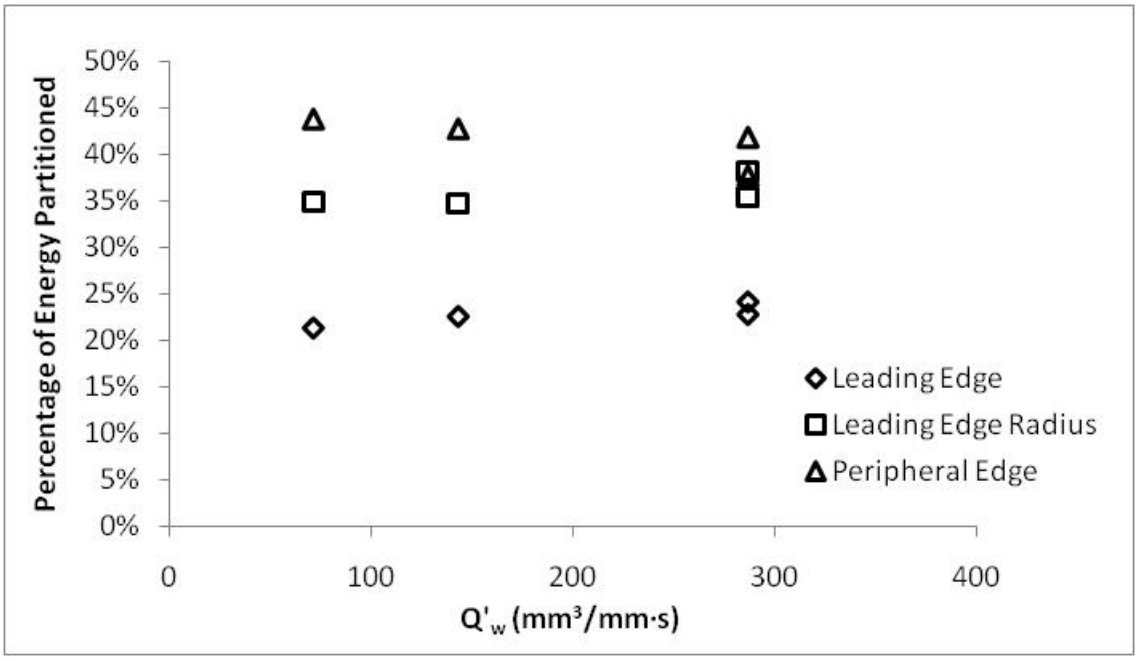

Figure 6.16 Percentage of energy partitioned to the contact surfaces of the workpiece as calculated from measured temperatures in the workpiece surface for cylindrical traverse grinding

Figure 6.17 shows Analysis of the energy partition between workpiece, chip and wheel by percentage using equations 6.37 and 6.38. It should be noted that in this case energy

partitioning to the workpiece was relatively constant, with variation in energy to the chip and wheel showing a similar trend to that for surface grinding.

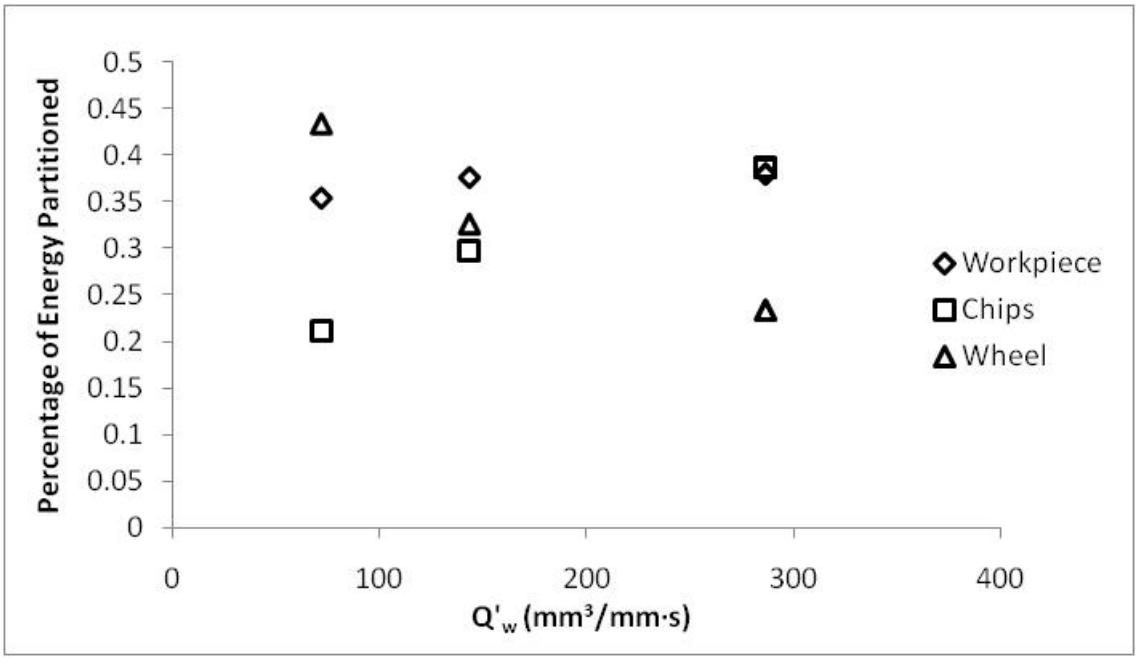

Figure 6.17 Percentage of energy partitioned to the workpiece, wheel and grinding chip as calculated from surface temperatures recorded in the workpiece surface for cylindrical traverse grinding

Section 6.3 has shown a relationship between the temperature in the sidewall and axis parallel surface of the trials undertaken. The heat flux partition calculated from the temperature measurements also shows a consistent partitioning to the three regions of the ground profile. Given knowledge of the total heat flux to the workpiece and its partitioning, hot spots can be isolated and the temperature which these achieve can be predicted. This allows the process designer to understand likely regions of damage and adjust feeds and speeds appropriately to leave sufficient material for controlled removal of damaged layers in subsequent finishing processes or to avoid parameters resulting in grinding damage.

This study of the partitioning allows for a more accurate prediction of the temperatures in the surface of the profile. Further we can now predict given knowledge of the temperature in the axis parallel surface and the grinding parameters used, what the temperature in the sidewall will be. This allows us to use the burn threshold model described in section 6.2 for the axis parallel surface and know how the sidewall behaves relative to this.

6.4 Summary

The results discussed in section 6.1.2 and 6.1.3 suggest a constant value of specific grinding energy at high removal rates. It can be seen that this minimum value is not related to the melting energy described by Malkin (1986) and is often significantly lower. Further, there is a disparity between the constant values of specific grinding energy between surface and cylindrical traverse grinding when the same material is ground. For this reason it is believed that the constant specific grinding energy witnessed is driven by the contact and cutting conditions in the surface.

Limiting temperature thresholds in the burn threshold diagram have been modified to incorporate the effect of the contact angle and the energy partitioning consistent with the HEDG regime. The result is a threshold line whose temperature fits with the results set witnessed in experimentation. However, the technique is limited to a single wheel speed and threshold lines would need recalculating whenever a change in wheel speed was undertaken.

Plots examining the ratio of the width of cut to the depth of cut and the effect of changes in this ratio on the melt depth in the two surfaces have shown that a thin width of cut can allow for an increased temperature in the sidewall over the surface. Further it is possible to predict the temperature in the vertical surface given knowledge of the predicted temperature in the horizontal surface and the grinding parameters at which this was achieved.

Finally, energy partitioned to the regions of the profile and the trend of the energy partitioned between wheel, workpiece and grinding chip have been presented. The lack of correlation between the geometrical areas present in both the surface and cylindrical grinding regimes suggests the source of heat to the relative surfaces is more complex than first thought. A consistency of value for the regions of the profile suggests that a predictive model can be derived from this work. It also provokes the idea that the axis parallel surface generates some proportion of the heat in the sidewall and corner radius and perhaps accounts for the disparity between results from temperature based calculations of heat flux and the calculations applied via the net grinding power.

7 Conclusions and Further Work

The study of temperatures in High Efficiency Deep Grinding has shown that for cylindrical traverse grinding very high specific material removal rates up to 4000mm^3/mm·s are achievable. In spite of heat fluxes to the workpiece surface increasing greatly, the net depth of penetration of the thermally affected zone is relatively small and indeed decreases with increasing specific material removal rate and heat flux. The result of this is a process where high temperatures in the workpiece surface are managed by a good knowledge of the depth of penetration with subsequent removal of heat affected regions during finishing operations.

- Curves of specific grinding energy have been shown to have an asymptotic form with increasing specific material removal rate. The specific grinding energy appears to reach a constant value in all examples described in the chapters 4 &5. Results presented for trials in SGCI suggested the constant value was independent of the application of grinding fluid, leading to the conclusion that the constant value is dependent on the cutting and contact conditions of the grinding process in question. Significantly, the results have shown the constant value of specific grinding energy to vary between different applications, indicating an independence of workpiece material, unlike the work presented by Malkin (1986) in which a minimum grinding energy was presented and linked to the melting energy of the workpiece material.
- The selection and positioning of coolant in the grinding process is critical to the success of those parameters considered in the thesis. The choice of coolant oil over water based fluids for cylindrical traverse grinding significantly reduces the net grinding power requirement and hence allows for a higher removal rate for the same specific grinding energy to be achieved. This allows for higher removal rates to be achieved before damage to the workpiece surface takes place.
- A new method of determining the limit of burn threshold has been proposed which corrects for the inappropriately high temperatures estimated for HEDG in previous works. This has been shown to give a good limit at a reasonable temperature for the limit of grinding burn.

- The available grinding power is significantly improved when the width of cut or feed per turn is reduced to a minimum. Chapter 4 demonstrated for cylindrical traverse grinding showing a decreasing power requirement with decreasing width of cut. Results considered a change in feed per turn from 15mm to 2.5mm, with the trend suggesting the smaller the feed per turn, the better the grinding solution. Results presented in Chapter 5 considered a feed per turn down to 200µm, which made sufficient power available to successfully approach specific material removal rates of 4000mm^3/mm·s.
- The circular arc of heat contact model was unsuitable for the very high speeds and feeds and small values of feed per turn in the cylindrical traverse grinding experiments at the higher removal rates.
- The initial study of the energy partitioning based on temperatures recorded in the workpiece surface showed the potential for an accurate prediction of the partitioning of energy between the various surfaces of the wheel-workpiece. The heat flux to the surface was estimated from the known maximum temperature. This suggested a consistent partitioning of heat flux to the three surfaces considered.
- It has been demonstrated that the temperature in the sidewall in surface grinding is higher than anticipated, yet the heat flux required to achieve this temperature is low. This is a combination of the contact conditions in the sidewall reducing the energy removed with the grinding chip and elongating the contact length and time.
- Trials in cylindrical traverse grinding at removal rates in excess of 1000mm^3/mm·s demonstrated high temperatures, yet penetration of the heat affected zone is low. As the heat flux increased with the removal rate, the speed of the heat source reduces the time available for thermal penetration and reduces this value. This results in very high removal rates and heat fluxes but with a thermally damaged layer sufficiently small to be removed with the finishing pass of the wheel.
- The relationship between the temperature in the sidewall and the surface follows a power law approximation. This approximation is valuable as a tool for

assessing the temperature in the sidewall with only limited knowledge of the surface temperature. The approximate relationship between width and depth of cut and the temperature in the axis parallel surface being used to predict the temperature in the sidewall.

These conclusions lead us to a number of preliminary recommendations for the SATURN process, these being:

- The use of cutting oils during grinding with the addition of the application of coolant to the wheel side to reduce net grinding power requirements
- A thin width of cut or feed per turn to maximise available machine power
- A very high workpiece speed to minimise temperature penetration in to the ground surface

The conclusions drawn from the thesis leave a number of avenues for potential further work. These are centred on further validation of the new relationships drawn in the burn threshold diagram and an improved understanding of the energy partitioning with a full breakdown of the temperature at multiple points on the surface. The recommendations are therefore:

- A breakdown of the temperatures at the workpiece surface with a wider selection of thermal coatings more suited to the high temperatures experienced in order to develop a full partitioning range around the profile
- Extension into more complex geometries using the temperature measurement technique for analysis of turbine blade root forms for example.
- A new analysis of the circular arc of heat contact model for very thin cuts at very high Peclet numbers
- Modelling of the specific grinding energy curve from cutting principles to allow for an improved understanding of the occurrence of the constant specific grinding energy for the parameters used.

References

Althaus (1982) Original unavailable, cited Brinksmeier et al. (1982)

Armarego, E J A & Brown, R H (1969). *The Machining of Metals*. New Jersey: Prentice Hall, Inc. p336-381.

Badger, J A & Torrance, A. (2000). Burn Awareness. *Cutting Tool Engineering*. 52 (12).

Batako, A D; Rowe, W B & Morgan, M N. (2005). Temperature measurement in high efficiency deep grinding. *International Journal of Machine Tools & Manufacture*. 45 (11), p1231-1245.

Bianchi, E C; Vargas, V L; Magagnin, T C; Monici, R D; Vicari Filho, O; de Aguiar, P R & Jannone da Silva, E. (2003). Transverse cylindrical grinding of a eutectic alloy. *Journal of the Brazilian Society of Mechanical Sciences and Engineering*. 25 (1).

Blain, P A. (1957). Influence of Residual Stress on Hardness. *Metal Progress*. 71 (1), p99-100.

Brinksmeier, E & Minke, E. (1993). High-Performance Surface Grinding - The Influence of Coolant on the Abrasive Process. *Annals of the CIRP*. 42 (1), p367-370.

Brinksmeier, E; Cammett, T J; Konig, W; Leskovar, P; Peters, J & Tonshoff, H K. (1982). Residual Stresses - Measurement and Causes in Machining Processes. *Annals of the CIRP*. 31 (2), p491-510.

Brinksmeier, E; Heinzel, C & Wittmann, M. (1999). Friction, Cooling and Lubrication in Grinding. *Annals of the CIRP*. 48 (2), p1-18.

Capello, E & Semeraro, Q. (2002). Process Parameters and Residual Stresses in Cylindrical Grinding. *Journal of Manufacturing Science and Engineering*. 124, p615-623.

Carmona Diaz, E. (2002). Influence of grinding fluids on high efficiency deep grinding of 51CrV4 high alloy steels. MSc Thesis. School of Industrial & Manufacturing Science. Cranfield University.

Chen, X; Rowe, W B & McCormack, D F. (2000). Analysis of the transitional temperature for tensile residual stress in grinding. *Journal of Materials Processing Technology*. 107, p216-221.

Comley, P. (2005) Grinding Processes and their Effects on Surface Integrity. PhD Thesis. School of Industrial & Manufacturing Science. Cranfield University.

Comley, P; Stephenson, D J & Corbett, J. (2004). High Efficiency Deep Grinding and the Effect on Surface Integrity. *Key Engineering Materials*. 257-258, p207-212.

Des Ruisseaux, N R & Zerkle, R D. (1970). Thermal Analysis of the Grinding Process. *ASME Journal of Engineering for Industry*. 92, p428-434.

Desvaux, S; Gualandri, J & Carrerot, H. (1999). Follow-Up of the Barkhausen Noise Signal on Bearings after Operation. *1st International Conference on Barkhausen Noise and Micromagnetic Testing*. Newcastle, United Kingdom. October 25th-26th, p65-77.

Ebbrell, S, Woolley, N H, Tridimas, Y D, Allanson, D R & Rowe, W B. (2000). The Effects of Cutting Fluid Application Methods on the Grinding Process. *International Journal of Machine Tools & Manufacture*. 40, p209-223.

Eliaz, N; Sheinkopf, H; Shemesh, G & Artzi, H. (2005). Cracking in cargo aircraft main landing gear truck beams due to abusive grinding following chromium plating. *Engineering Failure Analysis*. 12, p337-347.

Field, M & Kahles, J F. (1971). Review of Surface Integrity of Machined Components. *Annals of the CIRP*. 20 (2), p153-162.

Frankel, J; Abbate, A & Scholz, W. (1993). The Effect of Residual Stresses on Hardness Measurements. *Experimental Mechanics*. 33 (2), p164-168.

Ghosh, S; Chattopadhyay, A B & Paul, S. (2008). Modelling of specific energy requirement during high-efficiency deep grinding. *International Journal of Machine Tools & Manufacture*. 48, p1242-1253.

Guo, C & Malkin, S. (1992). Heat Transfer in Grinding. *Journal of Materials Processing & Manufacturing Science*. 1 (July), p16-27.

Hwang, J; Kompella, S; Chandrasekar, S & Farris, T N. (2003). Measurement of Temperature Field in Surface Grinding Using Infra-Red (IR) Imaging System. *Journal of Tribology*. 125, p377-383.

Hahn, R S. (1962). On the Nature of the Grinding Process. *Advances in Machine Tool Design and Research*. 3rd International M.T.D.R. Conference. University of Birmingham. September 1962.

Jackson, M J; Davis, C J; Hitchiner, M P & Mills, B. (2001). High-speed grinding with CBN grinding wheels - applications and future technology. *Journal of Materials Processing Technology*. 110, p78-88.

Jaeger, J C. (1942). Moving Sources of Heat and the Temperature at Sliding Contacts. *Proceedings of the Royal Society of New South Wales*. 76 ( ), p203-224.

Jin, T & Stephenson, D J. (2003). Investigation of the heat partitioning in high efficiency deep grinding. *International Journal of Machine tools & Manufacture*. 43, p1129-1134.

Jin, T & Stephenson, D J. (2004). Three Dimensional Finite Element Simulation of Transient Heat Transfer in High Efficiency Deep Grinding. *Annals of the CIRP*. 53 (1), p259-262.

Jin, T; Cai, G Q; Jeong, H D & Kim, N K. (2001). Study on heat transfer in super-high-speed grinding: energy partition to the workpiece in HEDG. *Journal of Materials Processing Technology*. 111, p261-264.

Jin, T; Stephenson, D J & Corbett, J. (2002). Burn threshold of high-carbon steel in high-efficiency deep grinding. *Proceedings of the Institution of Mechanical Engineers Part B: Journal of Engineering Manufacture*. 216, p357-364.

Jin, T; Stephenson D J & Rowe, W B. (2003). Estimation of the convection heat transfer coefficient of coolant within the grinding zone. *Proceedings of the Institution of Mechanical Engineers Part B: Journal of Engineering Manufacture*. 217, p397-407.

Johnstone, I. (2002). A Critical Study of High Efficiency Deep Grinding. PhD Thesis. School of Industrial & Manufacturing Science. Cranfield University.

Jones, P M; Tiwari, A; Roy, R & Corbett, J. (2004). Optimisation of the High Efficiency Deep Grinding Process with Fuzzy Fitness Function and Constraints. *Congress on Evolutionary Computation*. 1, p574-581.

Kato, T & Fujii, H. (1996). PVD Film Method for Measuring the Temperature Distribution in Cutting Tools. *Journal of Engineering for Industry*. 118, p117-122.

Kato, T & Fujii, H. (1997). Temperature Measurement of Workpiece in Surface Grinding by PVD Film Method. *Journal of Manufacturing Science and Engineering*. 119, p689-694.

Kato, T & Fujii, H. (2000). Temperature Measurement of Workpieces in Conventional Surface Grinding. *Journal of Manufacturing Science and Engineering*. 122, p297-303.

Kato, S; Yamaguchi, K; Watanabe, Y & Hiraiwa, Y. (1976). Measurement of Temperature Distribution Within Tool Uing Powders of Constant Melting Point. *Journal of Engineering for Industry*. p607-613.

Komanduri, R & Hou, Z B. (2001). A review of the experimental techniques for the measurement of heat and temperatures generated in some manufacturing processes and tribology. *Tribology International*. 34, p653-682.

Konig, W; Schreitmuller, H; Sperling, F; Werner, G & Younis, M. (1971). A Survey of the Present State of High Speed Grinding. *Annals of the CIRP*. Vol. 44, p275-283.

Lavine, A S & Jen T. (1991). Coupled Heat Transfer to Workpiece, Wheel and Fluid in Grinding and the Occurrence of Workpiece Burn. *International Journal of Heat and Mass Transfer*. 34 (4), p983-992.

Li, Y Y; Kim, J; Sun, Y & Yang, Y. (1999). Thermomechanical Analystical 3D Thermal/Stress Estimation Sidewall Grinding Model. *Transactions of the ASME*. 121, p378-384.

Mahdi, M & Zhang, L. (1997). Applied Mechanics in Grinding - V. Thermal Residual Stresses. *International Journal of Machine Tools & Manufacture*. 37 (5), p619-633.

Mahdi, M & Zhang, L. (1998). Applied mechanics in grinding - VI. Residual stresses and surface hardening by coupled thermo-plasticity and phase transformation. *International Journal of Machine Tools & manufacture*. 38, p1289-1304.

Mahdi, M & Zhang, L C. (1999a). Residual Stresses in Ground Components caused by Coupled Thermal and Mechanical Plastic Deformation. *Journal of Materials Processing Technology*. 95, p238-245.

Mahdi, M & Zhang, L. (1999b). Applied mechanics in grinding. Part 7: residual stresses induced by the full coupling of mechanical deformation, thermal deformation and phase transformation. *International Journal of Machine Tools & Manufacture*. 39 ( ), p1285-1298.

Malkin, S & Anderson, R B. (1974). Thermal Aspects of Grinding Part 1 - Energy Partition. *Journal of Engineering for Industry*. November, p1177-1183.

Malkin, S. (1974). Thermal Aspects of Grinding: Part 2 Surface Temperatures and Workpiece Burn. *Journal of Engineering for Industry*. 96, p484.

Malkin, S & Lenz, E. (1978). Burning Limit for Surface and Cylindrical Grinding of Steels. *Annals of the CIRP*. 27 (1), p233-236.

Malkin, S (1989). *Grinding Technology: theory and applications of machining with abrasives*. Michigan: Society of Manufacturing Engineers.

Massam, M. (2008) Private conversation on the development of grinding fluid applications.

McCormack, D F; Rowe, W B & Jin, T. (2001). MR01-236: Controlling the Surface Integrity of Ground Components. *4th International Machining & Grinding*. Troy, Michigan. May 7th-10th.

Merchant, M E. (1971). Delphi-Type Forecast of the Future of Production Engineering. *Annals of the CIRP*. Vol. 19-20, p213-225.

Mindek, R B & Howes, T D. (1996). Slot and Vertical Face Grinding of Aerospace Components. *Transactions of the ASME: Journal of Engineering for Gas Turbines and Power*. 118, p620-625.

Morgan, M N; Rowe, W B & Batako, A. (2004). Energy Limitations in HEDG and Conventional Grinding. *Key Engineering Materials*. 257-258, p63-68.

Müller, B & Renz, U. (2003). Time resolved temperature measurements in manufacturing. *Measurement*. 34, 363-370.

Nakayama, T; Wakuda, M & Ota, M. (2004). Ultra-High Speed Cylindrical Grinding Using CBN Wheel for High Efficiency. *Key Engineering Materials*. 257-258, p273-278.

Oberg, E; Jones, FD; Horton, HL & Ryffell, HH (2000). *Machinery's Handbook*. 6th ed. New York: Industrial Press Inc. p495.

Rowe, W B & Jin, T. (2001). Temperatures in High Efficiency Deep Grinding (HEDG). *Annals of the CIRP*. 50 (1), p205-208.

Rowe, W B. (2001). Thermal analysis of high efficiency deep grinding. *International Journal of Machine Tools & Manufacture*. 41, p1-19.

Rowe, W B; Morgan, M N & Black, S C E. (1998). Validation of Thermal Properties in Grinding. *Annals of the CIRP*. 47 (1), p275-279.

Sainz, P A. (2005) Investigation of High Efficiency Deep Form Grinding on 51CrV4 steel alloy. MSc Thesis. School of Industrial & Manufacturing Science. Cranfield University.

Shaw, M C (1996). *Principles of Abrasive Processing*. Oxford: Clarendon Press.

Shaw, B A; Hyde, T R & Evans, J T. (1998). Detection of Grinding Damage in Hardened Gear Steels Using Barkhausen Noise Analysis. *1st International Conference on Barkhausen Noise and Micromagnetic Testing*. Hannover, Germany. September 1st-2nd, p187-196.

Silva, F S. (2003). Analysis of a vehicle crankshaft failure. *Engineering Failure Analysis*. 10, p605-616.

Snoeys, R; Maris, M & Peters, J. (1978). Thermally induced damage in grinding. *Annals of the CIRP*. 27 (2), p571-581.

Stephenson, D J; Corbett, J; Laine, E; Johnstone, I & Baldwin, A. (2001). MR01-219 Burn Threshold Studies for Superabrasive Grinding Using Electroplated CBN Wheels. *4th International Machining & Grinding*. Troy, Michigan. May 7th-10th.

Stephenson, D J; Jin, T & Corbett, J. (2002). High Efficiency Deep Grinding of a Low Alloy Steel with Plated CBN Wheels. *Annals of the CIRP*. 51 (1), p241-244.

Stephenson, D J & Jin, T. (2003). Physical Basics in Grinding. *European Conference on Grinding*.WZL Aachen. November 6th-7th.

Takazawa (1966) Original unavailable; cited Kato & Fujii (2000)

Tawakoli, T (1993). *High Efficiency Deep Grinding*. Dusseldorf: VDI-Verlag.

Ueda, T; Hosokawa, A & Yamamoto, A. (1986). Measurement of Grinding Temperature Using Infrared Radiation Pyrometer With Optical Fiber. *Journal of Engineering for Industry*. 108, p247-251.

US Census Bureau. (2006). *Metalworking Machinery: 2005 Summary.* Available: http://www.census.gov/industry/1/mq333w055.pdf. Last accessed 03 February 2009.

Walton, I M; Stephenson, D J & Baldwin, A. (2006). The measurement of grinding temperatures at high specific material removal rates. *International Journal of Machine Tools & Manufacture*. 46 (12-13), p1617-1625.

Weck, M; Hennes, N & Schulz, A. (2001). Dynamic Behaviour of Cylindrical Traverse Grinding Processes. *Annals of the CIRP*. 50 (1), p213-216.

Werner, G & Tawakoli, T. (1988a). High-Efficiency Deep Grinding with CBN. *Industrial Diamond Review*. 3, p124-128.

Werner, G & Tawakoli, T. (1988b). Deep Grinding Narrow Slots with CBN Wheels. *Industrial Diamond Review*. 6, p285-288.

Werner, G. (1979). Application and Technical Fundamentals of Deep and Creep-Feed Grinding. *SME Technical Paper*. MR 79-319.

Wright, P K & Trent, E M. (May 1973). Metallographic Methods of Determining Temperature Gradients in Cutting Tools. *Journal of the Iron and Steel Institute*. p364-368.

Ye, N E & Pearce, T R A. (1984). A Comparison of Oil and Water as Grinding Fluids in the Creep Feed Grinding Process. *Proceedings of the Institution of Mechanical Engineers*. 198B (14), p229-237.

Zhang, L & Mahdi, M. (1995). Applied Mechanics in Grinding - IV. The Mechanism of Grinding Induced Phase Transformation. *International Journal of Machine Tools & Manufacture*. 35 (10), p1397-1409.

Appendix A

UNIVERSAL POWER CELLS

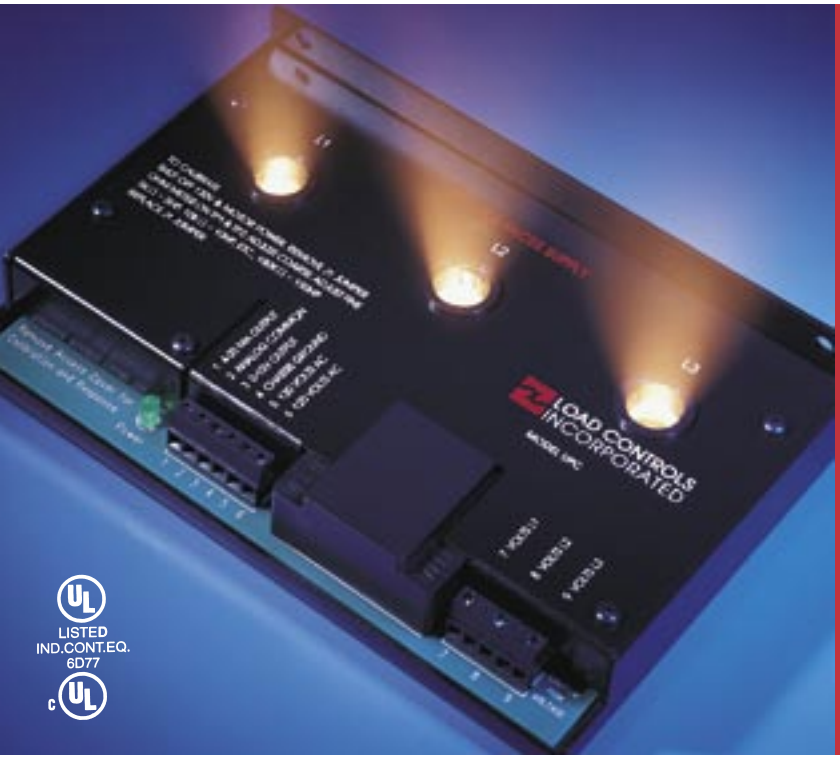

GIVES YOU VALUABLE INFORMATION ABOUT MACHINE AND PROCESS PERFORMANCE BY MONITORING MOTOR LOAD

- Mixture Viscosity
- Tool Condition
- Optimum Feed Rate
- Pump or Fan Flow
- Beginning or End Process
- Obstructions
- Overloads
- Loss of Load

THE UNIVERSAL POWER CELL SENSES TRUE MOTOR POWER— THREE PHASE, VARIABLE FREQUENCY, SINGLE PHASE OR DC

MODEL UPC

FULLY SELF CONTAINED

- Easy to install
- No Current Transformers
- No Voltage Transformers

COMPACT

- Only 1 3/4" x 5 3/8" x 8"

YOU CAN ADJUST FULL SCALE TO MATCH YOUR MOTOR

- Coarse and Fine Adjustment Pots
- 5HP to 150HP
- Take extra turns for small motors

VERSATILE

- Works on both Fixed and Variable Frequency Power
- ALSO Single Phase & DC

THREE BALANCED HALL EFFECT SENSORS

SAMPLE VOLTAGE DIRECTLY

- Up to 600 Volts

BUILT-IN POWER SUPPLY

- Powers the Analog Signals

BUILT-IN RESPONSE ADJUSTMENT

- Lets you slow the response of the Power Cell to average the readings

TWO ANALOG OUTPUTS

- 4-20 MA
- 0-10 Volts DC
- Electrically isolated

FREE 30 DAY TRIAL AVAILABLE

Model UPC $650 – Immediate Shipment

SPECIAL PURPOSE UNIVERSAL POWER CELLS

UPC-E Ethernet Universal Power Cell

EMBEDDED WEB SERVER

- View with your browser

WITH YOUR BROWSER

- Set full scale horsepower
- Set response time to average the load for a smooth signal
- Choose how often to receive data
- Or, respond to UDP or HTTP request

TCP/IP AND UDP PROTOCOL

10 BASE T 10 MEGABIT ETHERNET CONNECTION

ALSO 10 VOLT DC ANALOG OUTPUT

- Local display
- Troubleshooting

CHANGE SETTING ON THE FLY

- During a machine or process cycle
- Either UDP or HTTP
- Full scale 4HP to 125HP

UPC-KWH Energy Measuring Universal Power Cell

- Accumulates Kilowatt Hours, Kilowatt Minutes, Kilowatt Seconds
- Accumulates total power into the mixing process for consistent batches.
- Accumulates power—indicative of throughput.

Field Scaleable - 3 to 100 KW
Pulse - Dry contact
Analog Output - 0-10 Volts

The UPC-KWH measures true power (KW) and momentarily pulses a relay contact every KWH, KWM, or KWS which is selectable. The pulse can signal a computer, meter or counter for power totalizing. An analog 0-10 Volt output reflects the instantaneous power and can input a meter or computer directly.

UPC-FR Fast Response Universal Power Cell

- 0.050 Second Response Time
- Ideal for Machine Tool Monitoring
- Also used together with “V” Series Load Controls

UPC-230 230 Volt Power Supply Input

TYPICAL INSTALLATION–UPC

The Universal Power Cell is a Motor Load Sensor that monitors power (HP or KW). It works on both fixed and variable frequency power and has two analog outputs. It also works on single phase, DC, and brushless DC. The Universal Power Cell has Three Balanced Hall Effect Sensors, each with a flux concentrator. Each phase passes through a window. A voltage sample for each phase is also taken. The Hall Effect Semiconductor does a vector multiplication of the current flow and voltage which also calculates the power factor. The output is proportional to power (HP or KW).

WHY MONITOR POWER INSTEAD OF JUST AMPS?

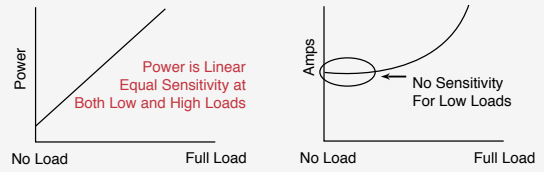

INPUT CONNECTIONS

Pass each of the phases through the L1, L2, L3 holes in the Cell. Be certain direction is correct. The Terminal side of the Cell faces the supply. Provide voltage sample for each phase. When a Variable Frequency Drive is being used, locate the Power Cell on the output side of the drive. Take the voltage samples on the output side also.

L1 Volts to Terminal 7
L2 Volts to Terminal 8
L3 Volts to Terminal 9

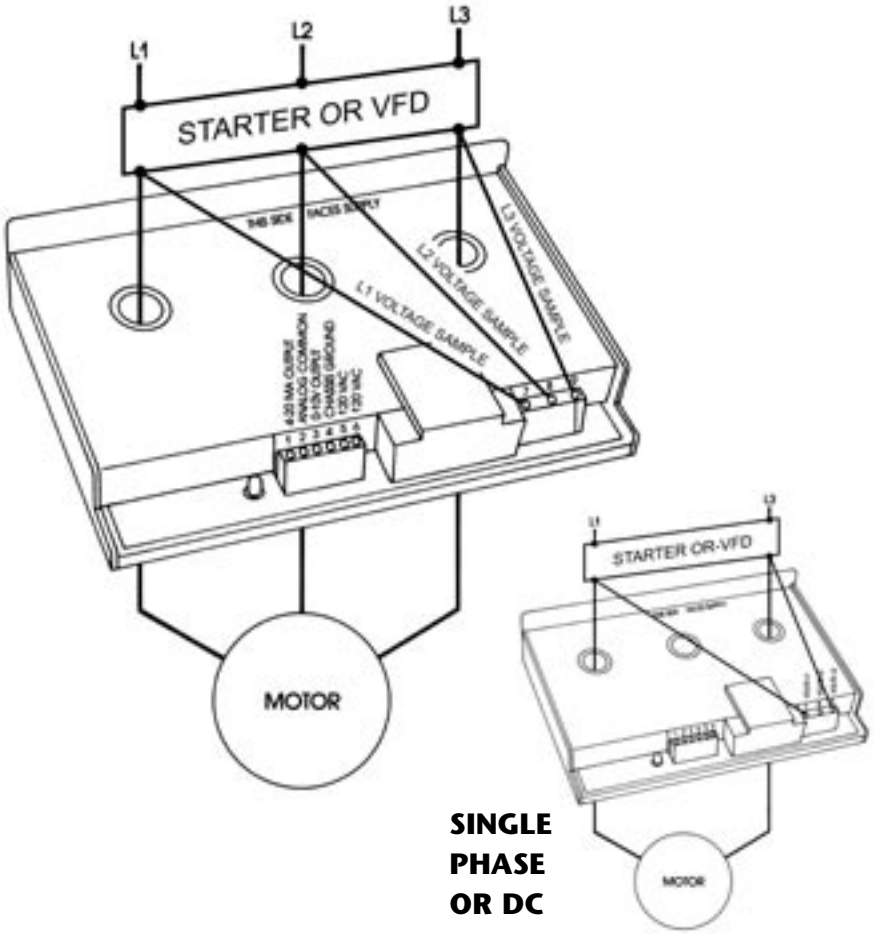

SINGLE PHASE OR DC

ANALOG OUTPUTS

The Analog Output is powered by the Power Cell.

4-20 Milliamp	Terminal 1
0-10 Volts DC	Terminal 3
Analog Common	Terminal 2

120 VOLT SUPPLY

Terminals 5 and 6

GROUND

Terminal 4

TO ADJUST FULL SCALE

The Full Scale can be adjusted to match your motor with the Coarse and Fine Pots located under the Access Cover. Put your Ohm meter on the test points.

Convenient Scaling

5K Ohm = 5HP (This is the minimum setting)
10K Ohm = 10HP
Etc.
150K Ohm = 150HP (This is the maximum setting)
(KW=HP x .746)

FOR SMALL MOTORS

Reduce the capacity by taking additional "Turns" through each hole for each phase (Mount the Power Cell on Standoffs). Example: 5HP Full Scale is reduced to 1HP with 5 Turns.

RESPONSE ADJUSTMENT

In some cases, the average power signal may be more useful than instantaneous power. The Response Adjustment slows the response of the Universal Power Cell. Pot is located under Access Cover. Clockwise is fastest.

SPECIFICATIONS

MODEL	UPC	UPC-E	UPC-KWH	UPC-FR	UPC-230
ACCURACY	.5% Full Scale	*	*	*	*
FULL SCALE CAPACITY	5HP** to 150HP	4HP** to 125HP	3 KW** to 100 KW	*	*
OUTPUTS	• 4-20 Milliamp, 500 Ohm Max Connected Impedance • 0-10 Volts DC 2000 Ohm Minimum Load	• Ethernet 10 Base T • 10 Megabit • 0-10 Volts DC	• Relay: 30 Volts, 5 Milliamp max, 50 MS duration pulse • 0-10 Volts DC	*	*
RESPONSE ADJUSTABLE	• .5 Sec. to 12 Sec.	.050 Sec. to 16 Sec.	KWH, KWM, KWS	.050 Sec to 1.2 Sec.	*
FREQUENCY	3HZ to 1KHZ	*	*	*	*
POWER CONSUMPTION	6 VA @ 120 Volts	*	*	*	3 VA @ 230 Volts

**Specifications same as UPC unless noted*

***For smaller motors take extra "turns"*

DIMENSIONS

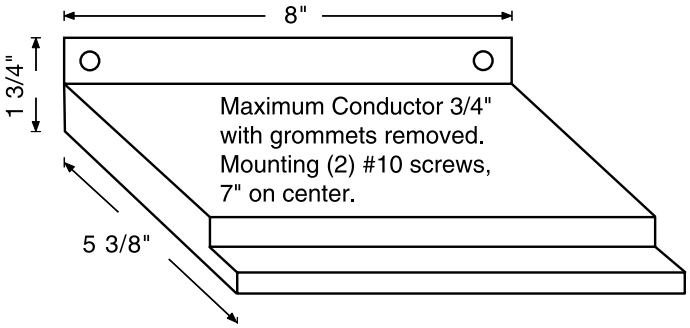

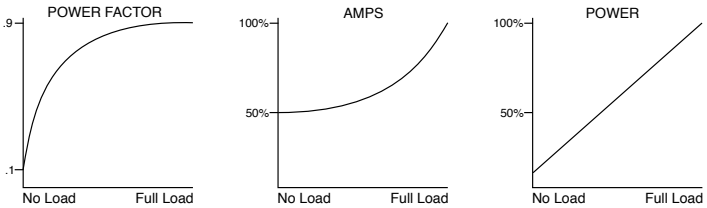

The Power Cell Uses Balanced Hall Effect Sensors

- Sensitive at low and high frequencies
- Fast Response
- Linear output
- Senses distorted waveforms
- Noise immune
- Accuracy is improved by eliminating the large phase shift errors from the CTs and PCs at low power factors

Balanced Hall Effect sensors are used to measure power with odd shapes and frequencies (like on a Variable Frequency Drive). A Hall Effect sensor has these two characteristics:

- It senses a magnetic field which is proportional to the current flowing through the conductor.
- The Hall Effect semiconductor can multiply two signals. Each Hall Effect Sensor is powered by the signal that comes from the voltage sample for that phase. The Hall device multiplies these voltage and current signals.

This is a vector multiplication which also calculates the lag of the current (power factor). The resulting output is then proportional to power (Volts x Amps x Power Factor).

LOAD CONTROLS INCORPORATED

53 Technology Park Road | Sturbridge, MA 01566 | ph: 888-600-3247 | fx: 508-347-2064 | loadcontrols.com

Appendix B

Product Data

Hysol X

Premium Quality Chlorine Free Soluble Cutting Fluid

DESCRIPTION

Castrol Hysol X has been formulated using chlorine-free high performance additives to ensure exceptional cutting characteristics where the cutting process is particularly arduous eg. broaching and where the metal is difficult to machine eg. Stainless Steel, nimonics etc.

APPLICATION

Castrol Hysol X contains specially developed extreme pressure and lubricity additives that are equal to the demands of creep feed grinding and may other arduous operations. It has such exceptional cutting properties that in some instances it is possible to replace some neat oil applications with it. The high performance additives also allow the product to be used for general purpose applications such as cutting of steel. Castrol Hysol X incorporates advanced additive technology to control fungal and bacterial growth ensuring exceptional bath life and means the product can be used equally well in central systems or single sump machines and reduces the need for fluid maintenance.

FEATURES	BENEFITS
High performance synthetic lubricity additives	Exceptional tool-life and surface finish
	Can replace neat oils in some applications
Optimised surfactant package	Inherently low foam
Advanced additive technology	Long bath life
	Reduced need for maintenance
Chlorine free	Environmentally acceptable

Castrol International
Pipers Way
Swindon
SN3 1RE
United Kingdom
Tel +44 (0)1793 452111
Fax +44 (0)1703 486083

For maximum service life, coolant systems should be cleaned and sterilised by treatment with Castrol System Cleaner before changing to Hysol X. Treatment entails the addition of approximately 1% System Cleaner to the previous charge of coolant the day before it is due to be discarded.

TYPICAL PHYSICAL CHARACTERISTICS

Concentrate		
Appearance	-	Dark Amber
Density at 20ºC kg/m³	-	0.990
Emulsion		
Appearance	-	Milky emulsion
pH at 3% Concentration	-	9.0 - 9.5
Refractometer Correction Factor	-	1.02

RECOMMENDED CONCENTRATIONS

Material	Mild and Low Carbon Content Steels	Stainless Steels	Nimonic Alloys	Heat Resistant
Operation				
Multi-Tool Lathes	4%	5%	5%	5%
Gear Cutting	4%	5%	6%	6%
Deep Hole Drilling	5%	7%	7%	7%
Creep feed grinding	5%	5%	5%	5%
Broaching	5%	6-7%	8%	8%
General Machining	4%	5%	5%	5%

ADDITIONAL INFORMATION

Note that if the concentration of Hysol X should become too high, above a maximum of 10% not only will the emulsion become unstable but there is also the possibility of skin complaints among operators.

Hysol X
30/04/2004

Castrol International
Pipers Way
Swindon
SN3 1RE
United Kingdom
Tel +44 (0)1793 452111
Fax +44 (0)1703 486083

Product Data

Castrol Variocut® G 600 SP

Neat Grinding Oil

Description

Castrol Variocut G600 SP is a low viscosity chlorine and zinc free neat grinding fluid.

Application

Castrol Variocut G600 SP is particularly suited to high speed, creep feed and especially gear grinding using. Its low viscosityalso gives it good performance in the process of belt or tape finishing where a thin oil with exceptional flushing properties is required.

Advantages

- Helps resist burning on gear teeth, gives good wheel life and oil life.
- Backed by manufacturers
- Even at high pressures and flow rates
- Easier to dispose off, and more environmentally friendly

Characteristics

	Unit	Test Method	Value
Appearance		Visual	Clear yellow fluid
Relative Density	@ 15 °C		0.833 – 0.853
Viscosity	cSt @ 40 °C (104 °F)	CN-TM-101	9 - 11
Flash Point	PMCC °C	CN-TM-039	>173.89
Flash Point	COC ° F		345 °F

Castrol Variocut G600 SP
03.09.2005, Version Number 2.0

Castrol Industrial North America Inc.
150 W. Warrenville Road
Naperville, IL 60563
Tel (877) 641 1600
Fax (877) 648 9801

www.castrol.com/industrial